Commissioning of a Compton camera for medical imaging

Saad Aldawood

München 2016

Commissioning of a Compton camera for medical imaging

Saad Aldawood

Dissertation
der Fakultät für Physik
der Ludwig-Maximilians-Universität
München

vorgelegt von
Saad Aldawood
geboren in Riyadh

München 2016

Erstgutachter: PD Dr. Peter Thirolf
Zweitgutachter: Prof. Dr. Otmar Biebel
Eingereicht am 23.11.2016
Tag der mündlichen Prüfung: 17.01.2017

Zusammenfassung

Das Interesse am Einsatz der Teilchentherapie in der Behandlung von Krebserkrankungen steigt kontinuierlich, insbesondere bei Tumoren in der Nähe von kritischen Organen, aufgrund der Fähigkeit dieser Behandlungsmethode zu einer präzisen Verabreichung der therapeutischen Dosis. Um diese vorteilhafte Eigenschaft in vollem Umfange nutzen zu können, bedarf es zwingend zu gewährleisten, dass die im Bragg-Peak gut lokalisierte Dosis im Tumorvolumen zu liegen kommt. Dies ruft nach einer präzisen in-vivo Kontrolle der Teilchenstrahl-Reichweite (für Protonen oder Ionen). Daher ist das Ziel unseres Projektes die Entwicklung eines in-vivo Bildgebungs-Systems, basierend auf einer Compton-Kamera, zur Überwachung der Teilchenstrahl-Reichweite durch den Nachweis von Multi-MeV prompten γ-Strahlen, die aus Kernreaktionen zwischen dem Teilchenstrahl und dem biologischen Gewebe stammen.
Im Zusammenhang mit dieser Arbeit wurde der Prototyp der LMU Compton-Kamera deutlich verbessert und ausgebaut und seine Eigenschaften sowohl im Labor als auch unter Online-Bedingungen mit Teilchenstrahlen an verschiedenen Beschleunigeranlagen charakterisiert.
Die Compton-Kamera besteht aus zwei Hauptbestandteilen: einem Streuer (Tracker) aus einem Stapel von sechs doppelseitigen Silizium-Streifenzählern (DSSSD) und einem monolithischen $LaBr_3$:Ce Szintillationsdetektor (5x5x3 cm^3), der als Absorber wirkt. Die Signale der hochsegmentierten Streifenzähler, jeweils mit 128 Streifen pro Seite (Streifenbreite 0.39 mm), werden von einer kompakten, ASIC-basierten Elektronik (1536 Signalkanäle) verarbeitet, während der Szintillationsdetektor von einem 256-fach segmentierten, ortsempfindlichen Photomultiplier ausgelesen wird und Energie- und Zeitinformation für jedes PMT-Segment liefert. Der schichtweise Aufbau des Streudetektors der LMU-Compton-Kamera ermöglicht nicht nur die Rekonstruktion des Ursprungs der einfallenden Photonen, sondern erlaubt auch die Spur-Rekonstruktion der Compton-gestreuten Elektronen, was wiederum eine Erhöhung der Rekonstruktionseffizienz im Vergleich zum konventionellen Kameraaufbau erlaubt.
Der Compton-Kamera-Absorber ($LaBr_3$:Ce Szintillationskristall) wurde für zwei verschiedene Weisen der Oberflächenverpackung charakterisiert: absorptiv oder reflektiv. Die (ortsabhängige) Energieauflösung und die Zeitauflösung wurde für beide Verpackungs-Szenarien bestimmt, wobei sich deutlich bessere Eigenschaften dieses modernen Szintillatormaterials für den Fall der reflektiven Seitenbeschichtung zeigten: eine exzellente und ortsunabhängige Energieauflösung ($\Delta E/E$ =3.8 % bei 662 keV) und eine hervorragende Zeitauflösung von 273(6) ps (FWHM). Zusätzlich wurde der Einfluß der Kristall-Verpackungsoptionen auf die Szintillationslicht-Verteilung untersucht, indem die 'Light-Spread-Function' (LSF) durch Bestrahlung des Kristalls mit einer kollimierten ^{137}Cs-Quelle ermittelt wurde. Hier zeigt wie erwartet der absorptiv verpackte Kristall einen etwas kleineren Wert der LSF-Halbwertsbreite im Vergleich zur reflektiven Version. Nichtsdestoweniger gaben die deutlich besseren sonstigen Detektoreigenschaften des reflektiv verpackten Kristalls den Ausschlag dafür, diese Version als Absorber der Compton-Kamera einzusetzen.
Die Fähigkeit des monolithischen $LaBr_3$:Ce Szintillators zur Positionsbestimmung des Photonen-Wechselwirkungsortes, eine Grundvoraussetzung für die angestrebte Ursprungs-Bestimmung der einfallenden Photonen mittels der Compton-Streuung, wurde durch den Einsatz zweier spezifischer Algorithmen bestimmt: 'k-nearest neigbour' (k-NN) und 'Categorical Average Pattern' (CAP)). Diese Algorithmen basieren auf einer großen Referenzbibliothek aus zweidimensionalen Szintillationslicht-Verteilungen, die durch die senkrechte Bestrahlung der Szintillator-Frontfläche mit einer eng kollimierten (1 mm Durchmesser) γ-Quelle auf einem feinen Raster (0.5 mm Schrittweite) erzeugt wurde. Zwei γ-Quellen, ^{137}Cs and ^{60}Co, wurden zur Erzeugung der benötigten Referenzbibliotheken und damit zur energieabhängigen Untersuchung der Ortsauflösung des $LaBr_3$:Ce Szintillators eingesetzt. Systematische Parameterstudien wurden für beide Algorithmen als Funktion der Photonen-Energie, der PMT-Segmentierung, der Bestrahlungs-Gitterschrittweite und der Zahl der in jeder der ca. 10^4 Bestrahlungspositionen aufgenommenen Photopeak-Ereignisse durchgeführt. Die besten Werte

der Ortsauflösung wurden mit 4.8(1) mm (FWHM) bei 662 keV und 3.7(1) mm (FWHM) bei 1.3 MeV mit dem CAP-Algorithmus erzielt, womit bereits nahezu das erst für den wesentlichen höheren Energiebereich der prompten Photonen bei 4-6 MeV angestrebte Designziel von 3 mm erreicht wurde. Mit dem beobachteten Trend einer Verbesserung der Ortsauflösung mit ansteigender Photonen-Energie wird es interessant sein, diese Detektor-Eigenschaft weit jenseits des Energiebereichs der Labor-γ-Quellen oberhalb von 4 MeV zu untersuchen. Dies setzt die Verfügbarkeit eines intensiven, monoenergetischen und kollimierten Photonenstrahls voraus.
Weiterhin wurde die Compton-Kamera an verschiedenen Teilchen-Beschleunigeranlagen charakterisiert. Die Detektorkomponenten wurden zuerst mit monoenergetischen 4.44 MeV-Photonen aus der Kernreaktion ^{15}N(p,$\alpha\gamma$)^{12}C* am Helmholtz-Zentrum Dresden-Rossendorf (HZDR) kalibriert und charakterisiert. Das Verhalten der Streu- und Absorberdetektoren erwies sich als in guter Übereinstimmung mit Monto-Carlo-Simulationen. Weiterhin wurde die Fähigkeit des Absorberkristalls zur Flugzeitmessung am Garchinger Tandem-Beschleuniger mit einem gepulsten (400 ns Pulsabstand) 20 MeV-Deuteronenstrahl untersucht, der auf ein Wasserphantom traf. Die prompte Komponente der γ-Strahlung konnte deutlich vom verzögerten Neutronenuntergrund getrennt werden. Schliesslich wurde die Kamera mit verschiedenen klinischen Protonenstrahlen (100 MeV, 160 MeV und 225 MeV) am Forschungs-Strahlrohr der Universitäts Protonen Therapie Dresden charakterisiert, wobei die Strahlen entweder auf ein Wasser- oder auf ein PMMA-Phantom trafen. Energiespektren wurden aufgenommen und durch Flugzeitmessung in ihre prompten und verzögerten Anteile zerlegt. Die Energie-Deposition der Compton-gestreuten Elektronen wurde in jedem der Si-Streifenzähler gemessen und stimmte sehr gut mit der Erwartung aus Simulationsrechnungen überein. Ansprech-Multiplizitäten und die damit verbundene Fähigkeit zur Bestimmung der Elektronen- Trajektorien in der Streuer-/Tracker-Einheit wurden untersucht und es wurden durch die derzeitige ASIC-Auslese-Elektronik auferlegte Begrenzungen wie auch Optionen für weitergehende Verbesserungen identiziert.

Summary

The interest of using hadron-therapy in cancer treatment, particularly for tumors in the vicinity of critical organs-at-risk, is continuously growing due the ability of this treatment modality to provide high precision dose delivery. In order to fully exploit this beneficial property, it is mandatory to ensure that the well-localized dose deposition (Bragg peak) is located in the tumor volume. This calls for a precise in-vivo monitoring of the particle (proton, ion) beam stopping range. Therefore, the purpose of our project is to develop an in-vivo imaging system based on a Compton camera to verify the particle beam range by detecting (multi-MeV) prompt γ rays, generated as a result of nuclear reactions between the particle beam and biological tissue.

In the context of this thesis the prototype of the LMU Compton camera was considerably improved and upgraded, and characterized both in the laboratory as well as under online conditions with particle beams at various accelerator facilities.

The Compton camera consists of two main components: a scatterer (tracker), formed by a stack of six double-sided Si-strip detectors (DSSSD), and a monolithic $LaBr_3$:Ce scintillation detector (5x5x3 cm^3), acting as absorber. The highly segmented DSSSD detectors, each with 128 strips per side (strip pitch: 0.39 mm), is processed by a compact ASIC-based electronics (1536 signal channels), while the scintillation detector is read out by a 256-fold segmented, position-sensitive multi-anode photomultiplier tube, providing energy and time information for each PMT segment. The stacked design of the LMU Compton camera scatter detector allows not only to reconstruct the incident photon origin, but it also allows to track Compton scattered electrons, thus enhancing the reconstruction efficiency compared to the conventional design.

The Compton camera absorber ($LaBr_3$:Ce scintillator crystal) was characterized in two different side-surface wrapping scenarios, absorptive and reflective. (Position-dependent) energy resolution and time resolution were determined for both coating scenarios, revealing the superior properties of the advanced scintillator material in case of the reflectively coated crystal, providing excellent energy (position independent: $\Delta E/E$ =3.8 $\%$ at 662 keV) and time resolution (273(6) ps FWHM). In addition, the impact of the crystal wrapping options on the scintillation light distribution was studied by extracting the Light Spread Function (LSF) from the crystal irradiation with a collimated ^{137}Cs source. Here, as can be expected, the absorptively coated crystal reveals a slightly better FWHM value of the LSF compared to the reflectively coated detector. Nevertheless, the drastic improvement of the other properties with reflective coating motivated this choice for the Compton camera absorber.

The capability of the monolithic $LaBr_3$:Ce scintillator to provide the γ-ray interaction position, which is a mandatory prerequisite for the targeted photon source reconstruction based on Compton scattering, was determined by applying two specific algorithms ('k-nearest neighbor' (k-NN) and 'Categorical Average Pattern' (CAP)). These algorithms require a large reference data base of 2D scintillation light amplitude distributions, acquired by perpendicularly irradiating the scintillator front surface with a tightly (1 mm diameter) collimated photon source on a fine grid (0.5 mm step size). Two γ-ray sources, ^{137}Cs and ^{60}Co, were used to generate the required reference libraries in order to study the energy-dependent spatial resolution of the $LaBr_3$:Ce scintillator. Systematic parameter studies were performed as a function of the photon energy, PMT granularity, irradiation grid size and number of photopeak events acquired in each of the 10^4 irradiation positions. Optimum values for the spatial resolution were achieved with 4.8(1) mm (FWHM) at 662 keV and 3.7(1) mm (FWHM) at 1.3 MeV using the CAP algorithm, thus almost reaching the final design goal of 3 mm envisaged for the prompt-γ energy region of 4-6 MeV. With the observed trend of improving spatial resolution with increasing photon energy, it will be interesting to study this property beyond the realm of γ-ray calibration sources in the higher energy region beyond 4 MeV, provided the availablility of an intense, monoenergetic

and collimated photon beam.
Furthermore, the Compton camera has been commissioned at different particle beam facilities. The camera components were first calibrated and characterized with monoenergetic 4.44 MeV γ rays generated via the nuclear ^{15}N(p,$\alpha\gamma$)^{12}C* reaction at the Helmholtz-Zentrum Dresden-Rossendorf (HZDR). The response of both the scatter and absorber detectors was found in good agreement with Monte-Carlo simulations. Moreover, the time-of-flight (TOF) measurement capability of the absorbing scintillator was studied at the Garching Tandem accelerator, using a 20 MeV pulsed (400 ns) deuteron beam hitting a water phantom, showing prompt γ rays well separated from the slower neutron background. The camera was finally commissioned with different clinical proton beams (100 MeV, 160 MeV and 225 MeV) at the research area of the Universitäts Protonen Therapie Dresden, stopping either in a water or a PMMA phantom. Energy spectra were acquired and separated into their prompt and delayed components, extracting the prompt photon contribution via TOF. The Compton electron energy deposit in each DSSSD layer was determined and found in very good agreement with simulation expectations. Hit multiplicities and the correlated electron tracking capability of the scatter/tracker array were investigated and limitations imposed by the present ASIC-based readout electronics, as well as options for further improvements, were identified.

Contents

Chapter 1

Introduction and Motivation

This chapter is intended to provide an introduction into the motivation of this thesis. The first part of this chapter emphasizes the rationale behind using hadron therapy instead of the conventional (photon-based) radiotherapy. Then, the origin of ion beam range uncertainties associated with hadron therapy will be addressed. This is followed by a list of different approaches that are being investigated to provide an in-vivo diagnostic tool for range monitoring during ion beam treatment. This list includes positron emission tomography (PET) and prompt γ rays-based imaging as well as the recent approach of ionoacoustic studies via ultrasound detection. Ion beam range monitoring via prompt γ-ray imaging can be developed into several technical approaches to tackle the good of ion beam range verification. These different approaches will be briefly introduced. Finally, the objectives of this thesis as well as its structural organization will be given.

1.1 Ion beam therapy

In recent years, cancer diseases figure among the leading causes of morbidity and mortality worldwide. In 2014, it was reported that approximately 1 in 7 worldwide recorded deaths were caused by cancer [1]. In the same year, nearly 14 million newly diagnosed cancer patients were recorded [1]. Meanwhile, huge scientific and economical efforts have been invested in developing various cancer treatment modalities (beyond surgery), namely radiation therapy and chemotherapy. The patient can be primarily treated by radiation or together with either chemotherapy or surgery. Conventional radiation therapy is based on bremsstrahlung photons, which are generated with a linear accelerator. The development of this therapy approach started immediately after the discovery of the X-rays by Röntgen in 1896 [2]. In the last decades, the interest in using accelerated charged particles in cancer treatment has continuously grown due the provided ability of high-precision dose delivery. This treatment modality is known as proton (or ion) beam therapy, which was first proposed by Wilson in 1946 [3].
Shortly after this pioneering proposal, the first cancer patient treatments with the proton beam were performed in the US at the Berkeley Radiation Laboratory (in 1954) and at Uppsala University in Sweden (in 1957) [4]. Since then, the hadron-therapy development gained a slow momentum until 1990, when the announcement of opening the first hospital-based proton facility in Loma Linda University (the USA) was released. From that moment, not only the number of proton-therapy facilities has been steadily increasing, but also other types of ions, such as predominantly ^{12}C, in the recent years also ^{16}O and ^{4}He, have gained a great interest. So far, about 15000 patients are treated by hadron therapy per year worldwide [5]. Most of the treatments are performed with proton beams, which represent 86% of the total treated patients per

year, while carbon ions and other type of ions contribute by 14% [5].

1.1.1 Rationale for particle therapy

The main aim of radiation therapy is to maximize the transferred dose in the targeted volume, while minimizing it in the surrounding regions. The ratio between these quantities is known as the radiotherapy ratio. In order to compare the radiotherapy ratio for the conventional radiotherapy and proton therapy, the dose-depth profile of 8 MV X-rays and a 200 MeV proton beam are plotted in Fig. 1.1.1. The dose distribution of radiotherapy is characterized by an increased dose deposition at the beginning of the targeted tissue, known as the build-up effect, followed by an exponential reduction of the dose deposition along the photon path. In order to deliver the prescribed dose into the targeted volume, several irradiation fields are required, resulting in a high dose in the intersection volume. In contrast, the proton dose distribution shows already a low dose deposition at the entrance into the tissue volume, since the Coulombic interaction is inversely proportional to the square of the proton velocity, which in turn results in a high and well-localized dose deposition at the end of its path, known as the Bragg peak. It can be inferred that the depth of the Bragg peak correlates with the initial kinetic energy of protons or ions. Thus, by sending a stacked sequence of several energy layers of the proton (or ion) beam into the tumour volume, the so-called Spread Out Bragg Peak (SOBP) is constituted with a specific plateau width adjusted to the targeted tumour volume [6]. The variation of the proton beam energy and the resulting SOBP, covering a 5 cm wide region, can be seen in Fig. 1.1.1, represented by several black curves and the resulting dashed blue curve, respectively. The advantages of the hadron therapy, represented by the proton beam in this case, can be realized by comparing the integrated dose of the SOBP at the entrance to the one deposited by the photon beam, as well as by the absence of the deposited dose in the healthy tissue behind the tumour

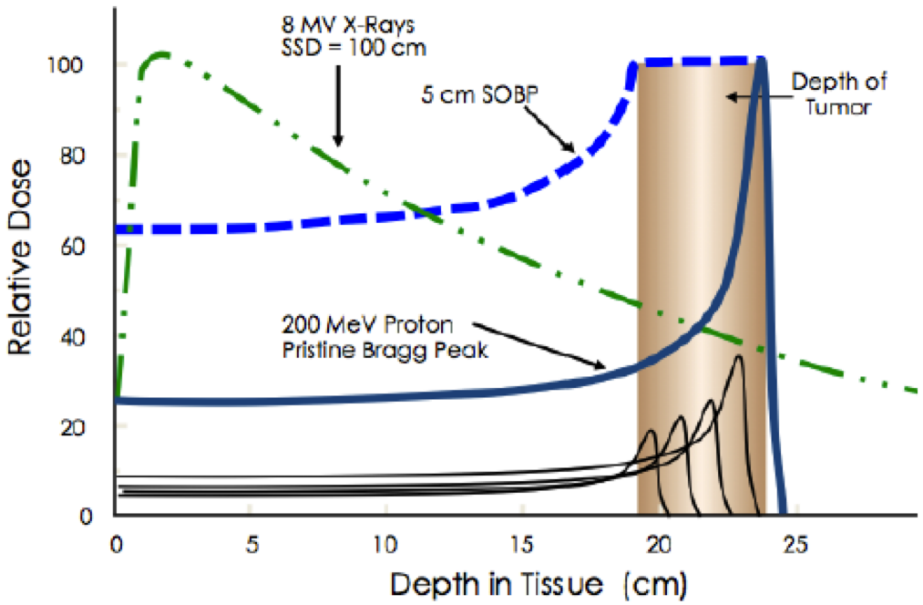

Figure 1.1.1: Exemplary illustration of the depth-dose profile of 8 MV X-rays (green dash-dotted curve) and a 200 MeV proton beam (solid blue curve). The black curves represent the result of a variation of the proton beam energy, which in turn varies the Bragg peak position in order to form the so-called Spread Out Bragg Peak (SOBP), required to cover the shaded target region [4].

volume. Moreover, the dose of the ion beam can conformally cover the region of interest with only a few irradiation fields, thanks to the SOBP. In addition, due to the dose deposition characteristics of the Bragg peak, potentially close-lying critical organs-at-risk can be saved from being irradiated, which is much harder to achieve with the conventional radiotherapy.

1.1.2 Range uncertainties

Despite the high accuracy of the ion beam energy provided by the beam delivery system, some external uncertainties affect the range of the depth-dose distribution in the target medium. The consequences of these range uncertainties are particularly severe for the case of ion beams, since the linear energy transfer (LET) reaches its maximum at the end of the ion path, which in turn increases the ionization density. An error associated with under-estimating the prescribed dose would result in a serious under-dosage of the target volume. On the other hand, a shift of the ion beam range beyond the expected Bragg peak region could cause damage to an organ-at-risk in this area.

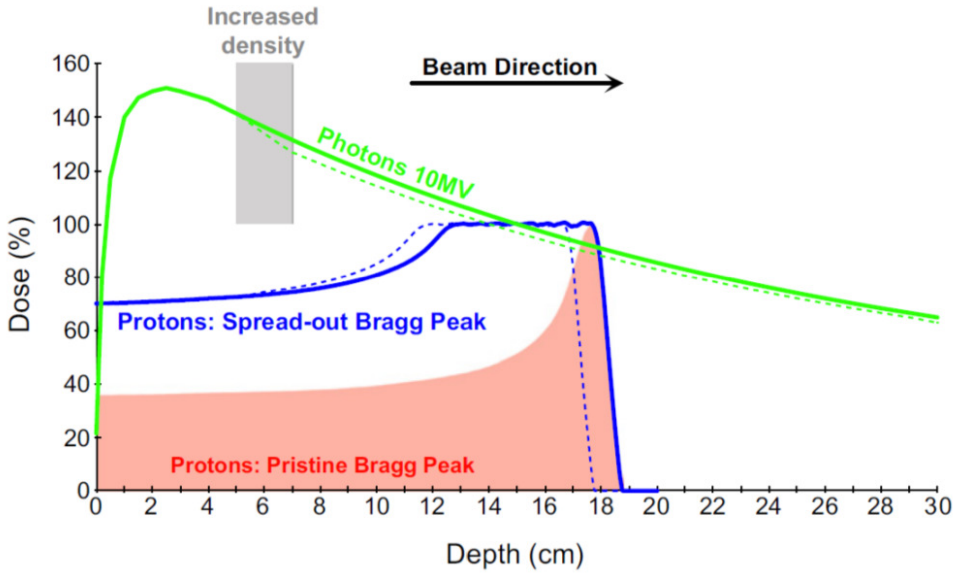

Figure 1.1.2: Depth-dose distributions of photons and the modulated proton beam (SOBP), represented by the solid green and blue curves, respectively. These distributions are subject to uncertainties (dashed curves), resulting, in this case, from an increasing medium density (grey shaded area) as an indication of an anatomical change that occurred to the patient [7].

The sources of the external range uncertainties can be divided into uncertainties associated with the calculated dose and an eventual mismatch between the treatment planning and the dose delivery. Since the dose calculation is based on an image obtained by X-ray computed tomography (CT), this branch of uncertainties can be attributed to the degree of image quality, the conversion of the CT number (Hounsfield unit) to the ion stopping power and to the used treatment planning approximations [8]. The second source of ion beam range uncertainties is related to potential anatomical variations of the patient during the treatment. This includes an eventual mispositioning of the patient before the treatment. Moreover, also organ motion or weight loss, which includes also the tumour size variation, strongly affect the ion beam range [9]. In order to avoid the risk associated with these uncertainties, a safety margin is added to the target volume. Using a proton beam, this margin varies from 2 mm to 15 mm, depending on the hospital policy [9]. For example, it is chosen to be 3.5% of the calculated proton range

plus 2 mm at the Universtäts Protonen Therapie Dresden [10], whereas a margin of 3.5% of the range plus 1 mm is applied at the Massachussetts General Hospital (MGH) [9]. Aiming to minimize the safety margins and to fully exploit the benefits of particle therapy, an in-vivo range verification is mandatory in proton and ion-beam therapy.

1.2 In-vivo ion beam range verification

Over the past 15 years, many groups of physicists and engineers have been extensively working towards a diagnostic tool that is capable of monitoring the proton (ion) beam during the treatment. This section is dedicated to explaining different approaches of in-vivo range verification that are based on different types of secondary emissions, namely ionoacoustic ultrasound signals, positron-annihilation γ rays and prompt γ rays, each resulting as the proton (ion) beam passes through a tissue. Shown in Fig. 1.2.1 (left panel), the ionoacoustic ultrasound signal, based on thermoacoustic effect, is generated as a result of the interaction between the incident proton and the atomic electrons, resulting in a local heat shock wave, which subsequently generates a pressure wave. Inelastic nuclear interactions between the proton beam and the medium constituents result in short-lived (β^+ emitting) radioisotopes, such as ^{11}C and ^{15}O, and excited nuclei, which decay to the ground state by emitting discrete prompt γ rays. These secondaries are indicated in the middle and right panel of Fig. 1.2.1. Different in-vivo range verification approaches, based on the above mentioned secondary radiation components, will be presented in the following subsections.

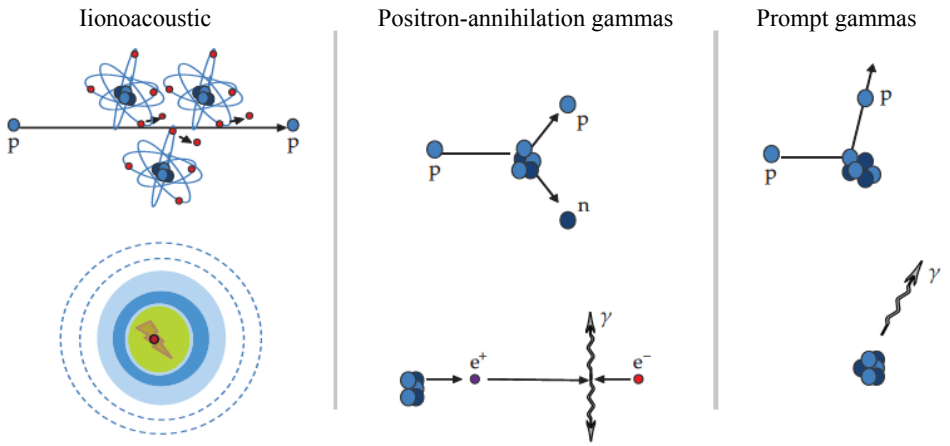

Figure 1.2.1: Possible secondary emissions, namely ionoacoustic ultrasound signal, positron-annihilation γ rays and prompt γ rays, associated with the proton (ion) beam passage through matter [1].

1.2.1 Ionoacoustic

A novel non-nuclear approach of localizing the Bragg peak in hadron therapy could be based on the thermoacoustic effect induced by the impinging ion beam. This idea is inspired by the widely used photoacoustic or optoacoustic effect, where pressure waves are generated due to the expansion process of an irradiated medium in response to the temperature increase during the local absorption of light. This phenomenon similarly occurs with ion beams, strongest at the Bragg peak, where most of the ion energy is transferred to the surrounding tissue. Thus, detecting the thermoacoustic waves using high frequency transducers will give direct information

about the range of the ion beam. The applicability of this technique into clinical conditions was examined by [11] at the Proton Medical Research Center Tsukuba in Japan. Recently, extensive simulation and experimental studies on the applicability of the ionoacoustic technique with a pencil proton beam as well as heavier ions using water phantom, have been carried out by different groups worldwide, such as at the Medical Physics department of LMU Munich [12, 13] and at the University of Pennsylvania and Purdue in the USA [14, 15]. Although this approach seems promising and less complex compared to secondary radiation (β^+ emitters and prompt γ rays) based techniques, its applicability to heterogeneous tissue has to be further investigated.

1.2.2 Positron emission tomography (PET)

During the passage of the particle (proton or ion) beam though the medium of the biological tissue, secondary radio-isotopes, including β^+ emitters, are induced via nuclear fragmentation reactions. These isotopes can be used to monitor the range of the ion (proton) beam by detecting the positron annihilation photons by utilizing the positron emission tomography (PET) technique. In 1969, this technique was initially proposed and experimentally tested by Maccabee et al. using an alpha particle beam [16]. Since then, many groups have investigated this approach for carbon ion [17] and proton therapy [18]. Table 1.1 summarizes the main β^+ emitter isotopes and their corresponding half-lives for the case of nuclear reactions between a proton beam and tissue target nuclei. In soft tissue, the most abundantly generated species are ^{15}O and ^{11}C, with half-lives of 2 min and 20 min, respectively [19]. Moreover, also β^+-decaying isotopes like ^{10}C and ^{14}O are generated, where the daughter isotope ends up in an excited state, which promptly de-excites to the ground state via the emission of a third photon in addition to the two annihilation photons. This triple coincidence is exploited in the proposed γ-PET technique discussed in Sect. 1.2.4

Isotope	Decay mode	Half-life [min]	Nuclear reaction channels
^{15}O	β^+	2.04	^{16}O(p,pn)^{15}O
^{11}C	β^+	20.39	^{12}C(p,pn)^{11}C
			^{14}N(p,2p2n)^{11}C
			^{16}O(p,3p3n)^{11}C
^{13}N	β^+	9.97	^{16}O(p,2p2n)^{13}N
			^{14}N(p,pn)^{13}N
^{10}C	β^++γ	0.32	^{12}C(p,p2n)^{10}C
			^{16}O(p,3p4n)^{10}C
^{14}O	β^++γ	1.18	^{14}N(p,n)^{14}O
			^{16}O(p,p2n)^{14}O

Table 1.1: Main β^+ emitter isotopes induced from nuclear reactions during the passage of a proton beam through an organic tissue.

The use of PET as a range verification technique in hadron therapy is so far the only approach implemented in clinical routine [20]. The practical workflow applied to this technique is displayed in Fig. 1.2.2 for a patient case with a one-field proton irradiation [19]. The planned dose (panel a) has to be simulated (panel b) in order to determine the simulated PET activity distribution (panel d). Once the planned and simulated doses are correlated, the simulated activity distribution should be compared to the measured PET activity distribution (panel c) in order to perform the treatment verification.
So far, three optional ways are currently used for PET verification of hadron therapy. Firstly, the offline-PET is used, where the patient is relocated to a nearby PET scanner room immedi-

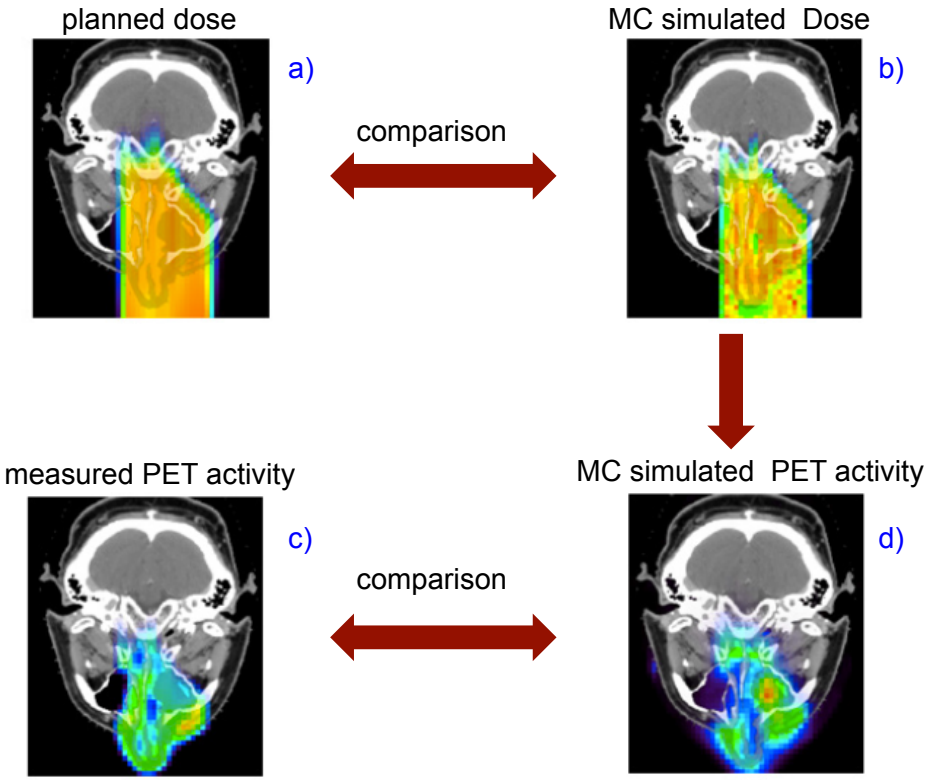

Figure 1.2.2: Exemplary illustration of the practical workflow used in the PET verification of hadron therapy for the case of a one-field proton beam irradiation. The planned dose distribution (panel a) has to match the simulated one (panel b), using Monte Carlo based simulation toolkits, before comparing the simulated (panel d) and measured (panel c) PET activity distribution. This data was taken from [19].

ately after the treatment. This approach is cost effective, since it uses the already established commercial PET system for a different application, which does not need any further hardware or software adaptation. However, the offline-PET suffers from the delay between the end of the treatment and the start of PET acquisition introduced by transporting the patient, which has negative consequences on the image quality. This delay may reach up to 30 minutes [19], leading to a signal loss from the short-lived β^+ emitter isotopes, such as ^{15}O (2 min. half-life). Thus, the method mostly relies on the ^{11}C activity. Moreover, the offline-PET image quality is strongly affected by the biological washout occurring during the patient transport period, that reduces the activity in the targeted region, thus affecting the relative activity distribution. The second PET modality used in hadron treatment verification is in-beam-PET [21], where dedicated PET detectors based on a dual-head configuration are integrated into the beam-delivery system. This approach has been used in some carbon or proton facilities around the world, such as the Gesellschaft für Schwerionenforschung (GSI) in Darmstadt, Germany [17, 22] and the Heavy Ion Medical Accelerator Center (HIMAC) in Chiba, Japan [23]. With this approach, there is no need to transport the patient, thus minimizing the issues associated with the offline-PET system. Using in-beam-PET, the data acquisition can start immediately after the dose delivery by the hadron beam for the case of a quasi-cw beam from a cyclotron even inbetween the pulse sequence from synchrotron accelerators, respectively. The drawback of this technique is that it is costly and technically demanding. Moreover, the restricted geometry of the dual-head based in-beam-PET setup with respect to the treatment beam line reduces the data collection efficiency, consequently lowering the system sensitivity and limiting its field of view.

Currently, at the National Institute of Radiological Science (NIRS) in Japan [24, 25], a huge effort has been made to overcome these limitations by developing an OpenPET system that is able to reconstruct data from all angular directions. The third PET technique used in hadron therapy treatment verification is in-room-PET [26], where a dedicated stand-alone PET scanner is implemented in the same treatment room without interfering with the beam-delivery system. As soon as the treatment is finished, the patient is moved to the PET scanner, while still on the treatment coach. This modality does not only reduce the delay time between the end of the treatment and the start of the PET imaging to about 2.5 min [19, 26], but it also minimizes the uncertainties associated with the patient repositioning. Despite the advantages and disadvantages of the above mentioned PET modalities in hadron therapy range verification, it is difficult for this technique to provide a real-time monitoring of the treatment due to the high production of prompt γ rays and neutrons.

1.2.3 Imaging based on prompt γ-rays

1.2.3.1 Scanning system

To prove of the applicability of prompt γ rays for proton range verification, as simulated by a Monte Carlo code, a scanning system was designed by [27] to observe the prompt γ rays in a small step size along the lateral path of the proton beam. This system was composed of a CsI (TI) scintillator placed behind a collimated hole, made of layers of shielding material (B_4C and Pb), as shown in Fig. 1.2.3 panel a). The idea of this shielding is to moderate neutrons via the B(n,γ) reaction and to absorb the unwanted induced γ rays by the lead material before they can reach the scintillator. A drop of the measured prompt γ-ray intensity beyond the Bragg peak was observed during the irradiation of a water phantom with different proton beam energies, as indicated in Fig. 1.2.3 panel b). Although this finding reveals a direct correlation between the prompt γ rays and the proton range, the scanning method would not be applicable for a clinical routine, since the required time for scanning along the particle beam range in the patient would take much longer than the actual treatment time.

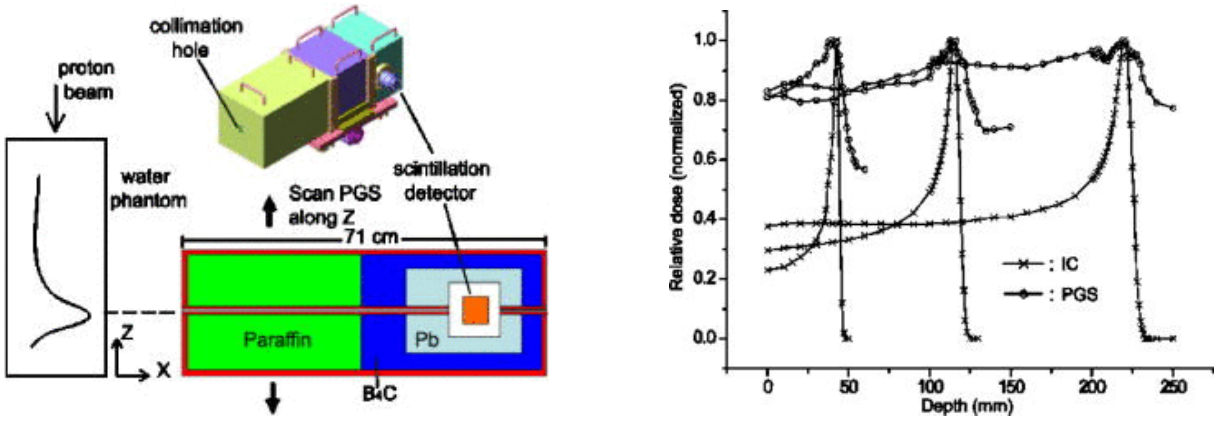

(a) (b)

Figure 1.2.3: a) Experimental design of the prompt γ-ray scanning system. Shown in b) is the correlation between the prompt γ-ray scanning (PGS) profile and the depth-dose distribution, measured by an ionization chamber (IC), for 100 MeV, 150 MeV and 200 MeV proton beams, respectively [27].

1.2.3.2 Knife-edge slit camera

Instead of the scanning method, another alternative approach for proton range monitoring is based on a slit collimation system. The concept of this camera, as shown in Fig. 1.2.4 [28], is to visualize the proton-induced prompt γ rays that pass through the slit collimation and imping onto 20 LYSO scintillator slabs of $4 \times 31.5 \times 100$ mm^3 each [29]. Due to the design of the tungsten based slit collimator, which has an acceptance angle of 53^o, and the detector arrangement, the 1D profile of prompt γ rays will be sensitively changed by proton beam range shifts. Simulation studies and corresponding experimental validations were reported in [30], revealing a potential for proton range verification. Recently, the camera has been investigated by irradiating water and head phantoms with pencil-beam scanning (PBS) proton beams of different energies at the OncoRay facility in Dresden (National Center for Radiation Research in Oncology and Universitäts Protonen Therapie Dresden [31]). The results show the capability of this camera to resolve down to 2 mm range shifts [32]. However, the applicability of this system is still under investigation for a passively double-scattered (DS) treatment proton beam, where neutron-induced background is very high, affecting the image quality.

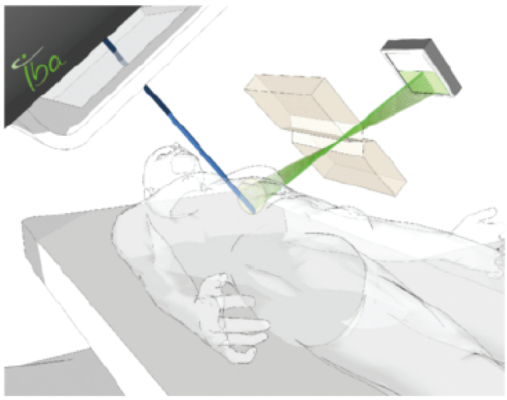

Figure 1.2.4: Conceptual design of the knife-edge slit camera for proton beam range verification via induced prompt γ-ray detection [28].

1.2.3.3 Prompt γ-ray spectroscopy

The basic principle of this approach, presently pursued at the Massachussetts General Hospital in Boston (MGH), is to directly match the detected discrete prompt γ-ray lines, induced mainly from ^{12}C and ^{16}O, with the experimentally acquired reaction cross sections. This prior determined cross sections were measured along the lateral side of the proton beam path (for energies up to 150 MeV) in a tissue equivalent phantom [33]. The imaging system used with the prompt γ ray spectroscopy method is based on a cylindrical $LaBr_3$:Ce scintillator with a length and diameter of 7.5 cm, placed behind a collimation system of $\sim$ 13 cm thick tungsten and a slit opening of 9.5 mm, as indicated in Fig. 1.2.5 [34]. The performance of this prototype was evaluated with a proton beam, revealing a precision of 1.0-1.4 mm [33]. This system is still in the phase of pre-clinical study at the Francis H. Burr Proton Therapy Center at MGH.

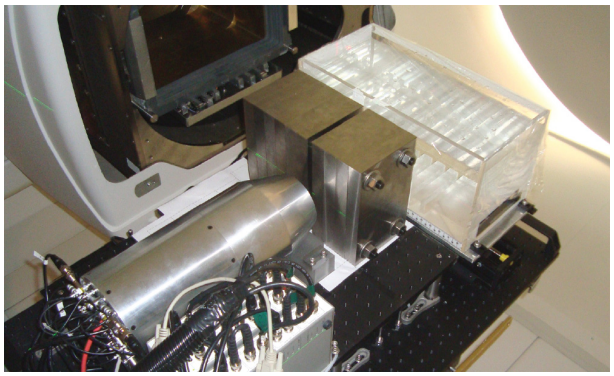

Figure 1.2.5: Prototype configuration setup of the prompt γ ray spectroscopy imaging system used for proton beam range verification [33].

1.2.3.4 Prompt γ timing

This approach is based on the transit time of the therapeutic ions in matter. This time can be measured indirectly, using the time-of-flight (ToF) technique between the stop signal provided by prompt γ rays, emitted along the beam path, and the accelerator RF start signal. This principle is simplified in Fig. 1.2.6. As indicated, the transit time becomes larger as the ion interaction is located more deeply in the target volume.

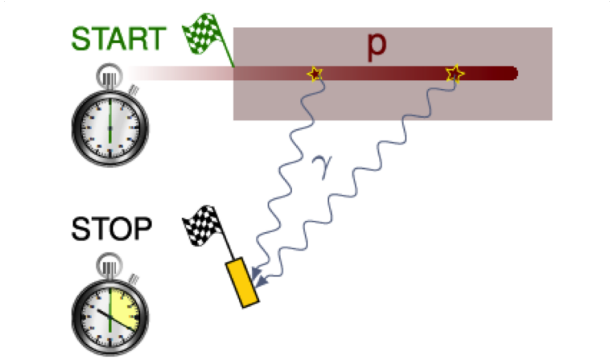

Figure 1.2.6: Descriptive illustration of the prompt γ rays timing imaging technique [10].

The prompt γ-ray timing technique for ion beam range verification has been recently introduced by [35]. It is still under investigation for a clinical use, despite promising results obtained at different proton beam energies and with various phantom types, as reported in [36, 37].

1.2.3.5 Compton camera

A Compton camera allows to reconstruct the origin of incident γ rays by exploiting their Compton scattering kinematics induced in the detector material. In contrast to the previous approaches, the Compton camera is able to provide up to three-dimensional images. The Compton kinematics can be exploited for reconstruction, either based on the scattered photon or the Compton recoil electrons. Correspondingly, the design of the Compton camera will be different depending whether or not Compton electrons are intended to be tracked or not. Based on that, the functional principle of a Compton camera can be explained as follows:

γ ray tracking

The basic principle of a Compton camera is displayed in the left panel of Fig. 1.2.7. It consists of scatter detector, usually formed by a low-Z material to increase the probability of the Compton scattering interaction, and an absorbing detector, which, in contrast, is made of a high-Z material to enhance the photo-absorption efficiency. The incoming photon gets deflected by the scatterer, where part of the incident photon energy $E_{\gamma,1}$ is transferred to the Compton-scattered recoil electron, while the scattered photon ($E_{\gamma,2}$) is absorbed by the subsequent absorbing detector. Knowing the Compton scattering kinematics from energy and interaction position measurements in both detectors and applying the energy and momentum conservation principles, the Compton scattering angle θ of the incident photon can be calculated as follows

$$cos\theta = 1 - m_e c^2 \frac{E_{\gamma,2}}{E_{\gamma,1}(E_{\gamma,1} - E_{\gamma,2})} \tag{1.2.1}$$

This angle θ also represents the opening angle of the so-called Compton cone, whose surface indicates the possible origin of the incident γ rays. This position can be further restricted by reconstructing several Compton scattering events, which then results in the intersection of many Compton cones, providing the calculated location of the photon source with a potential accuracy of a few millimeters. The derivation of Eq. (1.2.1), assuming an electron at rest to interact with the photon, does not take into account the realistic scenario of a moving bound electron, resulting in a Doppler broadening of the Compton cone, which is discussed in Sect. 2.1.1.2 for the LMU Compton camera. Figure 1.2.7 (right) shows an example of reconstructed

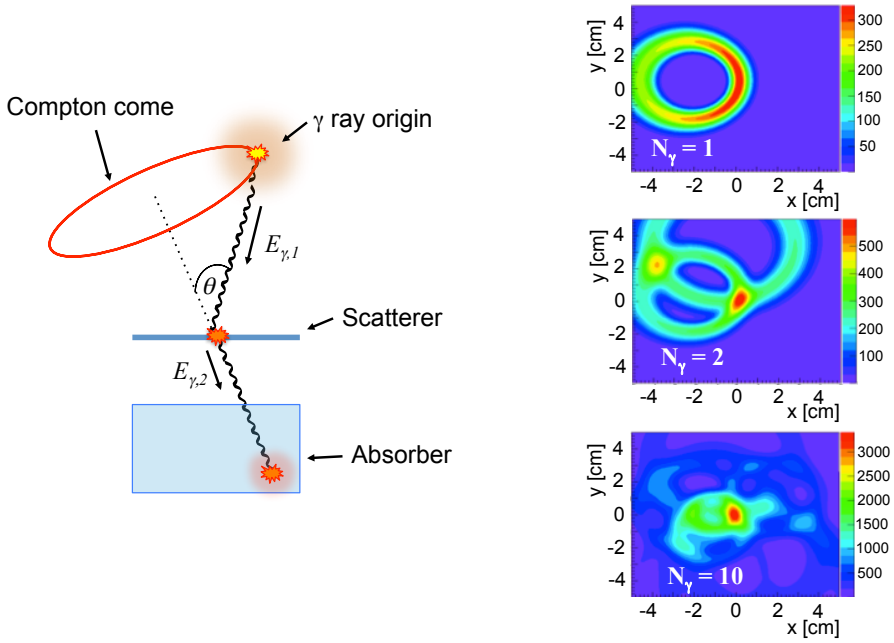

Figure 1.2.7: Left, illustration of the basic principle of the Compton camera, where only the photon information is traced. The surface of the "Compton cone", spanned by the Compton scattering angle θ, indicates the possible γ-ray source position that can be computed by exploiting the Compton scattering kinematics in both scatter and absorbing detectors. An exemplary illustration of the reconstructed Compton cones of one, two and ten (Geant4) simulated Compton scattering events are, respectively, shown in the top, middle and bottom of the right panel [38]. The intersection of many Compton cones points to the γ-ray source location.

Compton cones of one (top), two (middle) and ten (bottom) (Geant4) simulated Compton scattering events. The γ-ray source position becomes more localized when increasing the number of reconstructed events.

Electron and γ-ray tracking

The Compton camera design can be further advanced by substituting the single scatterer, presented in the previous design, by multiple thin detector layers in order to allow for an electron tracking, as displayed in the left panel of Fig. 1.2.8. Besides the photon tracking, the additional information gained from the Compton recoil electron (direction $\overrightarrow{e}$ and energy E_e) contributes to enhance the camera reconstruction efficiency, due to the ability of reconstructing also incompletely absorbed photon events. At the same time the camera sensitivity to the photon source position is enhanced by reducing the Compton cone to an arc segment [39, 40]. The length of this arc relies upon the precise measurement of the Compton recoil electron trajectory. An example of reconstructed Compton arc segments is shown in the right panel of Fig. 1.2.8 for one, two and ten (Geant4) simulated Compton scattering events.

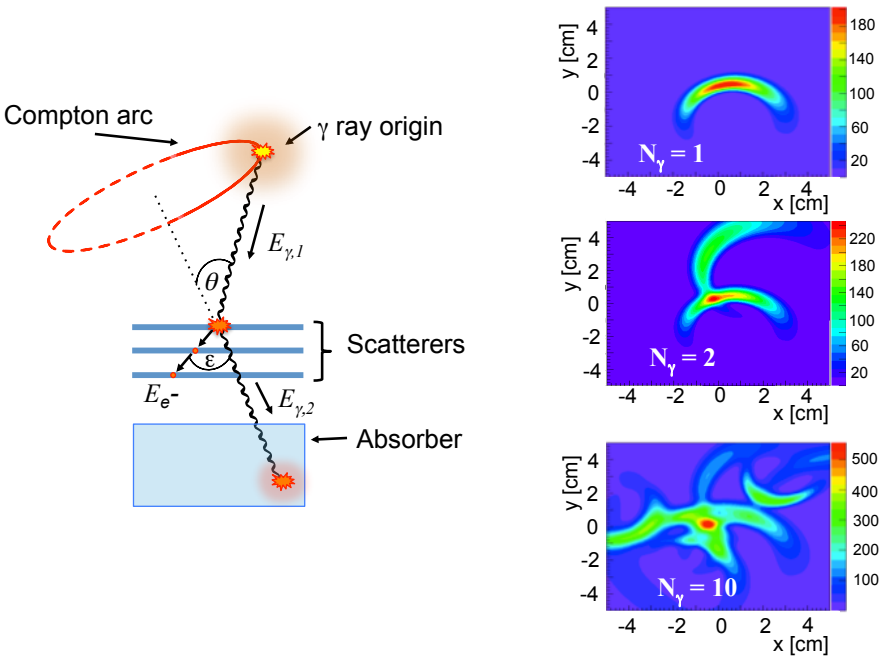

Figure 1.2.8: Conceptual design of the Compton camera with a capability of tracking the recoil Compton electron. The additional information gained from the electron tracking reduces the probability of the source position from the Compton cone to an arc segment. The exemplary illustration presented in the right panel shows the reconstructed arc segments of one (top), two (middle) and ten (bottom) (Geant4) simulated Compton scattering events. The overlap of many arc segments represents the γ-ray source position [38].

The status of the Compton camera approach in hadron therapy

The Compton camera approach has been one of the potential techniques for ion beam range verification since prompt γ rays were first proposed as a tool for this monitoring purpose. So far, many groups around the world have been investigating this approach with different detector configurations in terms of detector materials, properties and geometrical arrangements. Based

on the Compton camera principle, some groups follow the photon tracking route, while others combine both photon and Compton recoil electron tracking. In Lyon, a Compton camera prototype, formed by a stack of 10 double-sided Si-strip detector (DSSSD) layers ($90 \times 90 \times 2$ mm^3, 2×64 strips) acting as a scatterer and 100 BGO blocks ($38 \times 35 \times 30$ mm^3 for each block [41]) or alternatively LYSO scintillators ($300 \times 300 \times 40$ mm^2 [42]) as absorber, is under development. This camera is combined with an ion beam hodoscope in order to restrict the γ-ray source position to the intersection between the incoming ion trajectory and the Compton cone [43]. The ion beam range verification was simulated showing promising results [41]. The Lyon prototype is in a preparatory phase for tests with a clinical proton beam. In Dresden, a prototype was designed and commissioned based on a pixelated CdZnTe detector array ($20 \times 20 \times 5$ mm^2, 16×16 pixels) working as a scatterer and an LSO scintillator ($54 \times 54 \times 20$ mm^3, 13×13 pixels) as an absorbing component. The design specifications and optimization studies were simulated in Ref. [44], showing an angular resolution of 2.2^o at 3 MeV. This camera was experimentally tested with monoenergtic 4.4 MeV γ rays at the HZDR Tandetron facility, revealing a promising ability for proton range verification, despite a count-rate capability limitation that may become an issue for a clinical use [45]. At IFIC (Valencia), started in the framework of the European ENVISION project, a three-stages Compton camera is investigated, formed by three monolithic $LaBr_3$:Ce scintillators, each coupled to a position-sensitive SiPM. This camera was characterized in the laboratory, revealing 7.8 mm (FWHM) position resolution for a ^{22}Na source placed at 35 mm distance from the first detector [46]. Recently, two stages of the Valencia camera were tested with a 150 MeV clinical proton beam. Despite promising results that allow to identify a Bragg peak shift introduced by adjusting the PMMA phantom position with uncertainties of a few millimeters, a beam hodoscope and the use of the time-of-flight technique might be required to improve the camera's sensitivity and to suppress neutron-induced background, respectively [47]. Another four stages Compton camera based on semiconductor detectors has been investigated at the University of Maryland in Baltimore (USA) [48]. Each stage consists of a 2×2 array of pixelated (11×11 in x and y directions) CdZnTe crystals ($2 \times 2 \times 1.5$ cm^3) in total covering an area of 4×4 cm^2. The proton range verification capability was simulated [49] and experimentally examined using a 150 MeV clinical proton beam, showing the ability of the camera to resolve a range shift of as small as 3 mm [48]. For a Compton camera with Compton recoil electron tracking capability, a prototype system composed of a micro-TPC ($10 \times 10 \times 15$ cm^3, filled with air + C_2H_6 gas) acting as a scatterer and an 8×8 array of GSO(Ce) scintillators ($6 \times 6 \times 26$ mm^3 for each crystal) forming the absorbing component, is under development in Kyoto. This camera was characterized in the laboratory, revealing an angular resolution of 7^o at 662 keV [50]. The Kyoto prototype was investigated with a clinical proton beam, exhibiting a correlation between the imaged prompt γ rays and the Bragg peak position [51]. Finally to be mentioned is that a Compton camera with electron tracking capability that is under development in the framework of this thesis in Munich. It consists of a stack of six DSSSD layers, each with an area of 50×50 mm^2 (thickness of 0.5 mm), followed by a $LaBr_3$:Ce scintillator ($50 \times 50 \times 30$ mm^3), representing the absorbing detector [52]. The design specifications of this camera were simulated in Ref. [38], resulting in an expected spatial resolution of 1.5 mm for a 3 MeV point source placed at 5 cm distance from the first DSSSD layer.

1.2.4 "γ-PET"

Besides the 511 keV positron annihilation photons, some of the β^+ emitters, which are produced along the proton beam path during its passage through biological tissue (e.g. ^{10}C and ^{14}N, shown in Tab. 1.1), simultaneously emit a third (prompt) γ ray, resulting from the de-excitation of the

excited β-decay daughter nucleus. The resulting triple coincidences are the basic principle of the proposed γ-PET imaging technique, which requires an arrangement of at least three combined Compton cameras (or a hybrid system built from a conventional PET scanner plus at least one additional Compton camera system) in order to enable a PET-like imaging technique. With this system, the line-of-response (LOR) can be reconstructed by detecting the two opposite annihilation γ rays using the PET technique, while the Compton kinematics of the third prompt γ ray, registered in the Compton camera components, would result in a reconstructed Compton cone (or arc segment). Thus, the intersection of the LOR and the Compton cone represents the origin of the radiation emission, which then refers to the location of the initial proton beam interaction. The combination of two different trajectories (the LOR and the Compton cone) within one event significantly improves the image reconstruction sensitivity compared to the conventional PTE technique [53].
The γ-PET system can be used as a hybrid imaging technique for ion beam range verification. During the irradiation, the Compton camera principle can be exploited by detecting the induced prompt γ-rays. Then, the system can switch immediately to PET or γ-PET mode in order to measure the (delayed) activity distribution of the β^+ emitters, as an offline treatment verification.

1.3 Thesis context and objective

The Compton camera prototype presented in this thesis is under development at the Chair of Medical Physics at the Ludwig-Maximilians-Universität München (LMU) in the framework of developing an in-vivo particle range verification system, in particular to be applied for laser-accelerated proton beams as part of the main goals of the Center of Advanced Laser Application (CALA) project [54]. In a previous thesis project, the design specifications of this camera were simulated [38], providing the optimum detector materials and the dimensions of the imaging system arrangement that together give the optimum performance of the Compton camera. It was designed to add the Compton recoil electron trajectory information to the γ-ray tracking capability, in order to enhance the reconstruction efficiency of the camera. The camera prototype consists of two main components: a scatterer (tracker), formed by a stack of six customized double-sided Si-strip detectors (DSSSD), and a monolithic $LaBr_3$:Ce scintillation detector (50x50x30 mm^3) acting as an absorber detector.
The final objective of this thesis project was to commission the LMU Compton camera prototype at a clinical proton beam. In order to achieve that, some preparatory work, both offline in the laboratory and online using accelerated particle beams, was required to commission and characterize both camera components. Firstly, the signal processing electronics for more than 2000 channels needed to be set up and optimized, including work on the data acquisition (DAQ) system to synchronize the processed data from different detector components. This work will be discussed in Chap. 3, following the description of the interaction of photons and particles with matter, which will be presented in Chapt. 2.
Secondly, the impact of the scintillation crystal side-surface coating on the $LaBr_3$:Ce detector properties was investigated in order to provide an optimum performance of the camera absorbing detector. This investigation covers a characterization study of energy and time resolution, as well as the light spread function (LSF), of the $LaBr_3$:Ce scintillator wrapped with reflective and subsequently with absorptive crystal surface coating. The details of this study will be presented in Chap. 4.
Thirdly, aiming to extract the interaction position information of an incident γ ray in the monolithic $LaBr_3$:Ce scintillator in order to fulfill the Compton camera reconstruction requirements,

dedicated algorithms-the "k-Nearest-Neighbor" (kNN) and a modified version called "Categorical Average Pattern" (CAP)-needed to be implemented and adapted. These algorithms do not only provide the position information of the primary photon interaction, but they are also capable of deriving the spatial resolution achievable with the monolithic scintillator. The kNN and CAP algorithms require a large reference library of 2D scintillation light amplitude distributions, obtained by scanning the scintillator front face in a fine step size in x and y directions by a tightly collimated photon beam. Therefore, a motorized and remote-controlled translation system, capable of carrying ^{137}Cs and ^{60}Co was installed. This device allowed for studying the energy dependence of the spatial resolution. The description of the algorithms, the experimental procedure and the resulting data will be presented in Chapt. 5

Finally, the detector components of the Compton camera system were characterized and calibrated with multi-MeV prompt γ rays before operating them in a clinical proton beam environment. A test with 4.44 MeV monoenergetic γ rays, produced via the ^{15}N(p, $\alpha\gamma$)^{12}C* reaction was performed, providing a clean, almost background free experimental scenario. This experiment was performed at the Tandetron accelerator of the Helmholtz-Zentrum Dresden-Rossendorf (HZDR). This section is followed by a characterization study of the Compton camera components with prompt γ rays induced via nuclear reactions generated by the irradiation of a water phantom with a 20 MeV proton beam from the MLL Tandem accelerator in Garching. At the same facility, the time-of-flight (TOF) capability of the Compton camera absorber was tested with a 400 ns pulsed 20 MeV deuteron beam. Finally, the performance of the Compton camera components was studied with a clinical proton beam, provided by the cyclotron of the OncoRay facility (Dresden). The experimental procedures and the results of the mentioned online measurement campaigns will be presented in Chap. 6.

The thesis then concludes with a chapter, where a summary and perspectives for the development of the LMU Compton camera are given.

Chapter 2

Introduction to charged particle and photon interactions with matter

In this chapter, the basic physics of radiation interaction with matter will be explained. Namely, photons and neutrons, as representatives of indirect ionizing radiation, as well as directly ionizing charged particles will be addressed. Then, an overview of detector types relevant for the Compton camera project, i.e., semiconductor and scintillation detectors, will be presented.

2.1 Interaction of indirectly ionizing radiation with matter

In this type of radiation-matter interaction, the incident radiation transfers its energy to the traversed medium in two or three steps. Subsequently, secondary reaction products generated from the incident radiation, such as light or heavy charged particles, are responsible for ionizing the target medium. This interaction mechanism is specific for neutral radiation, like photons or neutrons, and will be discussed in the following section.

2.1.1 Photon interaction with matter

The electric charge neutrality of γ rays allows their passage through the target medium without experiencing an influence from the Coulomb force. Instead, γ rays interact with the atomic components of the target matter, resulting in absorption or scattering processes. The three major interaction processes, which leave a unique signature in such a detection system, are photoelectric absorption, Compton scattering and pair production. Throughout these interactions (except Compton scattering), the intensity of the incident photon flux exponentially decreases while passing through the medium. This can be described by the attenuation law

$$I(x) = I_0 \, . \, e^{-\mu_{tot} \, \cdot \, x} \tag{2.1.1}$$

where I_0 and $I(x)$ are the initial and attenuated photon flux intensity, respectively. x represents the medium thickness and μ_{tot} is the total mass attenuation coefficient, resulting from all mentioned interaction processes, taking into account the material density. The separation of the plane spanned by the atomic number of the absorber medium and the incident γ-ray energy into the regions dominated by the three interaction processes of photo absorption, Compton scattering and pair creation is shown in Fig. 2.1.1. The details of each interaction mechanism will be explained in the following sections.

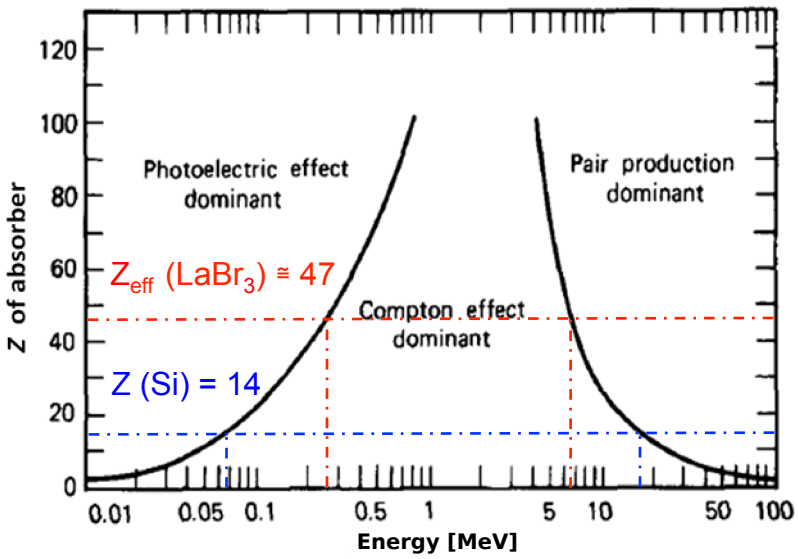

Figure 2.1.1: The curved lines indicate the borderlines of regions in the plane spanned by atomic numbers Z and incident photon energy dominated by one of the three main photon-matter interaction processes [55]. Additionally denoted by dashed lines are the atomic numbers of the Compton camera components and their interaction regions, depending on the incident photon energy.

2.1.1.1 Photoelectric Effect

The photoelectric effect is a photon interaction process, in which the incident photon transfers its entire energy to an orbital bound electron of an absorber atom. Consequently, if the photon energy exceeds the binding energy of the electron, a so-called photo-electron is ejected with a kinetic energy (E_e) equal to the difference between the incident photon energy ($h\nu$) and the electron binding energy E_b

$$E_e = h\nu - E_b \tag{2.1.2}$$

The vacancy, left by the emitted photo-electron, is rapidly filled by an electron from a higher atomic shell and the transition energy is released by either characteristic X-ray radiation (fluorescence) or an Auger electron. Due to the requirement of simultaneous momentum and energy conservation, photoelectric absorption cannot occur with a free electron. Figure 2.1.2 illustrates the photoelectric absorption cross section, represented by the mass attenuation coefficient μ_m, as a function of the incident photon energy for the LMU Compton camera detector materials: $LaBr_3$ (black curve) and silicon (red curve). The sharp discontinuities or sawtooth-like structures in both curves indicate the absorption edges and correspond to the electron binding energies of the K-, L-, etc shells of the absorbing material. So, an incident photon with an energy identical to one of the absorption edge energies will experience a sudden increase in the photo absorption cross section. As also indicated in Fig. 2.1.2, photoabsorptions is the dominant process at low incident photon energies. The probability of the photoelectric effect scales strongly with the absorber material atomic number (Z). Although this probability cannot be expressed by a strictly derived analytic expression over the full range of photon energies E_γ and Z numbers, an approximation parametrizes the photoelectric effect cross section σ as follows:

$$\sigma \cong constant \times \frac{Z^n}{E_\gamma^{3.5}} \tag{2.1.3}$$

where n varies between 3 and 5, depending on the incident photon energy [55].

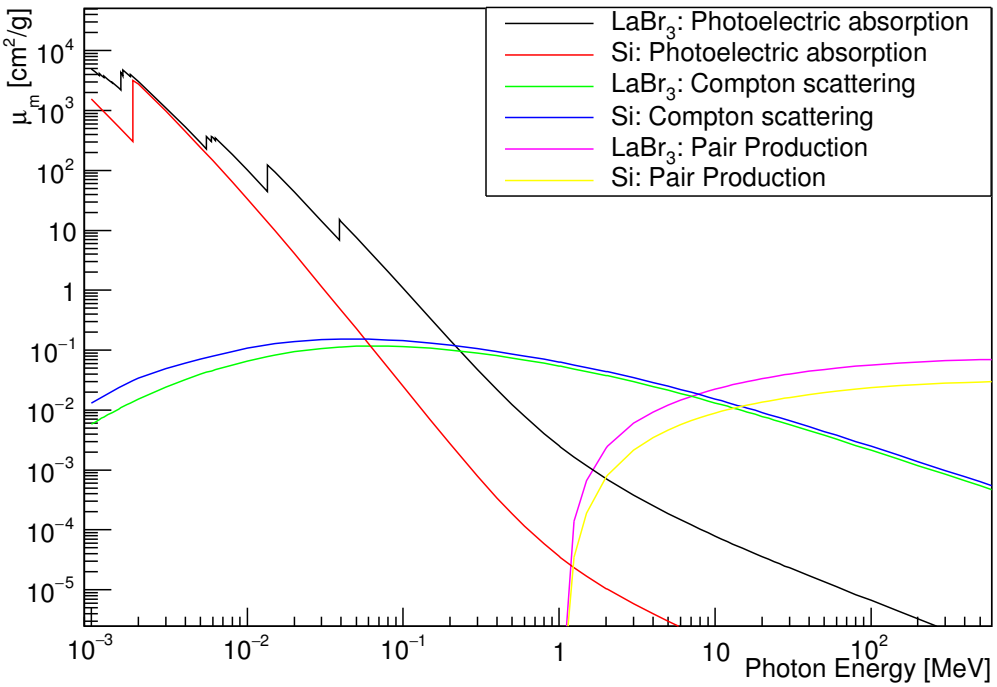

Figure 2.1.2: Photoelectric absorption, (incoherent) Compton scattering and pair production, represented by their respective mass attenuation coefficients μ_m, as a function of the incident photon energy for $LaBr_3$ and silicon [56].

2.1.1.2 Compton Scattering

In 1922, Arthur H. Compton observed a new photon-matter interaction mechanism, which led to the 1927 Nobel prize in physics being awarded to him. Moreover, this interaction was named Compton scattering. It describes an incoherent or inelastic interaction between an incident photon and a loosely bound orbital electron of an absorber atom. Figure 2.1.3 schematically illustrates this interaction mechanism, where part of the incident photon energy E_γ is transferred to an electron assumed to be resting, resulting in a recoil electron with scattering angle φ and a scattered photon with energy $E_{\gamma'}$, reduced from the initial photon energy. In contrast to the photoelectric effect, Compton scattering can occur with a free electron, since it satisfies the simultaneous energy and momentum conservation. Based on these two conservation principles and assuming the interaction to happen with a free electron at rest, one can derive the Compton wavelength shift between the incident (λ_i) and scattered (λ_s) photons

$$\lambda_s - \lambda_i = \Delta\lambda = \frac{h}{m_e c}(1 - \cos\theta) \tag{2.1.4}$$

where m_e is electron rest mass, c the speed of light and h the Planck constant. Using the relation between the photon energy and wavelength $E = \frac{hc}{\lambda}$, Eq. (2.1.4) can be rearranged to express the scattered photon energy (E_s) as a function of the incident photon energy (E_i) and the scattering angle θ as

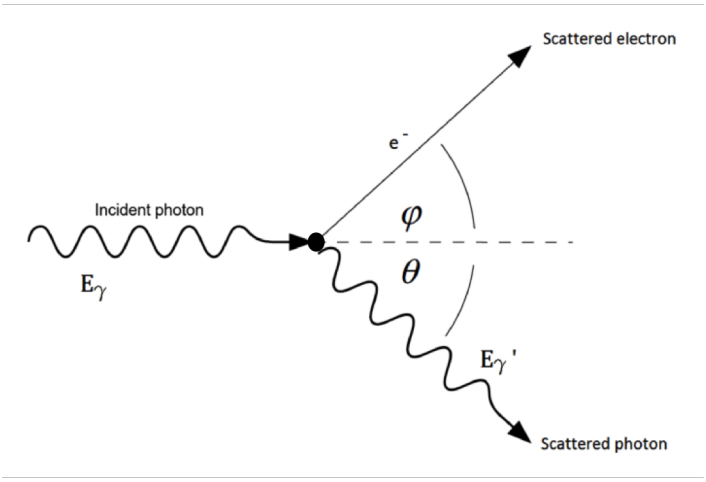

Figure 2.1.3: Schematic illustration of the (incoherent) Compton scattering process between an incident photon and an electron.

$$E_s = \frac{E_i}{1 + \frac{E_i}{m_e c^2}(1 - \cos\theta)} \tag{2.1.5}$$

The total energy E_e of the recoil electron is the sum of its kinetic energy E_e^k, which depends on the incident photon energy and scattering angle θ, and the electron rest mass energy (E_e=$m_e c^2$ + E_e^k). Using the total energy conservation principle and rearranging Eq. (2.1.5), the recoil electron kinetic energy follows as

$$E_e^k = E_i - E_s = E_i \left[\frac{\frac{E_i}{m_e c^2}(1 - \cos\theta)}{1 + \frac{E_i}{m_e c^2}(1 - \cos\theta)} \right] \tag{2.1.6}$$

Since the scattering angle θ ranges from 0° (forward scattering) through 90° (side scattering) to 180° (backscattering), the kinetic energy of the Compton electron varies for a given incident photon energy E_i. From Eq. (2.1.6), the minimum energy transfer to the Compton electron happens when the incident photon is barely deflected by the electron, i.e. for a scattering angle $\theta \cong 0°$ and the $E_i \cong E_s$. However, for the backscattering angle ($\theta = 180°$), the maximum energy of the incident photon is transferred to the recoil Compton electron. Applying this extreme scattering angle to Eq. (2.1.6), the maximum kinetic energy $E_e^{k_{max}}$ of the scattered electron can be obtained as

$$E_e^{k\ max} = E_i \left(\frac{2\frac{E_i}{m_e c^2}}{1 + 2\frac{E_i}{m_e c^2}} \right) \tag{2.1.7}$$

An exemplary illustration of a calculated Compton scattering kinematics of 5 MeV incident photons is shown in Fig. 2.1.4.

The azimuthal angular correlation of the differential Compton scattering cross section was derived shortly after the discovery of this interaction by Klein and Nishina in 1928 [58], expressed by

$$\frac{d\sigma}{d\Omega} = \frac{r_e^2}{2} \left(\frac{E_s}{E_i} \right)^2 \left(\frac{E_s}{E_i} + \frac{E_i}{E_s} - \sin^2\theta \right) \tag{2.1.8}$$

where r_0 is the classical electron radius (2.82 fm [58]). This equation also corresponds to the "unbound" Compton cross section, since it is derived for the interaction between an incident

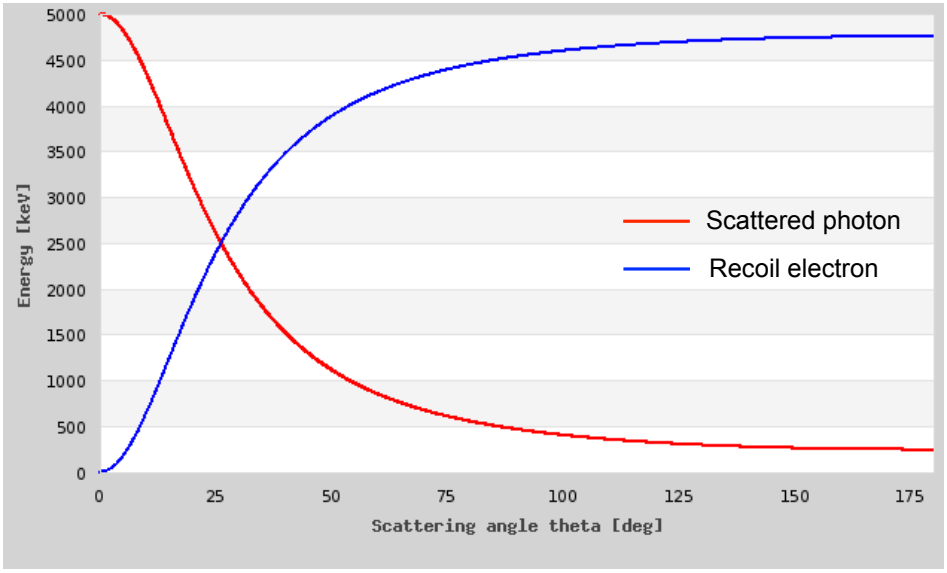

Figure 2.1.4: Compton scattering kinematics of 5 MeV incident photons [57].

photon and a free electron. Figure 2.1.5 graphically displays the Klein-Nishina cross section as a function of the azimuthal scattering angle for various incident photon energies. The smaller the photon energy, the larger the scattering angle, leading to a high energy transfer to the recoil electron as stated in Eq (2.1.6). In contrast, forward scattering, where the photon is barely interacting with the electron, is more pronounced for high incident photon energies.

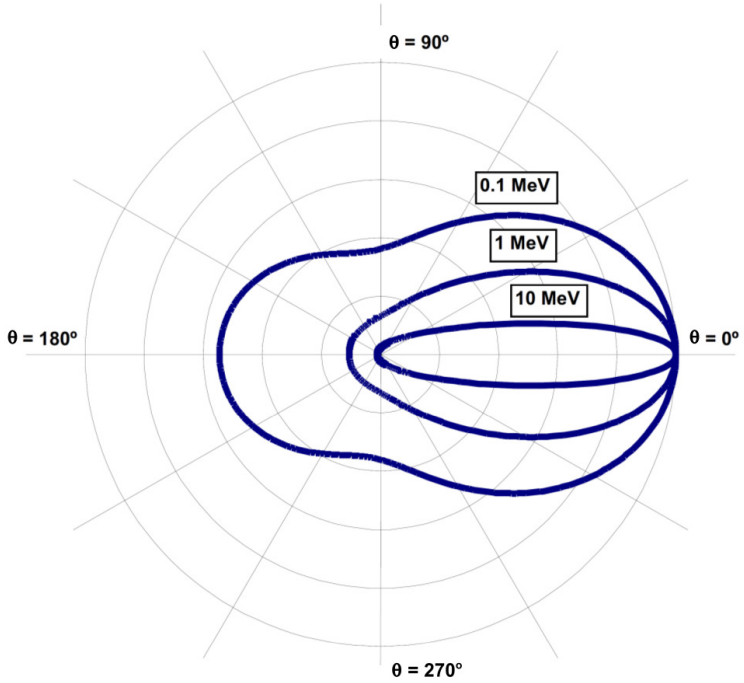

Figure 2.1.5: Illustration of the azimuthal angular dependence of the Compton scattering differential cross section for three different incident photon energies [39]. As the photon energy increases, the scattering angle becomes smaller, resulting in a strongly forward focussed scattering angle.

2.1.1.3 Doppler effect in Compton scattering

In a realistic detector system, the Compton interaction happens to an electron bound to a nucleus, where the electron is neither free nor at rest. In 1929, J. DuMond experimentally observed a broadening in the measured Compton spectra, due to the motional distribution of the target electrons [59]. He interpreted this effect as a Doppler broadening [59]. In order to evaluate this effect over all possible interaction angles, the Compton cross section has to take into account the momentum distribution of the bound electron. An expression, including this effect, was derived by Ribberfors [60] in 1975

$$\left(\frac{d\sigma}{d\Omega}\right)_{bound,i} = \left(\frac{d\sigma}{d\Omega}\right)_{unbound,i} S_i(E_i, \theta, Z) \tag{2.1.9}$$

where S_i is the incoherent scattering function of the i-th shell electron, E_i is the incident photon energy, θ the Compton scattering angle and Z the atomic number of the target material. The first term of Eq. (2.1.9) represents the Klein-Nishina differential cross section (see Eq. (2.1.8)), derived for a free electron.

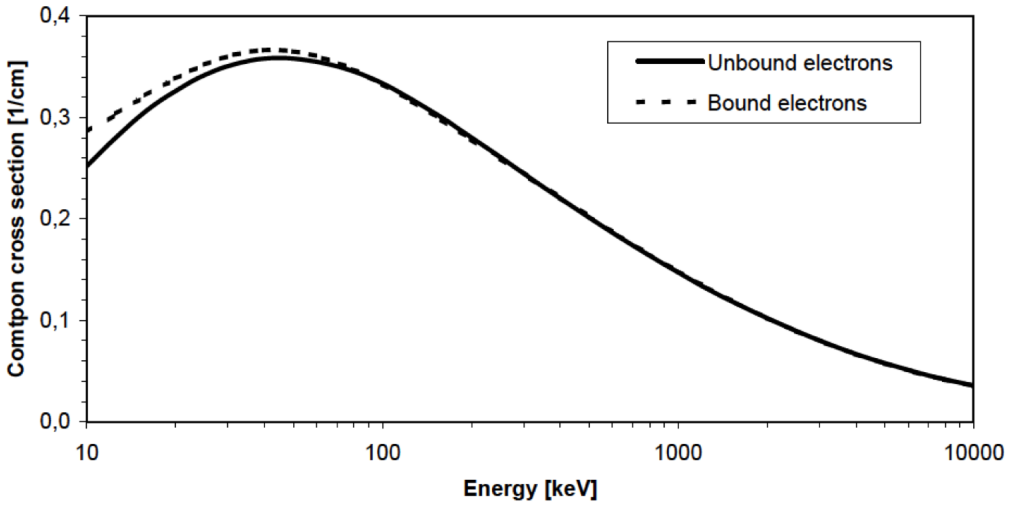

Figure 2.1.6: Compton scattering cross section for bound (dashed line) and unbound (solid line) electrons in silicon as a function of the initial photon energy. The probability of Compton scattering with bound electrons is slightly higher than the one predicted by the Klein-Nishina formula for low photon energies below 100 keV, while for higher energies the impact of the bound electrons is negligible and both models show an identical prediction of the cross section [61].

As Compton-based medical imaging is the main focus of this thesis, the effect of the Doppler broadening has to be evaluated for the Compton camera components, particularly the scatter detector. From previous design simulations of this camera system (see chapter 3 and [38] for more details), silicon detectors are chosen as scatterers. Therefore, the Compton scattering cross section for bound and unbound Compton scattering in silicon is compared in Fig. 2.1.6 as a function of the incident photon energy. There is a discrepancy visible between the Compton scattering probability from bound and unbound electrons at lower incident photon energies. For a given photon in this energy range, Fig. 2.1.7 illustrates the Compton scattering cross section as a function of the scattering angle. In the case of bound electrons, the interaction probability is slightly suppressed at large and small scattering angles, while in the angular range from $\sim 40^o$ - 130^o the Compton scattering probability from bound electrons exceeds the one from free

electrons. This obviously attributes to the motional distribution of the atomic orbital electrons of a silicon target before the interaction. However, this effect, as indicated in Fig. 2.1.6 [61], can be neglected for our purposes, where the energy range of interest for prompt γ rays lies in the multi-MeV region.

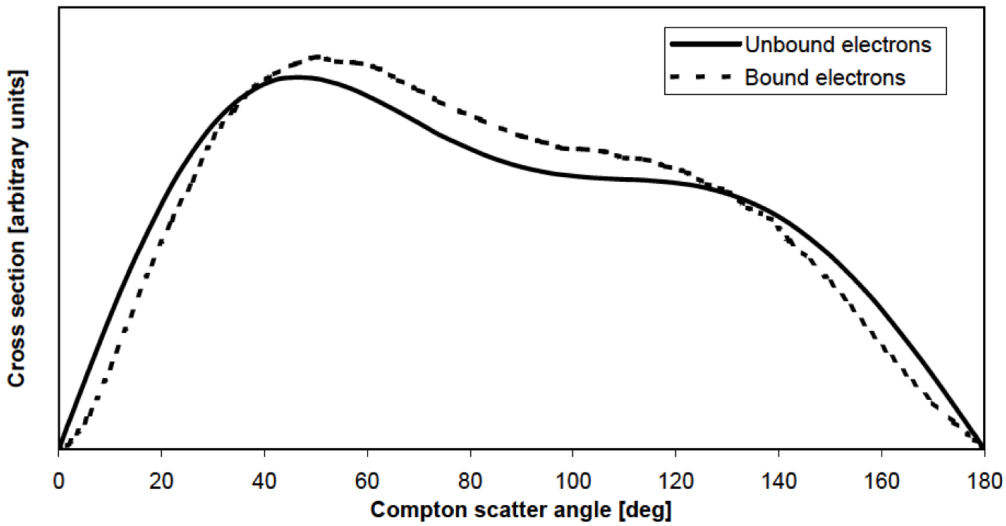

Figure 2.1.7: Evaluation of the angular dependence of the the Compton scattering cross section for bound and unbound electrons at a fixed incident photon energy of 100 keV. At small and large scattering angles, the probability of the Compton scattering from the bound electrons case is slightly suppressed [61].

2.1.1.4 Pair production

Pair production describes the process where an energetic photon in the vicinity of an atomic nucleus converts its energy into an electron-positron pair. This mechanism is only possible if the incident photon energy exceeds the rest mass energy of the electron and positron, which is 1.022 MeV. Such an interaction can take place in the Coulomb field of an atomic nucleus, in order to fulfill the momentum conservation condition. Therefore, pair production cannot happen in free space (without the presence of an ultra-strong electromagnetic field). As for the energy conservation, the energy of the incident primary photon is negligibly affected by the atomic nucleus during the momentum absorption process of the photon, since the nucleus is thousands of time more massive than the electron and positron [58]. Therefore, the energy of the incident photon is equally shared between the electron-positron pair. A reverse interaction process, called pair annihilation, occurs when the positron slows down and captures an electron from the medium. Then, the positron disappears and two 511 keV photons are emitted in (almost) opposite direction in order to satisfy the momentum conservation condition before and after the annihilation. The pair production cross section rises steeply with the increase in the incident photon energy, as indicated in Fig. 2.1.2 and scales quadratically with the atomic number Z of the absorbing medium.

2.1.2 Neutron interaction

As neutrons carry no electric charge, they can approach the atomic constituents without interference with the Coulomb force. In contrast to photons, neutrons mostly interact with the

atomic nucleus and, therefore, heavy charged particles and γ rays are the main products of their interactions that can be induced through either elastic or inelastic scattering processes, neutron capture, spallation or fission reactions. In an elastic scattering process, the neutron bombardment of a nucleus results in a change of the neutron flight path, associated with an energy transfer to the recoiling nucleus. In this interaction, the total momentum and the energy are conserved. Therefore, the neutron energy transfer strongly depends on the interaction angle. So, in head-on collisions (scattering angle θ = 0), the maximum energy of the incident neutron is transferred to the recoil nucleus. In case of proton-neutron head-on collisions, due to the almost equal masses of the scattering partners, almost the entire neutron energy will be transferred to the collision partner. In an inelastic scattering process, on the other hand, the neutron is intermediately absorbed by the nucleus and then reemitted with lower energy and in a direction that is different from the incident one. In the meanwhile, the nucleus is left in an excited state, which subsequently de-excites by emitting γ rays. The neutron capture is slightly different compared to the inelastic neutron scattering, due to the absence of neutron emission in the secondary products. These are mainly γ rays or protons, from reactions such as ${}^{1}_{1}\mathrm{H(n, }\gamma){}^{2}_{1}\mathrm{H}$ and ${}^{14}_{7}\mathrm{N(n, p)}{}^{14}_{6}\mathrm{C}$. The fourth possible neutron interaction process is spallation or fragmentation, where the target nucleus disintegrates into many residual components, such as α particles and nucleons. Finally, neutrons may induce nuclear fission reactions with high-Z nuclei. In this reaction process, the target nucleus fragments into two lighter daughter nuclei, accompanied by the production of several neutrons [58].
The probability of the above mentioned neutron reactions is governed by the neutron kinetic energy. Based on that, the neutron can be divided into slow ($E_k \approx 0.025$ eV) and fast ($E_k \gtrsim 0.1$ MeV) neutrons. So, the total neutron microscopic cross section Σ_{tot}, defined as the total cross section σ_{tot} multiplied by the number of nuclei per unit volume [55], of all reactions can be written as follows

$$\Sigma_{tot} = \Sigma_{scatter} + \Sigma_{rad\_capture} + ... \tag{2.1.10}$$

The mean free path length $\lambda = \frac{1}{\Sigma}$, which is the distance between two interactions, is of the order of centimetres or less for slow neutrons, whereas it is tens of centimetres for fast ones [58].

2.2 Interaction of directly ionizing radiation with matter

During an interaction of directly ionizing radiation with matter, the incident radiation transfers either a part or the entire amount of its energy directly to the absorber material. Based on the deposited energy value, an ionization track develops in the medium. This interaction occurs for impinging charged particles, which are mainly affected by the Coulomb force of the atomic components. In the following sections, the interaction mechanism of light (e.g. electrons) and heavy (e.g. protons) charged particles will be discussed.

2.2.1 Interaction of electrons in matter

As electrons pass through a medium, they elastically or inelastically interact with the atom's Coulomb potential. In an elastic interaction, the electron direction is deflected by the electrostatic field of the target (nucleus) without affecting the electron energy. Multiple elastic scattering, experienced by an electron, is known as Molière scattering [58]. To precisely track an electron, which is an important feature of the LMU Compton camera, this type of interaction has to be taken into account. The cumulative angular distribution of an electron experiencing Molière scattering is approximated by a Gaussian. The width of this distribution, projected onto the scattering plane, is given by

$$\delta_{proj} = \frac{13.6MeV}{\beta cp}\sqrt{\frac{r}{R_0}}\left(1 + 0.038\ln\frac{r}{R_0}\right) \tag{2.2.1}$$

where βcp = $\frac{E_e^2+2E_eE_0}{E_e+E_0}$ corresponds to the product of the velocity and the momentum of the electron (E_0 is the rest energy of the electron and β = v/c with v representing the electron velocity), R_0 is the radiation length of the material (9.35 cm for Si) and r represents the straight line between the start and end point of the electron trajectory in the medium. One can infer from Eq. (2.2.1) that the smaller the electron energy E_e, the more dominant Molière scattering will be.

The inelastic interaction of electrons in matter results in an energy loss in the absorbing medium. This energy loss is dissipated either by radiative emission (Bremsstrahlung) E_{rad}, as the electron decelerates in the electric field of the nucleus, or via collisions with atomic electrons or the nucleus E_{col}, causing ionization or excitation. So, the total energy loss E_{tot} can be written as

$$\left(\frac{dE}{dx}\right)_{tot} = \left(\frac{dE}{dx}\right)_{rad} + \left(\frac{dE}{dx}\right)_{col} \tag{2.2.2}$$

The differential energy loss for a given particle within the medium per differential path length is known as the linear stopping power. For a light charged particle, like the electron, the contribution of both components (radiative processes $\left(\frac{dE}{dx}\right)_{rad}$ and collision processes $\left(\frac{dE}{dx}\right)_{col}$) to the total energy loss is about equal if the critical energy E_{crit} of the electron is reached [58]. E_{crit} is material dependent and approximated by the expression

$$\frac{(dE/dx)_{rad}}{(dE/dx)_{col}} = 1 \; and \; E_{crit} = \frac{800MeV}{Z + 1.2} \tag{2.2.3}$$

where Z is the atomic number [62]. The critical electron energy of silicon, used as scatter material of the LMU Compton camera, is $E_{crit} \cong 53$ MeV. The energy loss via collision processes is more dominant for an electron, whose energy is much lower than the critical energy of the target material ($E < E_{crit}$). Therefore, the contribution of the Bremsstrahlung radiation in the electron energy loss is negligible in our case, since the maximum recoil Compton electron energy is less than 5 MeV, resulting from an incident prompt γ ray of 6.1 MeV, which is the most energetic prompt γ-ray line to be expected from nuclear interactions of a therapeutic proton (ion) beam and organic target material. This property turns into an advantage for our application, since minimizing the radiative process provides a clean condition for tracking the Compton electron, which predominantly loses its kinetic energy via collisions. This behaviour is described for fast electrons by the Bethe formula, which can be derived in a similar way as for heavy ions [55]

$$\begin{aligned} -\frac{dE}{dx} &= \frac{2\pi e^4 nZ}{m_e v^2}\left[ln\frac{m_e v^2 E}{2I^2(1-\beta^2)} - (ln2)(2\sqrt{1-\beta^2} - 1 + \beta^2)\right. \\ &\left. +(1-\beta^2) + \frac{1}{8}(1-\sqrt{1-\beta^2})^2\right] \end{aligned} \tag{2.2.4}$$

here v and e are the velocity and the charge of the electron, n and Z the number density and the atomic number of the absorber material, m_e the rest mass of the electron and $\beta = v/c$. The parameter I is the average excitation and ionization potential of the material that has to be determined experimentally for each element [55]. The electron collision rate is proportional to the electron density of the absorber material and inversely proportional to the incident electron energy. Since the masses of the collision pastures (incident electron and bound electron of the target material) are identical, the electron scattering can result in a large scattering angles while passing through the medium.

2.2.2 Interaction of ions in matter

The passage of ions through an absorber medium is associated with Coulomb interaction with the atomic components. Compared to light particles (electrons), energy loss through radiative processes (Bremsstrahlung) is negligible for ions (protons) due to their large masses [58]. Therefore, the main contribution to the ion's stopping power originates from electronic stopping, where the impinging particles collide with atomic electrons, causing ionization or excitation. The behaviour of the stopping power can be explained by the well-known Bethe-Bloch formula [58]

$$S(E) = -\frac{dE}{dx} = 2\pi r_e^2 m_e c^2 N_e \frac{Z^2}{\beta^2}\left[\ln\left(\frac{2m_e c^2 W_{max}\beta^2}{I^2(1-\beta^2)}\right) - 2\beta^2 - 2\frac{C}{Z_t} - \lambda\right] \tag{2.2.5}$$

where Z and β are the particle charge and velocity, respectively, r_e is the (classical) electron radius and m_e its rest mass. W_{max} is the maximum energy transfer in a single collision with an electron, while I and N_e represent the average ionization potential of the medium with atomic number Z_t and the electronic density, respectively. Eq. (2.2.5) incorporates two correction terms, namely the shell correction C, which dominates for slow particles, and the density correction λ, which is important for high energy particles. Considering these corrections, the stopping power S(E) can be calculated with an accuracy of a few percent. From the Bethe-Bloch equation it can be inferred that the stopping power increases when the particle slows down, i.e. when the interaction time in the Coulomb field of the electron increases. This finally leads to a well-localized energy deposition of the ions in the medium at the end of their stopping range, which is known as the Bragg peak, which is of particular interest in medical physics for particle therapy in tumor treatment. The distance that ions need to lose all of their energy is called the ion (particle) range, which can be approximated by integrating the ion stopping power:

$$R = \int_0^E \frac{1}{S(E)} dE. \tag{2.2.6}$$

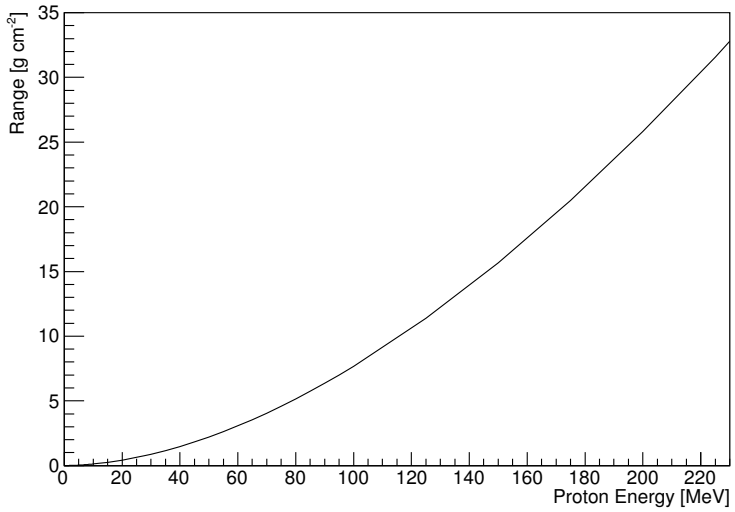

Figure 2.2.1: The range of a proton beam in water (given in a real density g/cm^2, which is equivalent to the range in cm due to ρ_{H_2O} = 1 g/cm^2) as a function of the incident proton energy [63].

Figure 2.2.1 shows the proton beam range as a function of its energy in the therapeutic energy range. It clearly states that the higher the energy of proton beam, the higher the penetration depth of the proton, in agreement with the Bethe-Bloch equation. A 230 MeV proton beam has a range of 33 cm in water. This allows the treatment of cancer tumors, located within this depth range inside the human body. For a given heavy particle beam, the range of each individual particle slightly differs due to statistical fluctuations of the interaction process. This effect is known as range straggling [55], which results in a spread of the dose delivered, e.g., by the treatment beam at the end of particle path (thus affecting the width of the Bragg peak).
Compared to light charged particles, ions are not strongly affected by elastic scattering with the atomic electrons. This implies that heavy charged particles exhibit a relatively straight path when passing through the stopping medium, besides the deflection originating from elastic and inelastic interactions with atomic nuclei. The latter processes produce nuclear fragments as well as secondary particles, e.g., protons, neutrons, electrons, positrons and prompt γ rays. Within the therapeutic proton energy range (60 to 250 MeV), fragmentation is the dominant nuclear reaction process, which occurs within 10^{-22} s after the collision. The (excited) fragments pass through a nuclear evaporation phase, followed by prompt γ-ray emission in about 10^{-21} - 10^{-16} s. Since the fragments and secondary products are absorbed close to the interaction position in the medium, the heavy charged particles are subject to range and dose uncertainties at the end of the particle path.

2.3 Radiation detector properties

The interaction of electromagnetic radiation with matter is the basic principle of any radiation detection system. As the radiation quanta enter the detector material, they create charge carriers, either electron-ion or electron-hole pairs, through the ionization processes discussed above. In semiconductor detectors, the electric field between the cathode and anode separates the created charge carrier pairs, causing them to move to their respective electrodes where a current signal will be generated. In scintillator materials, the primary energetic photon is converted to a multitude of low energy photons, which, e. g., subsequently generate photo-electrons at the photocathode of the (PMT) readout sensor. Consecutive dynode stages amplify this electron in order to finally generate a measurable signal. The total number of the created electron-hole pairs N_{eh} (in semiconductors) should be proportional to the deposited radiation energy E_{dep} in the active detector volume. The constant W represents the average energy required to generate an electron-hole pair. So, the number of the charge carrier pairs can be expressed as

$$N_{eh} = \frac{E_{dep}}{W} \tag{2.3.1}$$

W varies between different detector materials from 1 - 5 eV (semiconductors), 30 eV (gases) and 1 - 1000 eV (scintillators), respectively [55]. For silicon, W amounts to 3.6 eV. As the number of charge carriers is closely related to the energy of the detected radiation and follows the Poisson statistics, the energy resolution of such a detection system can theoretically be considered as limited by the fluctuation of the generated number of charge carrier, represented by the variance σ_{eh}^2, of the number of electron-hole pairs. However, this is only valid if the production process of each charge carrier pair is statistically independent, not fulfilled in the case of energy deposited in semiconductors, where the incident energy goes either into ionization (generating electron-hole pairs) or excitation (generating phonons). Thus, the available degrees of freedom for ionization depend on the complementary amount of excitation and thus are not uncorrelated. This leads to a discrepancy between the observed value of σ_{eh} and the one predicted by Poisson

statistics [55, 64]. The "Fano factor" is empirically introduced to take this effect into account. The variance of the total number of electron-hole pairs thus follows as

$$\sigma_{eh} = \sqrt{F N_{eh}} \tag{2.3.2}$$

A typical value of the Fano factor for scintillators is F $\simeq$ 1, whereas, F $<$ 1 for semiconductor and gas detectors (F = 0.1 in silicon). This is reflected by the superior energy resolution of semiconductors, besides the small band gap of these materials. Since the energy resolution is usually expressed as the full width at half maximum (FWHM) of a γ-ray line registered with, e. g., a semiconductor detector, Eq. (2.3.2) can be rewritten as

$$\Delta E(FWHM) = 2.35\ \sigma_{eh} = 2.35\sqrt{F\ \frac{E_{dep}}{W}} \tag{2.3.3}$$

For a given application, the selection of the optimum detector type will be based on the specific properties needed in this case. Besides the energy resolution, some applications may require to maximize the (material dependent) detection efficiency. Inorganic scintillators exhibit a high detection efficiency, compared to gases or semiconductors, due to their high density and atomic numbers, as well as the ability to manufacture them in large volumes. The timing performance of the detector may also be of interest in some applications. For scintillators, the decay time and the light yield (i.e. the number of photons created per MeV of incident radiation) are crucial factors for determining the time resolution. The material purity and the mobility of the charge carriers are strongly affecting the timing performance of semiconductor detectors. In addition, cost effectiveness and design flexibility should be added to the list of selection criteria when deciding about a specific detector type. For the Compton camera project pursued within this thesis, semiconductor and scintillation detectors are chosen for the prototype system, since they fulfill the requirements (see chapter 3). Therefore, the following sections are dedicated to explaining the basic principles of these detector types.

2.3.1 Semiconductor Detectors

The nature of the periodic lattice structure in crystalline semiconductor materials creates allowed energy levels for electrons, which group in bands, whose relative energetic position determines the electrical material properties. The conduction band, being the energetically highest band void of electrons, is separated by the band gap (where no solutions of the Schrödinger equation exist for electronic levels) from the valence band, the highest band structure filled with electrons. In semiconductors, typical band gap energies range from $\sim$ 0.7 eV to 3 eV and thermal energies can be sufficient to excite an electron from the valence band across the band gap into the conduction band, leaving a hole in the valence band. The movement of this electron-hole pair in the lattice contributes to the observed electrical conductivity. The probability per time unit of the thermal excitation mechanism is given by

$$P(T) = C T^{\frac{3}{2}}\ exp\left(-\frac{E_g}{2kT}\right) \tag{2.3.4}$$

where T is the absolute temperature and E_g is the band gap energy, while k and C represent the Boltzmann constant and a material dependent constant, respectively [55]. From Eq. (2.3.4) it can be inferred that the probability of a thermal excitation critically depends on the ratio between the band gap energy and the absolute temperature. This means, the smaller the band gap energy for a given material, the higher the chance of a thermal excitation and vice versa. However, comparing the thermal energy of kT = $\frac{1}{40}$ eV at room temperature with typical band

gap energies of semiconductors around 1 eV, it is evident that thermal excitation will not be an efficient mechanism to increase the electrical conductivity, unless when assisted by doping the material with n- or p-type impurities (donors or acceptors, respectively). This concept, relevant for the production of the Si-based semiconductor detectors, will be further discussed below. When applying the electrical field, the electron-hole pair is attracted to the oppositely charged electrodes. The relation between the drift velocity ν of either the electron or hole and the electric field strength $\vec{E}$ can be presented as follow

$$\vec{\nu_e} = \mu_e \vec{E} \tag{2.3.5}$$

$$\vec{\nu_h} = \mu_h \vec{E} \tag{2.3.6}$$

where μ_e and μ_h are the mobilities of the electron and hole, respectively. In the absence of an electric field, the thermally created electron-hole pair is subject to recombination. Then, an equilibrium level between thermally-induced newly generated charges and their recombination is reached, strongly influenced by the absolute temperature T. Therefore, the formation of thermally-induced charge carriers,which is unwanted background noise in radiation detectors based on semiconductors, will be reduced drastically by applying a cooling system. In particular for Germanium detectors with a band gap as small as 0.67 eV, cooling is essential to reduce thermal noise.

Ideally, the number of the free electrons in the conduction band equals the number of holes in the valence band. Then, the material is called an intrinsic semiconductor. However, in a real-life detector, it is almost impossible to achieve this condition, due to the smallest amount of residual impurities mixed with the semiconductor material. This feature can be applied on purpose (”doping”) to enhance the electrical conductivity of the semiconductor. The dopant elements are either from group III (acceptors) or V (donors) of the periodic table, which then can form n-type or p-type semiconductors, respectively. In the n-type case, the impurity atom has five electrons in the valence band, resulting in one excess electron after all covalent bonds have been created. The energy levels of these ”donor electrons” are located close to the border of the conduction band in the band gap region, thus requiring only a small energy to reach the conduction band without generating a corresponding hole in the valence band. In contrast, atoms from group V, lacking one electron relative to the 4 covalent bonds of silicon, will occupy energy levels closely above the upper border of the valence band (acceptor states), thus being able to accept an electron from the valence band with minimal energy requirement. Consequently, a hole will be created in the valence band. Both doping scenarios contribute to the electrical conductivity of the semiconductor material.

The basic principle of forming a semiconductor radiation detector is by combining the n-type and p-type material regions. As a result of this combination, a quasi-neutral region (depletion zone) will be emerge after recombination of free charges in the n-type (electrons) and p-type (holes) materials, joined into a p-n junction. Due to the diffusion of electrons and holes through the material, following the concentration gradients, positive and negative charge concentrations will be created on the n-type and p-type layer borders, respectively. This establishes an electric field across the depletion zone. The resulting field strength will balance the diffusive force, leading to an equilibrium width of the depletion region. This region can be extended by applying a reverse bias voltage. At this stage, the detector is practically ready to detect any incident radiation that causes an ionization in the depletion region. The implantation regions of n- and p-type contact surfaces can be segmented (e. g. in strips) on both sides (with orthogonal orientation) of either n- or p-type bulk material. This is the basic principle of position-sensitive strip

detectors. An example of this detector type is the double-sided silicon strip detector (DSSSD), which is used as a scatterer for the Compton camera project (see chapter 3).

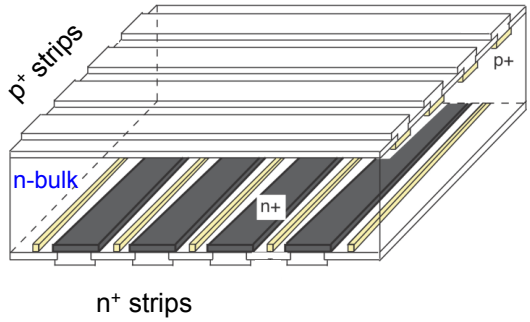

Figure 2.3.1: Illustration of the basic structure of a double-sided silicon strip detector (DSSSD), where the n^+- and p^+-type strips are implanted orthogonally on a n-type bulk forming an x and y mesh [65].

2.3.2 Scintillation Detectors

The basic principle of scintillation detectors is the conversion of the energy of the incident radiation to a multitude of low-energy visible or near-UV photons. This scintillation light is then registered in a photo sensor in order to be amplified to a measurable electronic signal.
Scintillators can be found in organic and inorganic materials. Organic scintillators (e. g. plastic scintillator materials) exploit fluorescence as light-generating process, based on suitable transitions in the molecular energy level structure. Depending on the deposited radiation energy in the medium, an electron is excited to a certain energy state, from where it rapidly de-excites to the ground state by emitting fluorescence light. This fast process takes about 1 - 2 ns [55], which reflects the superior timing performance of this material family. The energy spacing between the molecular energy levels is about 3 - 4 eV, thus preventing thermal excitation processes at room temperature.
Inorganic scintillators, on the other hand, possess a band structure energy as described in the previous paragraph. Deposited energy that exceeds the minimum excitation energy in the specific scintillator material leads to the excitation of an electron from the valence band across the band gap to the conduction band. Direct de-excitation of this electron to the valence band would be associated with the emission of a photon, whose energy would exceed the visible or near UV spectral range. Therefore, selected dopants, called activators or color center, are introduced to the lattice structure in order to create new energy levels in the band gap. Here electrons, first excited from the valence to the conduction band, can be captured first in an upper level before de-exciting (with a time structure according to the specific decay constant) to a lower level by emitting a visible or near-UV scintillation photon. Such a structure is schematically shown in Fig. 2.3.2.
Table 2.1 illustrates the properties of the most commonly used organic and inorganic scintillation materials. Organic scintillators specifically exhibit very fast decay times, making them ideal trigger detectors in high-rate applications. However, this material group, due to their low atomic number and density, possess only a poor detection efficiency. Compared to the organic scintillators, the high light yield of the inorganic species contributes to reduce statistical fluctuations and thus to an improvement of the time and energy resolution. Inorganic scintillation crystals over the last 6 decades have formed a vast spectrum of applications in many fields of

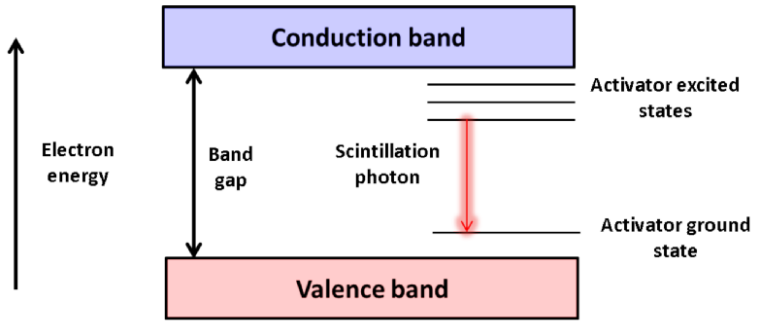

Figure 2.3.2: Energy band structures of an inorganic scintillator with additional activator states (color centers), introduced by doping the material with a small amount of specific impurities, in order to enhance the probability of emitting photons in the visible or near-UV light range.

research, including medical imaging, which is the topic this thesis. Particularly, the recently developed $LaBr_3$:Ce^{3+} scintillator exhibits the highest light yield (63000 scintillation photons per 1 MeV) and the fastest decay time of about 16 ns among its scintillator group. This translates in a very good relative energy resolution of (in our detector geometry) about 3.8 % at 662 keV and a superior time resolution of a few hundred picoseconds. These features motivate us to use a $LaBr_3$:Ce^{3+} scintillator for the absorber component of the Compton camera project.

Material	ρ [g/cm^3]	Z_{eff}	τ [ns]	Y [ph/MeV]	$\Delta E/E$ [%]	hygroscopic?
Inorganic						
NaI:Tl	3.67	51	230	38000	5.6	Yes
$LaCl_3$:5%Ce^{3+}	3.79	60	28	46000	3	Yes
$LaBr_3$:5%Ce^{3+}	5.29	47	16	63000	3	Yes
$CeBr_3$	5.2	46	17	68000	4	Yes
$Bi_4Ge_3O_{12}$(BGO)	7.13	74	300	8200	12	No
Lu_2SiO_5:Ce^{3+}(LSO)	7.40	66	47	25000	10	No
Gd_2SiO_5:Ce^{3+}(GSO)	6.71	59	60	9000	10	No
Y_2SiO_5(YSO)	4.54	34	70	24000	10	No
Organic						
BC-404, EJ 204, NE 104	1.03	-	1.8	$\sim$10000	-	-
BC-408, EJ 200, Pilot F	1.03	-	2.1	$\sim$10000	-	-
BC-418, EJ 228, Pilot U	1.03	-	1.4	$\sim$10000	-	-

Table 2.1: General overview of some commonly used organic and inorganic scintillator materials together with their properties [55, 66–68].

Chapter 3

Compton Camera design and experimental layout

This chapter will first refer to a previous simulation study of the LMU Compton camera prototype, emphasizing the relevant findings on which the further work of this thesis will be based upon. This includes a brief description of the simulation tool (MEGALib), based on a Monte-Carlo toolkit (Geant 4) and the ROOT framework, which can also be used for analyzing and reconstructing experimental data. Since the experimental part of the Compton camera development constitutes the focus of this thesis, the related hardware, readout electronics and mechanical setup will be explained for both Compton camera detector components in a second section.

3.1 Simulated Design Specifications

3.1.1 Monte-Carlo simulation and image reconstruction framework: MEGALib

The MEGALib software package [39] was developed to simulate and analyze data from a Compton telescope designed for Medium Energy Gamma-ray Astronomy (MEGA) [69] at the Garching Max-Planck-Institut für Extraterrestrische Physik. It consists of more than 300000 coded lines, written in C++. Figure 3.1.1 shows the basic modular layout of the MEGALib work flow. The simulation part of this package includes the 'MGGPOD' module , based on Geant 3, studying the orbital background environment, which is not relevant for our project. Moreover, the first generation of the Compton telescope simulation toolkit used ROOT [70] and Geant 3, represented by the 'GMega' module. This was replaced by the most recent and updated module 'Cosima', based on the ROOT and Geant4 (9.4) simulation toolkits. In this stage, the simulation starts after defining the geometrical design of the detector system. Additionally, the physics interactions are recorded in each detector component of the camera. Then, the recorded data is analyzed in the 'Revan' module, aiming to reconstruct events based on their interaction type, such as Compton scattering or pair creation. The 'Revan' module can also deal with experimental data after passing then through the 'MEGAlyze' module, which is not only responsible for controlling the Compton telescope detector and data acquisition (DAQ) system, but also the data calibration and filtration take place at this stage. For the LMU Compton camera, the detectors and DAQ are controlled by the MARABOU system (see section 3.2), which has a ROOT-based analysis platform [70] for calibrating and structuring the data of the Compton camera components. Finally, all advanced analysis and image reconstruction capability, based

on the list-mode maximum-likelihood expectation maximization algorithm (LM-MLEM), for both simulated and experimental data is provided by MEGALib's 'Mimrec' library, allowing for image reconstruction in spherical as well as Cartesian coordinates (2D, 3D), including different response calculation approaches for Compton and pair creation events. It takes care of the event selection, assessed by angular resolution, energy dispersion and scattering angle distributions. As well included is a performance assessment of the event reconstruction algorithms and tools for sensitivity and background calculation. A detailed description of the MEGALib software package can be found in the PhD thesis of Andreas Zoglauer [39].

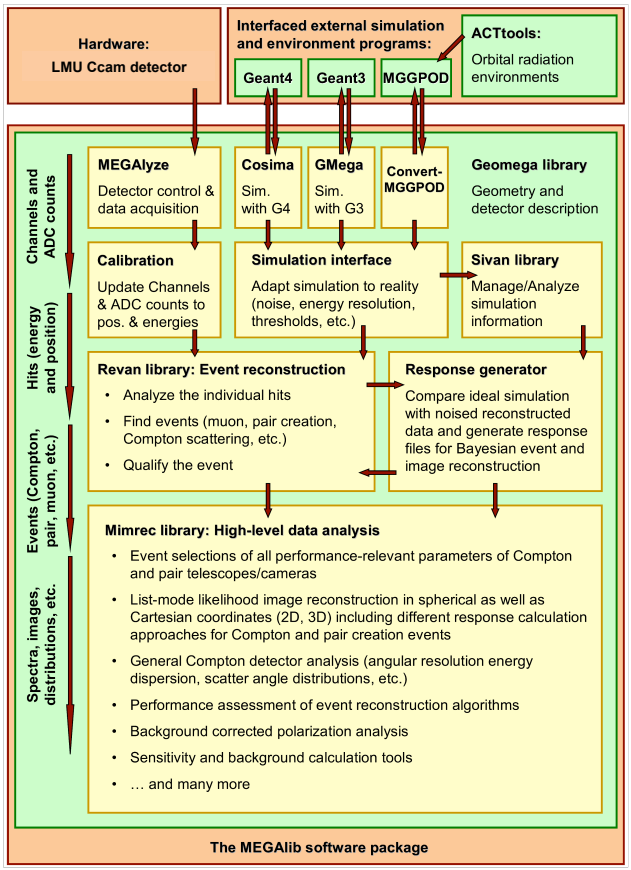

Figure 3.1.1: Overview of the modules and work flow of the MEGALib software package, available as a simulation and (event and image) reconstruction tool for Compton camera devices. The package is based on Geant (3 or 4) and ROOT, and allows as well for analyzing and visualizing the experimental data. For details, see the text and [39].

3.1.2 Simulation study of the LMU Compton camera

Specifying the layout of the Compton camera is a major part when designing such a system. The overall performance as well as alternative image reconstruction techniques, based, e.g., on photon tracking alone or in combination with recoil Compton electron tracking, needs to be investigated. Since the LMU Compton camera aims to provide the capability of tracking the Compton photon-scattered electrons from multi MeV impinging photons, the scatter detector has to be set up by multiple layers in order to allow for following the Compton electron trajectories. For this purpose, the scatter detector has to be thin enough to avoid the Compton electron to be absorbed, with simultaneously high scattering probability. In addition, the scatter detector should provide a high segmentation in order to allow for precisely localizing the

primary photon interaction. Given these requirements, semiconductor materials such as Silicon (Si), Cadmium Zinc Telluride (CdZnTe) or Germanium (Ge) are good candidates for a scatter detector. As Si detectors can be operated at room temperature and exhibit a minimum Doppler broadening (0.4^o) at 1 MeV incident photon energy, which affects the camera's spatial resolution, compared to CdZnTe (0.85^o) and Ge (0.65^o) detectors at the same photon energy [39], double-sided-Si strip detectors were chosen as scatter detectors for the LMU Compton camera. For its absorber component, a scintillation crystal was chosen, as such detectors can be formed in large volumes, thus increasing the absorption efficiency of the energetic Compton-scattered photon. $LaBr_3$:Ce was selected as it combines superb time resolution (typically a few 100 ps) with excellent energy resolution (in our case around 4 % @ 662 keV), both of these being important for the envisaged application as Compton camera absorber.

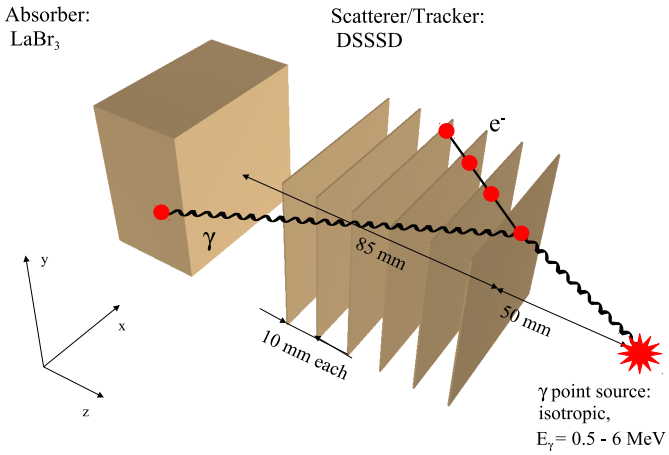

Figure 3.1.2: The LMU Compton camera is composed of six layers of double-sided-Si strip detectors (DSSSD), where each has an active area of 50×50 mm^2 and thickness of 500 μm, acting as scatter detectors, while the $50 \times 50 \times 30$ mm^3 $LaBr_3$:Ce scintillator represents the absorber detector. The geometrical arrangement of the camera was adjusted as a compromise between mechanical constraints and the camera performance [38].

Figure 3.1.2 shows the simulated configuration setup of the LMU Compton camera, as it was specified and characterized in a previous thesis project [38]. It consists of 6 layers of DSSSD, each with an area of 50×50 mm^2 (thickness of 0.5 mm), acting as scatter detectors, while the $50 \times 50 \times 30$ mm^3 $LaBr_3$:Ce crystal forms the absorber detector. The geometrical arrangement of the Compton camera was investigated and optimized for a small animal irradiation scenario, with a photon source placed in 50 mm distance from the first DSSSD layer. This study revealed that 10 mm distance between each DSSSD layer was sufficient as a compromise between the electron scattering angle and the geometrical constraints from the experimental setup. Moreover, the distance of the $LaBr_3$:Ce crystal front surface to the first layer of DSSSD was specified to be 85 mm as an optimum measure for the camera efficiency, as well as the quality of the reconstructed image. Having optimized the geometrical setup of the camera, its performance was characterized by placing a photon point source (0.5 - 6 MeV γ rays) at 50 mm distance from the first layer of the DSSSD. This study aimed to determine the appropriate DSSSD detector thickness and the achievable spatial resolution, based on the spatial resolution of the absorber crystal.

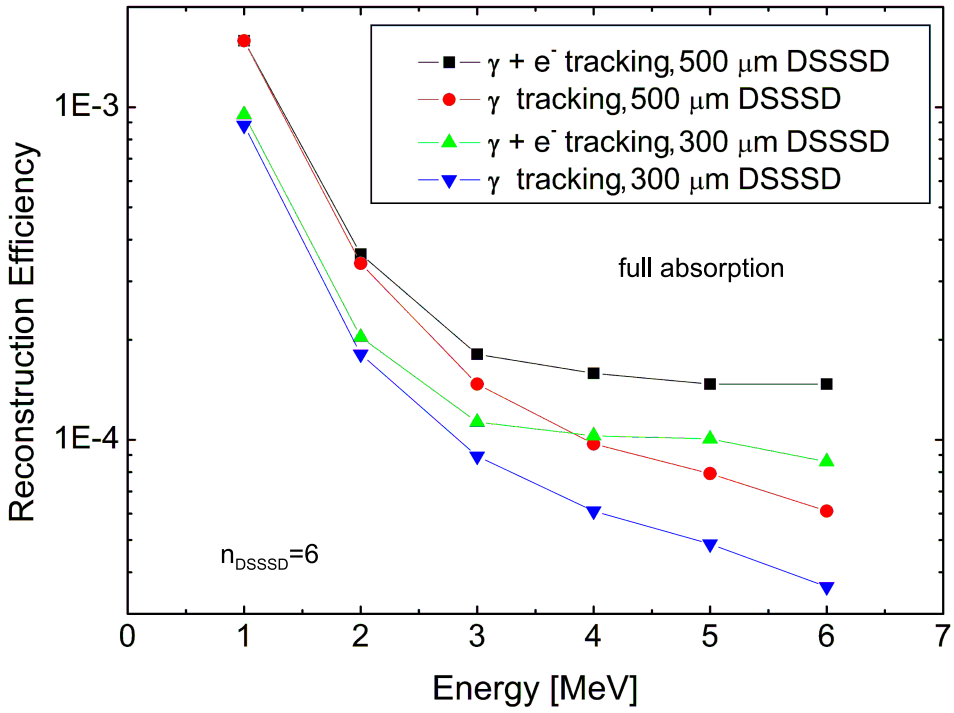

Figure 3.1.3: Result of a simulation study (performed in a preceding thesis project [38]) that quantifies the impact of the scatter detector thickness and the image reconstruction mode (γ tracking alone or Compton electron plus γ tracking) on the LMU Compton camera reconstruction efficiency as a function of the incident γ-rays energy. Up to 3 MeV the DSSSDs with 500 μm thickness provide a higher efficiency compared to 300 μm thick detectors regardless of the reconstruction mode. Beyond 3 MeV, e.g. in the prompt-γ energy region, the reconstruction efficiency improves for electron and γ tracking for both DSSSD thicknesses. The maximum reconstruction efficiency of the camera at the targeted photon energy (3 - 6 MeV) was found to be 1.5×10^{-4} with 500 μm thick DSSSDs and electron plus photon tracking.

Figure 3.1.3 shows the result of a simulation study of the Compton camera reconstruction efficiency for two different scatterer/tracker thickness values, comparing γ tracking alone and γ tracking together with Compton electron tracking, as a function of the incident γ-ray energies [38]. In the energy region from 0.5 - 3 MeV, the setup with DSSSDs of 500 μm thickness shows a higher reconstruction efficiency compared to the 300 μm case. This corresponds to the increase in the scattering probability, increasing the amount of reconstructable data either for γ tracking or electron-γ tracking, as the scatter material thickness is increased. In the targeted photon energy range between 3 and 6 MeV, resulting from prompt γ-rays emitted from nuclear reactions between the proton (or ion) beam and biological tissue (mainly originating from $^{16}O^{*}$ and $^{12}C^{*}$), the combined γ and electron tracking capability of the camera increases the efficiency for both thickness scenarios (black and green curves for 500 μm and 300 μm, respectively), due to the ability of reconstructing a class of events, where the scattered photon is not fully absorbed by the absorber detector. In this prompt-γ region, a maximum reconstruction efficiency of 1.5×10^{-4} can be obtained, using 500 μm thick DSSSD layers. So, this simulated finding did not only motivate us to use 500 μm DSSSDs in the experimental configuration, but also encourages us to develop the photon plus electron tracking mode as basis for the image reconstruction.

The Compton camera angular resolution measure (ARM), defined as the angular distance between the measured Compton cone and the known origin of the incident photon [39], as well

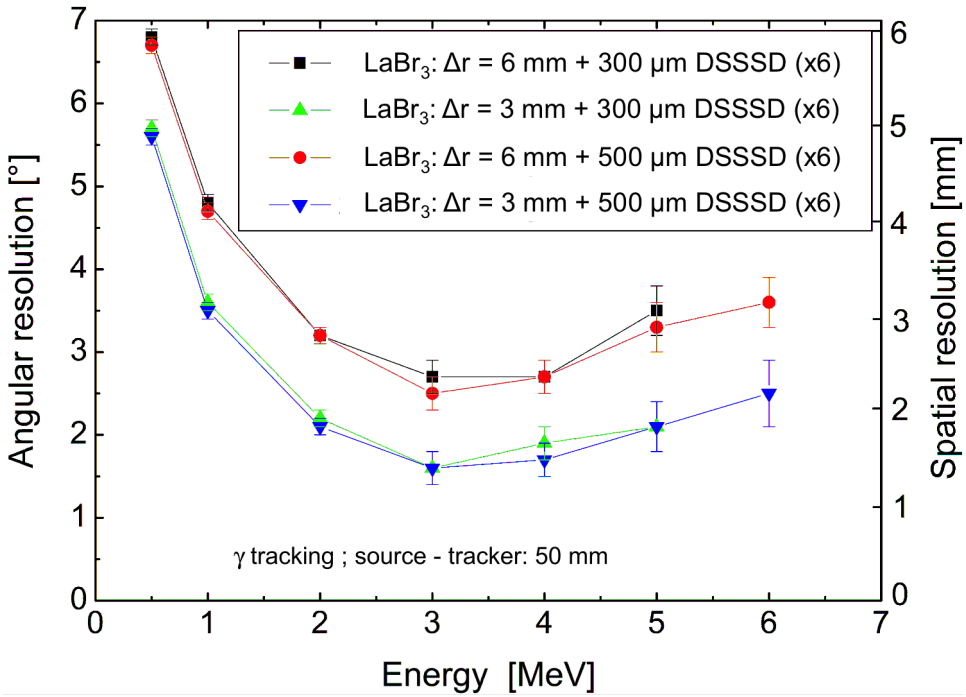

Figure 3.1.4: The Compton camera angular resolution measure (ARM) as well as the corresponding spatial resolution were evaluated for photon energy of 0.5 - 6 MeV, varying the absorber detector spatial resolution and the thickness of the scatter detectors. In this study, the spatial resolution of the $LaBr_3$:Ce detector was assumed to be 3 mm and 6 mm, respectively. These values were chosen according to the multi-anode PMT segmentation of either the Hamamatsu H9500 PMT module (256 pixels, 3 $\times$ 3 mm^2) or the H8500 PMT (64 pixels, 6 $\times$ 6 mm^2), used to read out the monolithic $LaBr_3$:Ce detector. In both spatial resolution scenarios, the angular resolution of the camera is not affected by the DSSSDs thickness, since the spatial resolution of the Compton camera is directly determined by the energy and photon interaction position in the scatter and absorber detectors. The best spatial resolution was found to be 1 - 2 mm at the targeted prompt γ energy from 3 to 6 MeV, achieved with the $LaBr_3$:Ce detector's spatial resolution assumed to be 3 mm [38].

as the correspondingly achievable spatial resolution, were studied in this first specification simulation study [38] to quantify the impact of the $LaBr_3$:Ce detector's spatial resolution and the DSSSD thickness on the camera performance at incident photon energies ranging between 0.5 and 6 MeV. This study was only considering the γ tracking mode for event reconstruction. The essential aim of this simulation study was to quantitatively assess the achievable angular resolution of the Compton camera for two different scenarios of position resolution in the monolithic absorber detector. So, two values of 3 mm and 6 mm, respectively, were assessed for the spatial resolution of the $LaBr_3$:Ce detector, inspired by the 256 and 64 pixels of the multi-anode PMT, respectively, while the DSSSDs' thickness was fixed to be 300 μm and 500 μm in these two scenarios. Figure 3.1.4 shows almost no influence of the scatterers' thickness on the camera's spatial and angular resolution. However, as expected, the ARM improves with higher spatial resolution of the $LaBr_3$:Ce detector, since the Compton camera spatial resolution is directly correlated with the energy and position resolution realized in both scatter and absorber detectors. As the camera is intended to be used with prompt γ-rays in an energy range from 3 to 6 MeV, the camera can achieve a spatial resolution of about 1 - 2 mm and 2.5 - 3 mm (corresponding to an angular resolution of 1^o - 2.5^o and 2.7^o - 3.7^o, respectively) in the case of a $LaBr_3$:Ce

spatial resolution of 3 mm and 6 mm, respectively. Based on this simulated finding, the spatial resolution of the monolithic $LaBr_3$:Ce detector will be investigated experimentally in chapter 5 for the two corresponding PMT readout scenarios of 64 and 256 multi-anode segments.
Further details about the above discussed simulation design study of the LMU Compton camera can be found in the PhD thesis of C. Lang [38].

3.2 Experimental Framework

Since the following context of this thesis will concentrate on the experimental results of either individual Compton camera components or the combined system, this section is dedicated to introduce the experimental Compton camera setup in terms of detector types, signal processing electronics and mechanical components .

3.2.1 The LMU Compton camera components: scatter and absorber detectors

This section focuses on the properties and the design specifications of the existing LMU Compton camera components.

3.2.1.1 Scatter array: Double-Sided Si Strip Detector (DSSSD)

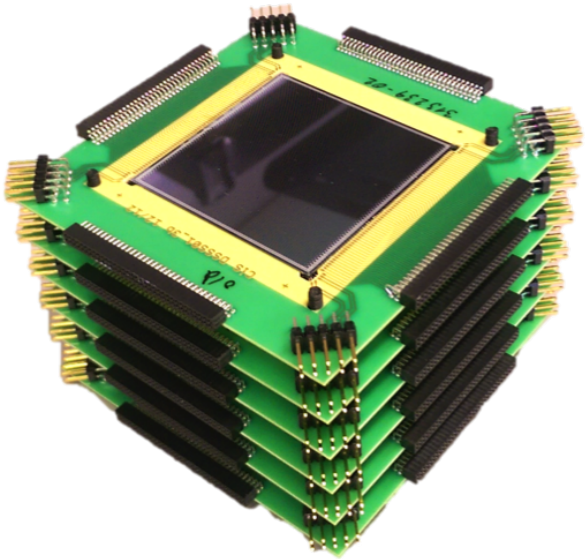

Figure 3.2.1: Photograph of the stacked array of six customized double-sided silicon strip (DSSSD) detectors, spaced by 10 mm.

According to the simulation study, the LMU Compton camera scatter detector is formed by a stack of six double-sided silicon strip (DSSSD) layers [71], as indicated in Fig 3.2.1. Each detector has an active area and a thickness of 50 $\times$ 50 mm^2 and 500μm, respectively. Since the photon interaction position is one of the essential parameters for image reconstruction, the DSSSD detector has 128 strips on each side with a pitch size of 390μm. Moreover, this detector features a relatively high resistivity of 10 kΩ cm, indicating a high purity of the wafer material. This leads to a low leakage current, facilitating detection of the low-energy Compton electron energy deposit. The DSSSD leakage current was measured by the manufacturer to be less than 1 μA. This value has been confirmed in the laboratory by using a four channel high voltage supply module (MHV-4, Mesytec [72]), which is capable to resolve currents down to 1 nA.

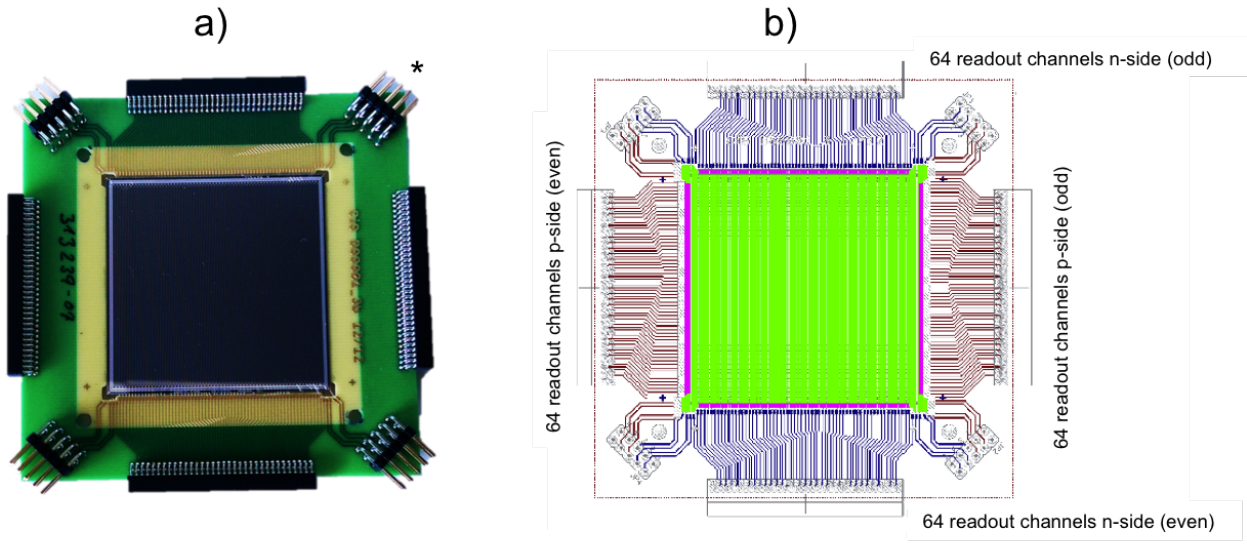

Figure 3.2.2: Photograph (a) and schematic layout (b) of a single DSSSD layer. Besides the multiple connections in the corners, used either for protection against the dicing edge leakage current or for biasing the sensor strips, the detector can be read out from four sides in order to simplify the geometrical arrangement of the detector readout electronics. The connection details of the asterisk-marked corner is indicated in Fig. 3.2.3.

Figure 3.2.2 shows a photograph (a) and a design schematic (b), provided by the manufacturer, of a single layer of the DSSSD detector. It was manufactured to be read out from four sides, i.e. 64 strips from each side, in order to reduce the geometrical complexity for the signal processing electronics. Moreover, further connectors can be seen at the corners of the detector, providing additional options to the sensor. Figure 3.2.3 illustrates a microscopic photograph of the upper right corner of the detector labeled by an asterisk in Fig 3.2.2 a). The outermost "Chip border" acts as a protection ring against dicing edge current flow, if it is set to a potential level identical to the strips values. The "bias ring" provides an additional option of biasing the sensor via the punch-through effect. This biasing technique is based on depleting the gap (< 10 μm) between the ring and the strip ends, which then bridges the high voltage to all strips. In our case, the detector strips are biased through the AC coupler (see section 3.2.2 for more details) and the "bias ring" is left floating. If, instead, the bias ring is set to a potential equivalent to the detector bias value, it works as protection ring as in the Chip border case. According to the manufacturer

[71], letting the Chip border and the bias ring on a floating potential does not affect the detector performance, since the noise induced from the dicing edge is negligibly small.

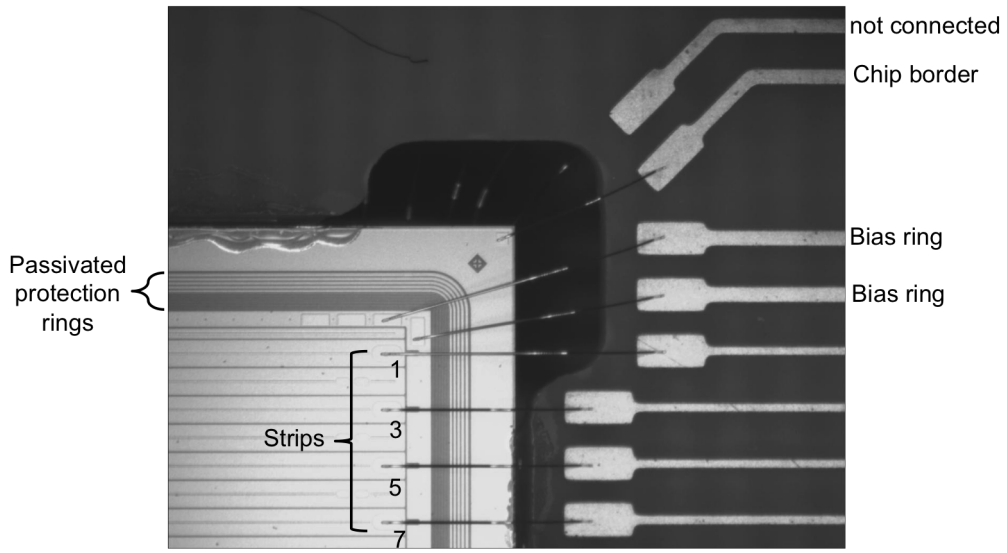

Figure 3.2.3: Photograph of the upper right detector corner, labeled by an asterisk in Fig3.2.2 a). The bonding of various structures (Chip border, bias ring) to the contact pads of the corner connector of the DSSSD module is visible.

3.2.1.2 Absorber: $LaBr_3$:Ce scintillator

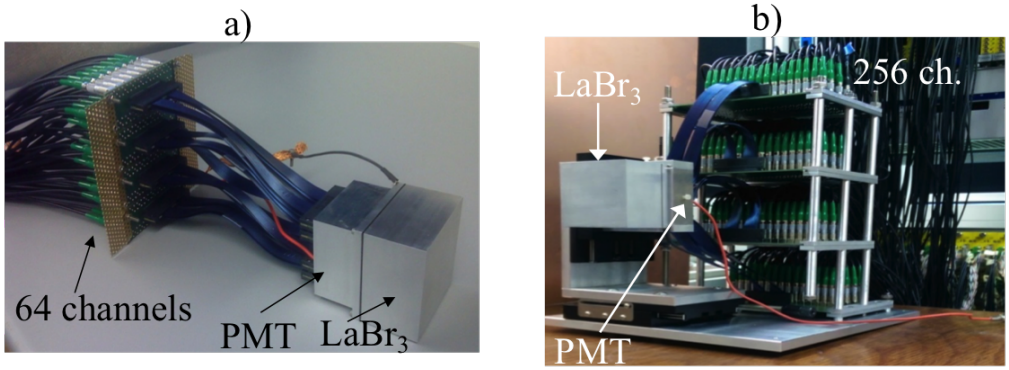

Figure 3.2.4: Photographs of the 50×50×30 mm^3 monolithic $LaBr_3$:Ce scintillator, encapsulated together with its readout sensor inside a light- and air-tight aluminum housing. Panel a) illustrates the starting version of the signal processing, where 4 neighbouring segments of the H9500 PMT were combined to form 64 output signals. Panel b) shows the present setup, in which all 256 PMT segments of the Compton camera absorbing detector are read out individually.

The LMU Compton camera absorbing detector is formed by a 50×50×30 mm^3 monolithic $LaBr_3$:Ce scintillator (BrilLanCe 380, Saint-Gobain [73]). Figure 3.2.4 shows photographs of the detector with its multi-anode readout sensor (H9500 PMT, Hamamatsu [74]), with panel (a) displaying the starting configuration, combining each four neighbouring segments to form

64 output signals and panel (b) showing the final arrangement with individual readout of all 256 segments (see section 3.2.2 for more details). The choice of this scintillation material was based on its favourable detector properties, compared to more commonly used scintillators shown in Tab. 2.1. The $LaBr_3$:Ce detector features a very high light yield (63000 photons/MeV, [75]) with a minor non-linearity of 6% between 60 and 1275 keV [76] and [77]. Moreover, this detector provides an excellent energy resolution from low photon energies ($\sim 3\%$ at 662 keV [75]) up to high energies. This is a mandatory feature for improving the overall primary Compton camera's spatial (angular) resolution, since it is governed by the precisely measured photon energy and interaction position in all Compton camera components. The superior timing properties of $LaBr_3$:Ce, due to the fast decay time of 16 ns [66] are reflected in typical time resolutions of a few hundred ps (depending on the crystal dimensions). This facilitates the use of the time-of-flight (TOF) technique, e.g., to suppress neutron background. Although the material density (5.06 g/cm^3 [77]) and effective atomic number (Z_{eff} = 46.9 [78]) are low compared to other inorganic scintillators, the photon stopping efficiency can be enhanced by enlarging the monolithic crystal volume.

Despite the mentioned superior properties of the $LaBr_3$:Ce detector, it suffers from hygroscopicity, which is the sensitivity to humidity. This means that environmental dry conditions are mandatory for handling or operating the detector. Therefore, the $LaBr_3$:Ce crystal together with its readout photomultiplier tube (PMT) is housed in a light- and air-tight aluminum box. The detector assembly was provided by the manufacturer (Saint-Gobain), with reflectively coated crystal side surface. In order to maximize the detectable scintillation light, which is very important for energy and time resolution, the crystal surfaces have to be polished and reflectively coated. This, in turn, will increase the amount of light scattering at the edges and corners of the monolithic scintillator, which consequently will negatively affect the detector spatial resolution. In principle, to minimize this effect, a crystal with a diffuse side surfaces and absorptive wrapping would be an alternative. However, as will be demonstrated in Chap. 4 by a comparative study of the detector performance in two wrapping scenarios, in view of our application of the scintillator, this second option has to be strongly disfavored.

Furthermore, the intrinsic radioactivity of the lanthanum halide scintillator family, including $LaBr_3$:Ce, is an unavoidable feature of this group of scintillator materials. This activity is generated from the presence of the ^{138}La isotope with a half-life of 1.02 $\times 10^{11}$ years, which represents 0.09% of the naturally occurring lanthanum abundance [79]. This isotope decays with 66.4% probability into ^{138}Ba by electron capture, emitting 1436 keV γ-rays in coincidence with either ^{138}Ba L or K X-rays with energies of 4.5 keV or 35.5 keV, respectively. With a remaining probability of 33.6% ^{138}La decays into ^{138}Ce via β^--decay under emission of a 789 keV γ ray. The contribution of this isotope to the internal radioactivity of our crystal was calculated to be 1.6 Bq/cm^3, by knowing the half-life, detector density and chemical composition. This value is in reasonable agreement with value of 1.45 Bq/cm^3 reported in [80]. The second source of the detector's internal radioactivity results from radiochemical impurities of ^{227}Ac and its daughters, emitting five sequential α particles through their decay chain to stable ^{207}Pb with energies between 1.6 MeV and 3 MeV. Despite the fact that the internal radioactivity of the $LaBr_3$:Ce scintillator may be considered a disadvantage in some applications, it can in turn be exploited for energy calibration purposes or in a correction step of the spatial resolution analysis, as it will be shown in chapter 5.

Figure 3.2.5 shows a pulse-height spectrum of the intrinsic radioactivity of the 50×50×30 mm^3 monolithic $LaBr_3$:Ce scintillator, shielded with lead against room background and measured under lead shielding conditions for 20 minutes. This activity covers an energy range from about 4 keV to 3000 keV. The β^- continuum, representing 33.6% of the ^{138}La decay, is clearly visible at the lower part of the energy spectrum until its β end-point energy of 255 keV. It is followed by

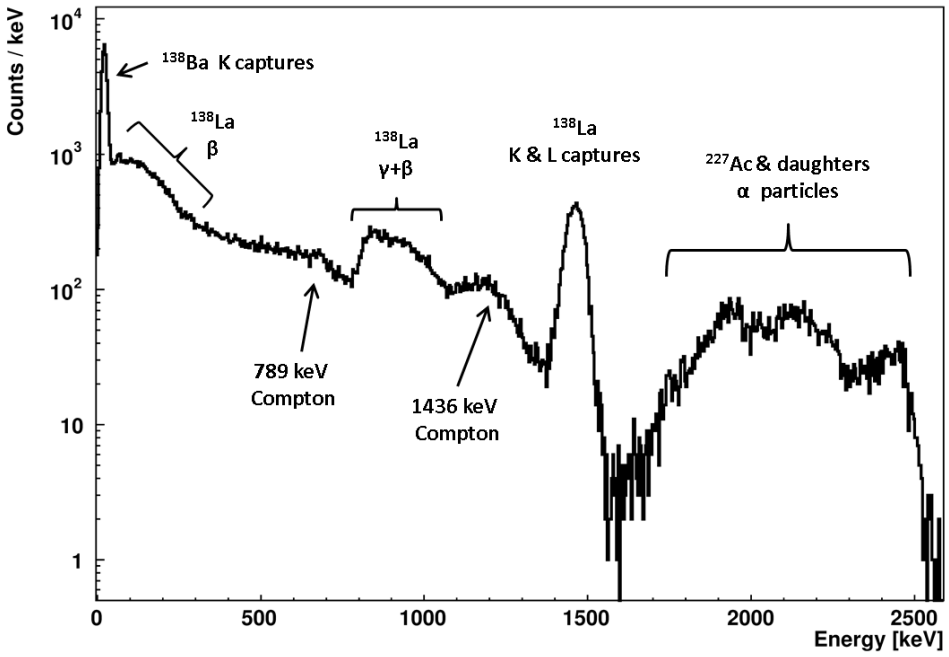

Figure 3.2.5: Internal radioactivity energy spectrum of a (lead-shielded) 50×50×30 mm^3 monolithic $LaBr_3$:Ce scintillator, measured for 20 minutes. It shows the two decay modes of the ^{138}La isotope, electron capture and β^- decay, as well as the contribution from the radiochemical impurities of ^{227}Ac and its daughters isotopes.

a γ-ray emission of 789 keV, whose photopeak is broadened due to pile-up with the low-energy γ rays and the β continuum. The prominent photopeak in the low energy region corresponds to the L (4.5 keV) and K (35.5 keV) X-rays of ^{138}Ba, which are emitted in coincidence with 1436 keV γ rays as part of the electron capture decay (66.4%) of ^{138}La. Consequently, the 1436 keV photopeak is shifted to either 1440 keV or 1472 keV, when it is detected together with ^{138}Ba L or K X-rays, respectively. In this energy region also 1461 keV γ rays from remaining room background originating from ^{40}K are expected. Beyond this energy, the contribution of ^{227}Ac with its α-decay daughters are measured up to about 3 MeV.

3.2.2 Signal processing and electronics layout

The Compton camera readout electronics combines ASIC and VME based electronics. In order to provide insight into the signal processing work flow of each detector, the readout electronics of the scatter/tracker and absorber detectors will be explained separately in the following paragraphs.

3.2.2.1 Compton camera scatter detector (DSSSD)

The Compton camera scatter detector component is formed by a stacked array of six layers of double-sided silicon strip detectors (DSSSD). Each of these layers has 128 strips (390 μm pitch size) on each side (128 n-side strips and 128 p-side strips) forming a 2D x and y grid. As can be seen in Fig. 3.2.6, the DSSSD detector is designed to be read out from all four sides. Each two opposite sides serve to transfer the odd and even strip signals of n- and p-side, respectively, to the subsequent signal processing chain. At each of these four outputs, either 64 odd or even strips of one detector side can be processed by one front-end (FE) electronic board, originally designed for the ring-imaging Cherenkov detector (RICH) in the High Acceptance Di-Electron

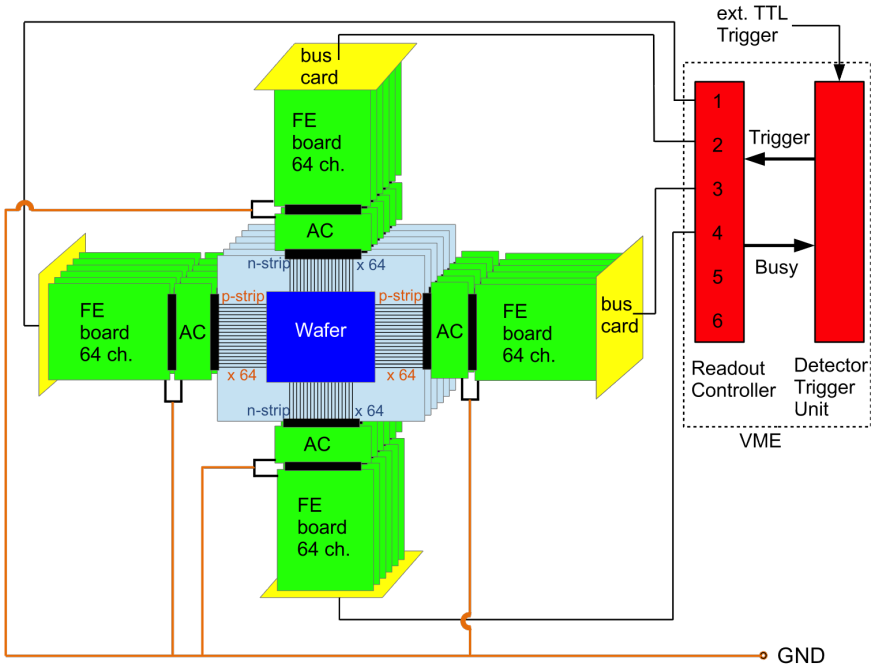

Figure 3.2.6: Schematical drawing illustrating the geometrical arrangement of the six DSSSD layers and their readout electronics. Each DSSSD layer with its 2×128 signal channels requires four 64 channel front-end (FE) boards, connected via AC couplers to 4×64-pin high density connectors in order to protect the GASSIPLEX ASICs [81] from the detector leakage current and bias voltage (see the text for more details). Each six FE boards on one of the detector sides, connected to the six DSSSD layers, are combined by a bus card. This card is responsible for collecting and transferring the FE board digital data, in a daisy-chain mode, to the VME-based detector readout controller. A VME-based trigger unit accepts an external TTL trigger signal, in our case generated by the $LaBr_3$:Ce scintillator, since the GASSIPLEX ASIC cannot generate an internal trigger signal [38].

Spectrometer (HADES) project [82]. This board (see Fig 3.2.10) contains 4 charge integrating GASSIPLEX ASIC chips (16 channels each). So, in total, 24 front-end boards are coupled to the six DSSSD layers via AC couplers. In order to collect the digitized data from these front-end boards, a bus card is designed to collect data from six front-end boards sequentially, connected to one of the four detector outputs of layer 1 to layer 6, in a daisy chained mode. Thus, 4 bus cards are needed to read out all of the 24 front-end boards of the DSSSD array. Since the FE board does not provide an internal trigger signal, a dedicated VME-based trigger module (Detector Trigger Unit) is applied to receive an external (TTL) trigger signal, generated by the absorber detector ($LaBr_3$:Ce scintillator). This concept allows to merge and synchronize the data streams of both scatter and absorber detectors. The DTU module also contributes to initialize and configure the FE boards via a VME-based detector readout controller (RC), which then accepts the trigger signal and returns a feedback (busy) signal. Then, the FE data are transferred in a daisy chained mode from the bus cards to the detector readout controller (RC) via a standard 0.635 mm pitch 50 pin flat ribbon cable. From these the data are finally transferred through the VME bus to the data acquisition PC via a VME-based frontend CPU (Power PC, CES RIO3, [83]) and ethernet cable, respectively [84].

A coupling capacitor (1 nF) between the detector signal and the input of the FE board is mandatory in our case to protect the GASSIPLEX-based circuitry from the detector bias

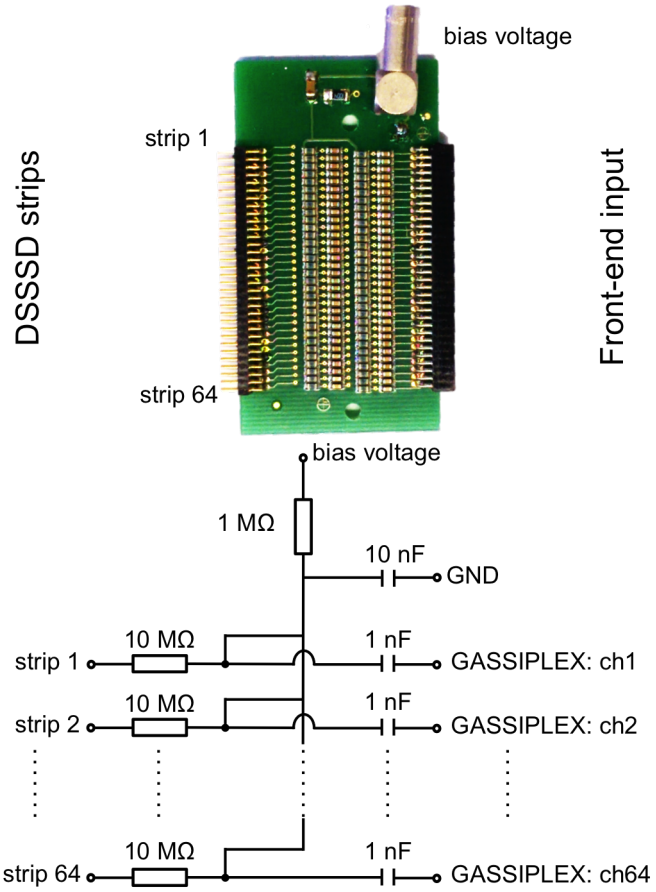

Figure 3.2.7: Photograph (top) and electronical circuit (bottom) of the AC coupler. It is not only used to protect the signal processing electronics from the detector leakage current and bias voltage, but it also allows to bias each p strip and set each n strip of the DSSSD detector to ground potential.

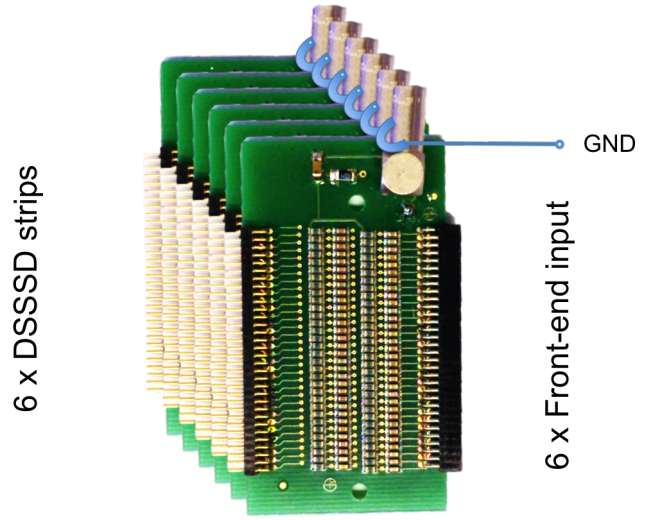

Figure 3.2.8: Illustration of fulfilling the common ground condition by connecting the lemo connector ground of the AC couplers together using a copper wire.

voltage as well as its leakage current, since the expected leakage current from the DSSSD detector is larger than the critical level of 1 nA [81]. Figure 3.2.7 shows a photograph (top) and

a schematic design of the AC coupler (bottom), as used in our Compton camera setup. It is also designed to feed in - 75 V as bias voltage to the p strips and ground all the n strip, ensuring a common grounding for both the FE modules and the n-strips of the DSSSD detectors, as indicated in Fig. 3.2.6. The AC coupler's ground potential, connected to a common grounding line, couples the FE modules ground and the detector ground beside the 50 Ω termination that is connected to the n-side strips. Due to a limited space between the six sequential AC coupler boards, coupled one side of the six DSSSD layers to their FE modules, the common ground potential line is guided by a flexible copper wire around the lemo connectors mass of the AC coupler, as illustrated in Fig. 3.2.8. In a first version, the AC coupler board was built on a 34 $\times$ 62 mm^2 standard printed circuit board (PCB, material FR4) with a thickness of 1.6 mm and a dielectric constant of 4.1 at 11 GHz [85]. The improved version, which is presently in use in the test setup for the potential readout electronics upgrade of the DSSSD detector, has an area of 42 $\times$ 62 mm^2 and a thickness of 0.8 mm. An optimized PCB material with a lower dielectric constant of 3.62 at 10 GHz was chosen to reduce the capacity of the AC coupler board (Megtron 6, Panasonic [86]). As a future perspective, the most recent Megtron 7 PCB material with its two versions (R-5785 and R-5785N) will be preferable choices for the AC coupler board, since this material provides the presently lower dielectric constant compared to the other PCB materials, as indicated in Fig. 3.2.9 [87].

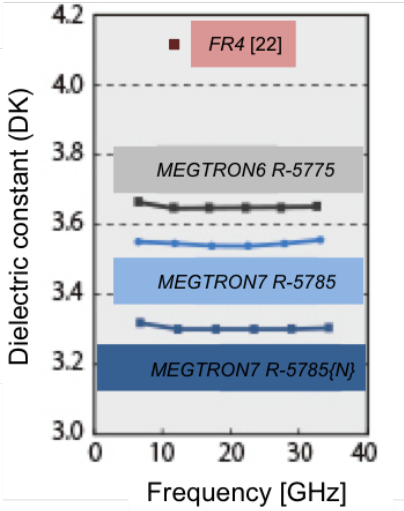

Figure 3.2.9: Comparison of different PCB materials, based on the value of the dielectric constant as a function of frequency [87]. The Megtron7 material with its two versions seems to be the best option for a future re-design of the AC coupler, since it exhibits the presently lowest available dielectric constant.

A single front-end module (FE), as displayed in Fig. 3.2.10, is capable of processing up to 64 input detector signals from the amplification stage to the digital output. In practice, the detector signals are distributed to four GASSIPLEX ASIC-based chips (16 channels each), in which they are amplified and shaped by charge sensitive amplifiers (CSA) and shapers, respectively. The shaped signal (semi-Gaussian signal) has a rise time of about 550 ns that determines the delay between the event arrival at the absorber detector and the trigger of the DSSSD, since no circular buffer is implemented at this stage. Then, the analog peak height information of the shaped signal of each channel is stored in a track and hold circuit. The 16 channels of each GASSIPLEX chip can be multiplexed to one output. Then, the outputs of the 4 GASSIPLEX chips are multiplexed to a 20 MHz 10-bit analog-to-digital converter (ADC, ADS820 [89]) by

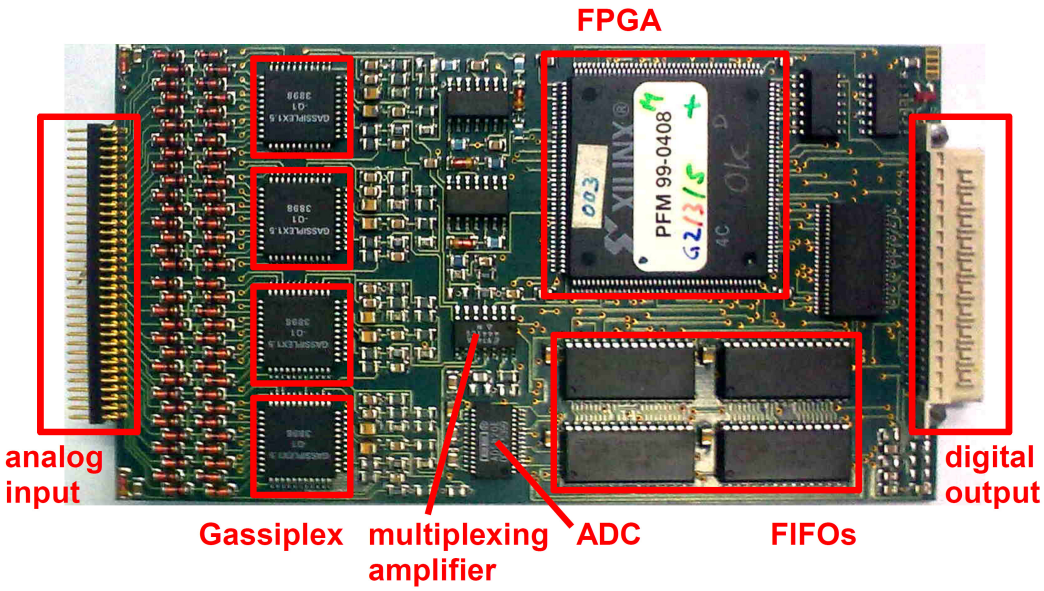

Figure 3.2.10: Photograph of the front-end (FE) electronics board. It can be divided into analog and digital parts. The analog part consists of four GASSIPLEX ASIC chips, which include a charge sensitive amplifier, shaper, track & hold unit and multiplexer together with a multiplexing amplifier that finally directs the GASSIPLEX outputs to the ADC. The digital part starts with the ADC and ends with the FIFO (First In First Out) memory, where the generated data are temporarily stored. Inbetween, assignment of the channel number, hit address and threshold comparison takes place in the Field Programmable Gate Array (FPGA, Xilinx XC4005E) [88].

a fast video multiplexed amplifier (élantec EL4441 [90]). The resulting 10 bit binary word is analyzed in a pipelined logic mode inside the Field Programmable Gate Array (FPGA, Xilinx XC4005E), where the zero suppression takes place, as well as adding a channel number to each data word and generating a hit address list for the 64 input channels. Finally, after the digitized data were compared to a digital threshold, which can be uploaded for each channel to the FPGA during the FE configuration, the valid pulse height data words and their corresponding hit addresses will be stored into a FIFO (First In First Out) memory bank (Cypress CY7C421/5) [88].

3.2.2.2 Electronics adaptation for the DSSSD detectors

The DSSSD detector readout electronics has to be able to accept both positive and negative signals, generated from p and n strips, respectively. However, as the front-end board was designed for a ring-imaging Cherenkov (RICH) experiment, it was optimized for the positive signal polarity from the RICH detector. Therefore, some modifications in the front-end module are required, concerning the voltage signal fed into the ADC with a dynamic range from + 0.25 V to + 4.25 V. One obvious solution to this situation could have been to invert the detector signal either at the GASSIPLEX amplification stage or at the multiplexing amplifier, both of which are operated in non-inverting mode. However, from the initial design of the GASSIPLEX ASIC, the charge sensitive amplifer (CSA) is capable to operate only in non-inverting mode. So, the signal cannot be manipulated at this stage. The multiplexing amplification stage incorporates four amplifiers, accepting the output signals from the four GASSIPLEX chips consecutively, followed by a multiplexing unit. Since the inverting inputs of the four amplifiers are internally

connected to a common feedback network, individual access to the inverting input of each amplifier is not possible. Therefore, the idea of inverting the detector signal to generate a positive input for the ADC had to be abandoned. Alternatively, setting the voltage of the common inverting input of the multiplexing amplifier to a lower (more negative) value leads to a rise of the output baseline to a more positive value. Consequently, a negative input signal, which is larger than the voltage at the inverting input U_{in-}, will lead to a positive output voltage. This means that the lowest input voltage at the amplifier non-inverting input and the resulting positive output signal are governed by the voltage at the inverting amplifier input, which can be calculated by applying Kirchhoff's rules to the resistor network displayed in Fig. 3.2.11.

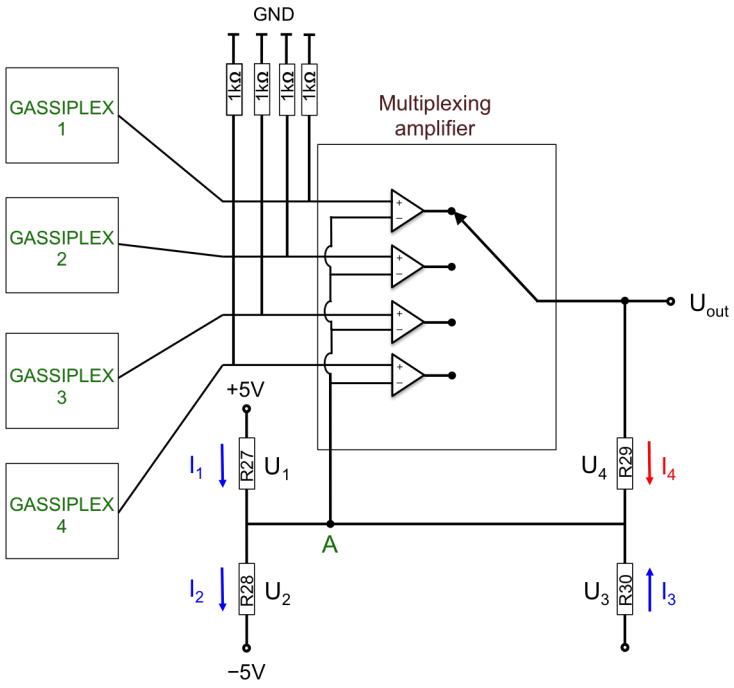

Figure 3.2.11: Schematic diagram of the multiplexing amplifier with four channels, connected to the outputs of four GASSIPLEX chips. The inverting input of the four amplifier channels are internally connected to a common feedback resistor network (R27 - R30), indicated as "A". The output baseline (U_{out}) can be raised by calculating the optimum resistor configuration, which then allows for negative input signals to be accepted in the positive dynamic range of the amplifier.

According to the circuitry drawn in Fig. 3.2.11, Kirchhoff's voltage law provides the following equations

$$U_1 + U_2 - 10V = 0 \tag{3.2.1}$$
$$U_3 + U_2 - 5V = 0 \tag{3.2.2}$$
$$U_1 - U_4 - 5V + U_{out} = 0 \tag{3.2.3}$$
$$U_4 - U_3 - U_{out} = 0 \tag{3.2.4}$$

Considering the current flowing in and out of the node 'A' and applying Kirchhoff's current law together with Ohm's law, one obtains

$$I_3 + I_4 + I_1 = I_2 \tag{3.2.5}$$
$$\frac{U_3}{R30} + \frac{U_4}{R29} + \frac{U_1}{R27} = \frac{U_2}{R28} \tag{3.2.6}$$

Applying the ideal amplifier voltage rule, which is U_{in+} = U_{in-}, gives:

$$U_{in} = 5V - U_1 \tag{3.2.7}$$

Thus, the baseline, which is the output voltage U_{out} of the amplifier, can be calculated as a function of the input voltage U_{in} via

$$U_{out} = R29\left(5V\left(\frac{1}{R28} - \frac{1}{R27}\right) + U_{in}\left(\frac{1}{R27} + \frac{1}{R28} + \frac{1}{R29} + \frac{1}{R30}\right)\right) \tag{3.2.8}$$

Knowing that the operational amplifier gain is defined as the ratio of the difference of two output voltages (U_{out1} - U_{out2}) to the difference of two input voltages (U_{in1} - U_{in2}), the gain factor G_U of the amplifier drawn in Fig. 3.2.11 can be derived from Eq (3.2.8):

$$G_U = R29\left(\frac{1}{R27} + \frac{1}{R28} + \frac{1}{R29} + \frac{1}{R30}\right) \tag{3.2.9}$$

The described electronics adaptation of the FE boards for negative input signal acceptance was first used by the HERMES experiment at DESY [91], where negative input signals were obtained from scintillating fiber detectors. Subsequently, the same method was used for the readout electronics of Micromegas tracking detectors (Micro-pattern gaseous detectors), developed for particle physics applications in the ATLAS collaboration at CERN [92]. Table 3.1 shows the multiplexing amplifier resistors, baseline and gain configurations for negative input signals optimized for HERMES and Micromegas and for positive input signals from HADES, for which the FE board was originally designed. Although the HERMES and Micromegas scenarios were both dealing with negative input signals, their multiplexing amplifier configurations were slightly different. In the HERMES configuration, the baseline was set to a high value of 3.5 V, leading to a large dynamic range for a detectable signal. However, this quickly drives the multiplexing amplifier to operate in saturation, which consequently causes side effects such as crosstalk, inefficiency and non-linearity. This had been investigated in detail while adapting the FE board for Micromegas applications [92]. Therefore, the readout electronics of the Compton camera scatter detectors uses the HADES and Micromegas configurations for the positive and negative input signals, respectively.

	HADES [93]	HERMES [91]	Micromegas [92]
R27 [Ω]	39k	33k	75k
R28 [Ω]	2.2k	4.5k	3.3k
R29 [Ω]	2.5k	3.3k	1.8k
R30 [Ω]	7.5k	8.2k	33k
baseline U_{out} [V]	0.47 ± 0.08	3.5 ± 0.11	2.85 ± 0.08
gain factor G_U	1.51	2.24	1.62

Table 3.1: Feedback resistor network configurations of the multiplexing amplifier, used for either positive or negative input signals, together with the corresponding gain factor and baseline (U_{out}). The readout electronics of the LMU Compton camera scatter detectors (DSSSDs) uses the HADES and Micromegas resistor configurations for the p and n strip signal readout, respectively.

Figure 3.2.12 displays the output of one layer of the Compton camera scatterer (i.e. 2×64 signals for n- and p-side, respectively), using the HADES and Micromegas FE multiplexing amplifier configurations for p strips and n strips. The baseline of the p-strip configuration was

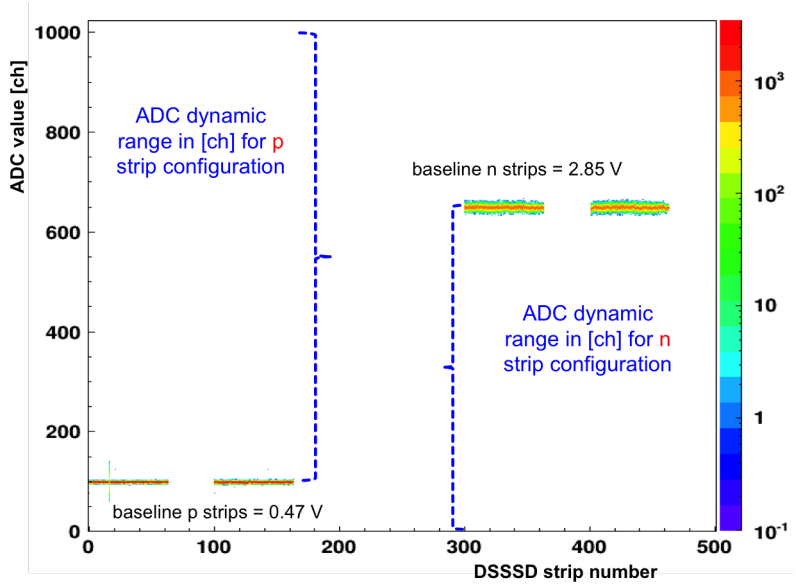

Figure 3.2.12: The p-strip (left) and n-strip (right) data of a DSSSD layer, read out by an FE board configured with the HADES and Micromegas FE resistor network configurations, respectively.

set to 0.47 V, translating into about 100 ADC channels. For the negative n-side signals, it was set to 2.85 V, which corresponds to about 600 ADC channels. It is obvious that the positive signal configuration provides a larger ADC dynamic range compared to the range for negative signals. This sacrifice was made in order to avoid an amplifier saturation and its problematic consequences, as explained above. As indicated in Fig. 3.2.12, the dynamic range of the negative n strip signals spans from about 600 ADC channels down to 0. This has to be considered when comparing with the digital threshold value in the FPGA, which for positive signals constitutes a lower threshold, while for negative signals the FPGA threshold corresponds to an upper threshold.

3.2.2.3 Compton camera absorber detector ($LaBr_3$:Ce)

The monolithic $LaBr_3$:Ce scintillator crystal [73] is read out by a multi-anode position sensitive PMT (H9500, Hamamatsu [74]), which features 256 segments with an area of 3×3 mm^2 each. As it is shown in the block diagram of the (in a first commissioning phase) reduced electronics setup (Fig. 3.2.13), the signals of all PMT segments were directed to an adapter board via 4×64 pin high-density coaxial ribbon cables (SEU-TEU-1, SAMTEC). This board was designed to combine the signals of each 4 neighbouring segments of the PMT, forming an 8×8 pixel grid with an area of 6×6 mm^2, in order to reduce the cost and complexity of the electronics readout system. Then, the 64 signals were transferred by 10 ns LEMO cables to four amplifier plus CFD (MCFD-16, Mesytec [94]) modules each, handling 16 channels. The (differential) amplified analog signals as well as the logic CFD output signals, acting as individual gates responsible for the charge integration time, were directed from each MCFD-16 module to the Charge-to-Digital converter (MQDC-32, Mesytec [95]) by 13 m and 8 m long ribbon cables (34-pin 3M^{TM} Twisted Pair Flat Cable, 3782 Series, 4.99 ns/m propagation delay), respectively. These two ribbon cables (for amplified energy signals and individual gates) have to be combined via an MQDC-32 adaptor cable (Mesytec [95]) as indicated in Fig. 3.2.14 before connecting to the MQDC-32 input. The MQDC-32 is capable of processing up to 32 channels, divided in two input banks. This means that each input bank of the MQDC-32 is responsible for all 16

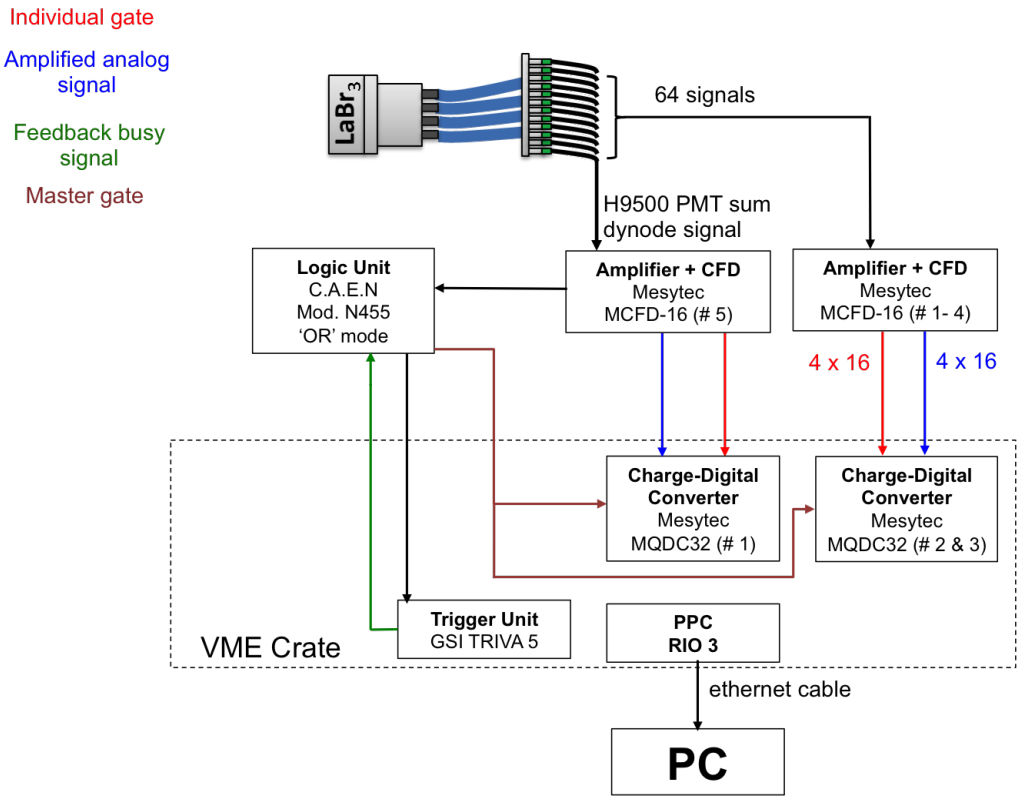

Figure 3.2.13: Block diagram of the first generation of the $LaBr_3$:Ce scintillator readout electronics, where four neighbouring H9500 PMT segments were combined. In total 64 signals plus the sum dynode signal were processed by 5 MCFD-16 (NIM) modules and 3 MQDC-32 (VME) modules.

signals of one MCFD-16 module. The PMT sum dynode signal (dynode 12, DY 12 [74]) was processed by one channel of an independent MCFD-16 module, since its common logic output signal (labelled as OR output signal) was generating the trigger signal for the DAQ system, as well as the gate of the MQDC, called master gate, responsible for controlling the activity of the module.

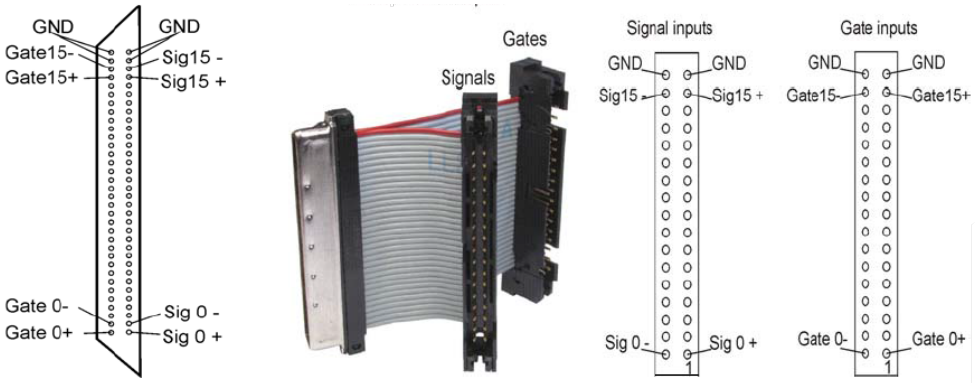

Figure 3.2.14: The MQDC-32 input connector, responsible for combining the differential amplified analog signals to their corresponding individual (logic) gate signals. The input signals have to follow a specified time sequence in order to enable a correct operation of this module.

Table 3.2 shows configuration parameter settings of the MCFD-16 modules that are used for processing the PMT signals of each individual segment, as well as of the sum dynode. The

MCFD modules	MCFD parameters					
	Polarity	Gain	Fraction	Delay	Dead Time	Width
# 1 - 4	Negative	3 (0 V to ± 1.2 V)	20%	5 ns	300 ns	105 ns
# 5 (sum dynode)	Positive	1 (0 V to ± 3.5 V)	20%	3 ns	300 ns	135 ns

Table 3.2: Configuration settings for the MCFD-16 modules 1 - 4, used to process the 64 PMT segments and MCFD-16 module number 5 used for the PMT sum dynode signal.

polarity was set according to the corresponding output signal type to be either negative or positive for the individual segments and the sum dynode, respectively. The amplification gain is optimized to avoid signal saturation from the targeted γ rays, which range up to about 8 MeV. In order to adjust the dynamic range in particular for the sum dynode signal, a ^{60}Co source was used to measure the signal amplitude of 1.332 MeV γ rays to be 300 mV with a gain setting of '3' as used for the individual signals (range: 0 to ± 1.2 V). In this case, the expected signal amplitude of the 6.1 MeV prompt-γ rays from ^{16}O* would result in about 1.4 V, which could exceed the dynamic range of the MCFD-16 in this configuration. Thus, the gain was chosen to be 1, with a resulting dynamic range between 0 to ± 3.5 V. Consequently, the prompt-γ energy range will only exploit the lower 40% of the available dynamic range, which is the preferred compromise to the alternative setting, where the prominent 6.1 MeV photon line would end in the spectral overflow. Similarly, the gain of the 64 individual PMT segments was set to 3, since the expected signal amplitude of E_γ = 6.1 MeV was about 1 V, thus within the dynamic range of the gain 3 setting. The CFD delay was set to be 3 ns and 5 ns for both sum dynode and each individual segment signal, respectively, corresponding to 70% of the signal rise time. The MCFD dead time can be adjusted to be longer than the recovery time of the MQDC-32, estimated to be 250 ns. Thus, 300 ns were selected as dead time for all MCFD-16 modules. The width of each logic signal (individual gate), generated from the 64 individual PMT segments, was adjusted to 105 ns to ensure the correct charge integration time for the corresponding analog signals (see Fig. 3.2.15). On the other hand, the width of the master gate, derived from the sum dynode signal, was fixed to 135 ns in order to fulfill the MQDC-32 timing requirements for the input signal. In order to operate correctly, the MQDC-32 modules require a timing configuration of the input signals (analog and logic signals) as indicated in Fig. 3.2.15. The minimum required time between starting the master gate and the start of the individual gate is 2 ns. Otherwise, the individual gate would not be recognized by the MQDC-32, resulting in a loss of this event. The second MQDC-32 time requirement requests the amplified analog signal not to start earlier than 6 ns after the falling edge of the individual gate to ensure the correct charge integration of the incoming signals. Therefore, the lengths of the flat ribbon cables were adjusted to fulfill these requirements, using an oscilloscope and 400 MHz differential probe (Tektronix, P6246), realizing a delay of 15 ns between the master and the individual gates as well as of 16 ns between the individual gates and the analog signals. Consequently, the cable lengths for the analog signals and the individual gates were fixed to 13 m and 8 m, respectively. Although these cable lengths nominally result in a shorter delay than what was estimated, this configuration anticipates already the additional signal delay introduced by two Fan-In-Fan-Out modules (LeCroy, 429A), required to distribute the master gate to each MQDC-32 module when upgrading the electronics to read out all the 256 PMT segments, which otherwise would spoil the required MQDC-32 input signal timing. So, the cable length configuration could be kept at 13 m and 8 m for the analog signals and individual gates, respectively, in order to reduce the cost and effort when upgrading the electronics. This setup was used in chapter 5 for studying the $LaBr_3$:Ce light spread function as well as in chapter 6 together with the DSSSD detectors as a starting setup of the Compton camera.

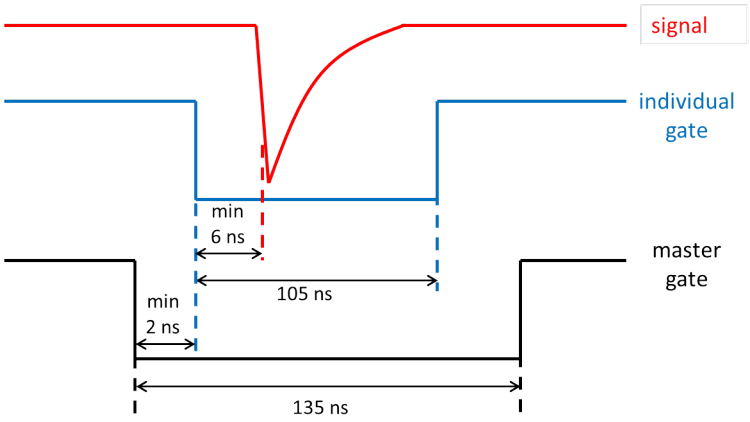

Figure 3.2.15: Timing requirements for the input signals of the MQDC-32 module. The minimum required time between the MQDC-32 trigger signal (master gate) to the individual gate, responsible for the charge integration period, is about 2 ns. The amplified analog signal should start at least 6 ns after the start of the individual gate, otherwise the event would be ignored.

In order to fully exploit the high granularity of the PMT to read out the $LaBr_3$:Ce crystal, each of the 256 segment signals has to be processed individually. This requires in total 17 MCFD-16 modules, as well as 9 MQDC-32 modules to process all of these channels, including the sum dynode signal. The settings of the MCFD-16 modules had to be slightly modified by an increase in the MCFD gain setting from previously '3' (0 V to $\pm$ 1.2 V) to '10' (0 V to $\pm$ 350 mV), taking into account the reduction of the PMT segment signals when they are read out individually. In order to design the electronics setup as flexible and modular as possible with regard to a potential transportation to external beam facilities, two delay boxes were designed to accommodate almost 360 m of ribbon cables required to carry the analog and individual gate signals from the MCFD-16 modules to the corresponding MQDC-32 digitizers. Figure 3.2.16 shows the arrangement of the signal processing electronics before cabling the detector.

The envisaged operation of the Compton camera close to a massive target emitting radiation from energetic ion (proton) beams may be affected by neutron background, originating from various nuclear reactions between the particle beam and the target materials. Therefore, the timing properties of the absorber detector ($LaBr_3$:Ce scintillator) are crucial in order to discriminate between neutrons and γ rays, using the Time-of-Flight technique. For this purpose, 9 VME-based Time-to-Digital converter modules (MTDC-32, Mesytec [96]) were additionally installed in the Compton camera electronics setup to process the timing signals from all 256 PMT segments and the sum dynode signal. Due to the resulting increase in the number of VME modules, exceeding the number of 21 available slots in the VME crate, a second VME crate had to be added to the setup, which further affected the complexity of the signal processing electronics. Figure 3.2.17 displays a block diagram of the $LaBr_3$:Ce scintillator readout electronics after installing the timing instruments and distributing the digitizers (charge and time) over two VME crates. In order to ensure data stream synchronization from the two VME crates, two trigger modules (TRIVA 5 [97]), bridged by a common trigger cable (customized by GSI), were required in addition to three Power PC frontend CPU modules (Rio 3 [83]), where two of them were responsible for data collection in their respective crates, while the third one acted as event builder. Figure 3.2.18 shows photographs of the Compton camera and its readout electronics before (a) and after (b) cabling, exploiting the timing and energy features of the $LaBr_3$:Ce scin-

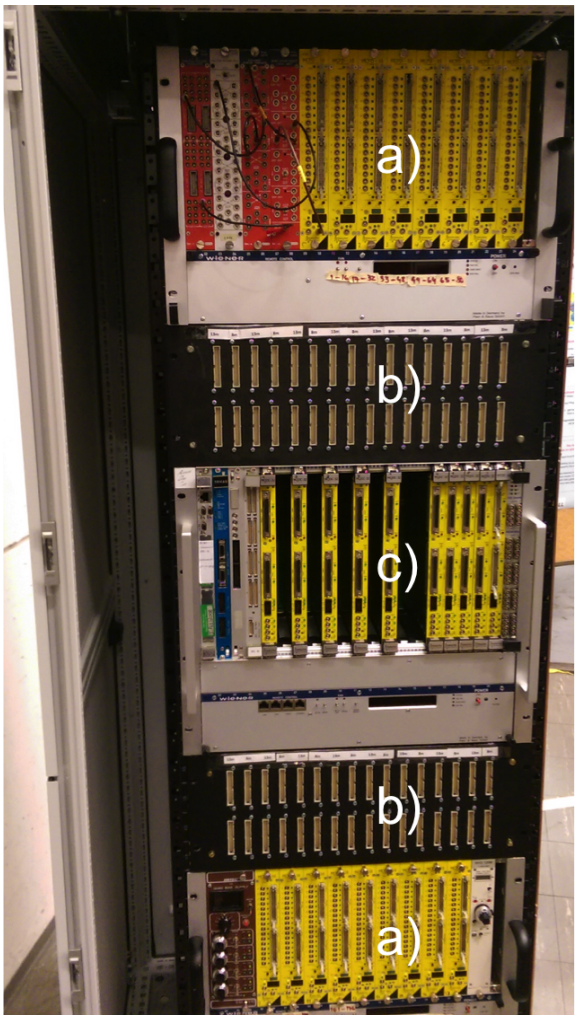

Figure 3.2.16: Photograph of the upgraded $LaBr_3$:Ce scintillator signal processing electronics, capable of processing the energy signals of 256 PMT segments plus the signal from the sum dynode. (a) represents 17 NIM-based amplifier plus CFD (MCFD) modules. Their analog and logic signals (individual gates) are delayed by 13 m and 8 m of flat ribbon cables, respectively. The delay ribbon cables are stored in customized delay boxes (b). (c) indicates the VME-based MQDC-32 modules, the trigger module (TRIVA 5) and VME-based data acquisition frontend CPU (Power PC, PPC RIO3 [83]) .

tillator. This setup was used to commission the Compton camera at low and high energy particle beam facilities, explained in detail in chapter 6.

In all following experiments, the data acquisition (DAQ) was controlled and visualized by the MBS (Multi Branch System), running under the operating system LynxOS [98], and the Root Based Online/Offline Utility MARABOU [99]. MARABOU consists of an MBS-based front-end, responsible for data readout, event building and data transport, and ROOT-based [70] back-end that deals with run controlling, histogramming and data analysis, since it builds upon the Root framework. Both parts are connected by a shared memory and message parsing module. The users can specify the experimental configuration in a ROOT-based macro, which then generates codes for the MBS-frontend and for the ROOT-based backend in the Linux workstation. Moreover, the back-end provides an analysis platform, based on ROOT, for either online or offline data handling. At this stage, the data of LMU Compton camera components are processed, filtered, calibrated and structured in a certain format suitable for the MEGAlib package,

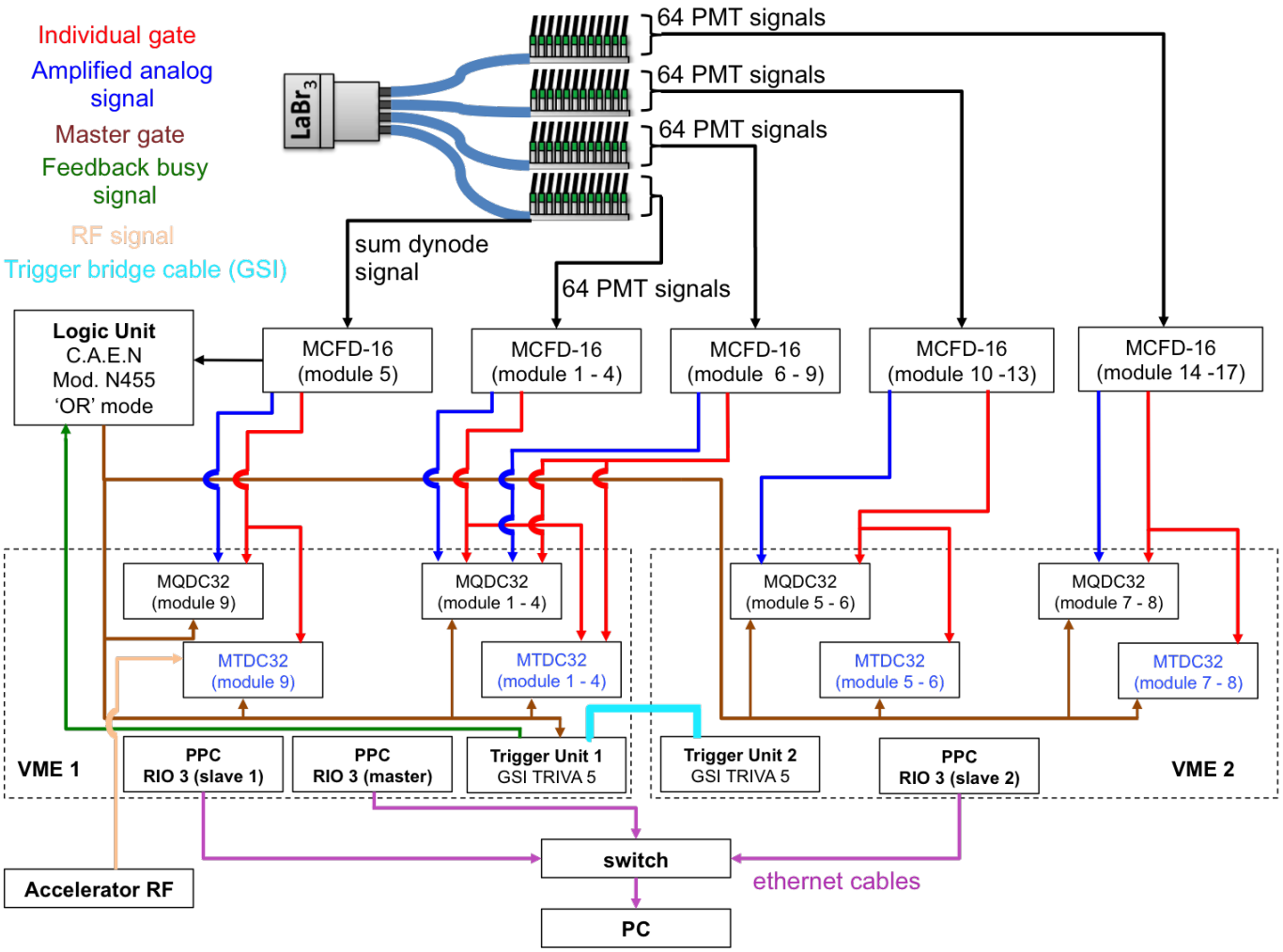

Figure 3.2.17: Block diagram of the $LaBr_3$:Ce scintillator readout electronics, which is capable of processing both energy and time information from 256 PMT segments as well as from the sum dynode signal. The increase in the number of processed VME channels, in total 514 channels, requires the use of 2 VME crates to host all digital electronics modules. This increases the system complexity, in terms of trigger synchronization and data merging of two VME data streams. Therefore, three frontend VME CPUs are used for data collection (slave 1 and 2) and event builder (master), besides the use of two trigger modules, bridged by a customized cable.

particularly for the 'Revan' module.

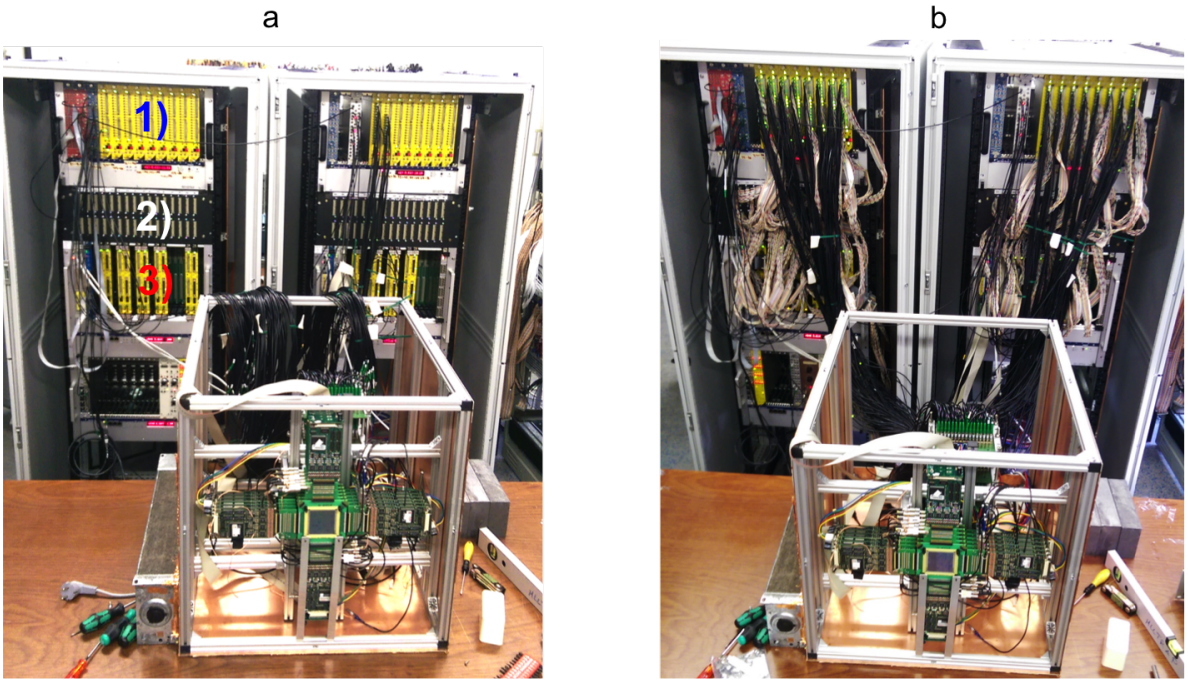

Figure 3.2.18: Photograph of the full and most recent setup of the Compton camera together with its uncabled (a) and cabled (b) readout and signal processing electronics. The readout electronics, mainly for the $LaBr_3$:Ce scintillator, was upgraded compared to the previously described starting version, in order to allow for the processing of the time and energy information from all 256 H9500 PMT segments. In total 514 VME channels require two VME crates to host the corresponding electronics modules. As can be seen in panel (a), two NIM crates for the MCFD-16 modules (1), two delay boxes (2) and two VME crates for both MQDC-32 and MTDC-32 modules (3) are distributed over two racks.

3.2.3 Mechanical setup

Positioning the Compton camera components (the DSSSD scatter array and the $LaBr_3$:Ce absorber detector) precisely relative to each other, while keeping enough flexibility to allow for distance variations, requires a flexible and precise support frame. In our case, aluminum ITEM [100] profile bars (2.5 cm thick) were chosen to form a cubic frame ($61 \times 54 \times 54$ cm^3) with additional support bars to mount the detectors and their attached cabling or readout boards. The stack array of six DSSSD detectors was customized by the manufacturer [71] such that a minimum distance of 10 mm could be realized in the stack that mechanically forms a block unit. The detector stack together with the directly attached readout electronics was fixed to the front frames of the support cube, as indicated in Fig. 3.2.19 (a). The $LaBr_3$:Ce scintillator with its corresponding cable adapter boards was mounted directly behind the DSSSD detector array (see Fig. 3.2.19 b). The distance between the front face of the $LaBr_3$:Ce detector and the last DSSSD layer was fixed to 3.5 cm according to the design simulation. In order to allow for a precise alignment of the scintillator relative to the DSSSD detectors, the $LaBr_3$:Ce detector was mounted to a precision positioning stage.

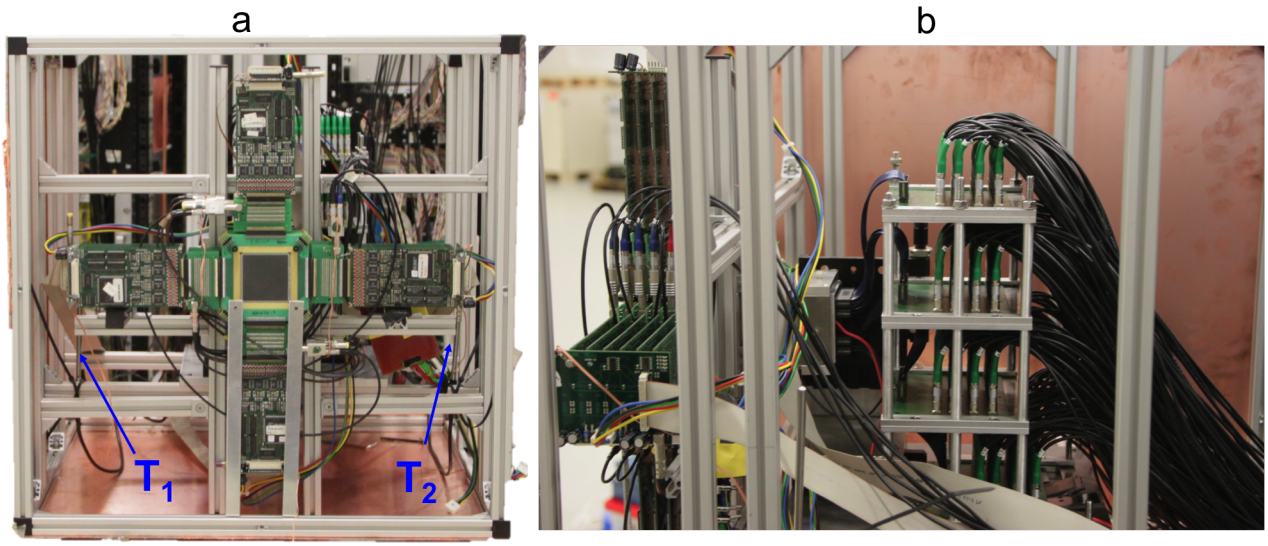

Figure 3.2.19: Front (a) and side (b) view of the Compton camera components, mounted in a cubic frame with support and positioning bars. The temperature sensors T_1 and T_2 (see text) are visible in panel (a). These sensors are responsible for monitoring the temperature inside the cubic box, while it is covered from all sides by copper plates, acting as a Faraday cage and light tight enclosure.

Having positioned the Compton camera components inside the cubic support frame, the frame covered from all sides by copper (front side) and copper-plated epoxy plates in order to form a light-tight box. This allows for operating the DSSSD detectors at air without driving them into saturation via light exposure. Since the cubic box ($61 \times 54 \times 54$ cm^3) was formed by 6 independent copper plates, small gaps had to be sealed at each edge of the cube. In order to achieve both the light-tight sealing as well as maintain the integrity of the Faraday cage, copper tape was used. Thus, electric shielding was provided for all detectors and their electronics, particularly for the charge integrating electronics of the DSSSD detectors. In order to minimize the passive scattering probability for photons entering the Faraday cage through the 1.6 mm thick copper front, an entrance window (11×11 cm^2) was inserted into the front plate at

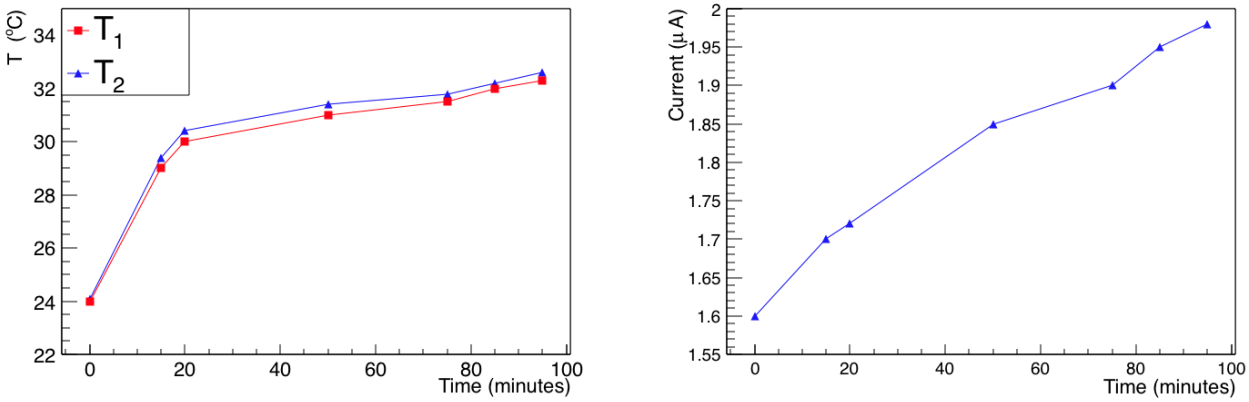

Figure 3.2.20: Monitoring study of the cage temperature (a) and the leakage current of a DSSSD layer (b) as a function of time, while the Compton camera components were in operation. There was no cooling system involved in this study. T_1 and T_2 denote the two temperature sensors placed in the Faraday cage at the position of centre-right (T_1) and centre-left (T_2).

the positon of the active area of the DSSSD detector. Light sealing and electric shielding was achieved by a 30 μm aluminum foil. A slit opening of 2 $\times$ 54 cm^2 was introduced to the bottom of the back plate of the cage as a feedthrough of the cables from both scatter and absorber detectors. Light-tightness was preserved by closing the unused gap of this slit with an aluminum foil attached via copper tape.

Placing the Compton camera components inside a closed box will lead to a temperature increase, due to the accumulated heat from the readout electronics (especially from the DSSSD detectors) of 38 W that was measured as power consumption using a Voltcraft probe (Model VC605). This may affect the detector performance, either by an increased thermal noise level, or even endanger the electronics, when critical temperature levels would be exceeded. Therefore, a temperature monitoring system, based on two PT-104 [101] sensors, was installed inside the cage. Two thermal sensors were installed, one at the centre-right (T_1) and the second one at the centre-left (T_2) of the Faraday cage (see Fig. 3.2.19 a). Figure 3.2.20 (a) shows a study of the cage temperature as a function of time, while the Compton camera was in operation and no cooling or ventilation system was active. In the first 15 minuts after powering the detectors, the temperature increased rapidly from 24 °C to almost 30 °C, due to the power consumption of the electronics during the initialization and configuration phase. Then, it gradually increased further over the remaining period of time until reaching about 32 °C. Simultaneously, as indicated in Fig. 3.2.20 (b) for one prototypical detector module, the leakage current of the DSSSD detectors was monitored. As expected, the current increased from 1.6 μA to 2 μA as the cage's temperature increased by 6 °C. Therefore, in order to limit the effect of power dissipation in the Faraday cage, a fan unit was installed in order to actively exchange the air inside the cage, thus assisting to reach an equilibrium temperature. Figure 3.2.21 a) and b) show the repeated study of the cage temperature and DSSSD leakage current characteristics, as a function of time, while the ventilating fan unit was in operation. The temperature reached an equilibrated plateau already 10 minutes after initializing and configuring the DSSSD electronics. Moreover, the leakage currents of all DSSSD layers remained below 1 μA, except for the first layer, which was probably affected by some stray light from the entrance window (see Fig. 3.2.22). From these studies, it can be inferred that the simple ventilation system was sufficient to obtain stable temperature conditions for the Compton camera, thus assuring also

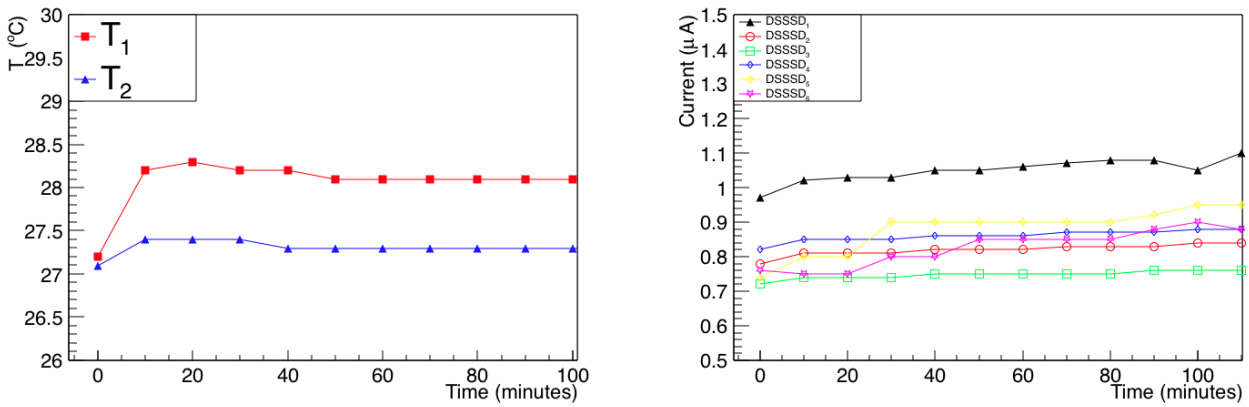

Figure 3.2.21: Monitoring study of the temperature development in the Compton camera cage (panel a)) and the leakage current of all six DSSSD layers, after installing a ventilation fan unit at the camera cage as a cooling system, as a function of time (panel b)).

stable operational conditions and detector performance. This is important to note, since some active cooling techniques, undoubtedly able to significantly reduce the electronic noise level, appear prohibitive in view of the envisaged clinical application of the final Compton camera. Cooling devices like liquid nitrogen dewars would most likely not be tolerated in the patient treatment environment. Alternatively, alcohol-based cooling techniques or peltier cooling might be options for the future as well.

In practice, the Compton camera box can be placed on a support stand in order to adjust the camera position relative to the target (in our case a water phantom). This support stand, shown in Fig. 3.2.22, allows to be adjusted to different heights, since it is composed of three different sub-units that can be vertically moved in a telescopic manner. It features a dynamic range of slightly below 1 m to 2 m height of the support platform. This facilitates the operation of the setup at different beam facilities with varying beam line heights.

Figure 3.2.22: Photograph of the compete Compton camera setup, mounted on its support stand and together with the signal processing electronics. The Compton camera system is housed inside a (light-tight) Faraday cage, which includes a ventilation fan used to exchange the hot air from inside the box, as well as an entrance window. The entrance window is covered by a thin aluminum foil (30 μm) in order to minimize the scattering probability for incoming photons. A backside slit was used as a feedthrough for the signal processing electronics cables of both the scatterer and absorber, directed to the signal processing and DAQ system standing in the back. The Compton camera box was placed on top of an adjustable stand, which offers an adjustable height range of 1 to 2 m.

Chapter 4

Offline Characterization of the Compton camera absorber detector ($LaBr_3$:Ce) with absorptive and reflective surface coating

The properties of a 50×50×30 mm^3 monolithic $LaBr_3$:5%Ce detector, coupled to a multi-anode photomultiplier tube (PMT, Hamamatsu H9500), were investigated with two surface wrapping options (absorptive and reflective), in order to determine the optimum performance of the Compton camera absorbing detector. Firstly, the relative energy resolution of the detector was studied as a function of the photon energy from 121 keV to 1408 keV. Moreover, the position-dependent energy resolution was investigated by scanning the detector front face using a 1 mm collimated ^{137}Cs source with a step size of 6 mm. This study generated an energy resolution map for each crystal coating modality. Secondly, the timing properties of the $LaBr_3$:5%Ce detector were examined relative to a fast plastic detector (BC-418), using a ^{60}Co source. The photopeak detection efficiency of the Compton camera absorbing detector was also evaluated over a wide energy range from 121 keV to 1408 keV. Finally, the impact of two different crystal wrapping modalities (absorptive and reflective) on the scintillation light profile inside the monolithic $LaBr_3$:Ce detector was investigated for the case of a 64-fold PMT granularity by deriving the Light Spread Function (LSF) of the 2D-light amplitude distribution of a central irradiation position, using a 1 mm collimated ^{137}Cs source. Moreover, the influence of the impinging γ ray energy on the spatial behaviour of the produced scintillation light of the reflectively wrapped $LaBr_3$:Ce scintillator was examined for two different PMT granularities (256 and 64 segments).

4.1 Energy resolution

The relative energy resolution $\frac{\Delta E}{E}$, expressed as the FWHM of the γ-ray energy peak recorded by the detector divided by the actual energy value of the incident γ ray of the absorptively and reflectively wrapped 50×50×30 mm^3 $LaBr_3$ scintillator, was evaluated at different photon energies. A diagram of the experimental setup used in this measurement is displayed in Fig. 3.2.13. The energy spectrum was derived from the H9500 PMT sum dynode signal, which was processed and digitized by an amplifier plus Constant Fraction Discriminator (CFD) module (MCFD16, Mesytec) and a Charge-to-Digital converter (MQDC32, Mesytec), respectively. The energy resolution study covered a γ-energy range from 121 keV to 1408 keV using ^{152}Eu (110 kBq), ^{60}Co (32 kBq), and ^{137}Cs (163 kBq) calibration sources, placed in an axial distance of 25 cm of the detector surface. The detector was irradiated by each source for about 15 minutes to

ensure sufficient statistics. The data was fitted using a two-parameter function expressed as

$$\frac{\Delta E}{E} = 100 \times \frac{\sqrt{A + B \times E}}{E} \tag{4.1.1}$$

where A and B are free parameters [102].

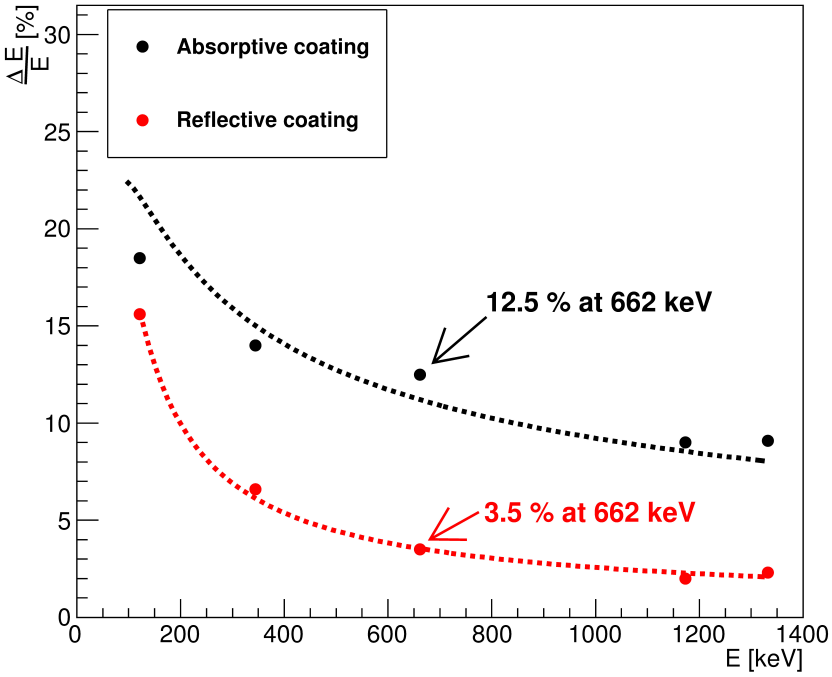

Figure 4.1.1: Energy resolution as a function of the photon energy values measured by a $LaBr_3$:Ce detector with reflective (red) and absorptive (black) side surface coating, obtained with ^{152}Eu, ^{137}Cs and ^{60}Co calibration sources. The dotted lines represent a two-parameter function fit as indicated in Eq (4.1.1).

Figure 4.1.1 displays the energy resolution for photon energies from 121 keV to 1332 keV, as determined for the reflectively and absorptively coated $LaBr_3$:Ce crystal, respectively. The dotted curves parameterize the energy dependence of the relative energy resolution according to the two-parameter function indicated in Eq. (4.1.1). The relative energy resolution $\frac{\Delta E}{E}$ was found to be 12.5% and 3.5% at 662 keV for the absorptively and reflectively wrapped crystal, respectively. Throughout the energy range, the reflectively wrapped crystal exhibited a significantly improved energy resolution. This can be illustrated via the pulse height spectrum of the intrinsic radioactivity of the $LaBr_3$:Ce scintillator, measured under well-shielded conditions for both coating modalities, absorptive (a) and reflective (b), as indicated in Fig 4.1.2. Here, the reflectively wrapped detector clearly resolves the details of all decay modes (β decay and electron capture) of ^{138}La, such as the 1472 keV transition and its Compton edge, as well as the decay chain of ^{227}Ac that starts from 1.6 MeV.
In general, the energy resolution ΔE/E of a scintillation detector read out by a photomultiplier can be expressed as

$$\left(\frac{\Delta E}{E}\right)^2 = \delta_{intr}^2 + \delta_{tran}^2 + \delta_{st}^2 \tag{4.1.2}$$

where δ_{intr} is the intrinsic detector resolution affected, e.g., by crystal inhomogeneities, δ_{tran}

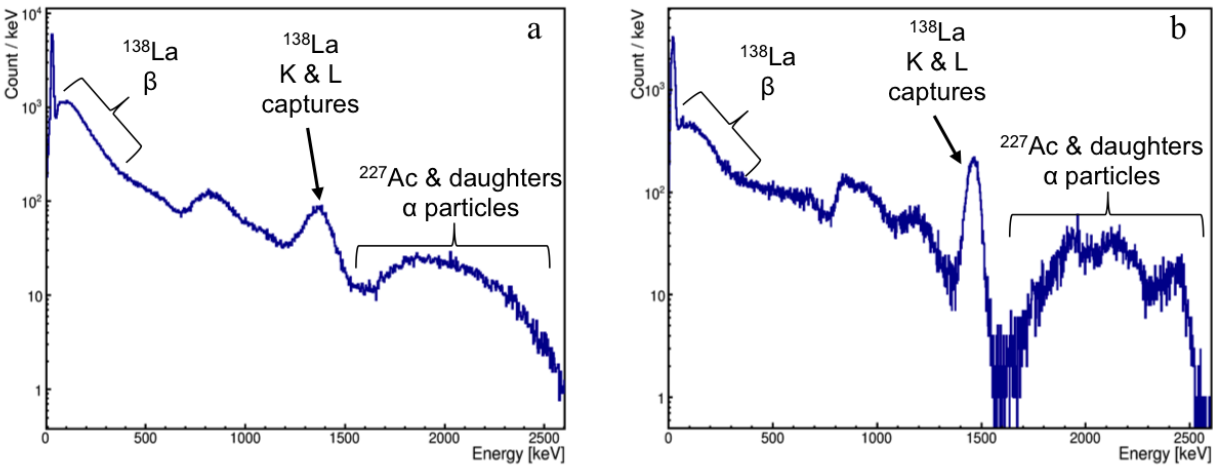

Figure 4.1.2: Intrinsic radioactivity spectrum of an absorptively (a) and reflectively (b) wrapped $LaBr_3$:Ce scintillator.

is the transfer resolution that is correlated to the optical coupling properties of the crystal to the PMT readout, including the photocathode quantum efficiency, as well as the focusing of photoelectrons to the first dynode, and δ_{st} is the statistical contribution of the PMT [103]. The last two factors will determine the statistical uncertainty of the PMT, as it is directly affected by the number of photoelectrons generated at the photocathode and the photoelectron collection efficiency at the first dynode [104].
Since the same crystal and optical coupling were used with reflective and absorptive crystal wrapping, the intrinsic term can safely be expected to give the same contributions to the overall energy resolution in both scenarios. As the generated scintillation light is partially absorbed by the absorbing wrapping material and consequently the number of the photoelectrons that reach the PMT is drastically reduced, the statistical term δ_{st} should contribute to the degradation of the energy resolution in the absorptively coated crystal, since δ_{st} is inversely proportional to the square root of the number of photoelectrons

$$\delta_{st} = 2.35\sqrt{\frac{1+\nu_M}{N_{phe}}} \tag{4.1.3}$$

where ν_M is the variance of the PMT gain, typically between 0.1 to 0.2, and N_{phe} is the number of photoelectrons [103]. The transfer term δ_{tran} is also expected to contribute to the energy resolution deterioration in the absorptively wrapped crystal, since in this crystal scenario the collection of the scintillation light at the photocathode strongly depends on the interaction position at which the scintillation light is generated. This can be noticed throughout the study of the spatial dependence of the energy resolution using the 1 mm collimated ^{137}Cs source. Moreover, even for a given position of interaction, the probability for a scintillation photon to arrive at the photocathode will depend much more strongly on the initial angle of emission than in the reflectively wrapped crystal.
Figure 4.1.3 shows the resulting 2D energy resolution map of the absorptively wrapped $LaBr_3$:Ce crystal at 662 keV. The energy resolution is gradually degrading from 8% in the central region to about 10% and 16% at the detector's edges and corners, respectively. This can be attributed to the reduction of scintillation light reaching the PMT (thus reducing the

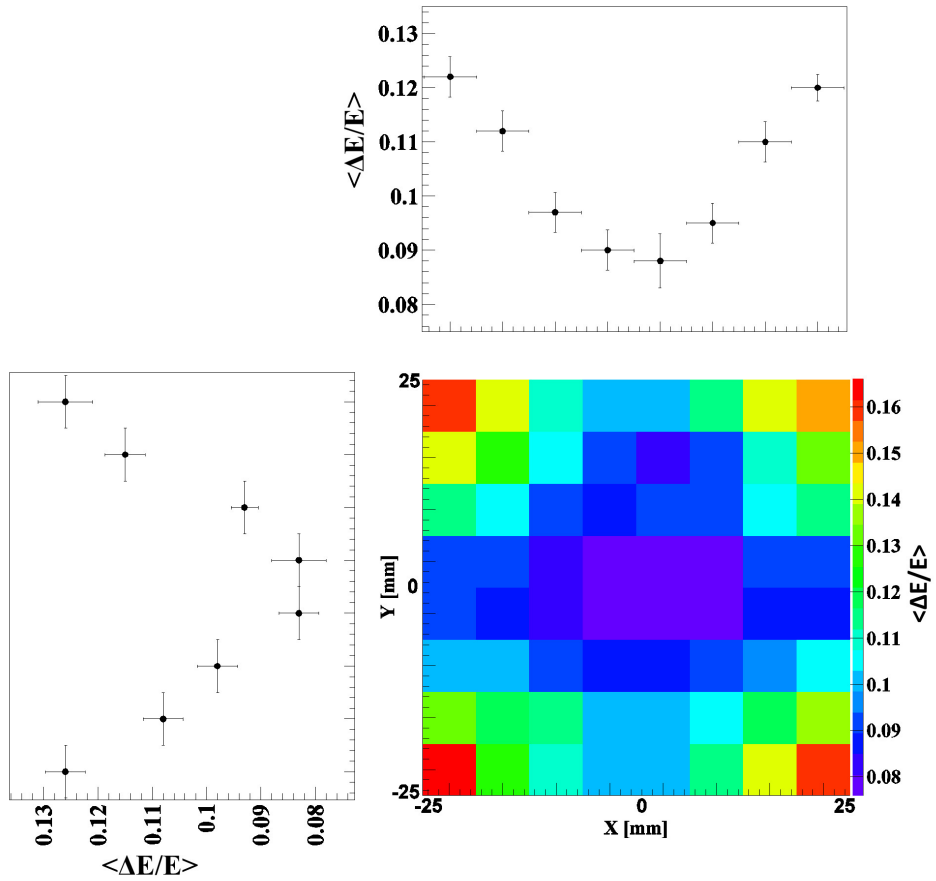

Figure 4.1.3: 2D energy resolution map together with its X and Y projection obtained by scanning the absorptively wrapped $LaBr_3$:Ce crystal with a 1mm collimated ^{137}Cs source and a step size of 6 mm in x and y direction.

number of photoelectrons), due to the absorption of scattered and reflected photons hitting the absorptively coated side surfaces of the scintillation crystal. This effect is much stronger for scintillation photons generated in the edge or corner regions compared to the central region of the crystal. In contrast, this effect disappears with the reflective coating of the $LaBr_3$:Ce crystal, as indicated in Fig. 4.1.4. The corresponding 2D energy resolution is only slightly varying with the irradiation position, as can be seen from the respective x and y projections (averaged over the complementary dimension). An averaged relative energy resolution $\frac{\Delta E}{E}$ = 3.8±0.04 % is achieved in this scenario. The drastic improvement by about a factor of 2.5-3.5 compared to the absorptive coating clearly emphasizes the need to preserve the full amount of scintillation light (and thus photoelectrons N_{phe}) via the reflective wrapping of the crystal, thus reducing the statistical fluctuations of N_{phe} at each irradiation position.

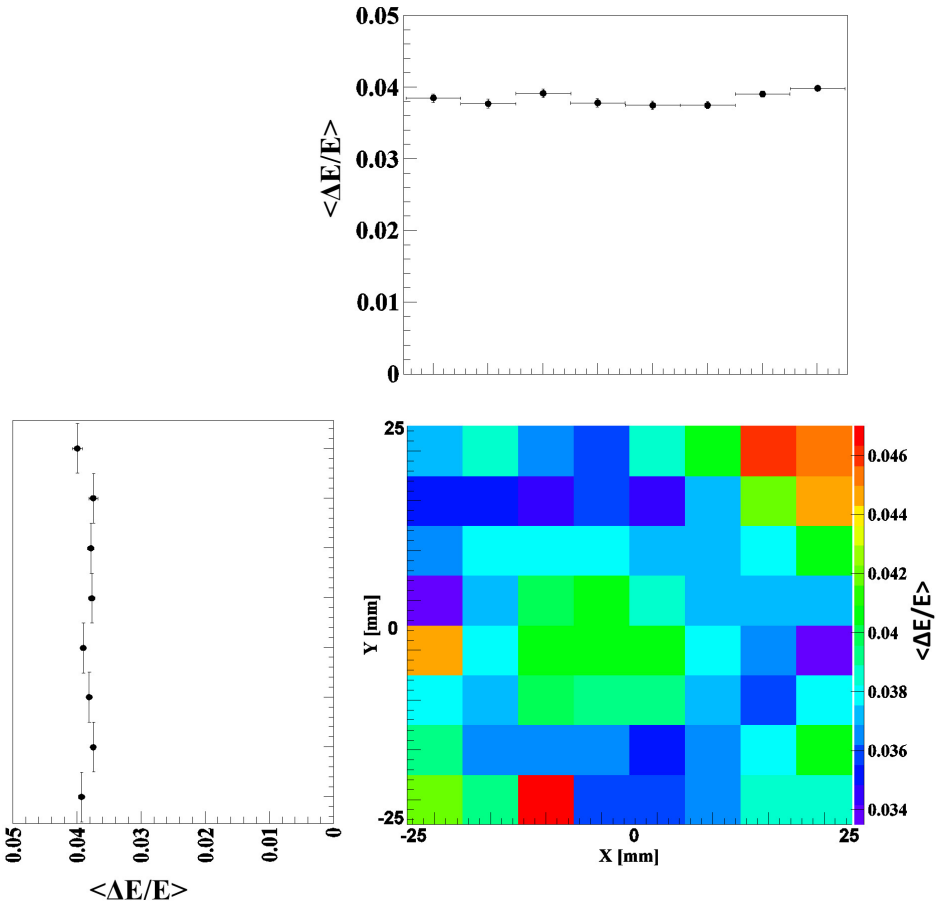

Figure 4.1.4: 2D energy resolution map measured by scanning the reflectively coated $LaBr_3$:Ce crystal with a 1 mm collimated ^{137}Cs source and a step size of 6 mm in x and y direction. The x and y projections (averaged over the complementary direction) show an almost position independent energy resolution of 3.8% on average.

4.2 Time resolution

The timing performance of the $LaBr_3$:Ce scintillator was investigated relative to a fast reference plastic detector (BC-418) using a coincidence method. Figure 4.2.1 indicates the electronics setup of the time resolution measurement. First, the time resolution of the reference detector

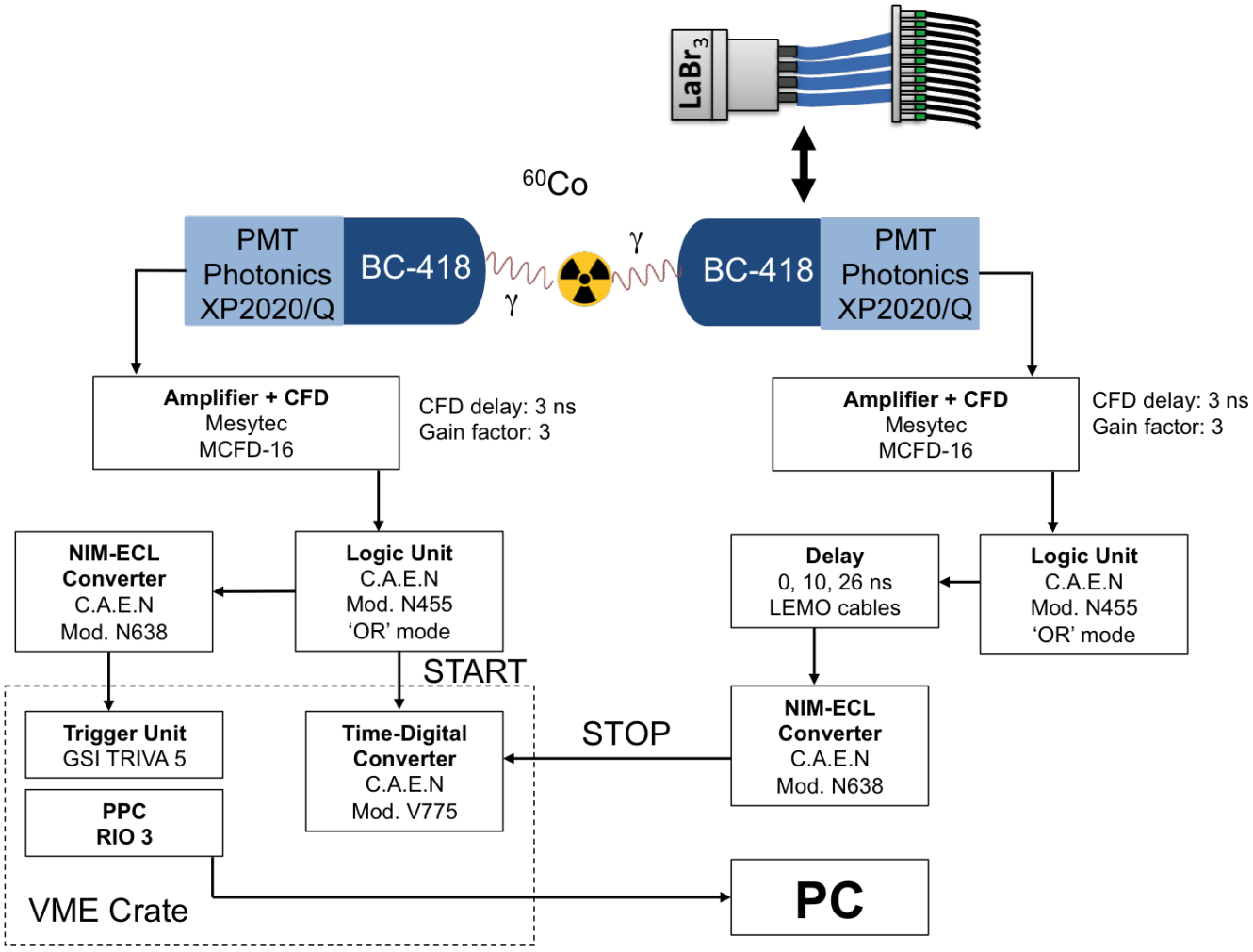

Figure 4.2.1: Schematics of the time resolution measurement that was performed in the first step using two identical plastic detectors (BC-418). Subsequently, one reference plastic detector was replaced by the $LaBr_3$:Ce scintillator in order to measure its time resolution.

was determined by measuring the coincidence time between two simultaneously emitted γ rays from a ^{60}Co source, using two identical plastic detectors (2" diameter, BC-418) coupled to fast PMTs (Photonis XP2020/Q). The two signals of these detectors were fed to an amplifier plus CFD module (Mesytec, MCFD-16) and subsequently to a Time-to-Digital Converter (TDC, C.A.E.N. Mod. V775). The signal of the STOP branch was delayed by 10 ns and 26 ns, respectively, using lemo cables in order to calibrate the time spectrum. Then, the time resolution of one reference detector $\triangle T_{plast.1}$ was extracted according to

$$\triangle T_{plast.1} = \sqrt{\frac{(\triangle T_{plast.1+2})^2}{2}} \tag{4.2.1}$$

where the $\triangle T_{plast.1+2}$ is the total time resolution measured by the two identical reference detectors.

Subsequently, one of the reference detectors was replaced by the $LaBr_3$:Ce detector in order to measure the coincidence time resolution of this system. Knowing the time resolution of the reference detector and the combined time resolution ($\triangle T_{tot}$) of plastic and $LaBr_3$:Ce scintillator, the time resolution of the $LaBr_3$:Ce detector can be obtained as

$$\triangle T_{LaBr_3} = \sqrt{(\triangle T_{tot})^2 - (\triangle T_{plast.1})^2} \tag{4.2.2}$$

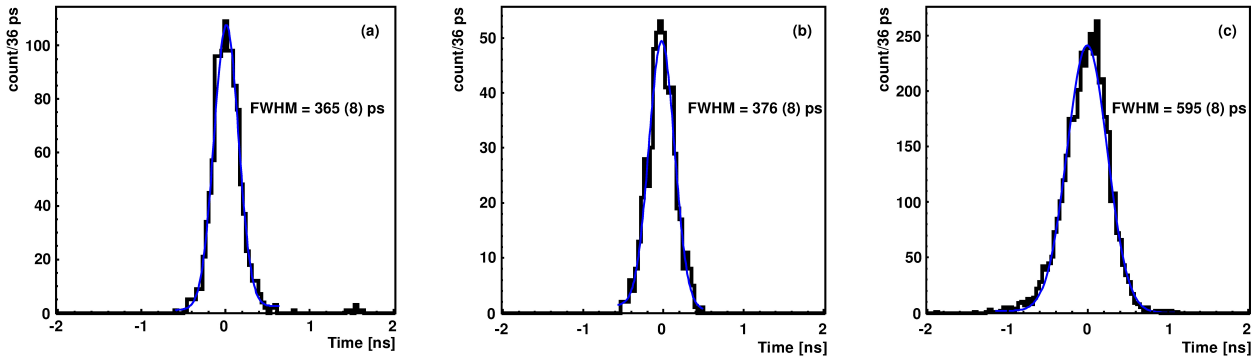

Figure 4.2.2: Coincidence time peak of two simultaneously emitted photons from ^{60}Co measured by two identical plastic detectors (BC418) (a) and by a reflectively (b) as well as an absorptively (c) wrapped $LaBr_3$:Ce detector, measured against the reference plastic detector. The blue curve represents a Gaussian fit used to derive the indicated FWHM values.

Figure 4.2.2(a) shows the coincidence time peak of two simultaneously emitted photons from ^{60}Co, measured by two identical plastic detectors (BC-418), exhibiting a FWHM of 365 $\pm$8 ps. From Eq. (4.2.1), the time resolution of a single reference detector was found to be 258 $\pm$ 5 ps (FWHM). A similar result was obtained for a BC-418 scintillation detector coupled to the same PMT type (photonis XP2020/Q) by [105] to be 235 ps (FWHM). Figure 4.3.1 (b) and (c) indicate 376 $\pm$ 8 ps (FWHM) and 595 $\pm$ 8 ps (FWHM) as the coincidence time measured for the reflectively and absorptively wrapped $LaBr_3$:Ce detector, respectively, in coincidence with the reference plastic detector. Using the measured time resolution of the reference detector, the time resolution of the $LaBr_3$:Ce detector was extracted using Eq. (4.2.2) to be 536 $\pm$ 6 ps (FWHM) with absorptive and 273 $\pm$ 6 ps (FWHM) with reflective wrapping. Since the same crystal, PMT, electronics and time pick-off method were used in both side surface wrapping scenarios, the improvement in the time resolution of the $LaBr_3$:Ce detector by more than a factor of 2 can clearly be attributed to the maximized light collection in the reflectively wrapped crystal. Consequently, the number of collected photoelectrons per event is correspondingly maximized, thus reducing the statistical fluctuations that affect the time resolution, which scales inversely proportional to the square root of the number of photoelectrons [106, 107].

4.3 Photopeak detection efficiency

The photopeak detection efficiency of the $LaBr_3$:Ce detector was determined using the known activities of the calibration sources. This required measuring the ratio of photons detected in the photopeak to the number of initially emitted γ rays for the specific transitions. In this case, a ^{152}Eu source of 110 kBq activity was used in order to cover a wide range of photon energies between 121 keV and 1408 keV. The experimental setup is the same as it was used for the energy resolution study (see Fig. 3.2.13). The energy spectrum was derived from the sum dynode of the PMT. The data were corrected by background subtraction. Dead time and solid angle corrections were applied. So, the photopeak efficiency, considering all the previous corrections, can be expressed as

$$\varepsilon_{ph} = \frac{(N_{ph,corr})/(1 - t_{dead})}{A_{curr} \times t_{meas} \times I \times (\Omega_{LaBr_3}/4\pi)} \tag{4.3.1}$$

where $N_{ph,corr}$ is the background-corrected number of photopeak counts, t_{dead} is the fraction of DAQ deadtime, A_{curr} is the current activity of the source, t_{meas} is the measurement time, I is the fractional intensity of the γ transition relative to the source activity and Ω_{LaBr_3} represents the solid angle of the $LaBr_3$ detector.

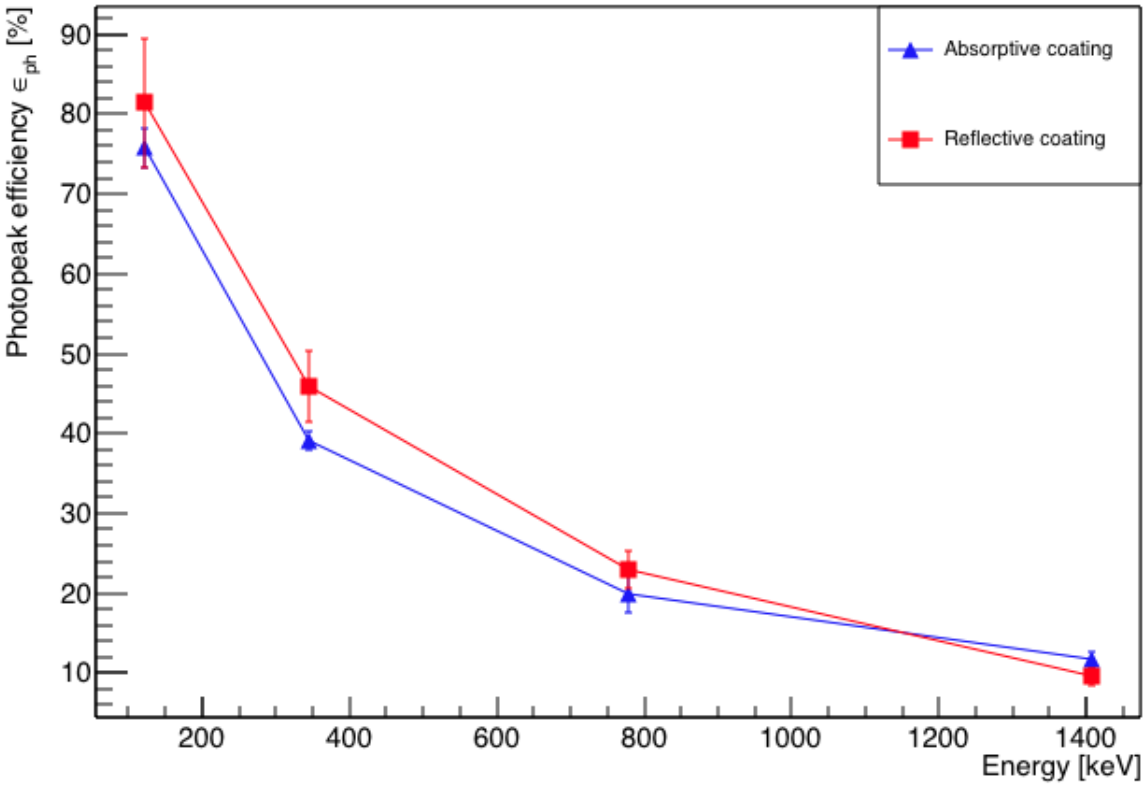

Figure 4.3.1: Photopeak detection efficiency of the absorptively (blue) and reflectively (red) wrapped $LaBr_3$:Ce crystal using a ^{152}Eu calibration source. Background, solid angle and DAQ dead time corrections were applied to these data. The solid lines are to guide the eye.

The $LaBr_3$:Ce photopeak detection efficiency ε_{ph} was determined with reflective and absorptive

crystal coating over an energy range between 121 and 1408 keV, as displayed in Fig. 4.3.1. With both types of crystal surface coating, the full energy detection efficiency, corrected for solid angle and data aquisition (DAQ) dead time, starts from high values of $\varepsilon_{ph} \approx 80\%$ at low energies (121 keV) due to the crystal thickness of 30 mm, the high effective atomic number Z_{eff} and the density of the detector material, rendering the probability of the photoelectric interaction to be dominant in this energy region. However, the observed drop of ε_{ph} with increasing photon energy correlates with the emerging dominance of multiple interactions, such as Compton scattering for high energy photons contributing to reduce the photopeak efficiency. Fig. 4.3.1 also shows that the photopeak detection efficiency, within experimental-uncertainties, is almost the same for both crystal side surface coating modalities. The reduction of the amount of scintillation light due to the absorption processes of in case of absorptive coating obviously does not prevent the identification of the incident photon's photopeak and thus mostly preserves the photopeak detection efficiency.

4.4 Light Spread Function (LSF)

The Light Spread Function (LSF), defined as the FWHM of the radial projection of the light amplitude distribution of the multi-anode PMT segments, is used to evaluate the scintillation light spread of a known incident photon energy in a monolithic crystal. In order to ensure a symmetric distribution of the light intensity, recorded by the PMT segments, a central irradiation position of the crystal was chosen using a 1 mm collimated γ-ray source. In order to generate the corresponding 2D light amplitude distribution, the acquired raw data have to pass through some correction steps, required either by readout electronics, the photosensor (PMT) or the light collection behaviour inside the crystal. The details of the corresponding correction steps and data handling procedure can be explained as follows:

- Gain matching

  Since each channel of the 64 PMT output signals was processed by individual spectroscopic electronics, potential gain variations between the channels have to be corrected. Therefore, two pulser signals with different amplitudes (50 mV and 100 mV) were injected to each amplifier channel, in order to match the relative amplification gains of all channels using the following equation.

  $$E_{cor} = gain \cdot E_{raw} + offset \tag{4.4.1}$$

  In practice, 4 customized 64-pin connectors can be connected to the 4 PMT output ribbon cables, after disconnecting them from the photosensor, in order to distribute the pulser signal to all 256 electronics channels via four adaptor boards that convert the high density cables to the individual 256 lemo cables connecting to the subsequent signal processing chain.

- QDC pedestal

  The charge-to-digital converter (QDC) continuously produces low-amplitude signals originating from the dark current "pedestal". The intensity and energetic position of this signal varies from channel to channel. Thus, digitized data were acquired without input signal to the QDC in order to define (after applying a Gaussian fit to the pedestal peaks) a fixed pedestal subtraction threshold that was determined as 3 σ above the pedestal peak centroid.

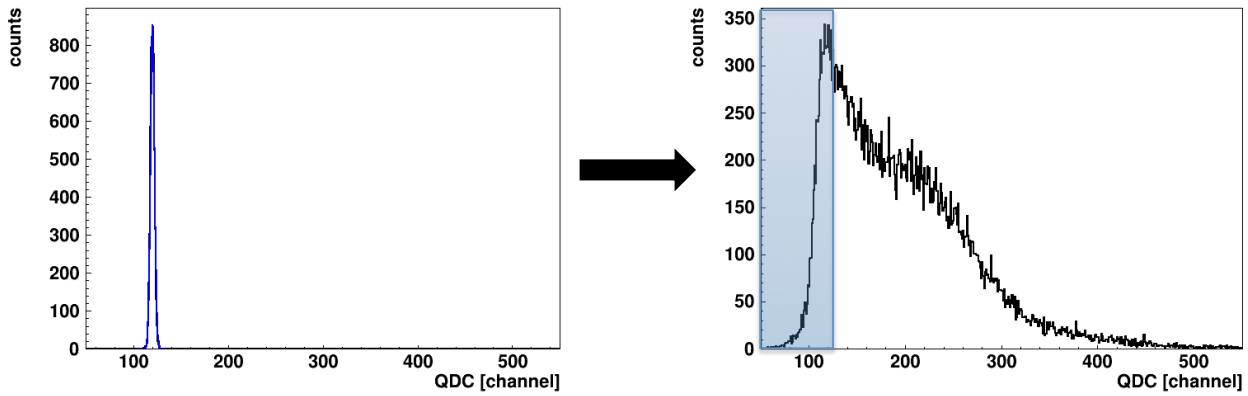

Figure 4.4.1: Exemplary illustration of the QDC pedestal correction method. The pedestal energy (left panel) was acquired while the input signal of the QDC was disconnected. Then, 3 σ of the Gaussian fit above the centroid of Gaussian fit (blue curve superimposed to the data) was chosen as an energy threshold that was applied to the detector raw signal, as indicated in the right panel for a prototypic channel.

- PMT non-uniformity

  In order to allow for a correction of potential gain variations between the 256 pixels of the multi-anode PMT (H9500), a gain non-uniformity matrix is provided by the PMT manufacturer (Hamamatsu). Since each 4 neighboring pixels of the PMT were electronically summed in this study, the corresponding gain values of the non-uniformity matrix were averaged to derive new correction factors for the 64 output channels. These relative correction factors range from 1.0 to 1.8.

- Crystal light distribution uniformity

  Scattering or reflections of the scintillation light mainly in the corner or edge regions of the crystal could lead to an inhomogeneous spatial response of the crystal to impinging radiation. This could be corrected by registering the light amplitude distribution, resulting from a homogeneous flood source covering the crystal front surface, allowing to derive a correction map. Fortunately, the $LaBr_3$:Ce crystal offers an elegant alternative. Since the internal radioactivity of the $LaBr_3$:Ce detector (here 140 Bq, exhibiting besides distinct transitions from ^{138}La and ^{227}Ac ([79] and [108]) a continuum ranging up to about 2.6 MeV) can be assumed to be homogeneously distributed inside the crystal with isotropic emission of the corresponding γ rays. The photon energy region of this background radiation, equivalent to the impinging γ ray energy, was used to determine the position dependent correction matrix. This takes into account the energy dependence of the scatter/reflection processes near corners and edges of the crystal, affecting the light collection behaviour.

- Gating at the energy of interest

  This filter enhances the chance of correctly recording the properties of incident calibration source γ rays by setting an energy gate around the photopeak energy region in the energy spectrum. A FWTM (full width at a tenth of the maximum) of the photopeak is selected as the energy gate for all reference library data.

The above given consecutive correction steps, except the manufacturer-provided PMT uniformity map, should be applied shortly before starting the measurements of 2D light amplitude distributions from collimated calibration sources, since they are subject to degradation after a period of time, e. g. due to temperature variations. Figure 4.4.2 illustrates the influence of each correction step on the appearance of the scintillation light distribution, recorded by the PMT pixels, starting from the raw data until reaching the correct visualization of the position of the collimated source, which is pointing to the upper right corner of the scintillator front surface (indicated by the black dot).
Once the above correction and analysis steps were acquired, the $LaBr_3$:Ce scintillator front surface was perpendicularly positioned in front of the collimator opening in order to investigate the spatial behaviour of the produced scintillation light of incident γ rays inside the monolithic crystal. The ability of resolving the collimated source position, when the step size equals the dimension of the readout PMT segment, was evaluated by scanning the detector with a grid size of 3 mm and 6 mm, respectively, in the case of 16 $\times$ 16 and 8 $\times$ 8 PMT segmentation. Based on these data, the 2D light amplitude distributions were generated by accumulating a preset amount of photopeak events per irradiation position.

4.4.1 LSF as a function of scintillation crystal's side surface coating options: reflective and absorptive

The impact of the crystal surface coating on the position sensitivity of the $LaBr_3$:Ce detector was studied using the 1 mm collimated ^{137}Cs source setup, indicated in Fig. 5.2.2. In this study, the first generation of the readout electronics, indicated in Fig. 3.2.13, was used, where four neighboring PMT segments were electronically summed using a dedicated PCB adapter board. Fig. 4.4.3 and Fig. 4.4.4 show 2D light amplitude distributions for each irradiation position on an 8$\times$8 grid with 6 mm step size in x and y direction. The irradiation position is clearly correlated with the shape of the measured light distribution, both with absorptive and reflective side surface wrapping after applying the correction steps discussed earlier.
The LSF, which corresponds to a radial projection of the 2D light amplitude distribution, is used to evaluate the impact of the crystal wrapping type on the detector's spatial resolution. The absorptively wrapped $LaBr_3$:Ce detector exhibits an LSF of 23.5$\pm$4.2 mm (FWHM), as derived from the radial projection fit of the 2D light distribution indicated in Fig 4.4.5. In contrast to this and derived from Fig 4.4.6, the LSF was measured to be 31.7$\pm$3 mm (FWHM) for the reflectively coated $LaBr_3$:Ce detector. As expected, the reflective coating degrades the position sensitivity of the detector due to the scintillation light scattering at the edges and corners of the crystal. However, this degradation does not prevent the detector from resolving the photon source-position correlation as shown in Fig. 4.4.4

Based on the excellent performance of the reflectively wrapped $LaBr_3$:Ce detector, discussed before, which should not be sacrificed, the reflective crystal surface coating was chosen for the absorbing detector of the Compton camera. Thus, this coating option will be used throughout the following $LaBr_3$:Ce detector study.

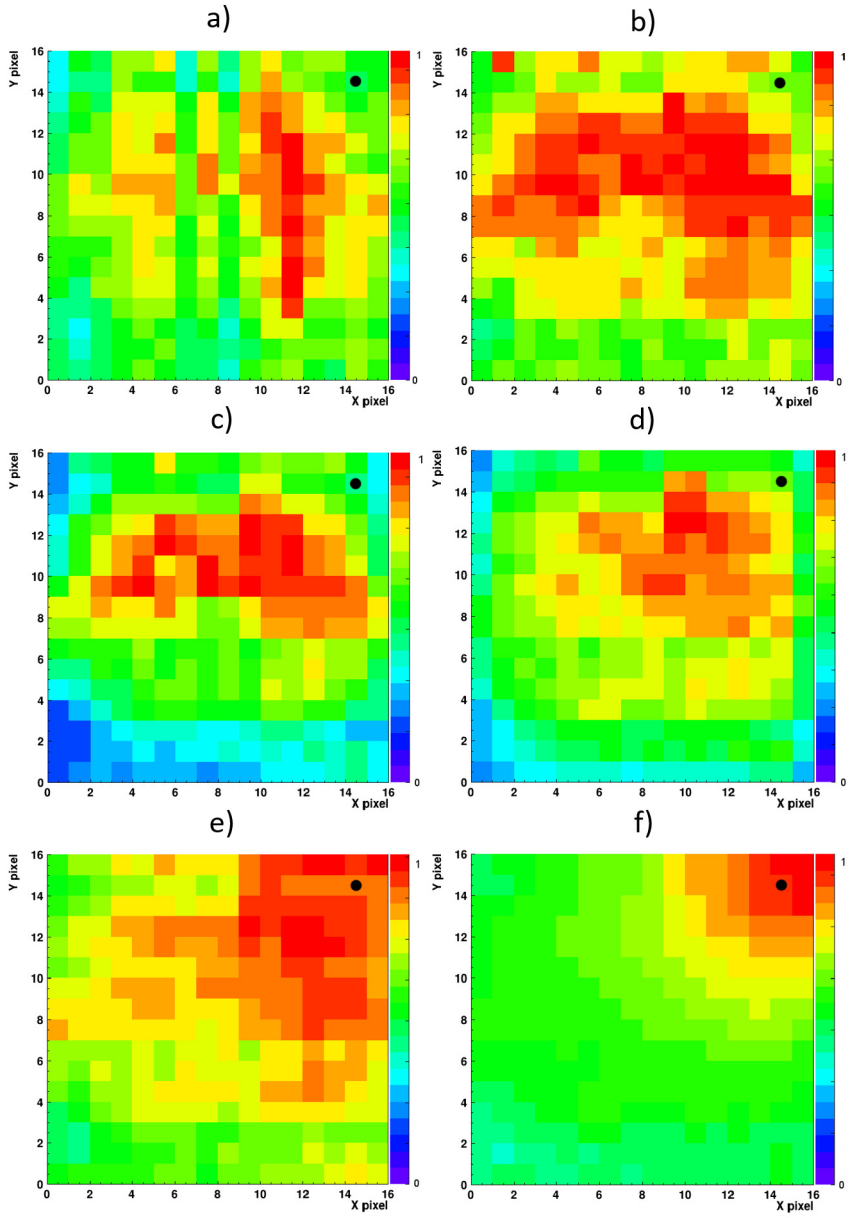

Figure 4.4.2: Visualization of the effect of the consecutive correction steps required to generate the 2D light-amplitude distribution of photons emitted from a collimated γ source. The raw data (a) consecutively pass through electronic gain matching of the signal processing readout electronic channels (b), energy pedestal subtraction (c), PMT pixels response uniformity correction (d) and light collection corrections (e). The final step (f) is given by applying an energy gate around the photopeak in the energy spectrum to exclusively consider scintillation light that results from the impinging γ ray.

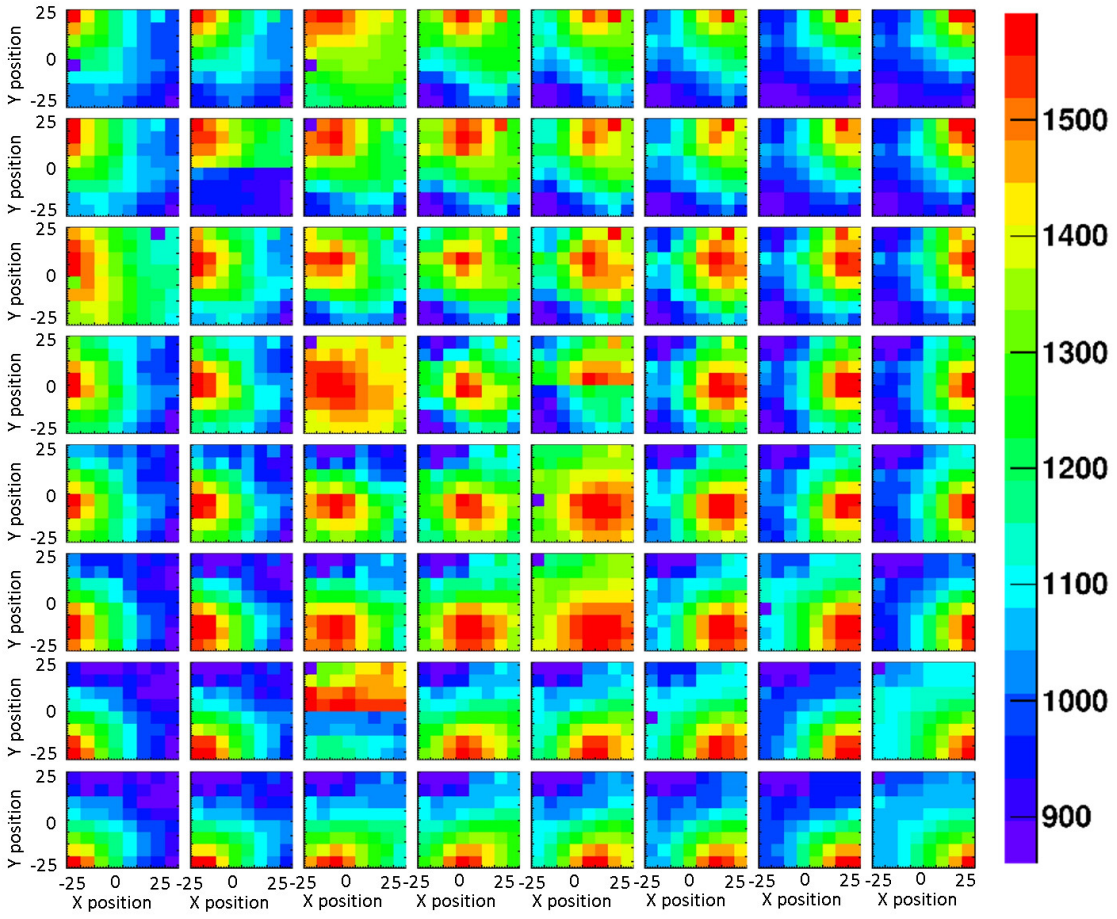

Figure 4.4.3: 2D light amplitude distribution obtained from an 8×8 grid scan of the absorptively wrapped $LaBr_3$:Ce detector, using a 1 mm collimated ^{137}Cs source with a step size of 6 mm in x and y direction. Each subpicture represents a light amplitude distribution of a specific irradiation position. The corresponding correlation of the resulting light amplitude distributions with the consecutive shift of the irradiation position from the upper left to the bottom right corner is clearly visible.

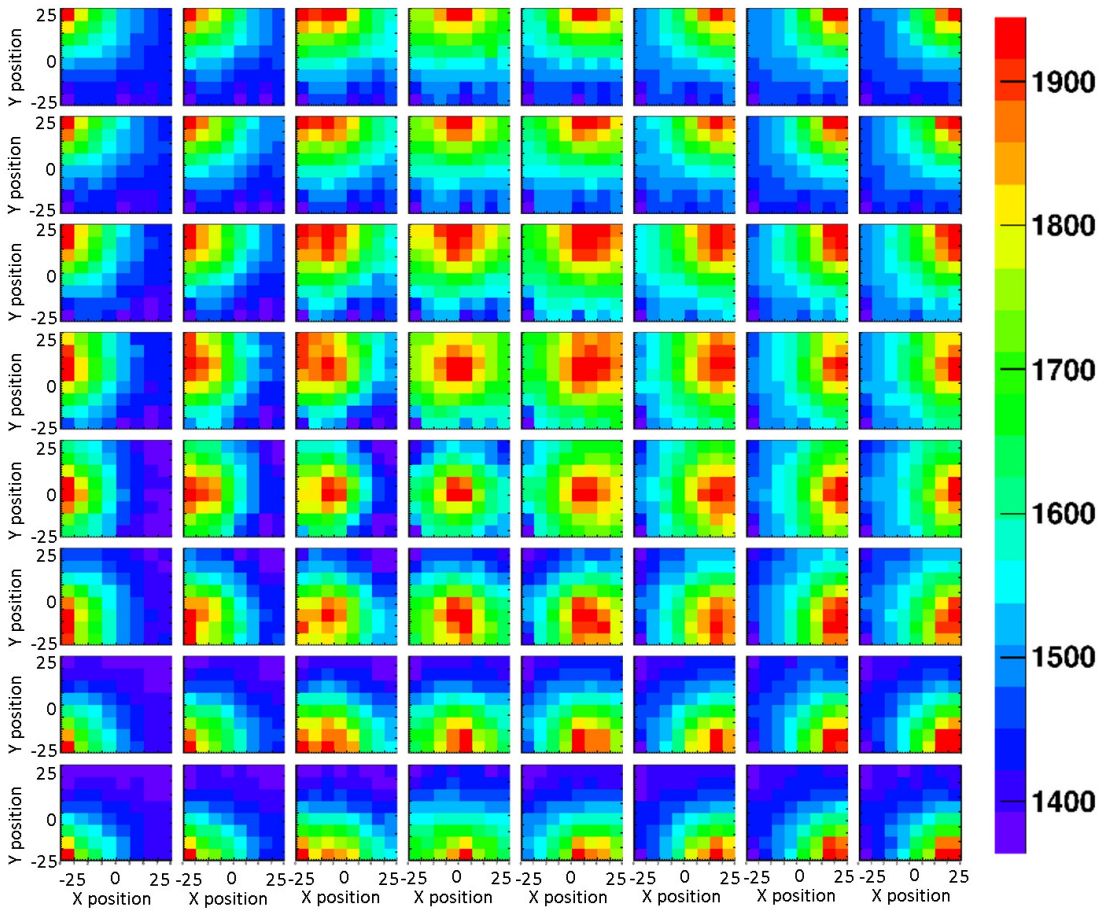

Figure 4.4.4: A grid scan of 8×8 irradiation positions of the reflectively coated $LaBr_3$:Ce detector, using a 1 mm collimated ^{137}Cs source. The source irradiation position can be clearly tracked by the spatial localization of the intensity maximum of the detector 2D light distribution.

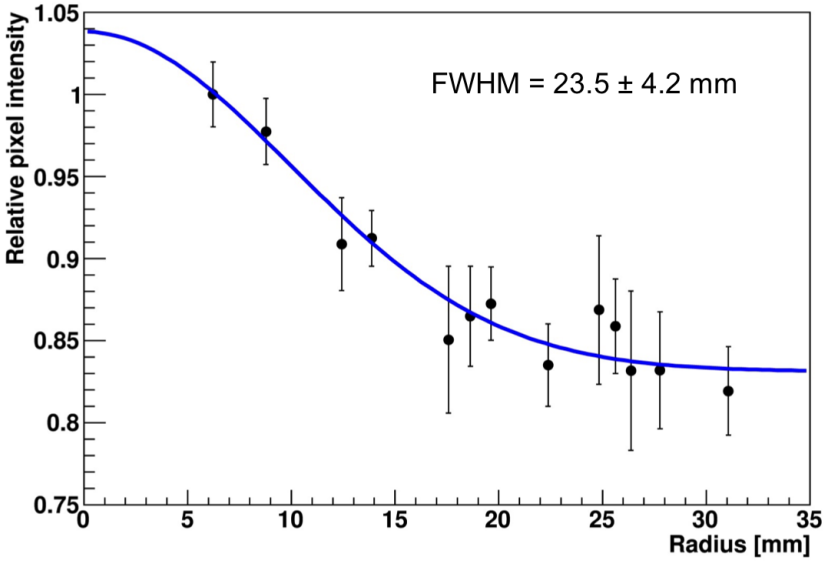

Figure 4.4.5: Radial projection of the 2D light amplitude distribution obtained from a central irradiation position of the absorptively wrapped $LaBr_3$:Ce detector, using a collimated ^{137}Cs source. In this study, each 4 neighboring segments of the 16×16 multi-anode PMT were combined. The blue curve represents a Gaussian fit to the data, the resulting width (FWHM) is indicated.

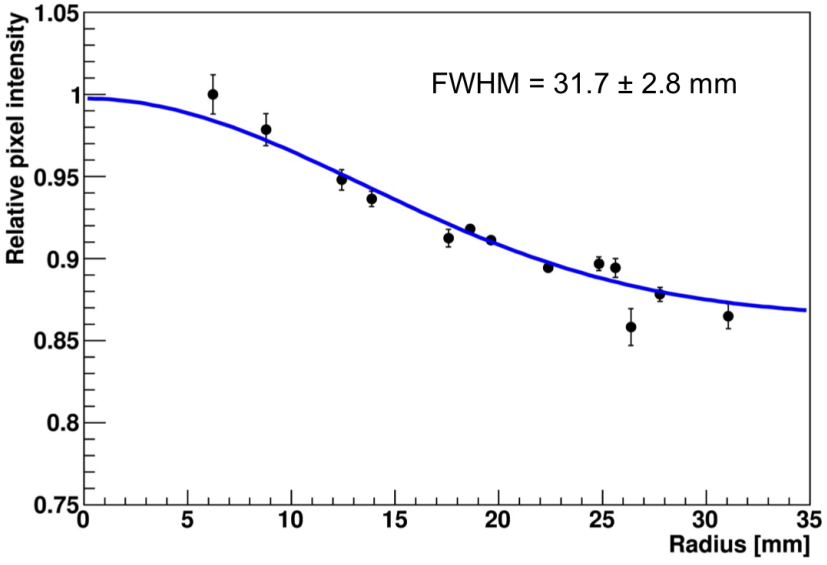

Figure 4.4.6: Radial projection of the 2D light amplitude distribution derived from a central irradiation position of the reflectively wrapped $LaBr_3$:Ce detector, using a collimated ^{137}Cs source. The blue curve represents a Gaussian fit to the data, the resulting width (FWHM) is indicated.

4.4.2 LSF as a function of the impinging γ-ray energy: ^{137}Cs and ^{60}Co sources

After upgrading the readout electronics of the $LaBr_3$:Ce detector, enabling to individually process all 256 segments of the H9500 multi-anode PMT (see Sect. 3.2.2.3 for more details), the detector was sequentially scanned by 1 mm collimated ^{137}Cs (662 keV) and ^{60}Co (1.33 MeV) sources with a fine step size of 3 mm, in order to visualize the spread of the produced scintillation light across the PMT segments for two different incident photon energies. Figure 4.4.7 and 4.4.9 show the 2D light amplitude distributions of 16 $\times$ 16 irradiation positions for ^{137}Cs and ^{60}Co γ-ray calibration sources, respectively. It can be noted that the intensity maximum that indicates the source position is larger for the ^{60}Co source, in particular obvious at the corner and lateral irradiation positions. In fact this is expected, since doubling the incident photon energy will also double the amount of scintillation light.

In order to evaluate the spatial response behaviour of the produced scintillation light inside the $LaBr_3$:Ce crystal as a function of the incident γ-ray energy, the LSF of a central irradiation position of both ^{137}Cs and ^{60}Co sources was derived, as displayed in Fig. 4.4.8 and 4.4.10, respectively. The LSF value slightly improved with the higher incident γ-ray energy, as it was measured to be 21.4 $\pm$ 0.9 mm (FWHM) for 1.33 MeV, compared to an LSF of 23.7 $\pm$ 0.7 mm (FWHM) found for the 662 keV γ ray emitted from ^{137}Cs. In both cases, the 1 mm collimated source was placed in a central position of the $LaBr_3$:Ce detector. The slightly improved LSF at 1.33 MeV originates from the increased light yield at the higher photon energy compared to the case of ^{137}Cs. This leads to a statistical improvement in the light intensity of the 2D light amplitude distribution, which will be transformed to its respective 1D radial projection, which corresponds to the LSF.

In the case of the ^{137}Cs source measurement and compared to Fig. 4.4.6, enhancing the PMT granularity by a factor of 4 seems to improve the LSF by about 30%. This improvement may be due to a reduction of the effects of light scattering, caused by the reflective crystal surface coating, by spreading the produced scintillation light to a larger number of PMT segments. As the LSF is derived from an accumulation of events forming the 2D light amplitude distribution, the scattering effect of the scintillation light is dominant for this method and directly transformed to the 1D radial projection. Besides this effect, a lower number of PMT segments leads to a lower number of sampling points in the 1D radial projection, which also statistically affects the LSF value.

In order to compare the LSF value with two different PMT granularities, similar to the measurement with the ^{137}Cs source also for a ^{60}Co source, each neighboring 4 pixels of the 2D light amplitude, measured with 256 PMT segments, were summed during the offline analysis. The radial projection of a central irradiation position of the summed 2D light amplitude is shown in Fig. 4.4.12. The width of the LSF for the case of 64 fold PMT granularity is found to be 23.7 $\pm$ 3.3 mm (FWHM), which is within experimental uncertainties similar to the value found for the higher 256-fold granularity. Compared to Fig. 4.4.4, where the reflectively coated $LaBr_3$:Ce scintillator was scanned by a 1 mm collimated ^{137}Cs source, Fig. 4.4.11 displays a visualization of the 2D light amplitude distribution obtained from 8 $\times$ 8 irradiation positions of the scintillation detector using a 1 mm collimated ^{60}Co source (gated on its 1.33 MeV transition). This measurement was performed with the full 256-fold granularity of the PMT segments, where during the offline analysis four neighboring pixel signals were combined in order to achieve a 64-fold PMT granularity. As mentioned earlier, doubling the incident photon energy leads to a corresponding increase of the amount of the produced scintillation light. This feature can also be weakly observed with a reduced PMT granularity of 64 segments when comparing Fig. 4.4.11 and Fig. 4.4.4, measured by ^{60}Co (1.33 MeV) and ^{137}Cs (662 keV) sources, respectively.

This effect is more clearly visible in the case of the 256-fold PMT granularity, as indicated in Fig. 4.4.9 and Fig. 4.4.7 for the same sources, respectively.

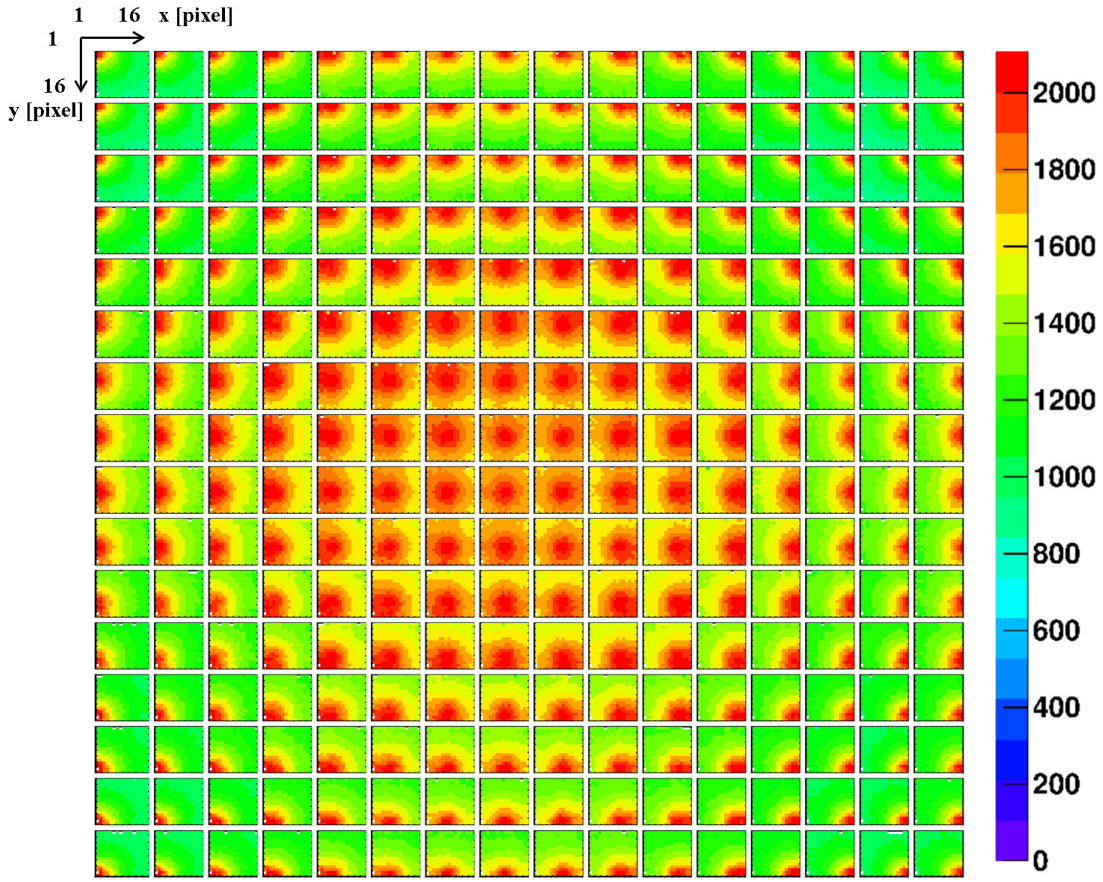

Figure 4.4.7: A grid scan of 16×16 irradiation positions of the reflectively coated monolithic $LaBr_3$:Ce detector is shown, using a 1 mm collimated ^{137}Cs source and a grid step size of 3 mm in x and y direction. All 256 segments of the multi-anode PMT are individually read out. The resulting 2D light amplitude distribution of each irradiation position clearly indicates the correlation with the 256 different source positions, moving consecutively from the top left to the bottom right position.

Throughout the spatial response evaluation study of the reflectively wrapped $LaBr_3$:Ce scintillator using the LSF method, the incident photon energy seems to have an impact on the spatial properties of the detector for both PMT-fold granularities (64 and 256 segments). This will be taken as incentive to follow this direction by using specific reconstruction algorithms in order to quantitatively investigate the detector's spatial resolution as a function of the incident photon energy and the granularity of the photosensor. This will be investigated in the following chapter.

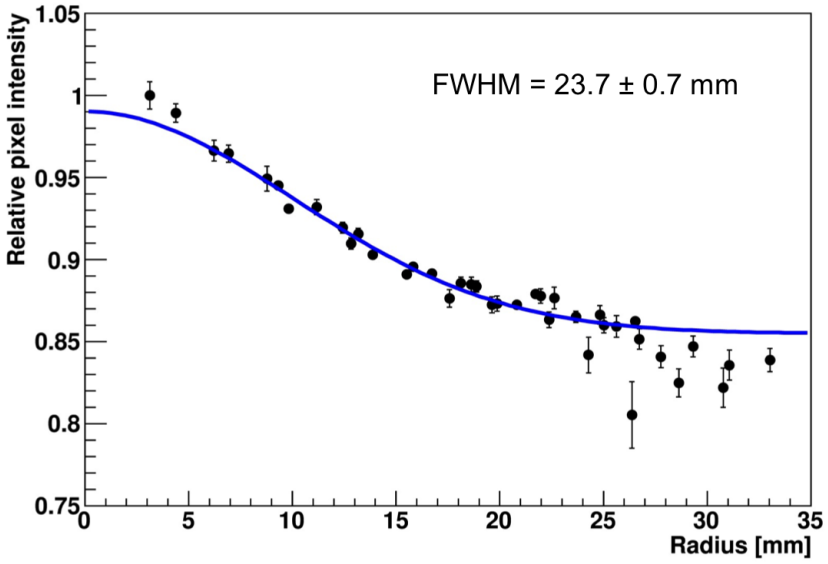

Figure 4.4.8: Radial projection of the 2D light amplitude distribution derived from a central irradiation position of the reflectively wrapped $LaBr_3$:Ce detector, coupled to a 16×16 multi-anode PMT and using a 1 mm collimated ^{137}Cs (662 keV) source. The blue curve represents a Gaussian offset fit to the data, the resulting width (FWHM) is indicated.

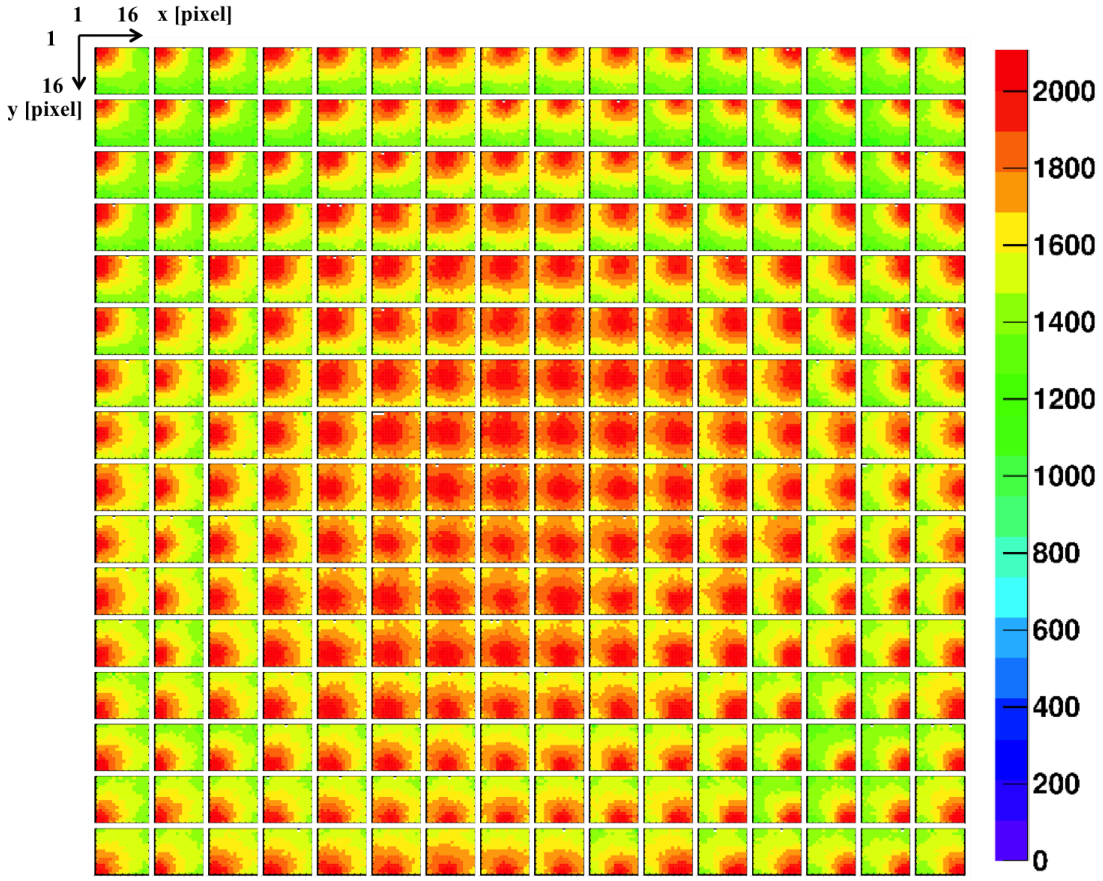

Figure 4.4.9: A grid scan of 16×16 irradiation positions of the reflectively coated monolithic $LaBr_3$:Ce detector, using a 1 mm collimated ^{60}Co source (gating on the 1.33 MeV transition) and a grid step size of 3 mm in x and y direction. The resulting 2D light amplitude distribution of each irradiation position clearly indicates the correlation with the 256 different source positions, moving from the top left to the bottom right corner.

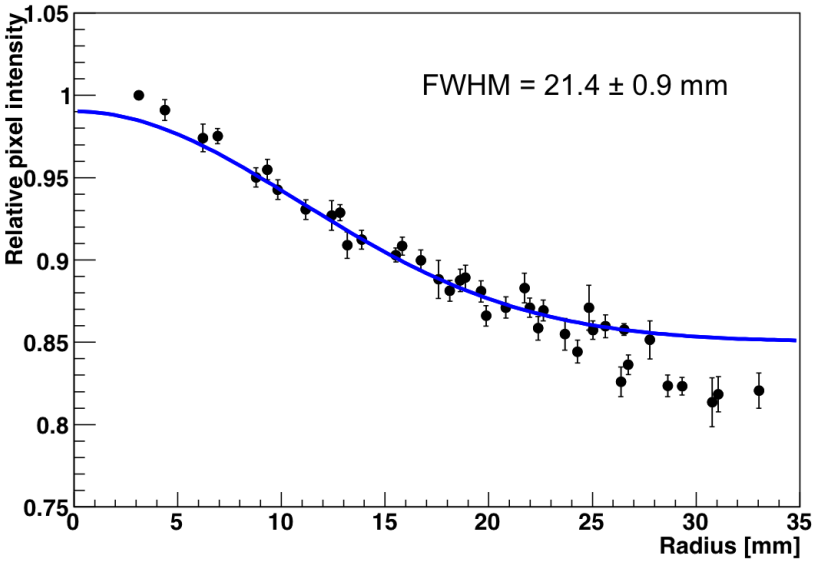

Figure 4.4.10: Radial projection of the 2D light amplitude distribution derived from a central irradiation position of the reflectively wrapped $LaBr_3$:Ce detector coupled to a 16×16 multi-anode PMT, using a 1 mm collimated ^{60}Co source (gated on the 1.33 MeV transition). The blue curve represents a Gaussian offset fit to the data, the resulting width (FWHM) is indicated.

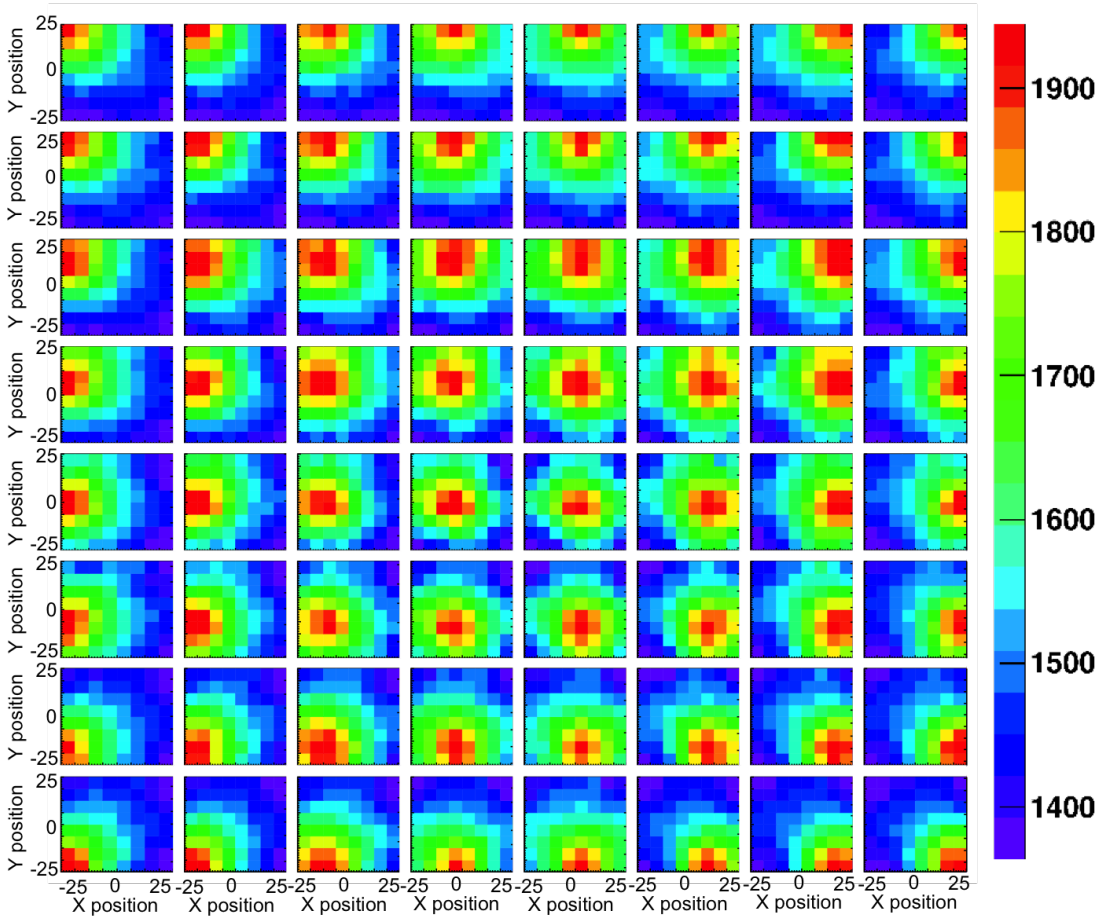

Figure 4.4.11: 2D light amplitude distribution obtained from 8 $\times$ 8 irradiation positions using a ^{60}Co source (gated on its 1.33 MeV transition). The distributions were analyzed for a 64-fold PMT granularity by combining each four neighboring PMT segment signals during the offline analysis.

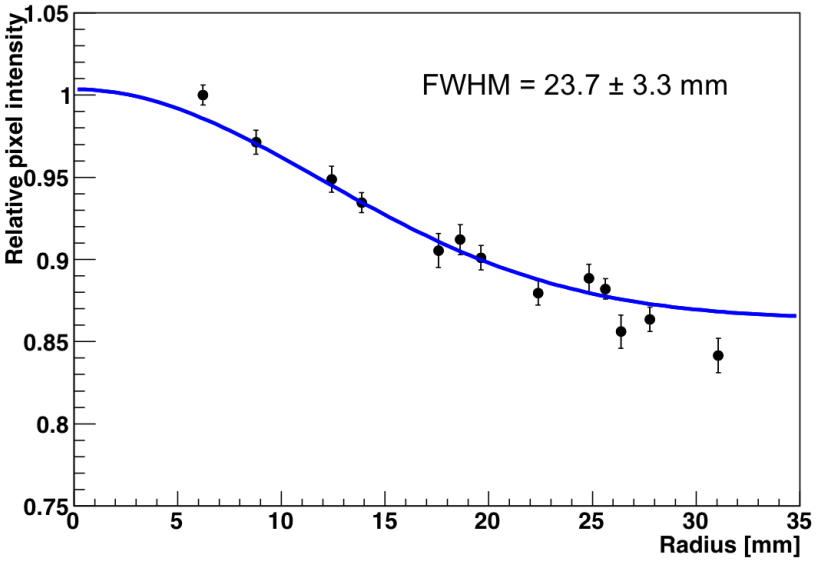

Figure 4.4.12: Radial projection of the 2D light amplitude distribution derived from a central irradiation position of the reflectively wrapped $LaBr_3$:Ce detector, coupled to a 16×16 multi-anode PMT, using a 1 mm collimated ^{60}Co source (gated on the 1.33 MeV transition). Each neighboring four PMT segments have been combined in the offline data analysis to achieve an LSF value from a 64-fold PMT granularity when using the ^{60}Co source. The blue curve represents a Gaussian fit to the data, the resulting width (FWHM) is indicated.

Chapter 5

Determination of the photon interaction position in the monolithic ($LaBr_3$:Ce) scintillator

The spatial resolution of the Compton camera absorbing detector is an essential factor that influences the overall camera imaging quality. Therefore, this chapter extensively focuses on studying the spatial resolution properties of a 50 $\times$ 50 $\times$ 30 mm^3 monolithic $LaBr_3$ scintillator using two algorithms, namely the k-Nearest-Neighbor (k-NN) method and its improved version Categorical Average Patterns (CAP). The first part of this chapter deals with describing the method of each algorithm. Then, the experimental setup and procedure, used to acquire the required data, will be shown. This includes the description of some analysis steps, applied to the raw data in order to extract the relevant information for all algorithms. Finally, the resulting data will be presented and discussed.

5.1 Description of the photon interaction position construction algorithms

The k-Nearest-Neighbor (k-NN) method and its improved version Categorical Average Patterns (CAP) algorithms are used to evaluate the spatial resolution properties of a 50 $\times$ 50 $\times$ 30 mm^3 monolithic $LaBr_3$ scintillator. They allow not only to determine the primary photon interaction position, but also to derive the overall spatial resolution of the monolithic scintillator. The details of each algorithms' workflow will be given in the following subsections.

5.1.1 The k-Nearest Neighbor (kNN) algorithm

The k-Nearest-Neighbor algorithm was developed at TU Delft [109] to be applied in the framework of positron emission tomography (PET) for determining the photon interaction position in a monolithic scintillator crystal. This algorithm requires a calibration measurement, in which the crystal front face is scanned by a tightly collimated photon source with a fine step-size in x and y directions. At each irradiation position, the 2D light amplitude distribution, resulting from each impinging photon, is recorded by the N PMT pixels as a vector $\mathbf{I} = (I_1, I_2, ..., I_N)$, where I_i is the scintillation light intensity of the i-th pixel. The total number of the reference library entries is the number of irradiation positions n_{pos} multiplied by the number n_{epp} of recorded photopeak events at each position.

$$n_{tot} = n_{pos} \cdot n_{epp} \tag{5.1.1}$$

For a given unknown photon interaction position, the resulting 2D light amplitude distribution $I_{unk,\,i}$ of this event is compared pixel by pixel to each of the reference library entries $I_{ref(l,i)}$ and the Euclidean distance is calculated as

$$D_l^{kNN} = \sqrt{\sum_{i=1}^{N}(I_{unk,i} - I_{ref(l,i)})^2}, \qquad l = 1, ..., (n_{pos} \cdot n_{epp}), \tag{5.1.2}$$

Then, a subset of the reference library is selected, containing a selectable number of k best matching entries, based on the k library events with smallest distance D_l^{kNN}. The (x,y) coordinates of these nearest neighbors are filled into a 2D histogram. After smoothing this histogram by a 5 $\times$ 5 average filter, the maximum of the smoothed distribution represents the calculated interaction position of the unknown incident event.
In order to characterize the accuracy of this algorithm, the "leave-one-out method" is applied, where 2D light amplitude distribution of a single event from the reference library is loaded as an unknown event. Then the calculated interaction position will be extracted by applying the k-NN algorithm and compared to the known actual irradiation position. In order to quantify the achievable spatial resolution with the standard k-NN algorithm, the leave-one-out method is repeated for all entries of this reference library and the coordinate differences (Δx, Δy) = (x_{calc} - x_{true}, y_{calc} - y_{true}) between the calculated position and the true irradiation position are filled in a 2D error histogram. The average FWHM of the1D histograms projected in x and y directions represents the spatial resolution of the monolithic scintillator crystal using the k-NN algorithm. The workflow of this algorithm, as well as the use of the leave-one-out method, is schematically shown in Fig. 5.1.1.

5.1.2 The Categorical Average Pattern (CAP) algorithm

This algorithm represents an improved version of the standard k-NN algorithm. The use of the reference library is slightly different when analyzing the unknown photo event. Instead of directly calculating the Euclidean distance D_l^{CAP} from every 2D light amplitude distribution of the library, a subset of the k_{CAP} closest matching is selected, representing the nearest neighbors for each irradiation position and an average light distribution is calculated for each of the n_{epp} subsets. Now, the 2D light intensity distribution of the unknown event $I_{unk,\,i}$ is compared to the averaged light distribution $I_{ave(l,\,i)}$ and the intensity difference is calculated as

$$D_l^{CAP} = \sqrt{\sum_{i=1}^{N}(I_{unk,\,i} - I_{ave(l,\,i)})^2}, \qquad l = 1, ..., n_{pos}, \tag{5.1.3}$$

This intensity difference is then filled in a 2D histogram spanned by their (x,y) coordinates. Then, a 5 $\times$ 5 moving average filter is applied to smooth the distribution and the minimum region is identified with the coordinate of the calculated interaction position of the unknown event.
The "leave-one-out method" as described before is subsequently applied to each entry of the reference library in order to characterize the detector's spatial resolution. The spatial difference (Δx, Δy) between the calculated position derived via the CAP algorithm and the true irradiation position is then filled to an error histogram. Finally, the average FWHM of the x and y projection of this distribution represents the spatial resolution of the monolithic scintillator crystal using the CAP algorithm.

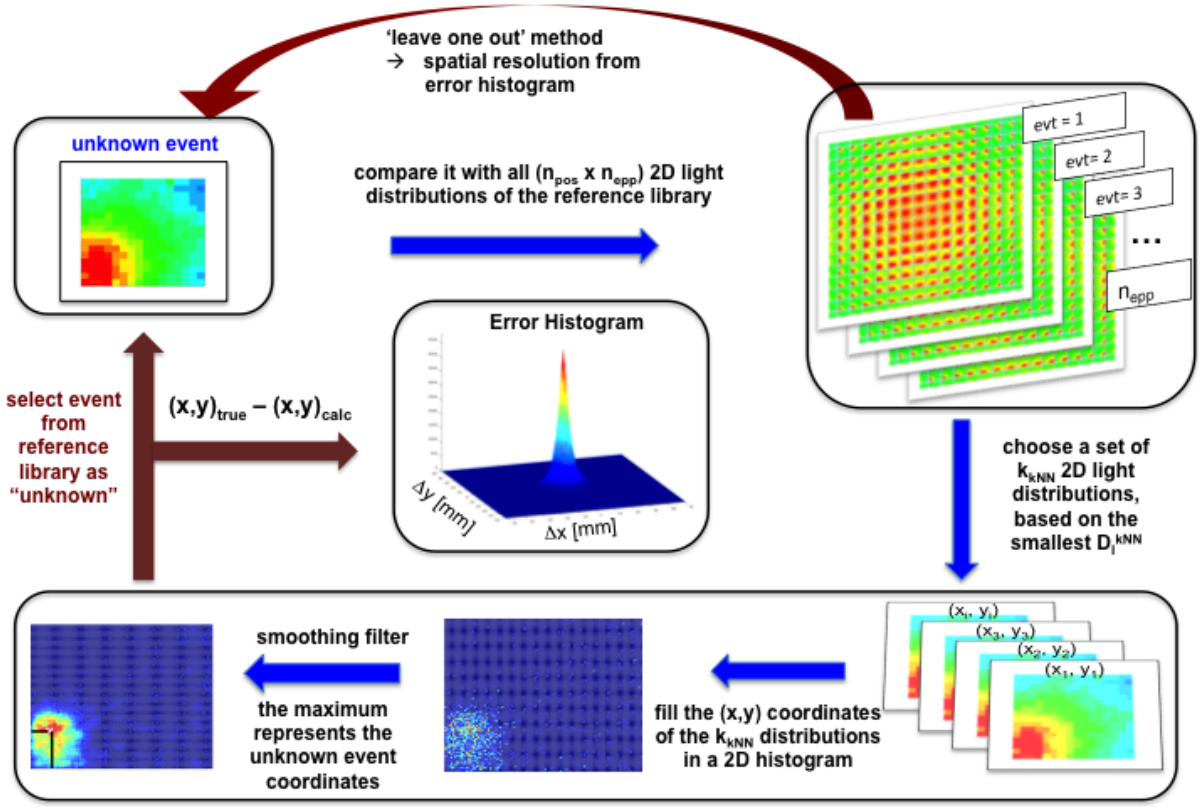

Figure 5.1.1: Illustration of the standard k-Nearest-Neighbor (k-NN) algorithm workflow used to determine the γ interaction position in a monolithic scintillator. For the detector's spatial resolution, the "leave-one-out method" is used, where the "unknown" event is repeatedly taken as input for the reconstruction algorithm from the reference library. The difference between the calculated and the true interaction position is filled in the so-called error histogram. The average FWHM of the x and y projections of this distribution represents the spatial resolution achieved with the k-NN algorithm.

5.2 Experimental setup and procedure

In this section, the experimental setup and procedure used to evaluate the spatial resolution properties of the $LaBr_3$:Ce scintillator will be introduced. Since the measurements were performed with two different γ sources, ^{137}Cs and ^{60}Co, both requiring, due to their different photon energy ranging from 662 keV (^{137}Cs) to 1.33 MeV (^{60}Co), different arrangements of the collimator and positioning system, both scenarios will be discussed independently. Then, the method of determining the crystal dimensions inside the aluminium housing by means of scanning across the detector edge in x and y directions will be presented.

5.2.1 Setup for the detector scan with a collimated ^{137}Cs source

The basis of generating the reference library of 2D light amplitude distributions is the collimated γ-ray source. When using the ^{60}Co source, the collimator and positioning setup had to be modified when changing the calibration source, since the starting configuration, used for

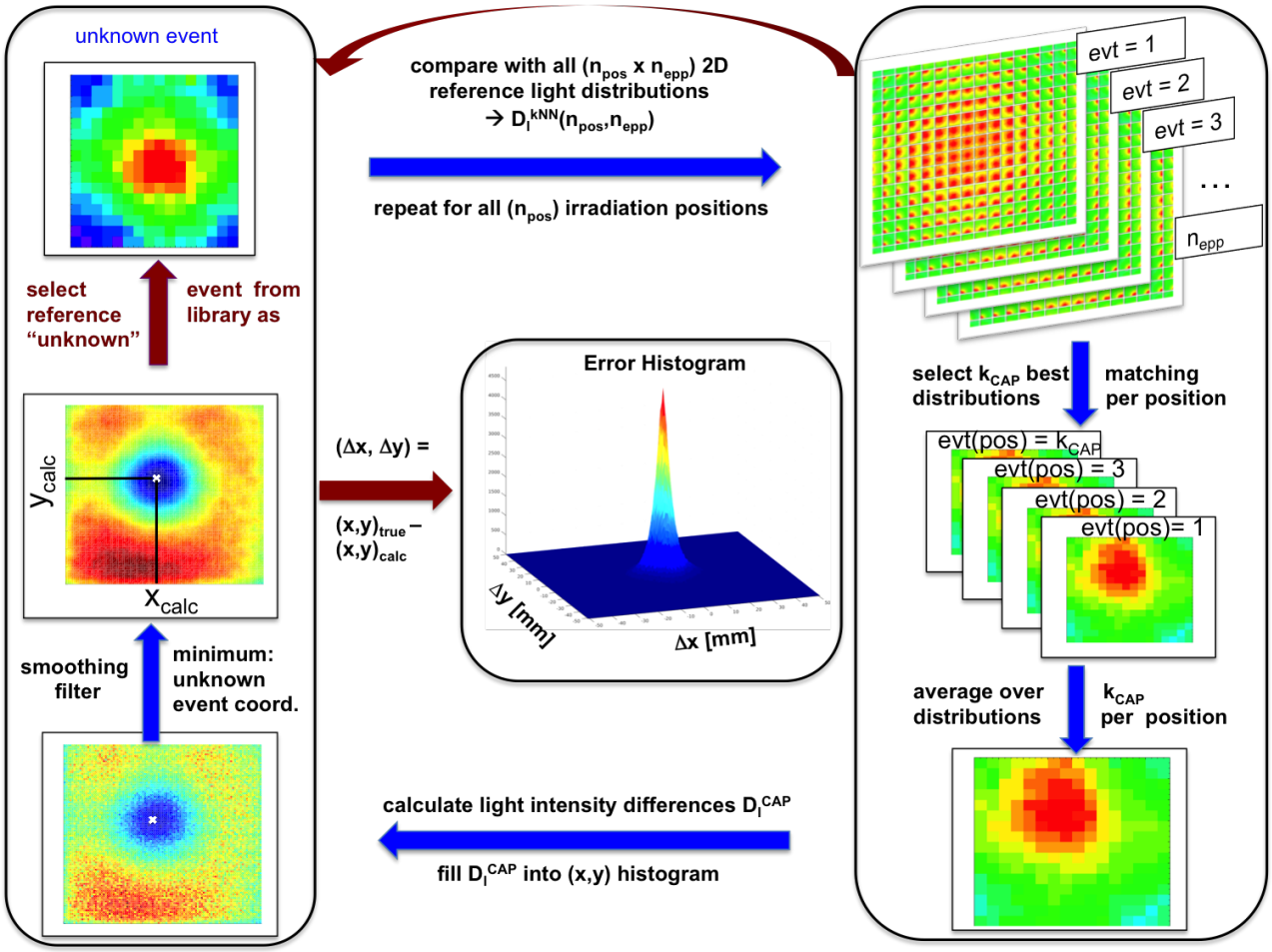

Figure 5.1.2: Workflow chart of the CAP algorithm for extracting the interaction position of an unknown impinging γ ray (see text for details). The "leave-one-out method", where in the case of the CAP algorithm the unknown event is sequentially selected from the reference library subset of each irradiation position, can be used to fill the error histogram by the difference between the calculated and the true photon interaction coordinates. The average FWHM of the x and y projections of this error distribution represents the spatial resolution of the detector when using the CAP algorithm.

generating the ^{137}Cs reference library, was not suitable for the subsequent case of ^{60}Co. The setup used for the ^{137}Cs source was initially borrowed from a collaborating group in the physics department of the TU Munich. Therefore, the existing design had to be used, which was based on a moving source in front of the stationary detector. In this setup arrangement, the collimator, made of DENSIMET (an alloy of tungsten, nickel and iron) [110], has a length of 48 mm and an opening diameter of 1 mm. The ^{137}Cs source (82 MBq) is encapsulated in an aluminum housing, which is inserted into a tantalum source holder of 30 mm length, as indicated in Fig. 5.2.1, such that the source disk is located on the axis of the 2 mm diameter collimator bore with a length of 20 mm inside the source holder. Thus, the γ source is located at a distance of 68 mm from the detector front surface. The tantalum source holder, together with the ^{137}Cs source, is attached to the back side of the DENSIMET collimator, and is adjusted in a way to ensure that the collimator axis of both the source holder and the surrounding collimator coincide in order to avoid any photon scattering affecting the measurement quality. In the arrangement of the ^{137}Cs source, the collimator source and additional Pb shielding block of the sides are placed

on a motorized and automatically controlled translation stage, that allows for sub-millimetre movements in x and y direction with micrometer precision.

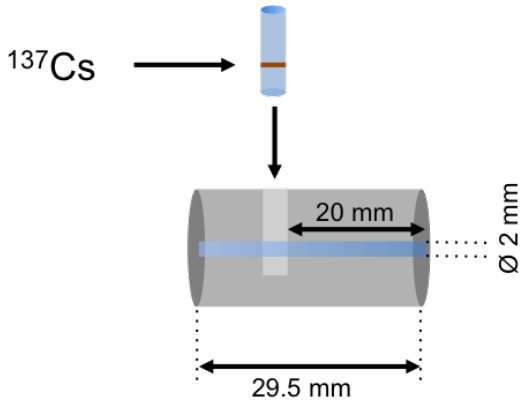

Figure 5.2.1: Illustration of the detailed design of the ^{137}Cs source, encapsulated in an aluminum housing, which is then installed into a tantalum holder. The aluminum housing is adjusted such that the source disc (indicated in the red) is positioned in the centre of the source holder collimation channel with a diameter of 2 mm.

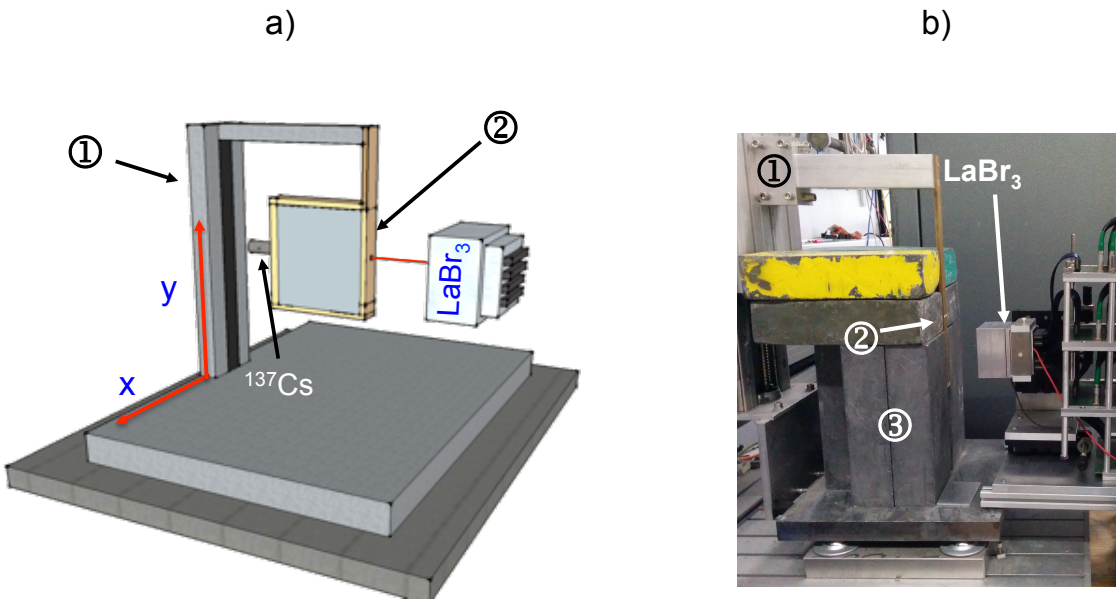

Figure 5.2.2: Sketch (panel a) and photograph (panel b) of the experimental setup used for the 2D detector scans with the collimated ^{137}Cs source. The $LaBr_3$:Ce scintillator is kept stationary and perpendicular to the collimator ②, which is attached to a motorized and automatic controlled x-y translational stage ①. The source arrangement is surrounded by lead blocks ③ in order to provide lateral shielding and suppress leakage of γ rays.

5.2.2 Setup for the collimated ^{60}Co source

Increasing the incident γ-ray energy by about a factor of two by using a ^{60}Co γ source (20 MBq) instead of a ^{137}Cs source will allow to study the energy dependence of the $LaBr_3$:Ce spa-

tial resolution as achieved from the reconstruction algorithm, which so far were mainly applied to the low-energy range of PET-like photon energies. However, this requires to reconsider the shielding and attenuation performance of the DENSIMET based collimator setup. Fig. 5.2.3 illustrates the attenuation of a 20 MBq ^{60}Co source (plotted for its largest photon energy of 1.3 MeV) passing through a 1 mm (black squares) or 0.6 mm (red circles) diameter collimator opening, respectively, as a function of the length of the collimator channel. The blue triangles denote the radiation leakage through the side of the shielding arrangement. For the 1 mm diameter, the signal to background ratio (corresponding to the ratio between the photon rate transmitted through the collimator channel to the radiation leakage through the side of the collimator and its surrounding shielding elements) equals 1 for a collimator length of 8 cm, which means that only for longer collimator lengths an identification of the γ-ray source photopeak above the background level of leaking source intensity will become possible. The same situation is reached for a 9 cm long collimator for the 0.6 mm case. At these intersection points between the blue and red data, the detector cannot distinguish between the collimated radiation and the one leaking through the side shielding. Thus, the working region of the collimation system lies beyond this intersection point. Since the γ radiation rate transmitted through the collimation channel is an essential parameter that critically affects the required measurement time per irradiation position, it is not realistic to choose a thickness of, e.g., 20 cm, where a signal to background ratio of ca. 4×10^{-6} could be achieved for the 1 mm collimator, given the boundary condition to restrict the measurement time per irradiation position to a range of a few tens of seconds for a few hundred of photopeak events, a Densimet collimator length of 10 cm was chosen as a reasonable compromise. As indicated in Fig. 5.2.3, the vertical lines point to the actual source position (12 cm) relative to the front surface of the detector, since the source is placed at a distance of 2 cm inside a tantalum source holder on the back side of the collimator block, as shown in Fig. 5.2.1

Once the length of the collimator for the 20 MBq ^{60}Co source was defined, it turned out to be a mechanical challenge to realize the required 1 mm hole over a length of 100 mm in a high-Z material. Mechanical drilling or spark erosion had to be excluded, due to the unavoidable uncertainties introduced by these methods. Also a stacked arrangement of individually drilled 4 mm thick slabs did not provide the required surface quality of the collimation channel.

Finally, the solution was found on the basis of a sintered tungsten carbide tube (90% WC, 10% Co, ρ = 14.4 g/ cm^3) [111]. The inner diameter of such tube can be as small as 0.6 mm, with an outer diameter of 4 mm. This tube can be inserted into a $\sim$ 4 mm diameter bore through a 100 $\times$ 100 $\times$ 100 mm^3 block of DENSIMET® [110], as indicated in Fig. 5.2.6 a). The dimensions of the collimator block, especially its width and height, were chosen to improve the quality of the collimated source measurement by covering the entire scanning range (50 $\times$ 50 mm^2) of the $LaBr_3$:Ce scintillator in both x and y direction, thus efficiently reducing side leakage of the γ radiation. This collimator design enables the flexible use of different collimation openings by simply exchanging the tungsten carbide tube. Figure 5.2.6 b) shows two exchangeable tubes of 1 mm and 0.6 mm inner diameter.

This collimation system not only replaces the previous 1mm collimator for the ^{137}Cs source, but also allows to explore an even smaller opening diameter of 0.6 mm, which was barely possible with the old setup, as illustrated by the green vertical line in Fig. 5.2.5. Of course, the radiation flux will be reduced quadratically, where doubling the collimator length. However, since the ^{137}Cs source activity is as high as 82 MBq, the expected photo count rates for the 1 mm and 0.6 mm collimators are $\sim$ 360 /s and $\sim$ 130 /s, respectively, still allowing for a reasonable measurement time per irradiation position with sufficient statistics.

Compared to the previous collimator setup of the ^{137}Cs source, illustrated in Fig. 5.2.2, the experimental setup of the new collimation system was modified in order to take into account the

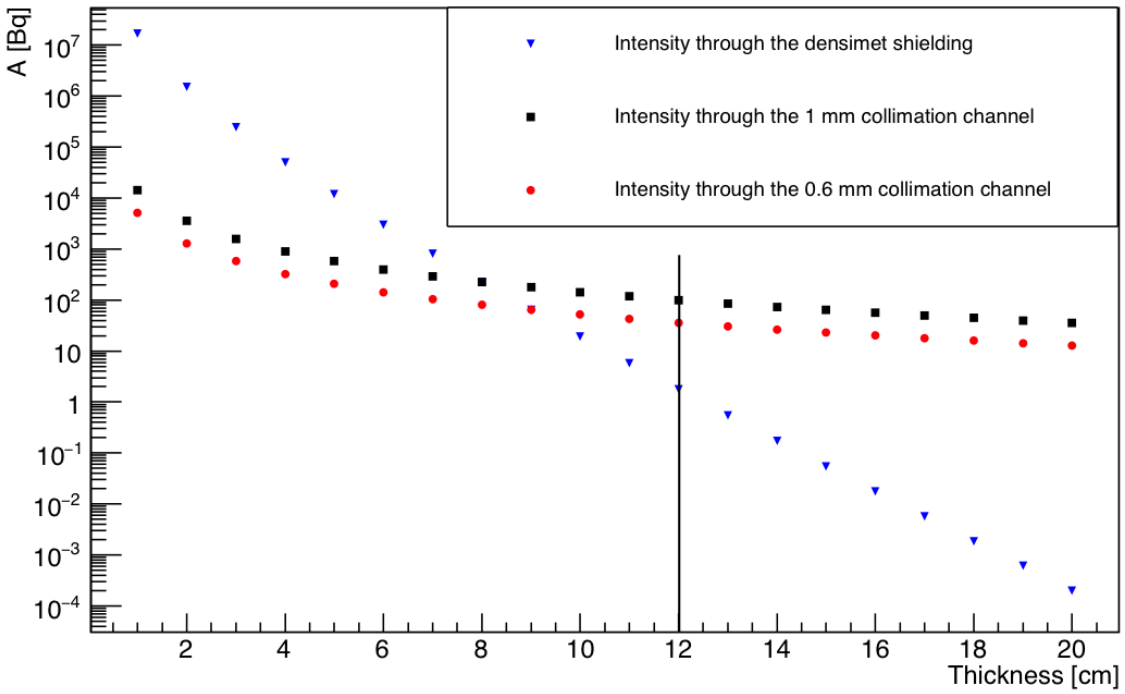

Figure 5.2.3: Attenuation performance of a DENSIMET-based collimator system, designed for a strong (20 MBq) ^{60}Co source. Displayed is the source related radiation intensity passing through the collimation channel (black and red data sets) and collimator medium (blue data sets), for two collimator opening diameters of 1 mm (square) and 0.6 mm (circle). The working region of this system starts after the intersection point between the red and blue curves, where the ratio between both intensities equals to one. The vertical line points to the finally chosen length of 10 cm of the collimator system, providing a signal to background ratio of $\sim 50:1$ for the 1 mm collimator, which keeps the transmitted photon flux high enough ($\sim$ 100 /s) to allow for reasonably short irradiation times in the 2D scan measurement. The length of 12 cm represents the thickness of the DENSIMET collimator block (100 mm) plus the 20 mm distance from the source position inside its holder to the collimator front surface, as indicated in Fig. 5.2.1.

extra weight introduced by the large DENSIMET block ($10 \times 10 \times 10\,\mathrm{cm}^3$) surrounded by side-shielding lead bricks. Figure 5.2.6 a) shows that the $LaBr_3$:Ce detector is now attached to the motorized translation stage, while the collimation system is kept stationary and perpendicular to the detector front surface. In order to allow for a flexible movement of the scintillator within the dynamic range of the translation stage in x and y directions, the PMT high-density coaxial ribbon cables (SEU-TEU-1, SAMTEC) were extended from 17 cm to 36 cm. These cables are distributed to 256 individual lemo cables via 4 adapter boards, which are mounted to the platform of the x-compound translation stage such that they will move together with the $LaBr_3$:Ce detector only in x-direction. A photograph showing the details of the real experimental setup is presented in Fig. 5.2.6 b).

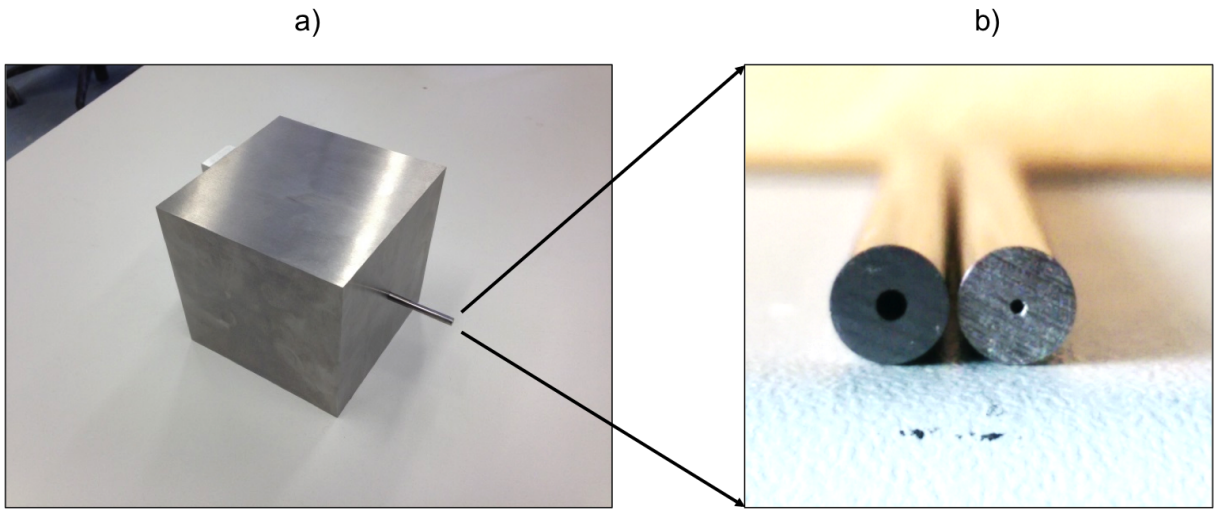

Figure 5.2.4: Photograph of the 100 × 100 × 100 mm^3 DENSIMET-based collimator block (a), containing a central bore of ∼ 4 mm diameter for an exchangeable collimator rod. WC rods with two opening diameters of 1 mm and 0.6 mm of the collimator channel are available in our laboratory, as shown in panel b).

5.2.3 Coordinate determination of the $LaBr_3$:Ce crystal: x and y edge scan

Before starting the collimated source measurements, the exact location of the $LaBr_3$:Ce crystal inside its aluminum encapsulation has to be determined. For this purpose, a so-called edge scan is performed by scanning the collimated γ source across the edge regions of the scintillation detector in x and y directions with a fine step size, e. g., 1 mm in order to visualize the crystal profile, indicated by the rise and fall of the detected count rate under the photopeak as a function of the irradiation position. The range of the scan was chosen larger than the known actual crystal size in order to be able to resolve the step function (falling and rising edge), where the collimated photon beam leaves and enters the crystal range. The rising (left) slope of both x and y photopeak count rate profiles are fitted by a Fermi function, given as

$$f(x) = \frac{A}{1 + e^{\frac{x - x_0}{B}}} + C \tag{5.2.1}$$

where A, B and C represent fit parameters,while x_0 denotes the origin of the x axis and x indicates the irradiation position in the x direction. Similarly, the falling (right) edges of both cases are also fitted using an inverse Fermi function

$$f(x) = \frac{A}{1 + e^{\frac{x_0 - x}{B}}} + C \tag{5.2.2}$$

The inflection points, resulting from both fit functions for a line scan along either the x or y axis, represent the starting and ending coordinates of the crystal. Consequently, the distance between these coordinates reflects the measured width of the crystal (which ideally reflects the crystal dimensions known from the manufacturer).
Figure 5.2.7 illustrates the x (panel a) and y (panel b) photopeak count rate profiles of the $LaBr_3$:Ce crystal, using a 1 mm ^{137}Cs collimated source as described in Sect. 5.2.1, with a step size and measurement time of 1 mm and 40 sec, respectively. The red curves in both scans

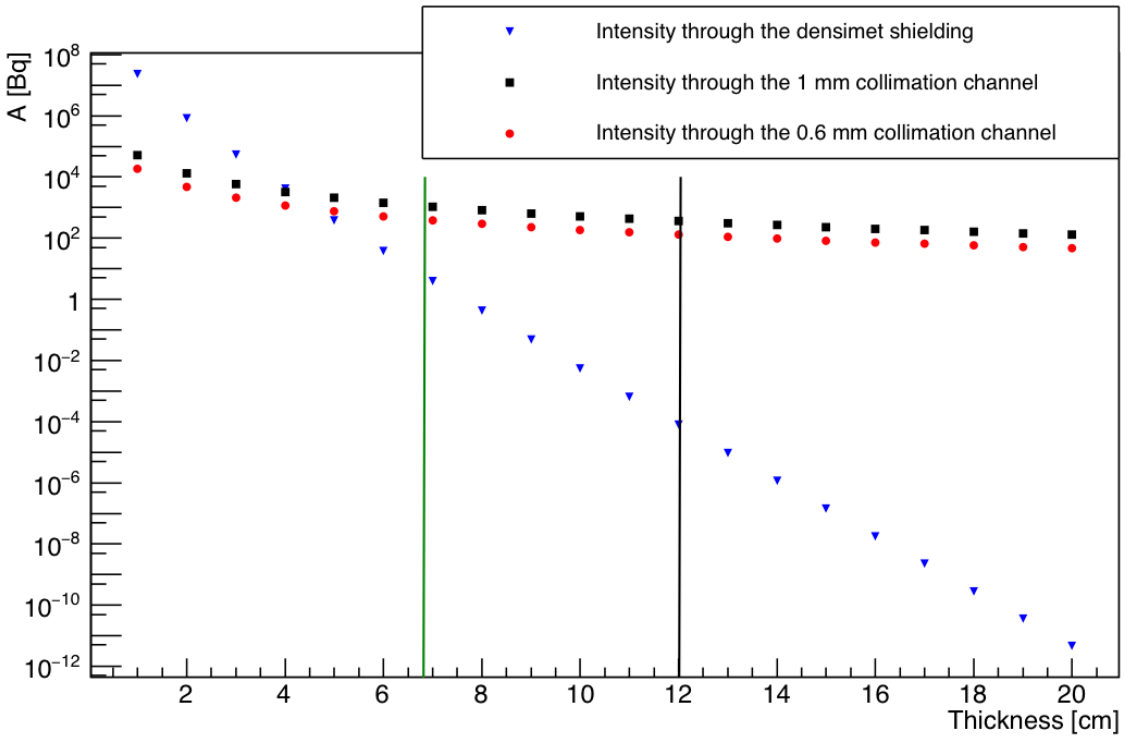

Figure 5.2.5: Attenuation behaviour of the 82 MBq ^{137}Cs source while being installed in the new collimation system. Compared to the ^{60}Co source and with both collimator openings, it provides a large working region, starting from a collimator length of $\sim$ 5 cm (as the intersection point with signal-to-background ratio $\sim$ 1), due to the large value of the linear attenuation coefficient of Densimet (μ_L = 1.95 cm^{-1}) at the photon energy of 662 keV. The green vertical line represents the length of the previous Densimet collimator block, whereas the black line denotes the length of the newly constructed collimator.

represent the fit curve of the count rate profiles using the Fermi functions as defined before. The measured crystal length, using the inflection point of each edge fit, was found to be 48.9 (2) mm and 48.2 (4) mm for the x and y scan profiles, respectively, and thus only slightly deviating from the 'true' dimensions of the crystal front face as stated by the manufacturer (50 $\times$ 50 mm^2). The reason of this deviation may be traced back to the degradation of the slope of the rising and falling edge of the scan profile, which affects the fit quality in the flat-top region of the scan and, consequently, the value of the derived inflection point. Since the scan profile is based on the photopeak count rate as a function of the irradiation position, obviously the photopeak count rates registered at the edge positions are lower than the ones measured in a central position. This may originate from crystal edge (scattering) effects, which influence the collection path of the scintillation light towards the PMT photosensor. Moreover, a fraction of the scintillation photons may escape from the crystal, since the reflectivity of the crystal surface wrapping material is not 100%. In total, these effects will create a tail on the low energy part of the photopeak in the energy spectrum, due to the resulting non-proportionality between the absorbed γ-ray energy and the corresponding scintillation light that reaches the PMT. This contributes to degrade the edge scan quality, as a fixed energy gate (FWTM) is applied to the photopeak at each irradiation position, leading to a loss of part of the photopeak counts near the edges of the crystal. From Fig. 5.2.7 it can be noticed that the y line scan

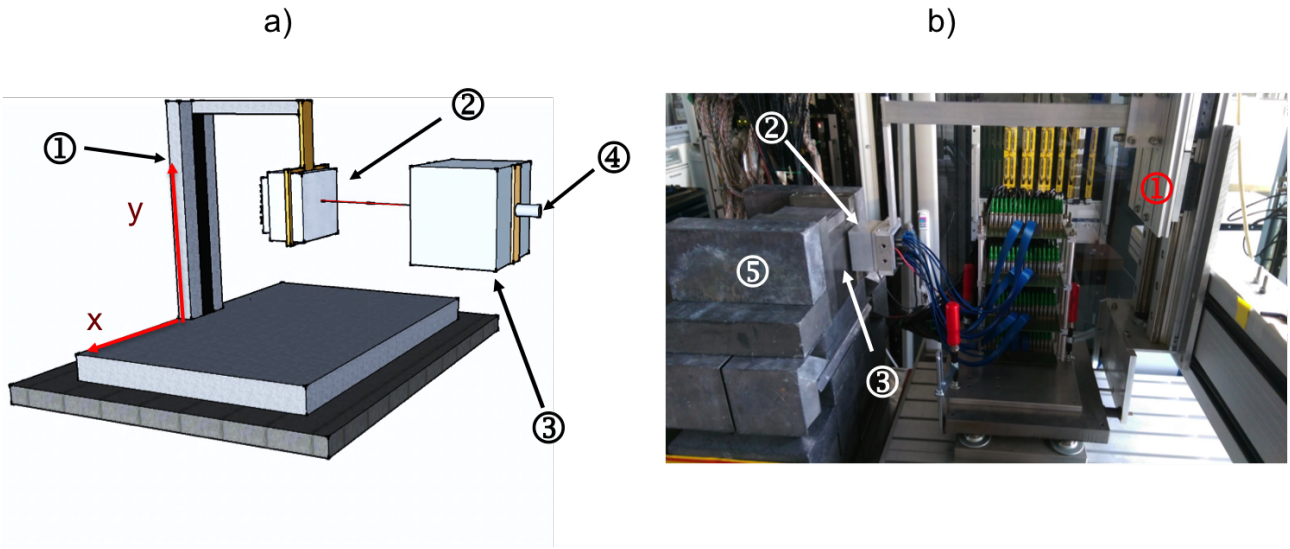

Figure 5.2.6: Drawing (a) and photograph (b) of the modified setup for the 2D detector scan using a collimated ^{60}Co source (20 MBq). Compared to the previous ^{137}Cs source collimator setup, the $LaBr_3$:Ce scintillator ② which was previously left stationary in front of the moving collimated source, is now attached to a motorized translation stage ①, while the collimator ③ together with its surrounding lead block shielding ⑤ are kept stationary. The ^{60}Co source ③ is inserted inside its Ta holder, as indicated in Fig. 5.2.1, and then attached to the back side of the collimator block.

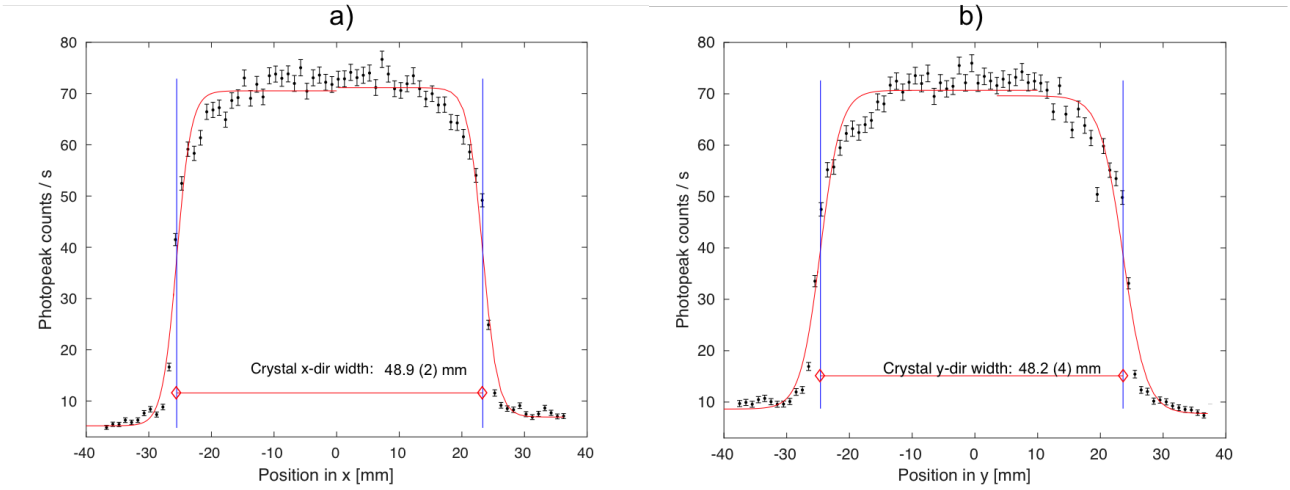

Figure 5.2.7: x (panel a) and y (panel b) line-scan profiles of the $LaBr_3$ scintillator crystal, representing the photopeak count rates as a function of the irradiation position. In this measurement, a 1 mm collimated ^{137}Cs source, attached to the first generation of the collimator setup (see Sect. 5.2.1), a 1 mm step size and 40 seconds of irradiation time per position were used. The red curves and blue vertical lines represent the fit to the profile curve, using the Fermi functions of Eq. (5.2.1) and (5.2.2), and its inflection points, respectively.

(panel b) has an inferior signal to background ratio (S/B) ($\sim$ 9) compared to the one in the x line scan ($\sim$ 14). This originates from an unavoidable design issue in the ^{137}Cs source setup (Sect. 5.2.1), particularly affecting the y edge scans. In this first version of the scan setup the

collimator, together with the source attached to it, was mounted to the translation stage (see Fig. 5.2.2). Translations in y direction occurred in a vertical gap inbetween the lead brick side shielding, leaving unwanted gaps on the top or bottom of the collimator block during its move, thus allowing for scattered radiation from the source behind the collimator block to reach the detector and contribute to the background. This effect is maximal when the collimated source is in the starting or ending position. This explains the enhancement of the background in the y-scan profile. This effect is not dominant in the x-scan profile, because in this case the collimated source moves horizontally across the center of the crystal, therefore the unwanted gaps on top and bottom of the collimator block are small and far from the detector.

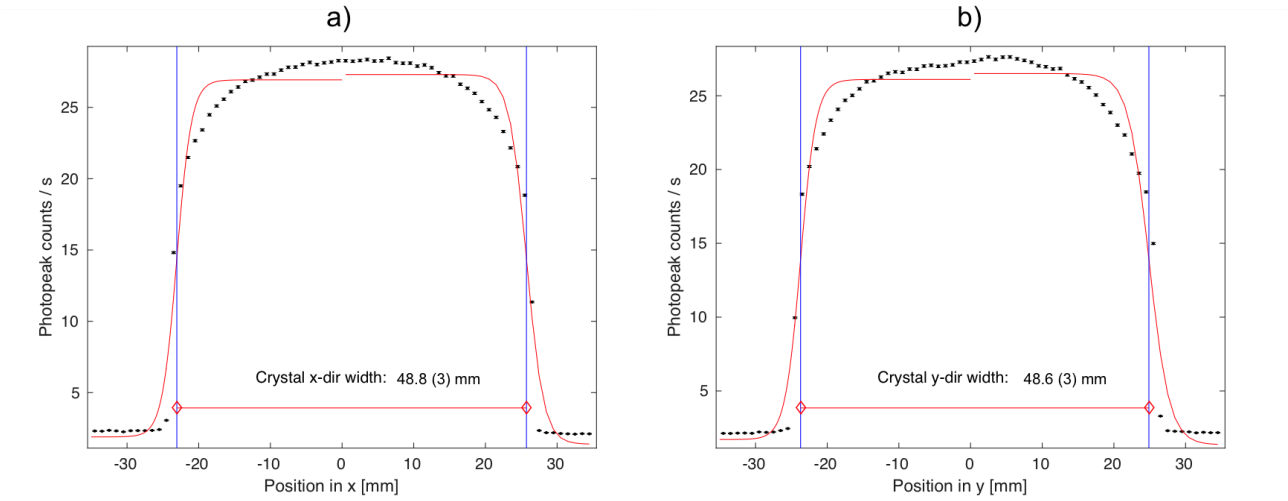

Figure 5.2.8: Photopeak count rate profiles achieved from a line scan along an x (panel a) and y (panel b) central line of the $LaBr_3$ scintillator crystal, using a 1 mm collimated ^{137}Cs source, attached to the second generation of the collimator setup (see Sect. 5.2.2). The measurement step size and irradiation time per irradiation position were 1 mm and 1 h, respectively. The calculated crystal dimension is the distance between the inflection points of the fit curves to the rising and falling slopes, indicated by the vertical blue lines.

When it was possible to use the ^{137}Cs source with the newly designed collimator setup (see Sect. 5.2.2), the x and y edge scans were repeated with a step size of 1 mm and an irradiation time of 1 h per position, using the 1 mm diameter collimator tube as indicated in Fig. 5.2.8. The measured crystal dimensions was found comparable to the ones obtained with the previous setup (described in Sect. 5.2.1). It can also be noted that the S/B ratio (~ 14) stays the same as the one obtained with the previous collimator setup, although it could have been expected to be reduced by a factor of two due to the correspoding increase in the collimator length, that reduces the transmitted source intensity. This is due to an improvement in the suppression of background originating from radiation leakage through the collimator side shielding which contributes to maintain a large S/B ratio for the new collimator setup. The few remaining background counts in the photopeak area, appearing at irradiation positions when the collimated source is still outside the crystal dimension, are related to the intrinsic radioactivity of the $LaBr_3$:Ce detector (~ 140 Bq).
Having now studied the $LaBr_3$:Ce scintillator crystal count rate profile using a ^{137}Cs source and two different collimator setups, the x and y edge scans were repeated for the scintillation detector using the ^{60}Co source that motivated the design of the new collimator setup (see Sect. 5.2.2), due to the requirement of a longer attenuation length than for the ^{137}Cs source. The

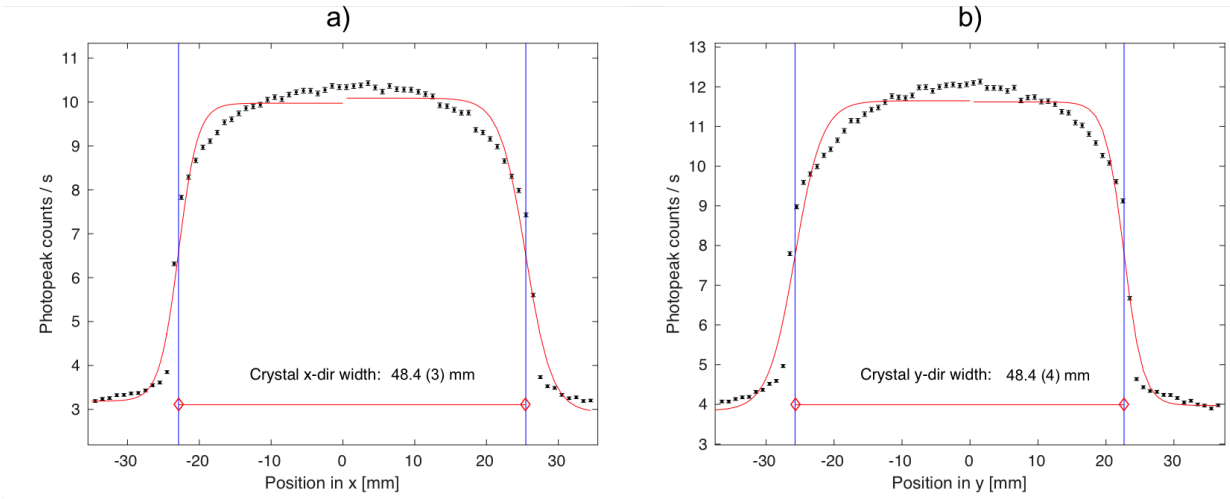

Figure 5.2.9: x (panel a) and y (panel b) edge scan count rate profiles of the $LaBr_3$ scintillator crystal, representing the photopeak count rates of 1.17 MeV γ rays emitted from a ^{60}Co source as a function of the irradiation position. The new collimator setup (see Sect. 5.2.1) with a 1 mm opening, 1 mm step size and 1 h irradiation time per irradiation position were used in this experiment. The measured crystal dimensions correspond to the ones obtained with the ^{137}Cs source, using the same setup, and shown in Fig. 5.2.8.

measurement parameters were identical to the ones applied to the ^{137}Cs source measurement with the new collimator setup. So, the collimator opening, step size and the irradiation time per position were 1 mm, 1 mm and 1 h, respectively. Figures 5.2.9 and 5.2.10 show the x and y count rate profiles for the ^{60}Co photon energies of 1.17 MeV and 1.33 MeV, respectively. Compared to the count rate profiles of the ^{137}Cs source shown in Fig. 5.2.8, the obvious reduction of the intensities can be attributed to the difference between the initial source activity, which is 20 MBq for the ^{60}Co source and 82 MBq for the ^{137}Cs source. Moreover, for the case of 1.17 MeV, the calculated x and y crystal lengths are, within the experimental uncertainties, similar to the ones obtained at 662 keV from the ^{136}Cs source. However, this is not the case for the x and y profiles of the 1.33 MeV count rate profiles, as shown in Fig. 5.2.10. This can be attributed to the reduction of the S/B ratio for the 1.33 MeV case, as well as to the rounded shape of the rising and falling slopes in the flat-top region, originating from edge effects (as explained above). The rounded shape becomes more pronounced for the higher γ ray energy, since in this case it is associated with a higher number of generated scintillation photons, which extends the edge effects along the line scan towards the center of the crystal. Thus, the amount of asymmetry in the shape of the photopeak, corresponding to the impinging γ ray, will gradually decrease until reaching its minimum in the center of the crystal. Since the scan profile is formed by the number of counts detected from a fixed energy gate condition to the photopeak energy as a function of the irradiation position, a gradual reduction of the number of photopeak counts will result due to the intensity loss in the tail region of the photopeak, which then leads to the rounded shape of the scan profile. Widening the energy gate condition will not entirely solve this effect, since it will lead to register background events at these irradiation positions, where the edge effects are not dominant. A possible solution, which may be considered in the future, is to apply a dynamically adjusted energy gate, depending on the photopeak line slope asymmetry. The rounded shape of the scan profile, together with the suppression of the S/B ratio, will affect the quality of the scan fit by pulling the fit towards the inner part of the profile. Consequently, the calculated inflection

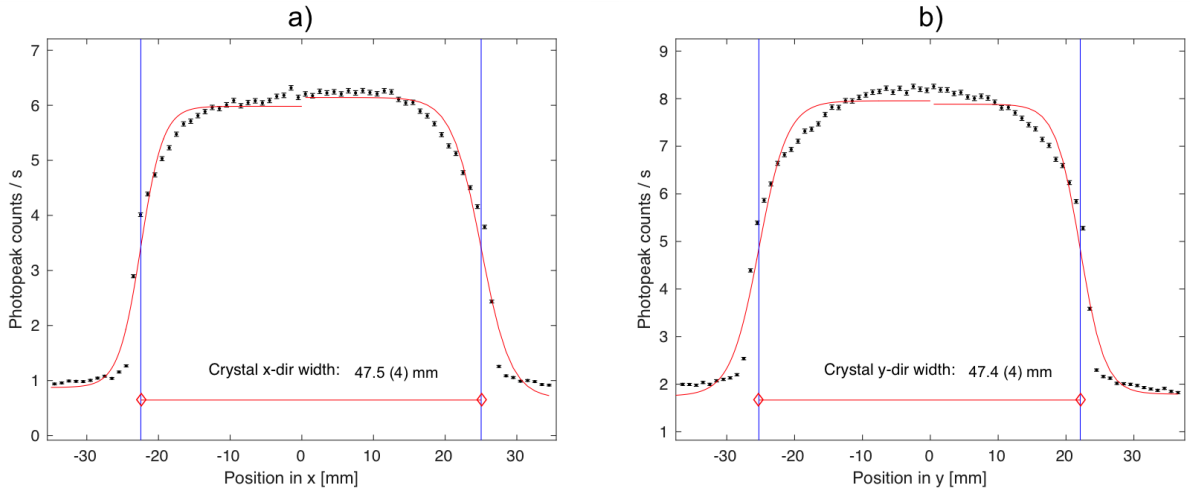

Figure 5.2.10: x (panel a) and y (panel b) count rates profiles of the $LaBr_3$ scintillator crystal, measured for 1.33 MeV γ ray from a ^{60}Co source, using collimator diameter of 1 mm, 1 mm step size and 1 h irradiation time per irradiation position. The fit quality is strongly influenced by the S/B ratio and rounded shape of the profile flat-top, originating from edge effects in the crystal (see text), leading to a deteriorate estimation of the inflection point and thus of the calculated crystal dimensions.

points of each edge slope, corresponding to either the start or end of the crystal, deviate from the ones obtained in the 1.17 MeV and 662 keV cases and deviate even farther from the true crystal dimension values. Another observation can be noticed in the background level of the edge scan profiles generated by the two γ lines of the ^{60}Co source, indicated in Fig. 5.2.9 and 5.2.10. The enhancement of this level for the 1.17 MeV case is attributed to the fact that this photopeak lies on top of the Compton continuum of the 1.33 MeV peak, as well as of the 1.439 MeV peak, originating from the intrinsic radioactivity of the $LaBr_3$:Ce (electron capture decay of ^{138}La into ^{138}Ba).
Since the measured crystal length (x and y), determined by the Fermi function inflection points, in all of the above cases slightly differ from the true crystal length, the measured dimensions in either x or y scans are symmetrically normalized in order to cover the full crystal dimension.

5.2.4 Generation of the light amplitude reference libraries

Having determined the edge coordinates of the $LaBr_3$:Ce scintillator crystal and taking into account the correction and analysis steps already mentioned in Sect. 4.4, the detector is ready to be scanned with a millimetric step size. The general procedure creating the 2D reference light amplitude distributions, required to apply the photon interaction position reconstruction algorithms, has already been mentioned in Chap. 4. Now, after having introduced the preparatory measurements and hardware provisions to allow creating high resolution detector scans for different photon energies, the specific experimental scenarios around different reference libraries will be introduced. A finer step size than used in Chap. 4, when extracting the Light Spread Function (LSF) is required for the kNN and CAP algorithms in order to build up the event-wise reference library of position dependent 2D light amplitude distributions, covering the entire detector front surface area. The scan step size was selected to be 0.5 mm, corresponding to the radius of the collimator opening. Since each photopeak event acquired at a given irradiation position becomes a member of the reference library, the total library size is the number of pho-

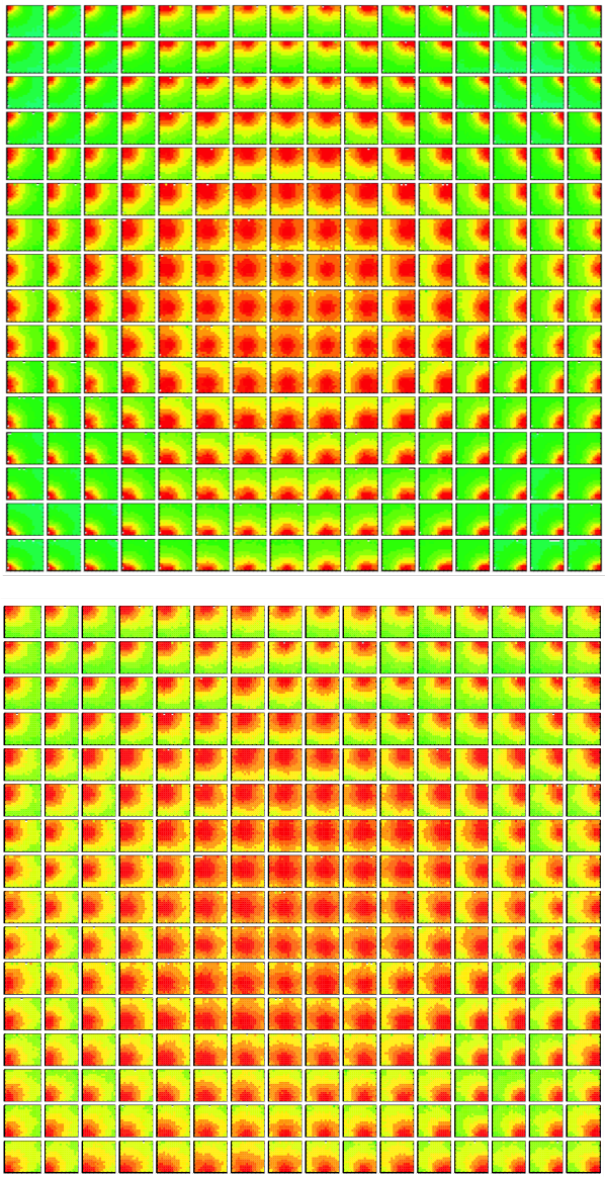

Figure 5.2.11: Exemplary illustration of sub-sets of the 2D light amplitude distribution reference libraries generated with a ^{137}Cs source (top) and a ^{60}Co source, the latter gated at the 1.33 MeV photopeak, (bottom). The scan grid size of both libraries was 3 mm, i. e. 16 $\times$ 16 irradiation positions are shown that cover the area of the $LaBr_3$:Ce scintillator's front face.

topeak events per position (n_{epp}) multiplied by the total number n_{pos} of irradiation positions, which in our case amounts to 102 $\times$ 102 for the scanned detector area of 51 $\times$ 51 mm^2. Figure 5.2.11 illustrates an example of sub-libraries generated with the ^{137}Cs (top) and ^{60}Co source (bottom, gated at 1.33 MeV), using the 1 mm collimator and 3 mm scan pitch size.

In order to efficiently and accurately acquire the requested reference library, the data acquisition system (DAQ) is synchronized together with the motor controller via a script linked to the MARABOU system, described in Sect. 3.2.2.3. In case of the ^{137}Cs source, the irradiation time had to be set ensuring enough statistics (photopeak events per irradiation position) in the corner and side positions, where the photopeak was expected to be weak. This is due not only to the high probability of the incident γ rays to scatter out of the crystal, but also to the fact that the produced scintillation light is subject to scattering resulting from the crystal surface coating.

Thus, 30 seconds, including additional time as a safety margin, per irradiation position was found as a good compromise time for the mentioned critical irradiation positions. So, about 4 days of continuous measurement were required to scan the entire area of the detector's front face (102 $\times$ 102 irradiation positions) for the case of the ^{137}Cs (82 MBq) source reference library. Using the identical method during the reference library measurement of the ^{60}Co source would be prohibitive, due to the unrealistic long estimated measurement time ($\sim$ 130 days), which can be extrapolated from the measurement of the ^{137}Cs source after considering some factors related to the ^{60}Co source and its collimator setup. First, the source activity was lower by a factor of four compared to the ^{137}Cs source. From Fig. 4.3.1, the photopeak detection efficiency of the $LaBr_3$:Ce scintillator at a photon energy of 1.33 MeV is lower by about a factor of two compared to the one at 662 keV. Moreover, since the collimator used with the ^{60}Co source is twice longer as the one used with the ^{137}Cs source, the radiation flux will be reduced to 114 compared to the previous setup. However, this reduction of flux led to a recovery of the dead time of the DQA system from 46% to 12% for the case of the ^{137}Cs and ^{60}Co sources, respectively. Consequently, the estimated measurement time of the ^{60}Co source reference library could be reduced even further by a factor of $\sim$ 4 to about 32 days. From the ^{137}Cs source reference library, it was noticed that 46% of the measured data were in excess of the envisaged 400 photopeak events per irradiation position. This implied that the required time for reaching the number of photopeak events per position (n_{epp}) varies from one position to another, which offered an additional opportunity for reducing the estimated measurement time for the ^{60}Co source reference library. Therefore, the synchronizing script was upgraded for the ^{60}Co source reference library, allowing for a dynamic adjustment of the acquisition time per irradiation position according to a pre-selected (and dynamically integrated) amount of photopeak events at each irradiation position. With this method and using the 1mm collimated ^{60}Co source, the 2D scan for 102 $\times$ 102 irradiation positions providing a reference library of 400 photopeak events per position was completed within about 10 days.

5.3 Results

The spatial resolution of the monolithic $LaBr_3$:Ce scintillator was determined using the so-called "leave-one-out method" of the k-NN and CAP algorithms, described in Sect. 5.1.1 and 5.1.2, respectively. The performance of both reconstruction algorithms was systematically studied by varying the key parameters, such as the step size of the 2D grid scan (thus determining the number of irradiation positions n_{pos}), the number of photopeak events analyzed at each irradiation position (n_{epp}) and particularly the parameters k of best matching reference library light distributions. Moreover, experimental quantities like the granularity of the photomultiplier (multi-anode PMT segmentation) and the energy of the incident photons was varied as well in order to study their impact on the detector's spatial resolution. A detailed description of these parameters is listed below:

- Reference library: pitch size and number of photopeak events per irradiation position (n_{epp})
  Aiming to reduce the experimental measurement time needed to acquire the reference library data and avoiding any impact on the detector properties, the detector's spatial resolution was evaluated as a function of the reference library pitch size and the number of photopeak events per irradiation position n_{epp}. Since the scan step size of the original reference library of both ^{137}Cs and ^{60}Co sources is 0.5 mm, which corresponds to the radius of the collimator opening (1 mm), new libraries of 1 mm grid size were created during the offline data analysis by selecting only every second irradiation position of the

main library. For the variation of the parameter n_{epp}, 11 sub-libraries, containing different n_{epp} values, were extracted from the main library according to

$$n_{epp} = \{5, 20, 30, 40, 50, 75, 100, 150, 200, 300, 400\} \tag{5.3.1}$$

The number of photopeak events per irradiation position (n_{epp}), listed in the vector of Eq. (5.3.1), was selected in ascending order from the original main library, i.e the n_{epp} = 5 sub-library contains the first 5 photopeak events of each irradiation position from the full library.

- PMT granularity
  Presently, absorber crystal readout is done via the highest available multi-anode PMT segmentation of 16 × 16 pixel, leading to a complex signal processing setup. However, expanding the existing Compton camera prototype from one arm to, e. g., four arms is one of the future perspectives of this project. This would not only allow for increasing the camera's field of view and thus its reconstruction efficiency, but it would also enable the imaging of triple coincidences (e.g. from β^+ annihilation plus subsequent prompt γ emission from an excited daughter decay during either proton-beam irradiation or offline from β^+-γ-decay of isotopes like ^{44}Sc). However, such an upgrade would require four times as much signal processing electronics as presently in use, which would be prohibitive in view of costs and complexity. A foreseeable solution for this scenario might be reducing the granularity of the PMT segmentation, thus enlarging the area of each PMT segment, in order to reduce the number of signal processing channels. Since the main reference library was acquired with the full 256-fold PMT segmentation, a new reference library was artificially created by summing each four neighboring pixels of the 2D light distributions in order to mimic the behaviour of an 8 × 8 multi-anode PMT. Then, the impact of enlarging the readout sensor area on the $LaBr_3$:Ce detector's spatial resolution was evaluated. This study was performed using the grid size and the number of photopeak events per irradiation position (n_{epp}) of both ^{137}Cs and ^{60}Co main reference libraries.

- Incident photon energy
  Since the LMU Compton camera has been designed to image and localize prompt γ rays (about 3 - 6 MeV), emitted from nuclear reactions between proton (ion) beams and biological tissue, the spatial resolution properties of the $LaBr_3$:Ce absorbing detector have to be investigated as a function of the photon energy. From the practical point of view with regard to the k-NN and CAP reconstruction algorithms, intense γ-ray calibration sources are needed to generate the reference libraries of the light amplitude distribution following a 2D detector scan with a tightly collimated photon beam. Therefore, the energy dependent spatial resolution of the Compton camera's absorbing detector was investigated using 1 mm collimated ^{137}Cs (662 keV) and ^{60}Co (1.17 and 1.33 MeV) γ-ray sources, respectively. Although the energy range of these sources is still considerably below the targeted photon energy range, this study will give an impression of the behaviour of the $LaBr_3$:Ce detector's spatial resolution as a function of the incident γ ray energy.

5.3.1 Spatial resolution as a function of the k parameter of the k-NN and CAP algorithms

Before going into details of the above mentioned systematic studies, the k parameter of both k-NN and CAP algorithms has to be optimized, based on the goal of achieving the optimum spatial resolution of the $LaBr_3$:Ce detector. For the k-NN algorithm, where k represents a set of

2D light amplitude distributions of the reference library, representing the closest match to the measured 2D light amplitude distribution of an unknown incident photon event, the value of k was varied between 1 and 4000 in steps as listed in the following vector

$$k_{kNN} = \{1, 3, 5, 10, 20, 40, 50, 70, 100, 200, 300, 400, 500, 700, 1000, 1200, 1500, 2000, 3000, 4000\} \quad (5.3.2)$$

Figure 5.3.1 shows the resulting spatial resolution as a function of k_{kNN}, using the full data set (n_{epp} = 400) of the reference libraries acquired with γ sources at photon energies of 0.662, 1.17 and 1.33 MeV, alternatively considering a scan pitch size of 0.5 mm and 1 mm, respectively. This study also covered the scenarios of 64- or 256-fold PMT granularity. For all cases presented in Fig. 5.3.1, the trends of the detector's spatial resolution are similar over the studied range of k_{kNN}. At (unrealistically low) k_{k-NN} values of 1 and 3, the spatial detector resolution is clearly statistically limited, due to the low number of nearest-neighbor (k) coordinates contributing to the reconstruction of the photon interaction position, which returns a calculated interaction position far from the mean value. Therefore, the difference between the true and the reconstructed γ-interaction position, used to fill the 2D error histogram, will be large and, consequently, the spatial resolution (FWHM) will degrade. Beyond a value of k_{k-NN} = 5, the spatial resolution starts to improve until reaching its best value around $k_{k-NN} \sim 1000$. Therefore, this value was chosen as the optimum k_{kNN} value when applying the k-NN algorithm in all subsequently performed parametric studies, since increasing the k_{kNN} value further would lead to an oversampling of the reconstructed photon interaction position, resulting in a degradation of the detector's spatial resolution. An obvious feature of the spatial resolution as a function of the incident photon energy can already be inferred from this first exploratory systematic study: the cases shown in Fig. 5.3.1 separate in two groups, where consistently the resolution achieved with the ^{60}Co source outperforms the one achieved with the lower energy of ^{137}Cs source. This promising feature will be investigated in more details in the context of this section.

As the k value of the CAP algorithm represents the number of closest matching 2D light-amplitude distributions per irradiation position, from which an average 2D light amplitude distribution will be calculated and compared to the unknown incident event, this parameter was varied in steps of

$$k_{CAP} = \{1, 5, 10, 12, 14, 15, 25, 30, 40, 50\} \quad (5.3.3)$$

Figure 5.3.2 shows this study for different detector scan scenarios, such as PMT granularity, reference library pitch size and impinging photon energy. For all cases, a similar behaviour of the $LaBr_3$:Ce scintillator's spatial resolution is observed over the range of k_{CAP} values. As the value of k_{CAP} increases, the detector's spatial resolution starts to improve until reaching its best value at $k_{CAP} \sim$12. The reason of this improvement can be attributed to the increasing photon statistics in the resulting average 2D light distribution for increasing values of k_{CAP}. On the other hand, beyond the optimum value of k_{CAP}, the detector's spatial resolution slowly but steadily degrades. This might be due to an accumulation of the effect of scintillation light scattering, caused by the reflective crystal surface coating, particularly strong at the crystal border or corner irradiation positions. This effect can blur the correlation between source position and measured intensity maximum and thus affect the spatial resolution of the reconstructed photon interaction position via the CAP algorithm.

As already stated for the investigation of the standard k-NN algorithm presented in Fig. 5.3.1, also for the study using the CAP algorithm (Fig. 5.3.2), a clear separation between the $LaBr_3$:Ce scintillator spatial resolution obtained from ^{137}Cs and ^{60}Co can be observed. This again indicates an energy dependent spatial resolution. As for the k-NN algorithm, the best spatial resolution of the $LaBr_3$:Ce scintillator was determined for reference libraries obtained

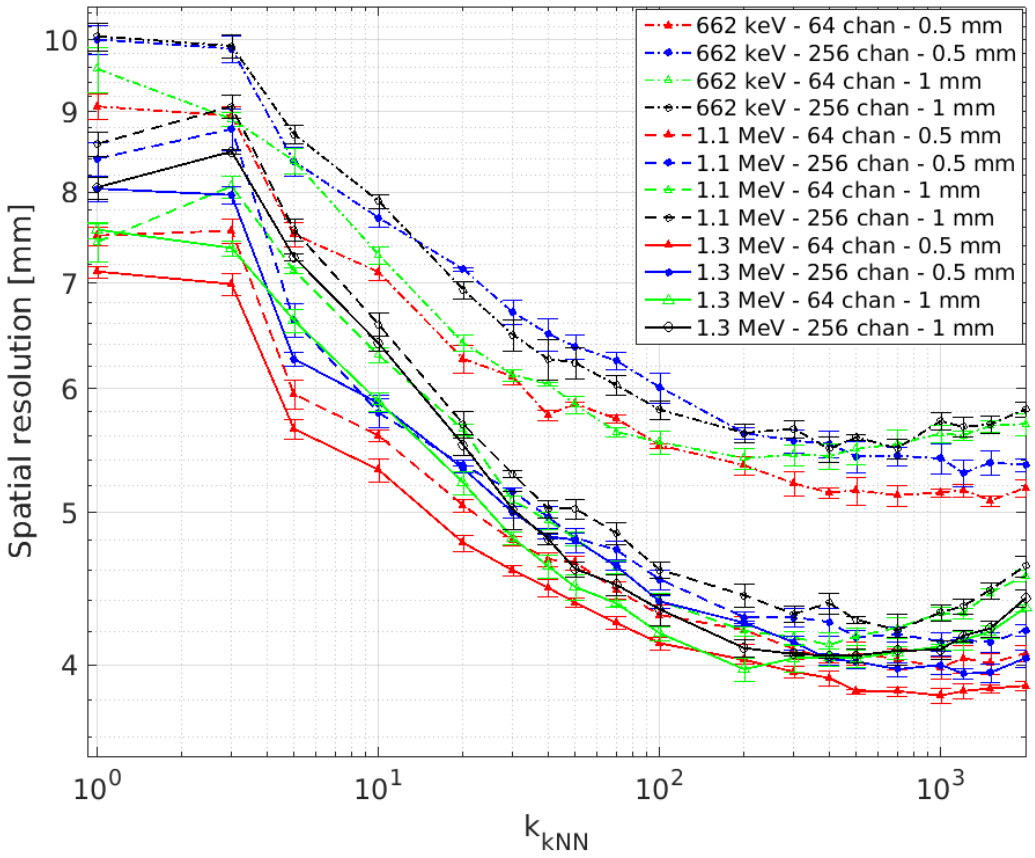

Figure 5.3.1: Systematic investigation of the $LaBr_3$:Ce scintillator spatial resolution as a function of the k variable of the k-NN algorithm (i. e. the number of best matching light amplitude distributions from a reference library, when comparing an unknown incident photon event). This study covered different parameters applied to the full reference library (n_{epp} = 400), such as the grid spacing of irradiation positions, impinging γ-ray energy and PMT granularity. For all the mentioned systematic studies, the optimum value of k_{kNN} was found to be $\sim$ 1000, where the best spatial resolution was obtained.

with a 0.5 mm scan pitch size and a 64-fold PMT granularity. These features will be discussed in more details later in this chapter.

Determination of the experimental uncertainties

The determination of the experimental uncertainties associated with the spatial resolution data shown in this section is based on the statistical uncertainties of the spatial resolution, derived from sub-samples of the main reference library. Four sub-libraries, each of them containing 100 photo-peak events per irradiation position, were created from the main library, which contains n_{epp} = 400 photopeak events per position. It should be noted that the selection of the 100 photopeak event was performed in ascending order, i.e. the first 100 events of the main library were extracted for the first sub-library and so on. Then, the ”leave-one-out method” was applied to each sub-library to determine the corresponding spatial resolution, using the set of k values indicated in Eq.(5.3.2 and Eq.(5.3.3) for the k-NN and CAP algorithms, respectively. The standard deviation was calculated for each set of four resulting spatial resolution values

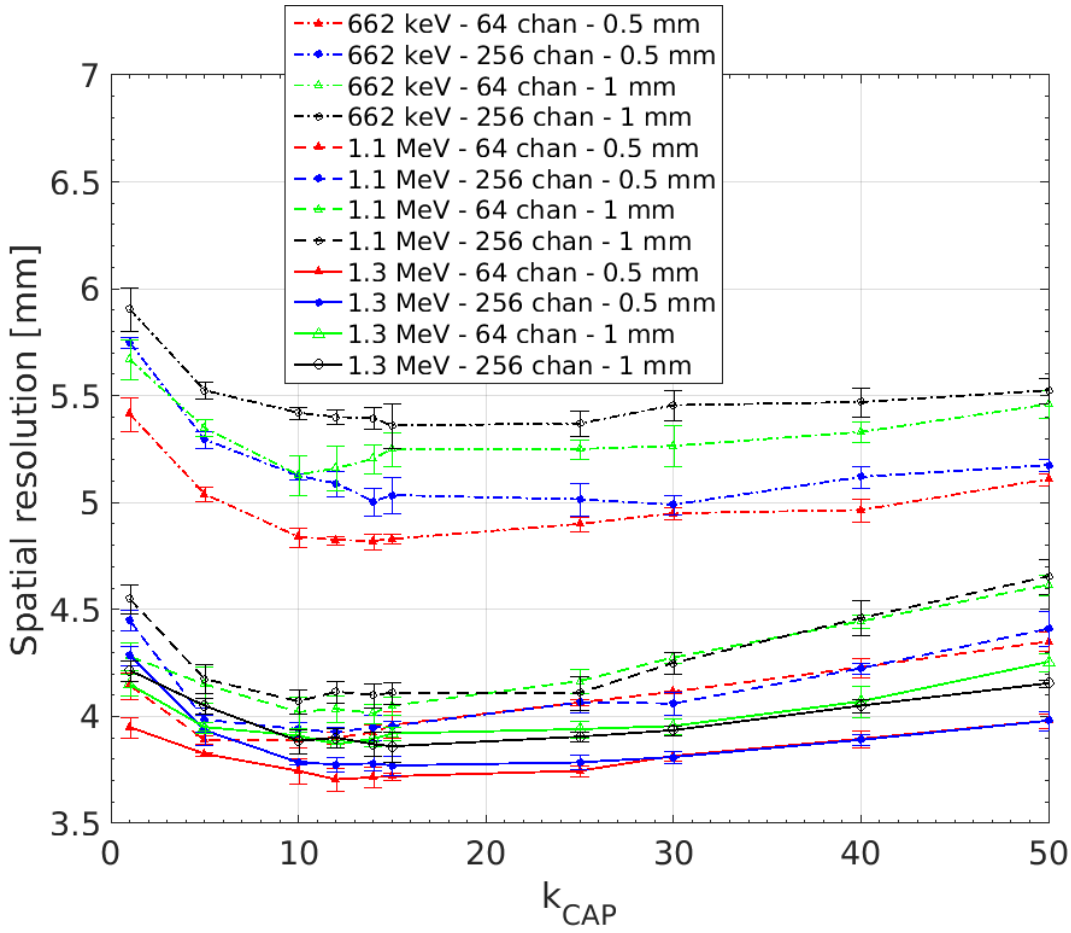

Figure 5.3.2: Determination of the $LaBr_3$:Ce scintillator's spatial resolution based on the k variable value of the CAP algorithm (i. e. the number of best matching reference light amplitude distributions per irradiation position). This study covered different parameters applied to the full reference library with 400 photopeak events per irradiation position, such as the grid spacing of the irradiation position, the impinging γ-ray energy value and the PMT granularity. For all the mentioned systematic studies, the optimum k_{CAP} parameter was found to be $\sim$ 12, where the best detector spatial resolution was obtained.

obtained from the four n_{epp} = 100 sub-libraries and was assigned as the corresponding experimental uncertainty. This method was applied for all main libraries of ^{137}Cs (662 keV) and ^{60}Co (1.17 MeV and 1.33 MeV), including all their corresponding parametric studies. Figure 5.3.3 illustrates an example of applying this method, using the CAP algorithm, to the case of two PMT granularities and a photon energy of 1.33 MeV. Strictly, this method provides an estimate of the experimental uncertainty for n_{epp} = 100.
In order to determine the uncertainties of the spatial resolution for different values of n_{epp}, in particular for the resolution derived from a library with n_{epp} = 400, four time the size of the existing $LaBr_3$:Ce scintillator and ^{60}Co main libraries would be needed. This, in fact, would increase the experimental time for acquiring the reference library in a prohibitive way. Therefore, the uncertainties of the detector spatial resolution as a function of the number of photopeak events per position n_{epp} was extrapolated from the one obtained with n_{epp} = 100 as follows:

$$\sigma(k, n_{epp}) = \sigma(k, 100) \times \sqrt{\frac{100}{n_{epp}}} \tag{5.3.4}$$

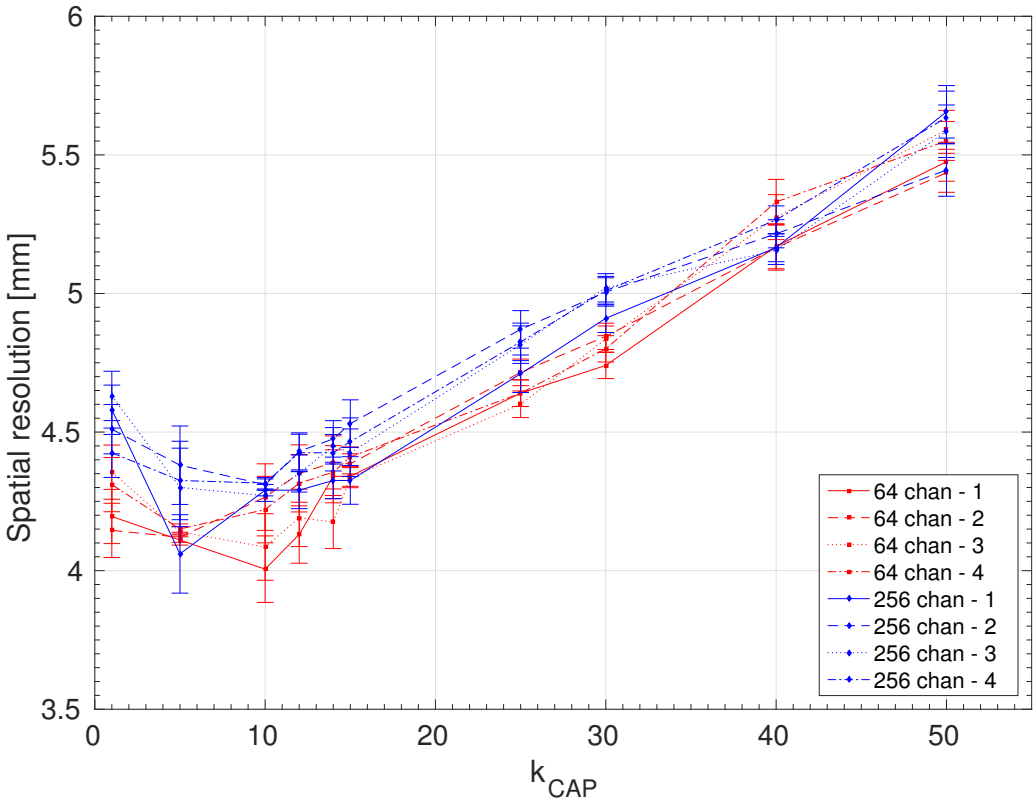

Figure 5.3.3: Uncertainty determination of the $LaBr_3$:Ce scintillator's spatial resolution. The main reference library with n_{epp} = 400 reference photopeak events per irradiation position (acquired at E_γ = 1.33 MeV with a scan pitch size of 0.5 mm) was split into four sub-libraries with n_{epp} = 100 each (indicated by the index 1-4 to the different curve legends). The CAP reconstruction algorithm was applied to the case of 256 (blue curves) and 64 (red curves) PMT channels. At each value of k, the standard deviation of the four resulting spatial resolution values was calculated for each case of the PMT granularity.

5.3.2 Spatial resolution as a function of the number of photopeak events per irradiation position (n_{epp})

Based on the determination of the optimum k value for both k-NN and CAP algorithms, the dependence of the $LaBr_3$:Ce scintillator's spatial resolution (FWHM) on the number of photopeak events per irradiation position (n_{epp}) of the reference library will be examined. Due to the computational effort required to compare unknown photon events with the entries of the reference library, it will be crucial to determine the minimum value of n_{epp} that does not compromise the optimum value of the spatial resolution achieved in a specific irradiation scenario. This study is applied to reference libraries representing different experimental scenarios, such as PMT granularity, grid spacing between irradiation positions and impinging γ-ray energy values. For each of these parametric studies, the performance of the k-NN and CAP algorithms, respectively, are compared. In order to structure the representation of this study, the results will be displayed separately for each of the impinging γ ray energies.

Incident photon energy E_γ = 662 keV

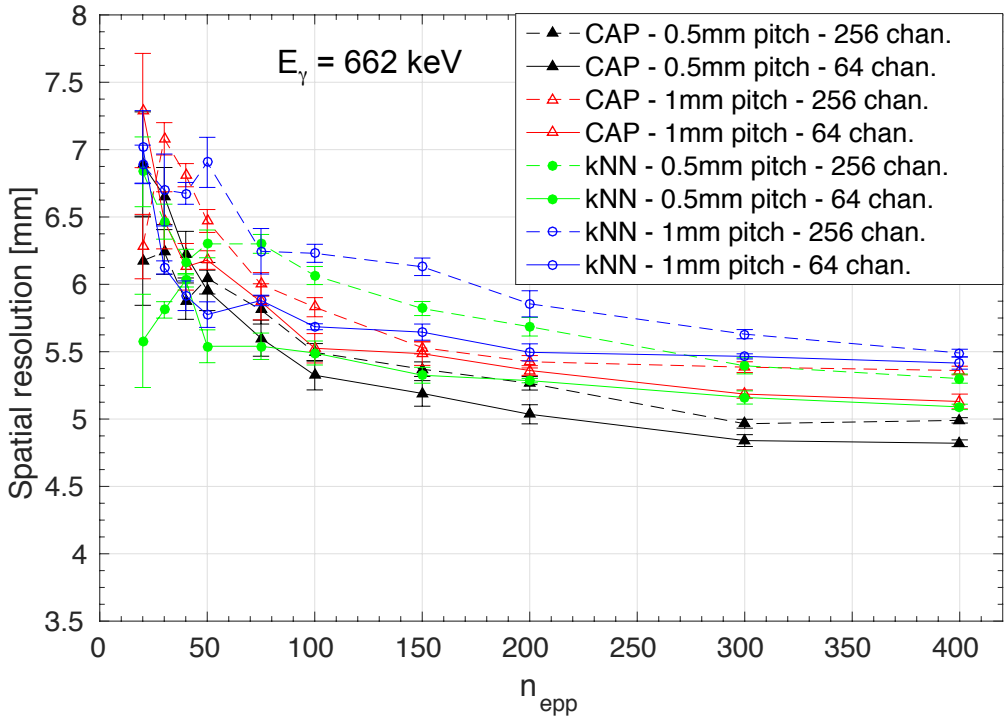

Figure 5.3.4: Systematic study of the spatial resolution of the $LaBr_3$:Ce scintillator as a function of the number of reference photopeak events (n_{epp}) per irradiation position of a (1 mm) collimated ^{137}Cs γ-ray source. This investigation is applied to a comparison of different parameters, such as the PMT granularity and grid spacing between the scan irradiation positions. The standard k-NN and CAP algorithms are used in this study each with their optimum k values, as determined from Fig. 5.3.1 and 5.3.2, respectively.

Figure 5.3.4 displays a comparative study of the spatial resolution (FWHM) as a function of different numbers of n_{epp} obtained from a 1 mm collimated ^{137}Cs source. In general, the data reveal consistent trends in all parametric cases, besides their differences in the absolute value of the spatial resolution. For the lower n_{epp} values (n_{epp} = 50 - 75), the observed fluctuations of the spatial resolution can be attributed to the low number of statistics. This means that the unknown event can be compared only to a few reference light amplitude distributions, thus limiting the opportunity to average over larger set of k coordinates. Beyond n_{epp} = 75, the spatial resolution in all parametric cases seems to fluctuate and follow a smooth trend of improved resolution with increasing value of n_{epp}. For n_{epp} larger than about 200, this trend flattens out and in some cases the spatial resolution (within the error bars) tends to stay constant with increasing n_{epp}.
Comparing the spatial resolution obtained for two different PMT granularities (64- and 256-fold segmentation), the $LaBr_3$:Ce scintillator's spatial resolution (FWHM) reveals improved values for the 64-fold segmentation compared to the higher granularity (256 fold) for both algorithms. This can be inferred by comparing the values of the spatial resolution in Fig. 5.3.4 for each pair of curves with the same color, where the solid line represents the case of the 64-fold segmentation, while the dashed curves correspond to the higher 256-fold PMT granularity. The reason for this behaviour can be attributed to the improved photon statistics in the light intensity distributions per pixel.
Figure 5.3.4 also compares the dependence of the scintillator's spatial resolution for two values of the scan pitch size of 0.5 and 1 mm. For a given reconstruction algorithm and PMT granularity, a reference library generated from a 0.5 mm pitch size exhibits the better spatial resolution.

This is not surprising, given the fact that a finer grid of the response matrix (i. e. the reference library) will necessarily allow for a higher sensitivity to spatial differences between incident γ-rays (provided that the grid size is equal or slightly smaller than the photon beam diameter).
The two reconstruction algorithms used in this study are compared for different settings of scan pitch size and PMT granularity. When fixing these two parameters, the CAP algorithm exhibits a better performance over a wide range of n_{epp} ($100 \leqslant n_{epp} \leqslant 400$) compared to the standard k-NN algorithm. This can be seen in Fig. 5.3.4 by comparing the data set with triangular marks (for CAP) with that denoted by circular marks (for k-NN) for pairs with the same color and line style.
The message extracted from the data shown in Fig. 5.3.4 is that the CAP algorithm applied to a reference library acquired with a 0.5 mm scan grid size and 64 PMT segments provides the best spatial resolution for the $LaBr_3$:Ce scintillator at 662 keV. Applying these parameters to a reference library of n_{epp} = 400 results in a spatial resolution of 4.8 (1) mm.

Incident photon energy E_γ = 1.17 MeV

The systematic study of the $LaBr_3$:Ce scintillator's spatial resolution as a function of n_{epp} (number of photopeak events per reference irradiation position) was repeated in a similar way as presented for the ^{137}Cs source, also using a 1 mm collimated ^{60}Co source (gated on the photopeak at 1.17 MeV). The resulting data using the k-NN and CAP algorithms, in each case utilizing their respective optimum k values, are compared and displayed in Fig. 5.3.5 as a function of n_{epp}. Overall properties and trends turn out to be rather similar as found before when using the ^{137}Cs source. Low numbers of n_{epp} (below n_{epp} = 50) cause fluctuations in the spatial resolution values of both algorithms. Within the experimental uncertainties, no significant improvement of the spatial resolution was observed for $n_{epp} \geqslant 200$. In general, the behaviour of the spatial resolution trends is similar to what was obtained and discussed in the 662 keV case. The influence of the PMT granularity on the spatial resolution, exhibiting an improved resolution for the case of 64-fold segmentation compared to the higher value of 256-fold pixels, is still distinguishable, although this feature is reduced compared to the 662 keV case. This reduction may be attributed to the increase of the scintillation light produced by the higher incident γ-ray energy, which in turn improves the photon statistics in the 2D light amplitude distributions for each individual PMT segment in both PMT granularity scenarios, reducing performance differences between them. The increase of the light yield might also be the reason behind the improved performance of the k-NN reconstruction algorithm of E_γ = 1.17 MeV, since it directly compares the 2D light amplitude distribution of the unknown event to all entries of the total reference library. Thus statistical improvements of the 2D light amplitude distribution via the increased light yield will help to better define the k_{k-NN} closest matching reference distributions, thus improving the precision of the calculated interaction position. Nevertheless, despite the improvement of the performance of the k-NN algorithm, the best value of the spatial resolution for the $LaBr_3$:Ce scintillator was obtained with the CAP algorithm, for any of the chains of parameters applied to obtain the reference library. As already discussed in the 662 keV case, using a library with a finer pitch size improves the detector's spatial resolution.
As can be seen from Fig.5.3.5, the best spatial resolution of the $LaBr_3$:Ce scintillator measured at 1.17 MeV was found to be 3.9 (1) mm when applying the CAP algorithm and using a reference library of n_{epp} = 400, 64-fold PMT granularity and a scan pitch size of 0.5 mm.

Incident photon energy E_γ = 1.33 MeV

The dependence of the $LaBr_3$:Ce scintillator's spatial resolution on the number of photo-peak

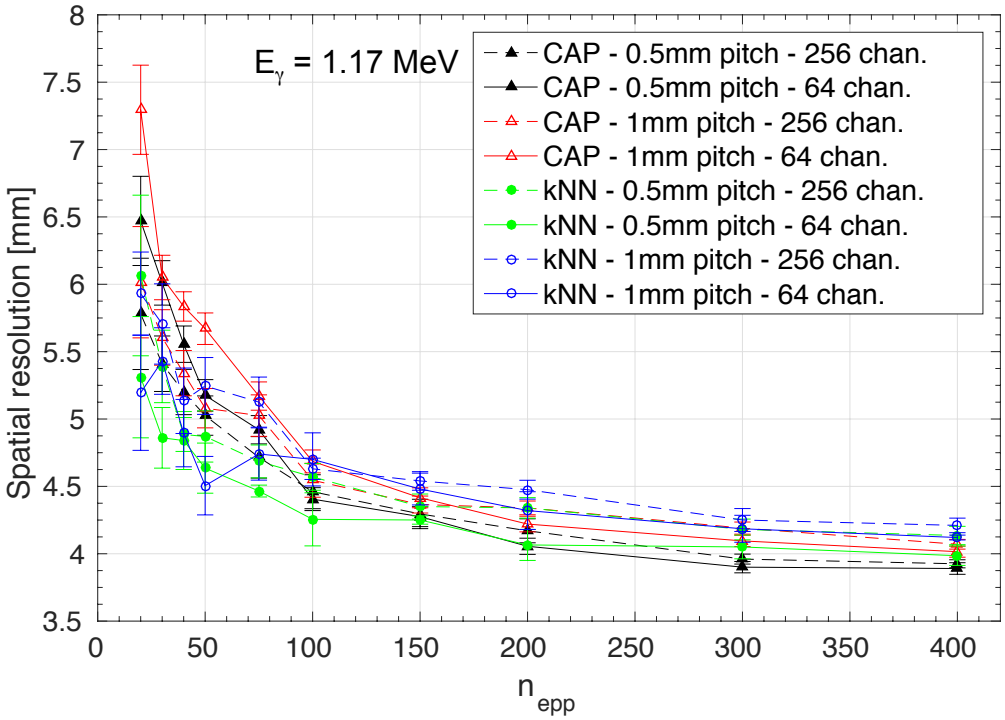

Figure 5.3.5: Systematic investigation of the $LaBr_3$:Ce scintillator's spatial resolution as a function of n_{epp} of the reference library, measured by a 1 mm collimated ^{60}Co source (gated at the 1.17 MeV photopeak). The impact of the reference library parameters on the detector spatial resolution, such as PMT granularity and scan pitch size, was studied using the k-NN and CAP algorithms, in each case applying the respective optimum k values as determined before.

events per position n_{epp} was also investigated at the higher energy transition of the ^{60}Co source with E_γ = 1.33 MeV, again using a 1 mm collimation. The resulting cases of the spatial resolution derived from the same scenario as before are displayed in Fig. 5.3.6. Compared to the 1.17 MeV case, the impact of the reference library parameters, such as PMT granularity and scan pitch size, as well as the type of reconstruction algorithm (k-NN and CAP) on the spatial resolution value turns out to be similar as described before. Nevertheless, a slight improvement of the best achievable spatial resolution was found for 1.33 MeV. Based on a reference library with n_{epp} = 400, a 64-fold PMT granularity and 0.5 mm scan pitch size, the CAP algorithm provided 3.7(1) mm as the best spatial resolution obtained for the $LaBr_3$:Ce scintillator.

Besides the findings obtained from the comparison of different reference library scenarios (PMT granularity, scan pitch size) for two different reconstruction algorithms and three incident photon energies, the main purpose of the systematic studies presented in this section was to quantity the behaviour of the spatial resolution as a function of the size of the reference library of light amplitude distributions, represented by the number of photopeak events acquired at each irradiation position when scanning the scintillator's front surface with a tightly collimated calibration source. This parameter critically affects both the measurement time to generate the reference library as well as its computational efforts needed during reconstruction of the interaction position of the unknown photon events when comparing them consecutively to each entry of the reference library. Therefore, it is important to conclude from the studies shown in this section, that the spatial resolution does not significantly improve (within the experimental uncertainties), when pushing the number of photopeak events per position beyond a value of n_{epp} = 200. This

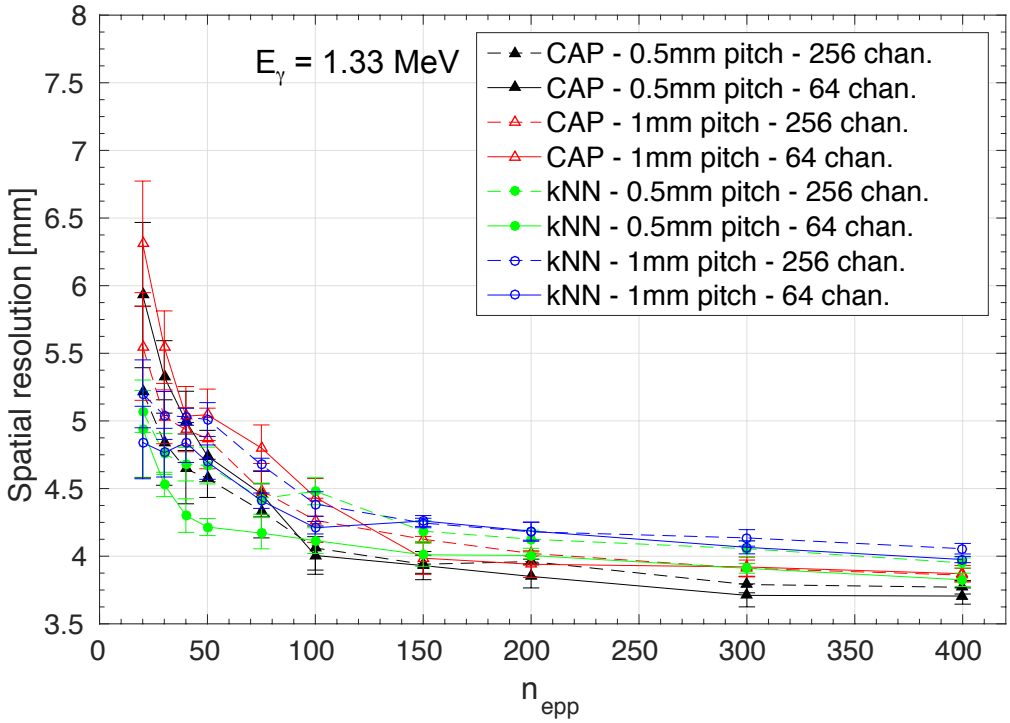

Figure 5.3.6: Systematic study of the $LaBr_3$:Ce scintillator's spatial resolution as a function of the number of reference photopeak events per irradiation position (n_{epp}), measured using a 1 mm collimated ^{60}Co source (gated at the 1.33 MeV photo-peak). The segmentation of the multi-anode PMT and the scan step size were varied to quantify their influence on the spatial resolution, using the k-NN and CAP algorithms, in each case applying their respective optimum k values.

means that reducing the number of photopeak events per irradiation position compared to the presently acquired reference library based on n_{epp} = 400 by a factor of two would not considerably affect the detector spatial resolution. However, the corresponding gain in measurement time needed to generate the reference library brings the use of an even smaller collimator opening (0.6 mm) into realistic reach, as will be discussed in Sect. 5.3.4. Moreover, a clear energy dependence of the spatial resolution could be observed consistently over the full range of the values of n_{epp}. This will be highlighted in the following paragraph.

5.3.3 Spatial resolution as a function of the impinging γ-ray energy

Figure 5.3.7 shows the dependence of the $LaBr_3$:Ce scintillator's spatial resolution on the impinging γ-ray energy for the case of two PMT granularities, processed by the standard k-NN and CAP algorithms, respectively. The optimized k values for each reconstruction algorithm were applied. Reference libraries with a scan pitch size of 0.5 mm and n_{epp} = 400 were used. At 662 keV and consistently achieved with both reconstruction algorithms, Fig. 5.3.7 shows that the best spatial resolution of the $LaBr_3$:Ce scintillator was found for a 64-fold PMT granularity, compared to the full segmentation of 256 pixel provided by the multi-anode PMT. This can be attributed to the improved photon statistics of the scintillation light registered in each pixel of the 2D light amplitude distributions. This effect is more prominently visible at lower photon energies and, while still observable, is reduced for higher incident energies. Thus, the amount of scintillation light is increased, leading to an improved photon statistics, and thus the spatial resolution obtained with both PMT granularities shows, within the error bars, comparable values. What can be clearly stated to be valid for the full studied energy range is that the CAP algorithm always provides the best spatial detector resolution.

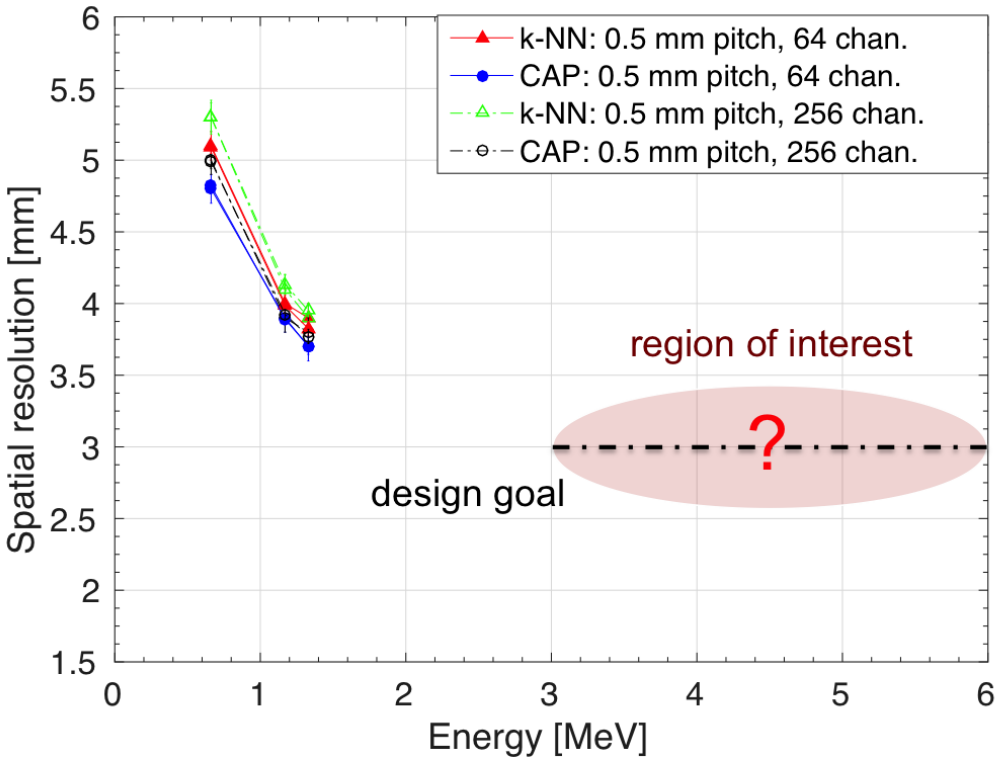

Figure 5.3.7: Spatial resolution of the $LaBr_3$:Ce scintillator as a function of the impinging γ-ray energy. For each γ-ray energy, two PMT granularities were evaluated, using the k-NN and CAP algorithms. In each case the optimum k value of the specific algorithm was used. The scan pitch size and number of photopeak events per irradiation position (n_{epp}) of the reference library were fixed to be 0.5 mm and 400, respectively.

The comparison in Fig. 5.3.7 reveals that as the value of the incident γ-ray energy increases, the spatial resolution of the $LaBr_3$:Ce scintillator improves. Again, as discussed for the comparison of PMT granularity, this can be attributed to the increase of the scintillation light yield, in turn improving the statistics of the intensity maxima in the reference library. The fact that not only the performance difference between low and high PMT granularity, but also between the

two alternative reconstruction algorithms reduces with increasing photon energy, may as well be traced back to the increased light yield. The better the localization of the primary photon interaction position due to an improved photon statistics in the reference library of 2D-light amplitude distributions, the better the corresponding determination of the best-matching nearest neighbor distribution used to calculate the coordinates of the unknown γ-interaction position.
In conclusion, the presented systematic studies of the k-NN reconstruction algorithm (and its modified CAP version) provide very promising results for the energy-dependent behaviour of the spatial resolution realized in the monolithic absorber detector of the Compton camera: already for the still rather low photon energy of 1.33 MeV, a promising value of 3.7(1) mm could be achieved with the CAP algorithm. This value is not far from the envisaged design goal of 3 mm for the spatial resolution of the $LaBr_3$:Ce scintillator in the much higher energy range of prompt-γ rays ($\sim$ 3 - 6 MeV) to be expected from nuclear interactions of therapeutic proton (ion) beams with organic tissue. Earlier simulation studies [38, 53] had recommended targeting this spatial resolution in the absorber, as it would allow to reach an overall spatial resolution of the Compton camera in reconstructing the primary photon source position of about 2 mm in case of a small-animal irradiation scenario (i. e. 50 mm distance from γ-source to the first scatter detector).
Confidence in reaching the design goal is nourished by the fact that with increasing photon energies to out 3-6 MeV, the probability of primary photon interactions with the absorbing detector material based on pair creation rather than photo effect or Compton scattering will considerably increase. With positron annihilation being a rather localized interaction, the definition of the intensity maximum of the resulting 2D light amplitude distribution will benefit from an increase of photon energies towards the relevant energy range of prompt-γ emission. Figure 5.3.7 expresses confidence to reach the design goal for multi-MeV photons by the shaded region inserted in the energy region of interest.

5.3.4 Towards a further reduced source collimation

Having reached a very promising result for the spatial resolution of the monolithic scintillator of the Compton camera, still the goal is to further improve this property towards the envisaged design goal. While increasing the photon energy cannot be achieved in the laboratory, due to the lack of multi-MeV calibration sources, one may expect improved performance of the reconstruction algorithms when starting from an even better defined reference library. This may be achievable by further reducing the incident photon beam diameter by a reduction of the diameter of the collimation channel. As discussed in Sect. 5.2.2, the obvious advantage of the newly designed collimator setup is the flexibility provided to vary the opening, e. g., from the presently used value of 1 mm to an even reduced collimation of 0.6 mm. In order to characterize this irradiation scenario, the x and y edge scan profiles of the $LaBr_3$:Ce scintillator crystal were repeated using the ^{137}Cs (662 keV) and ^{60}Co (1.17 and 1.33 MeV) sources with the 0.6 mm collimator tube inserted to the shielding arrangement introduced in Sect. 5.2.2. Figure. 5.3.8, 5.3.9 and 5.3.10 show the resulting count rate profiles. A first observation from these figures is the reduction of the photopeak intensity compared to the 1 mm collimator cases (for otherwise identical measurement conditions of 1 mm step size and 1 hour irradiation time per position). This, in fact, is expected as the collimator diameter becomes smaller (0.6 mm), thus reducing the transmitted photon flux by about a factor of 3. This leads to a degradation in the S/B ratio, since the background, mainly caused by radiation leakage through the collimator side shielding and by the intrinsic radioactivity of the $LaBr_3$:Ce scintillator, remains constant for both collimator diameters. Consequently, the quality of defining the inflection point of the fit curve to the count rate profile fit is degraded. This is more pronounced when using the ^{60}Co source (1.17 MeV and 1.33 MeV), due to the reduction of the S/B contrast as well as due to the rounded shape on the upper part of the rising and falling profile slopes, resulting from edge scattering effects. These two factors contribute to worsen the fit quality and, consequently, the determination of the measured crystal dimension, as can be seen from the x- and y crystal length dimensions indicated in the figures of this section, which deviate more significantly from the true crystal front face dimension of 50 $\times$ 50 mm^2 than found earlier for the 1 mm collimation measurement.

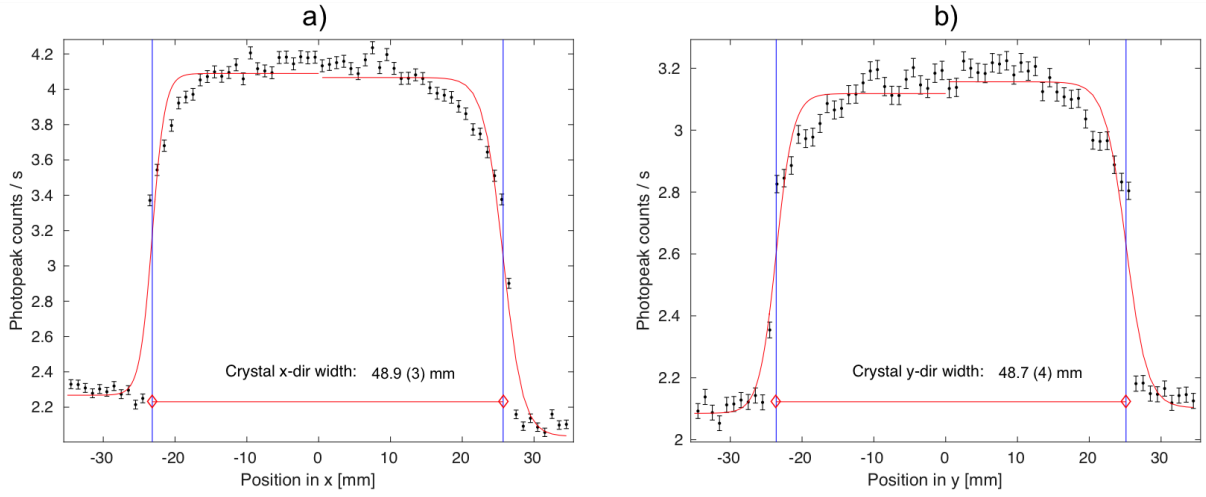

Figure 5.3.8: x (panel a) and y (panel b) edge scan count-rate profiles of a $LaBr_3$ scintillator crystal using a 0.6 mm collimated ^{137}Cs source. The measurement was performed with a scan step size and irradiation time of 1 mm and 1 h, respectively.

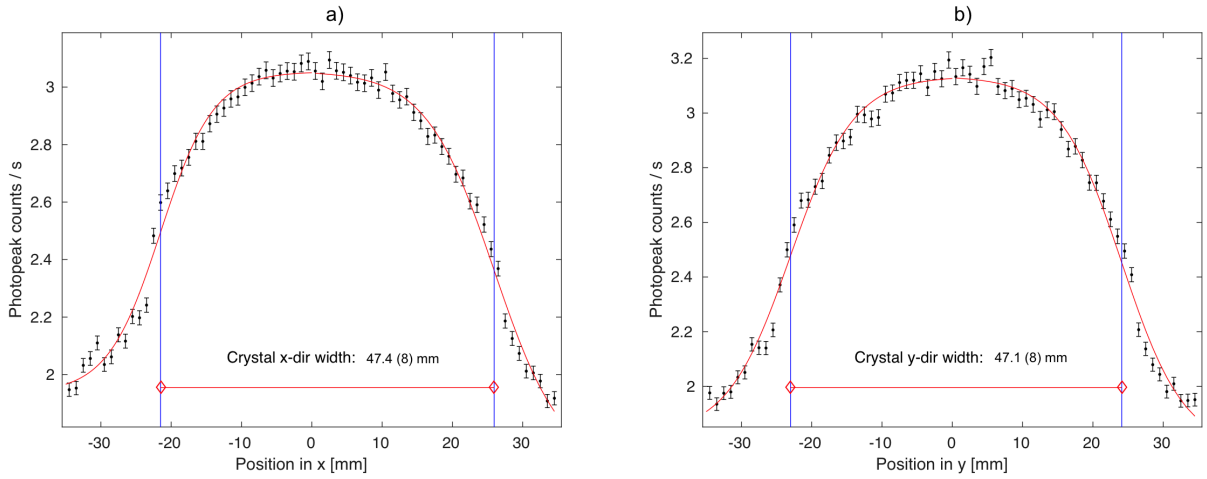

Figure 5.3.9: x (panel a) and y (panel b) edge scan count-rate profiles of the $LaBr_3$ scintillator crystal, representing the photopeak count rates of a 1.17 MeV γ-ray peak from a ^{60}Co source, measured as a function of the irradiation position. The measurement was performed with a 0.6 mm collimator, a scan step size of 1 mm and an irradiation time of 1 h per irradiation position.

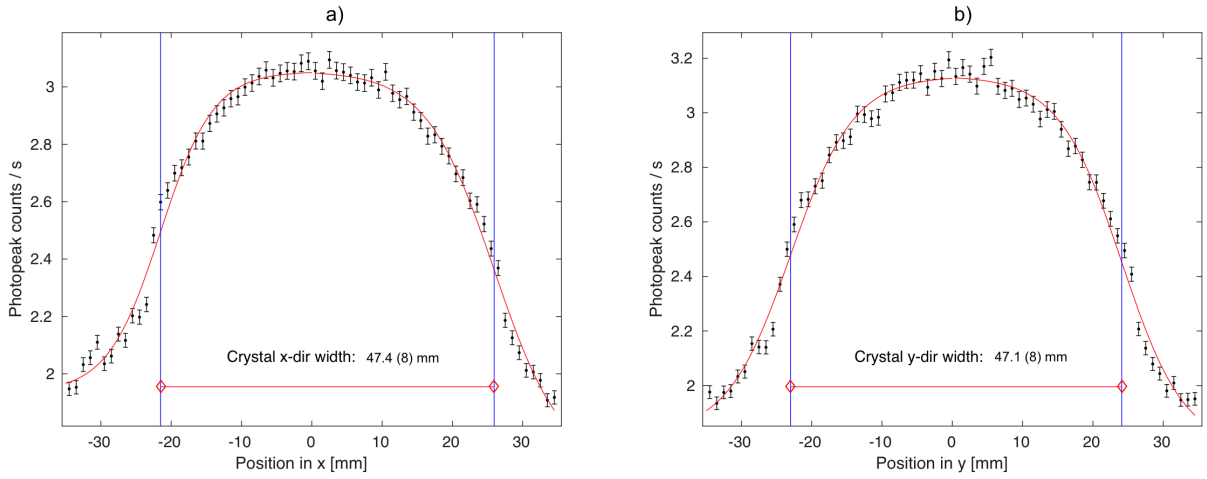

Figure 5.3.10: x (a panel) and y (b panel) edge scan count-rate profiles of the $LaBr_3$ scintillator crystal, representing the photopeak count rates of a 1.33 MeV γ-ray peak from a ^{60}Co source, measured as a function of the irradiation position. In this experiment, a collimator of 0.6 mm diameter, a 1 mm scan step size and 1 h irradiation time per position were used.

Despite the degradation of the S/B ratio obtained from the 0.6 mm collimator opening, the source position can be still resolved by the $LaBr_3$ scintillator. This optimistic statement is justified by exploratory studies with the 0.6 mm collimator opening. Figure 5.3.11 shows the resulting 2D light amplitude distributions of 16 $\times$ 16 irradiation positions, using the ^{137}Cs (panel a) and ^{60}Co (gated at 1.33 MeV, panel b) sources. In these two reference libraries, 1500 photopeak events were measured at each position. Since the S/B ratio of both sources differs, as indicated earlier in the edge-scan study, the color scales of the two maps are set differently in order to visualize their individual characteristics. This preliminary result opens a promising road for investigating the spatial resolution of the $LaBr_3$ scintillator using a sub-millimetre collimator opening. However, due to the reduced transmitted photon flux and reduced signal-to-background count rate, a corresponding measurement of the full reference libraries with more than 10^4 irradiation positions is not straightforward possible, since it would require a prohibitively long measurement time.

However, there is room for improvement of the S/B ratio of the ^{60}Co source case by introducing a time coincidence measurement between the two simultaneously emitted photons. This technique would ensure a clean reference library by accepting only the photopeak events registered within a narrow time-coincidence window. This would play a major role in reducing the required number of photo-peak events per irradiation position, which would help to reduce the data acquisition time. Also the determination of the crystal dimensions by performing the x and y edge scans is expected to improve, since the S/B ratio would recover after suppressing most of the background events. The expected S/B ratio after applying this method is ~ 4 and ~ 3 for 1.17 MeV and 1.33 MeV, respectively, based on the available source intensity of 20 MBq. Yet it has to be confirmed that the coincidence efficiency achieved with the modified collimator and scan unit setup provides sufficient count rate to realize the time consuming 2D scan in a realistic period of , e. g., less than ca. 4 weeks of continuous data taking. Further exploratory studies in this context are performed beyond the scope of this thesis.

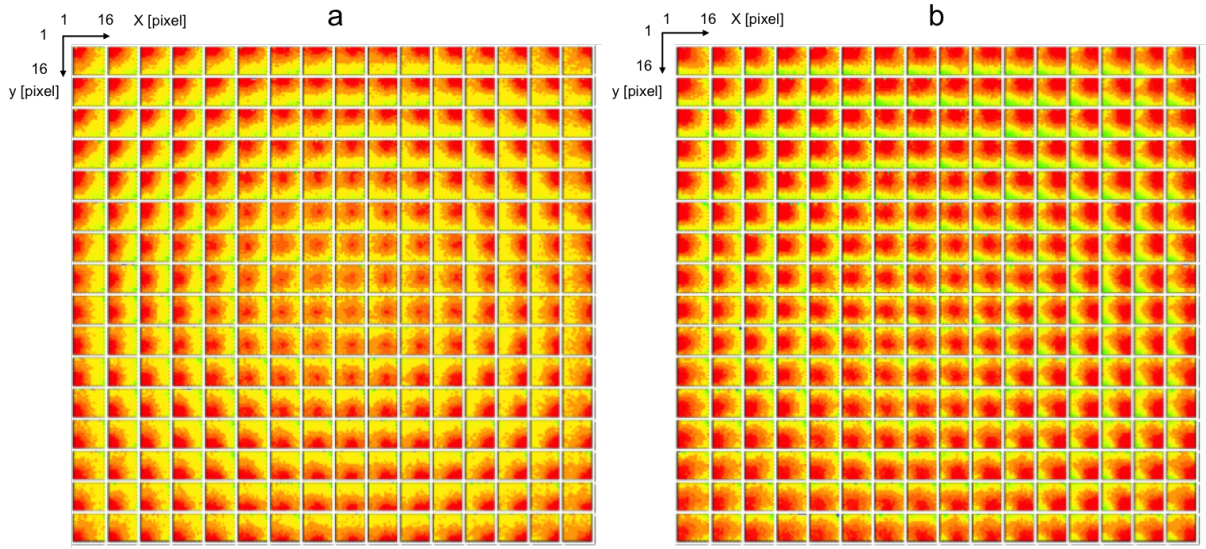

Figure 5.3.11: 2D light amplitude distributions for 16 $\times$ 16 irradiation positions obtained by scanning the $LaBr_3$ scintillator with a grid size of 3 mm and using the 0.6 mm collimated ^{137}Cs (panel a) and ^{60}Co (panel b) sources. The two panels are shown with different color scales to allow an optimized representation of each photon energy.

Chapter 6

Online commissioning of the LMU Compton camera components

As detecting multi-MeV prompt γ rays is the key objective when using the Compton camera for proton range verification, this chapter focuses on studying the ability of the LMU Compton camera prototype system in this radiation energy range. Consequently, various online measurement campaigns were performed at different accelerator facilities. The first part of this chapter deals with a characterization study of the individual Compton camera components using monoenergetic 4.439 MeV γ rays, produced via the ^{15}N(p, $\alpha\gamma$)^{12}C reaction. This test allows to study the detection system in a rather clean situation, where only one prominent γ-ray energy from the prompt γ-ray energy spectrum to be expected in particle therapy will be registered. This section is followed by a characterization study of the $LaBr_3$ scintillator exposed to the prompt γ radiation induced by nuclear reactions between a 20 MeV proton beam and a water phantom, performed at the MLL Tandem accelerator. Subsequently, following an upgrade of the readout electronics by installing a time signal digitization system, the timing properties of the $LaBr_3$:Ce scintillator are studied by performing a time-of-flight (ToF) measurement using a 20 MeV pulsed deuteron beam, generated by the MLL Tandem accelerator and hitting a water phantom. Finally, the performance of the Compton camera prototype is evaluated at a clinical proton beam, provided by the OncoRay facility in Dresden. This part covers various studies for both the scatter and absorbing components during the irradiation of water and PMMA phantoms with clinical proton beam energies.

6.1 Calibration of the Compton Camera components with 4.4 MeV γ rays

The aim of this experiment was to individually calibrate the LMU Compton camera components with γ rays, whose energy range is comparable to the targeted prompt γ-ray energies ($\sim$ 3 - 6 MeV). Such an energy range of multi-MeV γ rays is not available as a laboratory based radiation source, therefore nuclear reactions from an accelerated particle beam served as an alternative. At the Tandetron accelerator of the Helmholtz-Zentrum Dresden-Rossendorf (HZDR), a nuclear reaction setup, originally built for astrophysical applications [112], allows to generate monoenergetic γ rays of 4.439 MeV via a proton capture reaction, when irradiating a TiN target with a low energy ($\sim$ 0.9 MeV) proton beam. In this ^{15}N(p, $\alpha\ \gamma_{4.439MeV}$)^{12}C reaction, the naturally abundant ^{15}N is excited to the 2^- state of ^{16}O by capturing a proton. Subsequently, the excited $^{16}O^*$ nucleus de-excites by α emission to the 2^+ first excited state of ^{12}C, which then decays to the ground state by emitting 4.439 MeV γ rays. These γ rays are very favourable

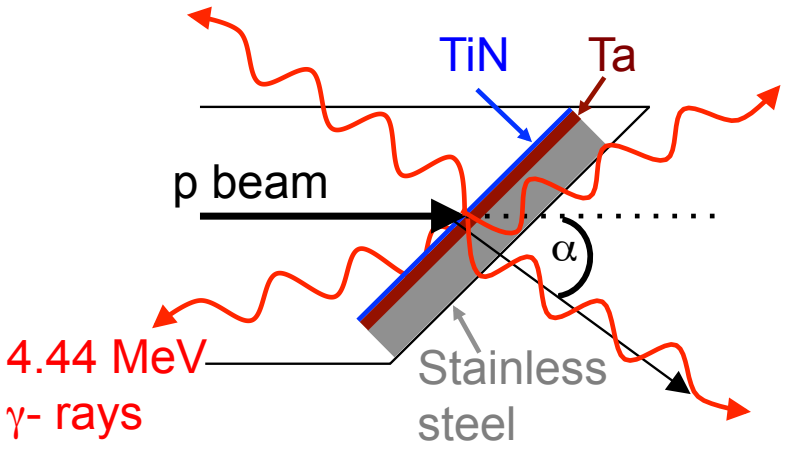

Figure 6.1.1: Illustration of the experimental setup used for the production of the monoenergetic 4.439 MeV γ rays. The proton beam of 0.9 MeV kinetic energy impinges onto a 400 nm thick TiN target, which is placed on a 200 μm thick Ta plate. Both the target and the Ta plate are stacked on a 2 cm thick water cooled stainless-steel plate, which is tilted by $\alpha = 55^o$ with respect to the proton beam direction [45].

for calibrating the LMU Compton camera components, because not only they are associated with almost no background [45], but this energy also is identical to the energy of the one of the prominent lines of the targeted prompt γ ray spectrum, induced from nuclear reactions between biological tissue and the proton beam via ^{12}C(p, p$'$ γ)^{12}C during cancer treatment.
Figure 6.1.1 shows a drawing of the experimental setup used for the production of the monoenergetic 4.439 MeV γ rays. The 0.9 MeV proton beam slowed down in a 400 nm thick TiN target and finally stopped in a 200 μm Ta plate. Both of them were attached to a 2 cm thick water cooled stainless-steel plate. The TiN target with its corresponding structures was positioned inside the evacuated beam line under an angle of $\alpha = 55^o$ with respect to the proton beam direction.
Figure 6.1.2 shows the experimental setup of the LMU Compton camera's absorbing (panel a) and scatter components (panel b), enclosed inside a light tight copper plated box. The $LaBr_3$:Ce scintillator (panel a) was placed in 42 mm distance from the outer surface of a tilted stainless-steel flange, behind which the TiN target was placed. The detector was positioned under an angle of $\alpha = 55^o$ with respect to the beam line, in parallel to the TiN target. In this geometry, the detector registered $\sim$ 700 cps. For the calibration test of the scatter detectors, the DSSSDs were kept inside a copper plated light tight box, acting as a Faraday cage (see Sect. 3.2.3 for more details). Due to geometrical constraints around the experimental beam line, the distance of point-like source to the first DSSSD layer was limited to 80 mm. Since the DSSSD's readout electronics cannot provide the trigger signal, it was generated by the PMT sum dynode of the $LaBr_3$:Ce scintillator, which was placed in 35 mm distance behind the last DSSSD layer. Thus, the distance between the trigger detector's front face and the source was fixed to be 165 mm, resulting in $\sim$ 220 cps as accepted count rate.
Figure 6.1.3 [38] and 6.1.4 show the (GEANT4) simulated and the measured energy spectrum of the 4.439 MeV γ rays as detected by the absorbing detector of the LMU Compton camera, respectively. The two additional peaks, below the energy of the 4.439 MeV photopeak, represent the single-escape (SE) and double-escape (DE) peaks. Their higher intensities are not surprising, since the pair creation cross section of the interaction between the incident 4.439 MeV γ ray and the $LaBr_3$:Ce scintillator material is already considerably high (see Fig. 2.1.2). The struc-

ture inbetween the 4.439 MeV photopeak and the single-escape peak belongs to the Compton continuum of the photopeak, which ends at its high energy side at 4.197 MeV, representing the maximum energy transferred by the incident photon to the Compton electron (Compton edge). Similarly, the Compton continuum of the single-escape peak spreads between the single- and double-escape peak, until reaching the Compton edge at 3.688 MeV. The Compton tails of both the photopeak and the single-escape peak are enough to cover the signature of the Compton continuum of the double-escape peak.
The energy resolution of the Compton camera absorbing scintillator was investigated in the range of the targeted prompt-γ energies via the point-like 4.439 MeV source and its single- and double-escape peaks. There, the relative energy resolution of the $LaBr_3$:Ce scintillator was found to vary between 2.4 % and 2.2 %. These values are displayed in Fig. 6.1.5 together with the energy resolution data measured at low γ ray energies using laboratory based calibration sources, in order to visualize the detector energy resolution over the full energy range. This comparison reveals the excellent properties of the $LaBr_3$:Ce scintillator over a wide range of incident photon energies up to 4.439 MeV.
The expected energy response of the six DSSSD layers, representing the scatter components of the Compton camera, to 4.439 MeV monoenergetic γ rays was simulated using the Geant4 simulation toolkit [38], as illustrated in Fig. 6.1.6. The detector geometry of the simulated setup as well as the trigger condition, which was provided by the $LaBr_3$:Ce scintillator, was chosen identical to the one used experimentally. The resulting data shows a sequential increase of the intensity of the energy loss peak observed by each DSSSD layer along the path of the primary photon. Moreover, the structure peaking around 140 keV refers to an energy distribution of Compton electrons originating from different incident photon angles. This distribution starts to be visible from the second DSSSD layer on, as the first Compton interactions take place in the first layer (and neglecting any prior interactions, e.g., in the target material).
Experimentally, the signal processing electronics (GASSIPLEX ASIC) of the DSSSDs requires preparatory measures in order to enhance the performance of the DAQ system. In the absence

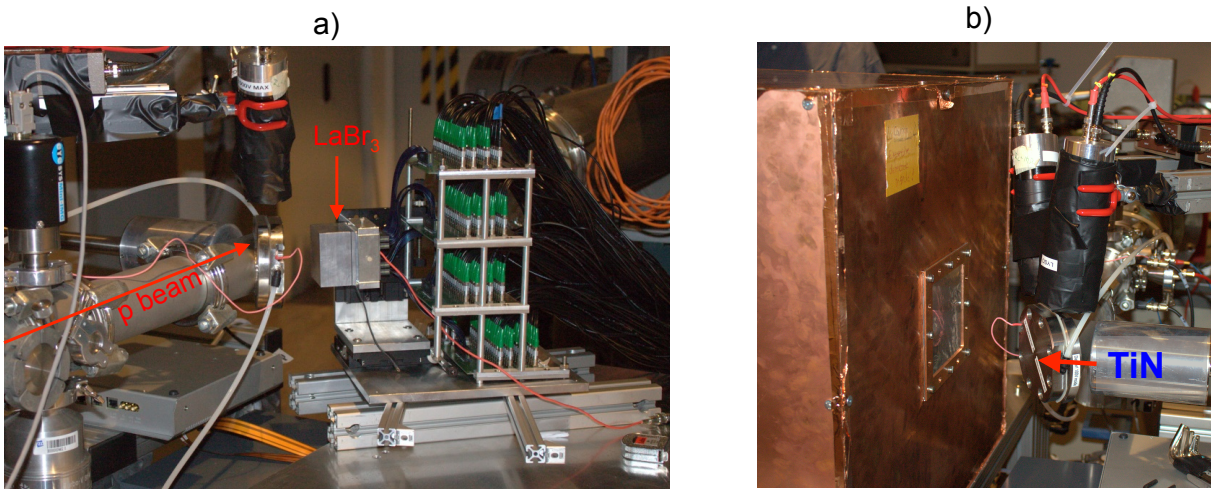

Figure 6.1.2: Photographs of the experimental setup used for the calibration test of the Compton camera components at 4.439 MeV γ-ray energy. The $LaBr_3$:Ce scintillator (panel a) was placed in 42 mm distance from the the tilted stainless-steel flange, behind which the TiN target was attached. In panel b) the full Compton camera setup was exposed to the 4.439 MeV photons. The DSSSD layers had to be enclosed inside a light tight copper plated cubic box, acting also as a Faraday cage. The distance between the point-like source to the first DSSSD layer was set to 80 mm.

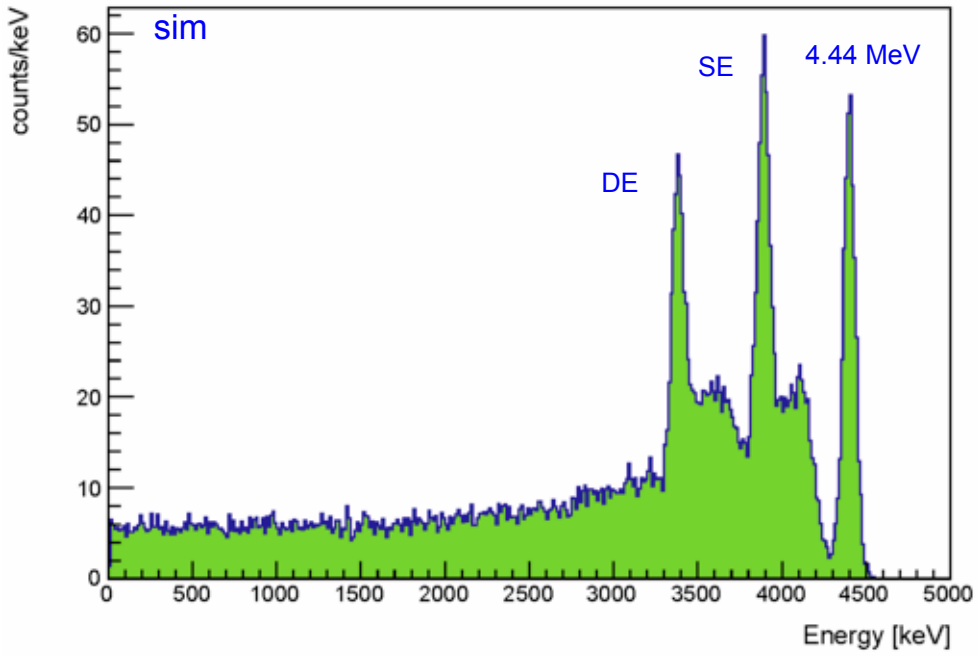

Figure 6.1.3: Simulated energy spectrum of 4.439 MeV γ rays detected by the $LaBr_3$:Ce scintillator, using the Geant4 simulation toolkit [38].

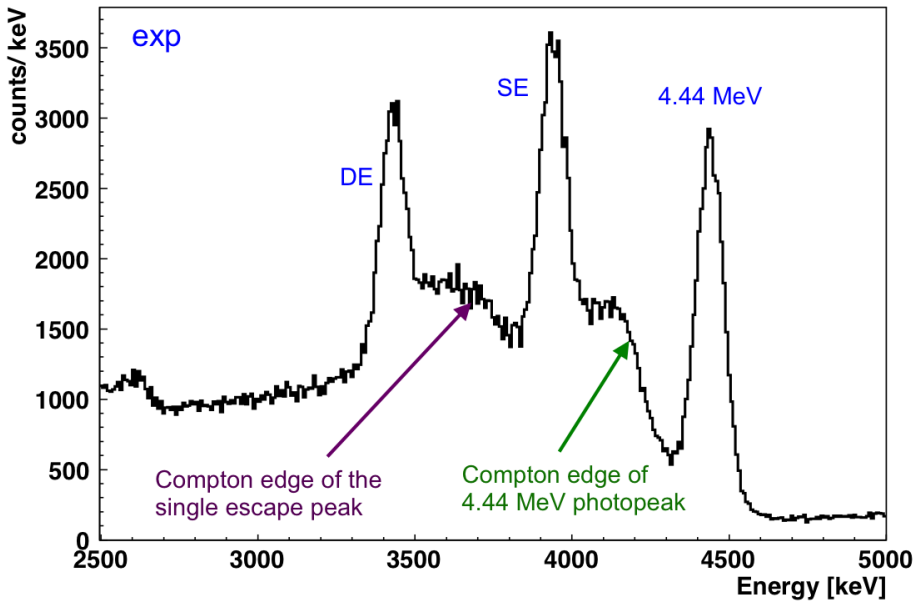

Figure 6.1.4: Energy spectrum of 4.439 MeV γ rays, measured by the $LaBr_3$:Ce scintillator. The two peaks below the photopeak correspond to the single-escape (SE) and double-escape (DE) peaks. Also indicated are the Compton edge positions of the photopeak and SE.

of correlated events between the trigger detector ($LaBr_3$:Ce), which continuously (with about 140 cps) triggers due to its internal radioactivity, and (at least) one strip of all six scatterers, unwanted background data from the integration of the multiplexing amplifier's dark current is registered, forming an energy pedestal peak. This, in fact, not only increases the dead time of the DAQ system due to the long data processing and transfer time, but it also enlarges the output file

size. Therefore, the resulting data, extracted from either p- or n-side strips, had to be corrected for the energy pedestal by applying an online energy threshold. This threshold was determined from a (Gaussian) fit to the pedestal peaks and found to be most effective when chosen as 3σ of the width of the Gaussian fit plus the energy pedestal centroid value. This pedestal correction took place at the FPGA stage of each front-end module (FE), where the decision between true and false events is made. A potential disadvantage of this method is that the online filtered data cannot be recovered later. Therefore, a remaining part of the pedestal peak was intentionally kept in order to avoid any rejection of the low-energy Compton electron signals. Moreover, the centroid values of the energy pedestal peaks were adjusted for all signal processing electronics channels to be located at a digitized baseline value of 100 ADC channels for p-side strips and 600 ADC channels for n-side strips in order to enable analyzing the complete statistics of the detector data without blurring jitter effects. The selection of the digitized baseline value is based on the average of all channel baselines, which are almost constant for the p-side strips electronics, while showing larger fluctuations for the n-side strips.
Figure 6.1.7 shows the energy spectra measured by the n-type strips of the 6 DSSSD layers (128 strips $\times$ 6). The high-intensity energies appearing at the beginning of each layer represent the remaining part of the energy pedestal, as discussed before. It is obvious that the energy deposition of the Compton electrons observed in the simulated data cannot be observed in the spectra of the n-side strips of the scatterers. The reason for this can be attributed to accumulated factors related to the signal processing electronics of the n-side strips (FE). Firstly, despite the ability of the GASSIPLEX's charge sensitive amplifier to process the negative signals resulting from the n-side strips, the amplification gain in this case is a factor of two less compared to the one for a positive signal [81]. The second reason can be related to the modification made to the multiplexing amplifier baseline in order to be able to digitize the negative signal, as discussed in Sect. 3.2.2.2. This adaptation enlarges the dark current level of each channel by more than

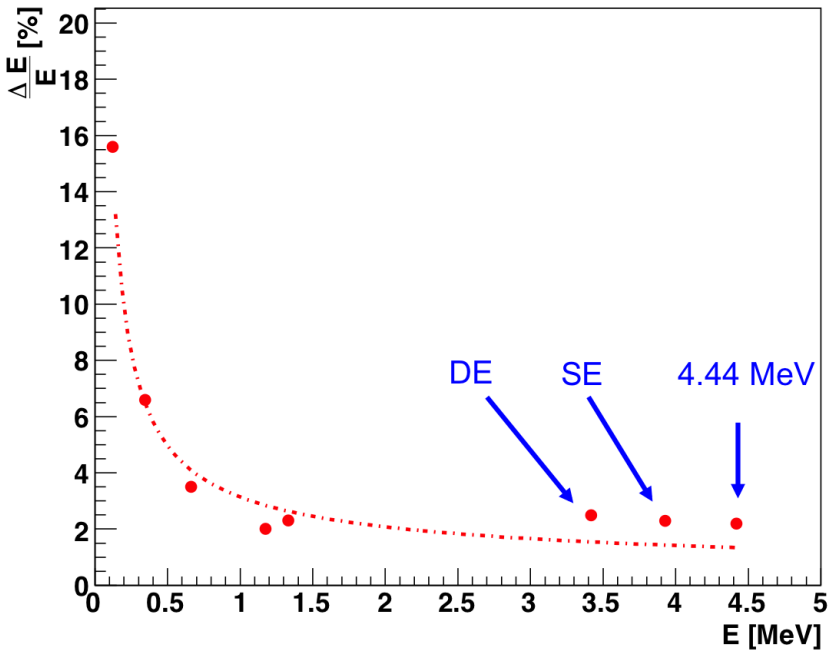

Figure 6.1.5: Relative energy resolution of the $LaBr_3$:Ce scintillator plotted as a function of the incident γ ray energy, ranging from 121 keV to 4.439 MeV. The dotted curve represents a two-parameter function fit as indicated in Eq. (4.1.1).

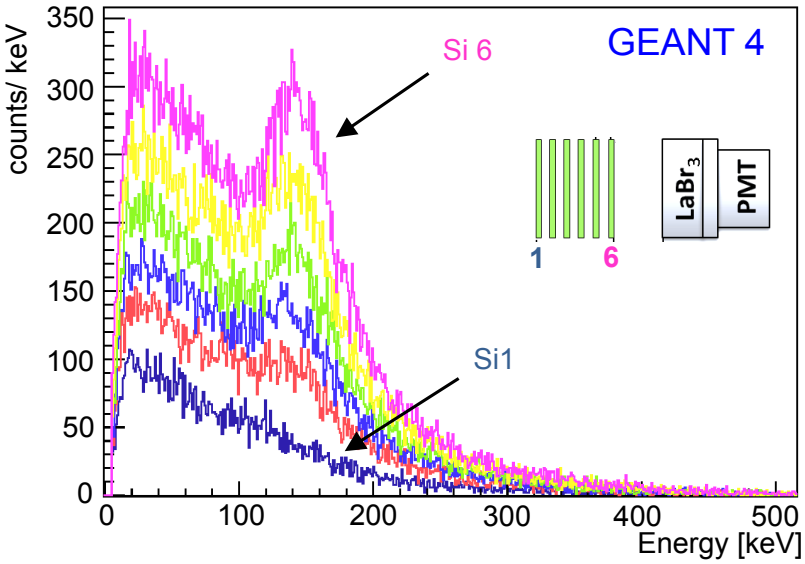

Figure 6.1.6: Geant4 simulation study of the energy loss measured by the DSSSD array for an impinging 4.439 MeV γ ray [38]. The resulting data shows a sequential intensity increase of the energy deposition, caused by the scattered Compton electron, across the DSSSD layers towards the scintillator. It can be noticed that the simulated energy spectrum of the first DSSSD layer shows no electron peak around 140 keV compared to the measured one, displayed in Fig. 6.1.8. This is due to the absence of the massive material (2 cm thick stainless steel provided by the beamline end flange with the target layers as shown in 6.1.1) inbetween the origin of the 4.439 MeV photon and the DSSSD array in the simulated data, which causes the first occurrence of a Compton interaction in front of the first DSSSD layer. Thus, in the simulated data, the accumulation of the Compton electron energy deposit starts only from the second DSSSD layer, continuously increasing until reaching the sixth one, forming an energy loss peak at around 140 keV.

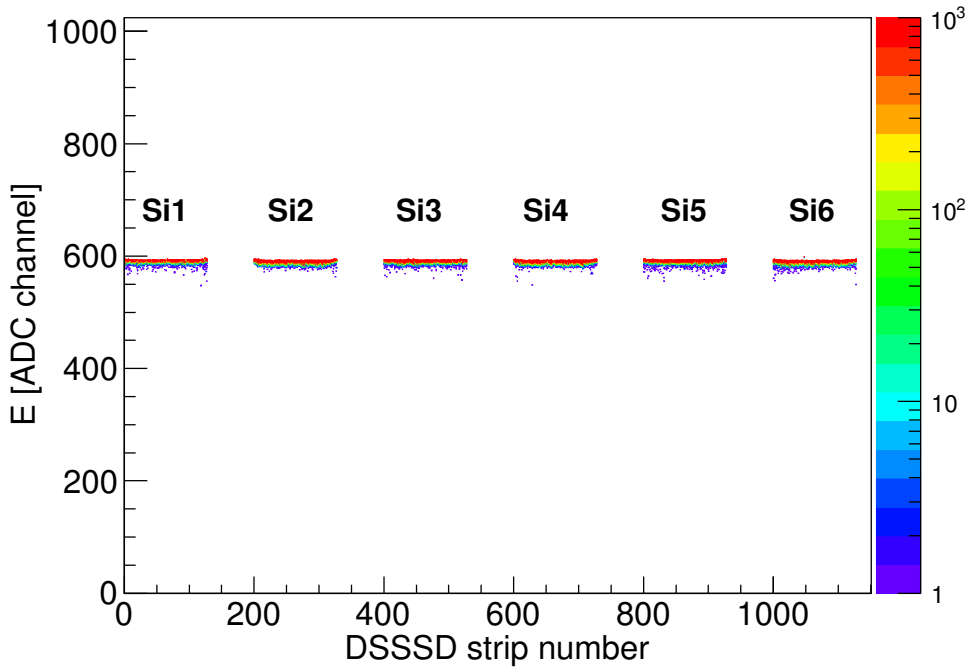

Figure 6.1.7: Energy spectra measured by the 6 $\times$ 128 n-type strips of the six DSSSD layers. Due to the electronics adaptation required to allow for the acceptance of the negative signals in the GASSIPLEX ASIC modules, the dynamic range of the n-side energy spectra ranges from about $\sim$ 600 ADC channels (before energy correction) down to zero (see Sect. 3.2.2.2). The expected energy loss of the Compton electrons appears to be buried by the noise associated with the signal processing electronics (see text for more details).

a factor of two to a width of the energy pedestal peak of $\sigma \sim 7$ ADC channels compared to $\sigma \sim 3$ ADC channels for the p-side electronics. Moreover, since the maximum range of the multiplexing amplifier was set to 2.85 V, which was carefully selected to avoid any saturation (see Sect. 3.2.2.2), the dynamic range of the n-side strips is squeezed to only $\sim$ 600 ADC channels out of the 1024 channels provided by the 10 bit ADC. Thus, the charge deposited by the Compton electrons in a 500 μm thick DSSSD layer cannot be distinguished any more from the energy pedestal peak. This is the major drawback of the readily available DSSSD signal processing electronics that was identified during the characterization studies presented here. Due to the lack of an adequate ASIC-based replacement readout module, this deficit had to be accepted for the time of this thesis work, however, intensive work has been started to evaluate the options for an upgraded replacement of the GASSIPLEX-based FE modules to cure the deficits related to their use.

Nevertheless, the energy deposition of the Compton electrons resulting from 4.439 MeV incident γ-rays can be clearly seen in the energy spectra acquired by the p-type strips of the six DSSSD layers, as illustrated in Fig. 6.1.8. It can be observed from the left panel that the intensity of the energy deposition, indicated by a light blue color in the region between the two dashed lines, gradually increases from layer one to layer six. This feature can be emphasized by projecting the highlighted area onto the energy axis, as indicated in the right panel and can readily be explained by the accumulation of energy deposits by Compton-scattered electrons along the path of the electrons, which are typically carrying enough energy to traverse several or even all of the six DSSSD layers. This agrees very well with what is observed in the simulated data

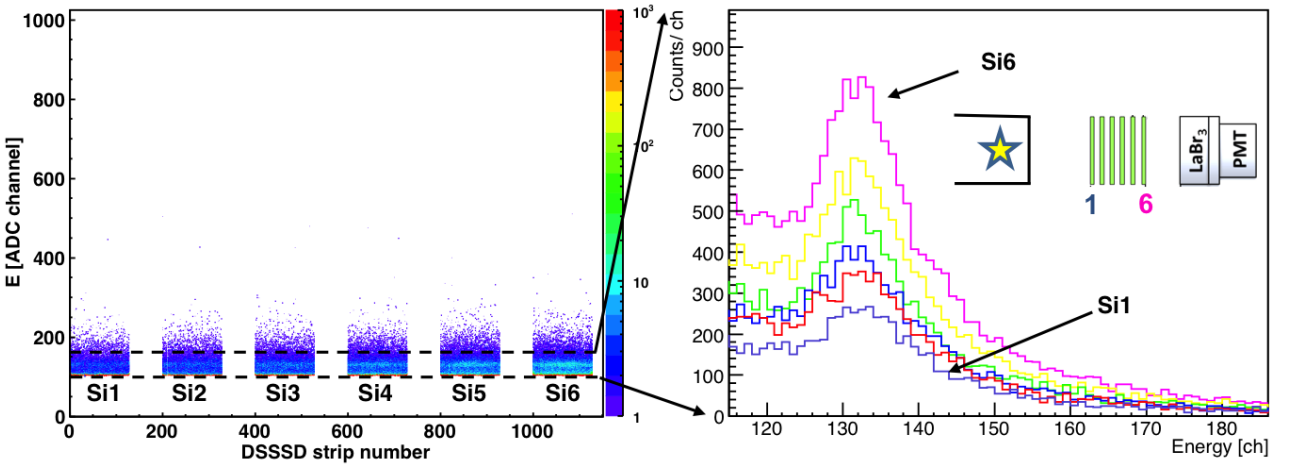

Figure 6.1.8: Energy deposition spectra of the DSSSD array resulting from the irradiation with 4.439 MeV γ rays. The data represent the digitized energies of the p-type strips of detector 1 to detector 6 (6 $\times$ 128 channels). The projection of the highlighted area (between the dashed lines) onto the energy axis emphasizes the sequential intensity increase of the energy deposition of the scattered Compton electrons along the primary photon path. Since the 4.439 MeV γ ray was generated by a nuclear reaction between a low energy proton beam and a TiN target taking place inside the evacuated beam line, a high chance of Compton scattering interaction occurring in front of the DSSSD array can be expected, creating a signature of energy deposition of the Compton electron already in the first detector (in contrast to Fig. 6.1.6, where the simulated geometry contained no material between the photon source and the first DSSSD layer).

presented in Fig. 6.1.6. However, the simulated data sees no Compton electron-related peak in the first layer, whereas it is clearly visible in the measured spectrum. Since the production of 4.439 MeV monoenergetic γ-rays took place inside the vacuum beam line behind a 2 cm thick stainless-steel flange (see Fig. 6.1.1), Compton interactions will already be induced in this massive material, resulting in the Compton electron energy signature to be visible already in the first layer. This feature was not considered in the early simulation design geometry.
The measured energy distribution of the Compton electrons, calculated to peak at about 120-130 keV, fortunately appeared already at room temperature above, yet close to the energy pedestal peak position. In comparison to the situation for the n-side strips, this fact can explain the absence of the Compton electron peaks in the n-type spectra, since here the amplifier gain was intrinsically reduced by a factor of two compared to the one of the p-type strips, thus preventing the low-energy Compton electron signal to exceed the low-energy background.

6.2 Prompt γ ray energy measurement with a 20 MeV proton beam

At the MLL Tandem accelerator in Garching, which is capable of providing a 20 MeV proton beam, the Compton camera absorbing detector was examined in the prompt γ-ray energy range relevant for beam interactions in particle therapy. Figure 6.2.1 shows the experimental setup of this measurement. The $LaBr_3$:Ce detector was placed at 90^o with respect to the beam line (b) inside a Faraday cage (a), providing a light tight and electrical shielding for the Compton camera scatter components. The 20 MeV proton beam (with a typical beam current of 1-2 nA, equivalent to 0.6 - 1.2 $\times$ 10^{10} protons per second) left the beam line through a 30 μm thick

Kapton window and hit a water target (c) filled into a Plexiglass cylinder (30 mm long and 30 mm in diameter). The irradiated side of the water phantom was made of a 30 μm thick Kapton foil, in order to minimize the energy loss of the proton beam (with a stopping range in water of about 4 mm). A block diagram of the signal processing electronics used in this experiment to read out the monolithic $LaBr_3$:Ce scintillator is shown in Fig. 3.2.13.

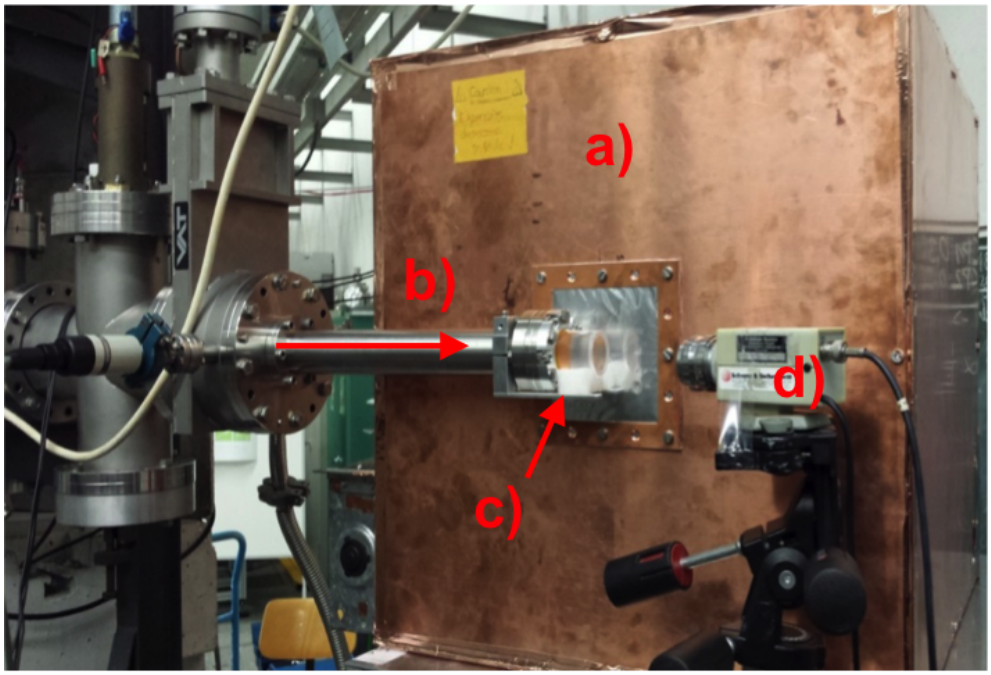

Figure 6.2.1: Experimental setup used to evaluate the performance of the $LaBr_3$:Ce scintillator with prompt γ rays, generated by inelastic nuclear reactions between a 20 MeV proton beam and a water target. The detector was kept inside a Faraday cage (a), which was positioned under 90^o with respect to the proton beam line (b) and the cylindrical water phantom (c). Marked with d) is a digital camera, used to record the beam spot visible in a CsI crystal attached to the beam line exit during the beam tuning process.

The energy response of the $LaBr_3$:Ce scintillator to the resulting prompt γ rays induced by nuclear reactions between the 20 MeV proton beam and the water target was simulated, using Geant4, and experimentally measured, as indicated in Fig. 6.2.2 (top) and (bottom), respectively. In both spectra, the prominently observed energy peaks can be attributed to the prompt γ emission during the deexcitation of excited ^{12}C and ^{16}O nuclei. 20 MeV proton energy is sufficient to excite ^{16}O to the first 1^-, 2^+ and 3^- excited states, which subsequently decay to the ground state via γ-ray emission of 7.116 MeV, 6.917 MeV and 6.129 MeV, respectively, since their respective (p, p$'$) reaction channels open between 8 MeV and 9 MeV of proton energy [113]. These prompt γ-ray lines are labeled in the energy spectra by color-coded arrows. As the pair creation cross section in this γ-ray energy range in the $LaBr_3$:Ce scintillator material is already sizeable (see Fig. 2.1.2), single- and double-escape (SE and DE) peaks can be seen in the simulated and measured energy spectra as a signature of this interaction process. The double-escape peaks of 7.116 MeV (DE = 6.094 MeV) and 6.917 MeV (DE = 5.895 MeV) are hidden under the 6.129 MeV photopeak and its Compton edge (5.881 MeV), respectively. Comparing the prompt γ-ray intensity of ^{16}O(p,p$'\gamma$) reactions, the 6.129 MeV energy peak dominates due to the high cross section of the ^{16}O(p, p$'$ $\gamma_{6.129MeV}$)^{16}O* reaction at 20 MeV proton beam energy [113]. Due to inelastic reactions of the impinging proton beam with the Kapton windows of the beam line and the water target (and as well of some beam halo reacting with steel com-

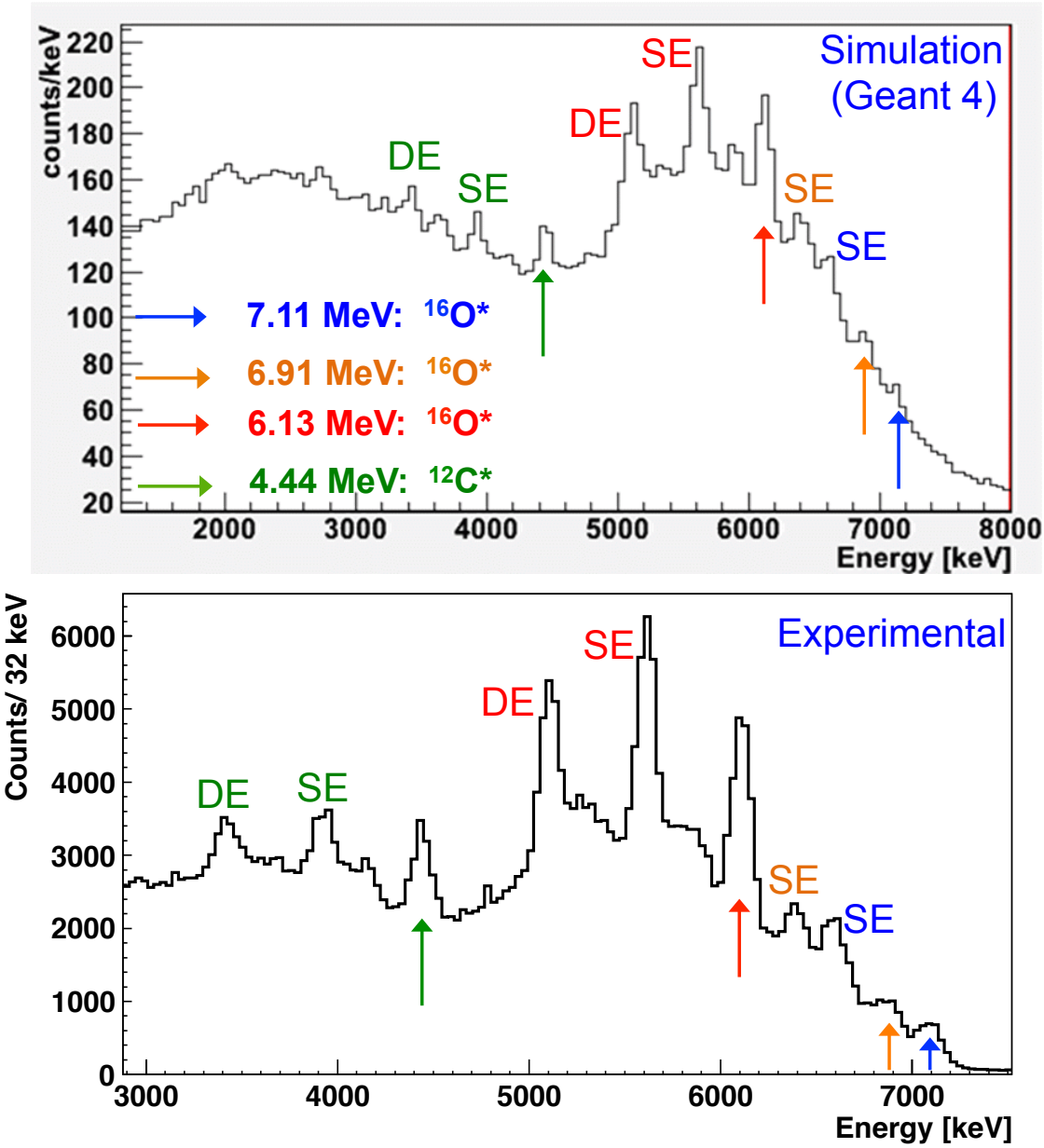

Figure 6.2.2: Simulated [38] (top) and measured (bottom) prompt γ ray energy spectrum of the $LaBr_3$:Ce scintillator, induced by exposing a water target to a 20 MeV proton beam. In both panels, the photopeak energy of the prompt γ-ray emissions followed the deexcitation process of the excited $^{16}O^*$ (blue, brown and red arrow) and $^{12}C^*$ (green arrow) are clearly labeled with their respective single- and double-escape peaks.

ponents of the beam line and flange), the measured energy spectrum features a much stronger component from the deexctiation of the first excited state of ^{12}C via the $^{12}C(p, p^{'} \gamma_{4.439MeV})^{12}C$ reaction, with its energy threshold located at 4 MeV proton energy [113]. The 4.439 MeV prompt γ transition with its respective single- and double-escape peaks may be mixed with the same γ-ray energy resulting from the nuclear fragmentation of $^{16}O(p, x \gamma_{4.439MeV})^{12}C$, which is energetically allowed above 10 MeV proton energy. From these assignments, it can be stated that the simulated energy response of the $LaBr_3$ scintillator to the prompt γ rays, resulting from a 20 MeV proton beam impinging into a water, can be validated experimentally.

6.3 Prompt γ ray energy and ToF measurement with a 20 MeV deuteron beam

Aiming to exploit the superior timing properties of the $LaBr_3$:Ce scintillator to suppress the neutron background induced during the particle beam irradiation, the signal processing electronics of the LMU Compton camera was equipped with Time-to-Digital converter modules (MTDC-32, Mesytec [96]). In order to test these newly integrated electronics, an experiment was conducted at the MLL Tandem accelerator in Garching using a pulsed 20 MeV deuteron beam. The use of this particle beam instead of a proton beam was decided to take advantage of the high emission rate of neutrons following deuteron dissociation as they collide with the target.

The experimental setup used during the time-of-flight measurement is illustrated in Fig. 6.3.1. The $LaBr_3$:Ce scintillator was positioned on a support stand (see Sect. 3.2.3) adjusted to set the detector's central height on the same level as the beamline axis. The scintillator was placed under 30^o with respect to the deuteron beam path and in a distance of 200 cm from the irradiated cylindrical water phantom, described in Sect. 6.2. Three water containers were placed in the deuteron beam direction behind the water phantom in order to moderate the emitted fast neutrons, thus protecting the scintillator from detecting the neutrons backscattering from the nearby massive concrete wall of the experimental hall.

The MLL Tandem accelerator is capable of providing 5 MHz pulsed beams, i.e. with a period of 200 ns between two consecutive pulses. However, for the case of this experiment, every second pulse of the deuteron beam was removed by a beam chopper system to realize a longer time period of 400 ns between beam bunches, which helps to avoid any spectral mixing between slow neutrons of a first pulse and prompt γ rays or fast neutrons from the next one. The radio frequency (RF) signal of the accelerator pulsing system was used as Common Stop signal for the timing measurement, while the start signal, as well as the trigger of the DAQ system, was derived from the PMT sum dynode of the $LaBr_3$:Ce scintillator. The time interval between the start and stop signals was digitized by the TDC with a resolution of 7.8 ps per channel, while its range was set to 500 ns in order to be able to cover a full time-of-flight cycle of the 400 ns pulsed beam.

The measured time-of-flight spectra, indicated in panel a) of Fig. 6.3.2, show a clear separation between the prompt γ rays and the slower neutrons. The shape of the prompt peak reflects the pulse structure of the deuteron beam, which is strongly influenced by the fine tuning and optimization of the pulsing system. Additional contribution to the width of the prompt peak could come from the transit time of the prompt γ rays, which varies depending on the primary reaction position. Thus, the width of this peak does not reflect the time resolution of the $LaBr_3$:Ce scintillator, discussed in Chap. 4. It can be also noticed in Fig. 6.3.2 a) that the prompt peak has an extended delayed tail on the falling edge region. This tail can be investigated by plotting the correlation between the TOF and energy signals registered in the $LaBr_3$:Ce scintillator, as shown in Fig. 6.3.3. Suppressing the neutrons related background contributes to visualize the prompt γ rays in the energy region above 3 MeV. However, in the low-energy region of Fig. 6.3.3, e.g. below 600 keV, the separation of the fast and slow components will be blurred due to the contribution of the continuously emitted 511 keV γ rays and their corresponding Compton continum during the annihilation process of the online generated short-lived isotopes, such as ^{15}O ($t_{1/2}$ = 2.04 min) and ^{11}C ($t_{1/2}$ = 20.39 min). This, in fact, explains the delayed tail on the falling edge of the prompt peak of Fig. 6.3.2 a). By setting an energy gate between 1.5 MeV and 7 MeV, the delayed shoulder is reduced and the prompt peak is completely separated from

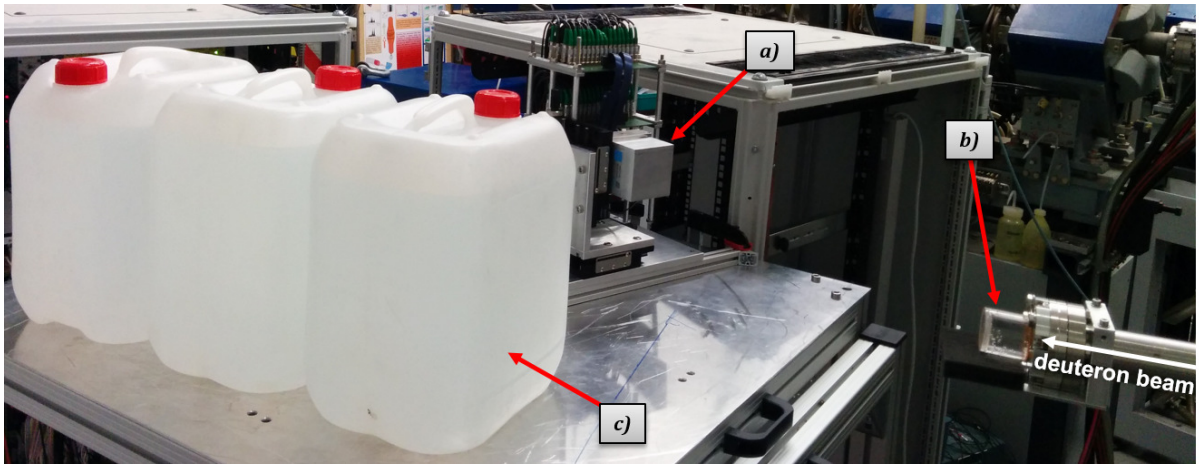

A)

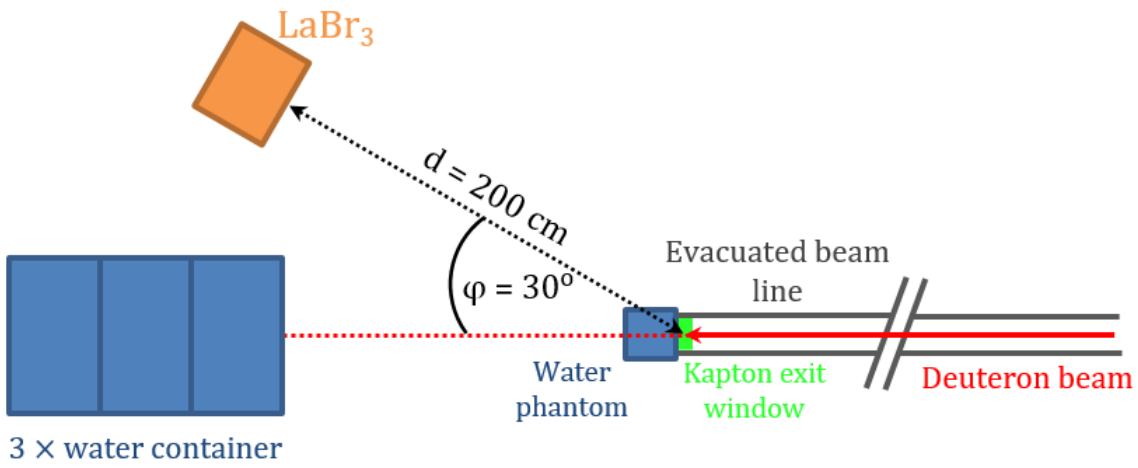

B)

Figure 6.3.1: A photograph (A) and illustrative sketch (B) of the experimental setup used during the time-of-flight measurement, aimed to test the newly integrated TDC modules into the signal processing electronics of the Compton camera absorbing detector, as used at the MLL Tandem accelerator in Garching. The $LaBr_3$:Ce scintillator (a) was placed under 30^o with respect to the beam line and in 200 cm distance from the cylindrical water phantom (b). It was mounted directly in front of the beam exit window, made of a 30 μm Kapton foil, through which the deuteron beam left the vacuum. Three water containers (c) were positioned in the same direction as the deuteron beam path in order to moderate the fast neutrons and prevent them from back-scattering off the nearby massive concrete wall.

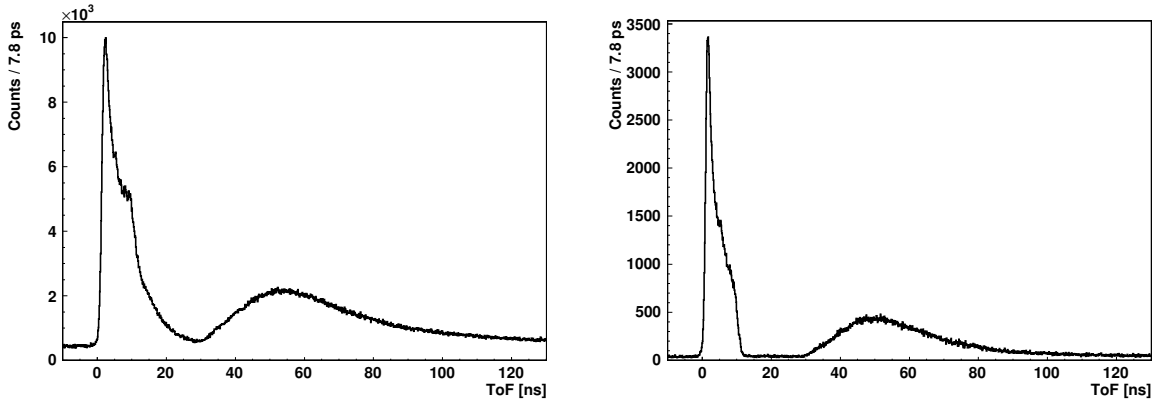

(a) (b)

Figure 6.3.2: Time-of-flight spectra measured with a 20 MeV pulsed deuteron beam, using a $LaBr_3$:Ce scintillator placed at a distance of 200 cm from the beam exit. Panel a) indicates the case, where all energy events were recorded in the scintillator, while an energy window between 1.5 MeV and 7 MeV was applied for the case shown in panel b). It is obvious from panel a) that low energy photons, such as 511 keV, contribute to the prolonged falling shoulder of the prompt peak (see also Fig. 6.3.3).

the slow component, as indicated in panel b) of Fig. 6.3.2.
Figure 6.3.2 a) also shows a neutron component with a time-of-flight peaking at about 50 ns. This nicely reflects the flight time of the fastest neutrons with the full beam velocity, recoiling from an inelastic proton collision. In fact, this can be verified using the following formula [114]:

$$\beta = 0.04635 \cdot \sqrt{\frac{E[MeV]}{A}} \tag{6.3.1}$$

where $\beta = \frac{v}{c}$ represents the particle velocity in units of the speed of light c, E is the particle beam energy, while A represents the mass number of the particle, thus 2 for deuterons. The parameter β amounts to 0.145 for E = 20 MeV, which then equals to a velocity of 4.35 cm/ ns. Since the $LaBr_3$:Ce scintillator was placed at a distance of 200 cm from the beam exit (see Fig. 6.3.1), the time required for the fastest neutrons to reach the detector is 46 ns, which pretty well agrees with the measured value.
As already shown in Fig. 6.3.3, the energy of all signals registered in the $LaBr_3$:Ce scintillator is registered based on their arrival time. By applying a proper timing window on the TOF axis and projecting onto the energy axis, the measured energy spectrum can be disentangled into its prompt and delayed components, as illustrated in Fig. 6.3.4. In the absence of the TOF condition (black curve), most of the promptly emitted γ rays are buried by the neutron background, except for the 6.126 MeV line, emitted during the deexcitation of the excited 3^- state of $^{16}O^*$ nuclei to the ground state, together with its corresponding single- and double-escape peaks. The energy spectrum of the delayed component (red curve) features a continuum of neutron energies and a prominent γ line at 2.2 MeV with its single escape peak, representing the deuteron binding energy emitted during the neutron capture reaction $^1H(n,\gamma)^2H$. Having subtracted the contribution of the delayed component from the full energy spectrum, several prompt γ-ray lines start to be visible in the resulting prompt γ-ray spectrum (green curve). The γ peaks at 1.64 MeV and 2.31 MeV illustrate the (1^+, $^oO^+$, 1^+) cascade decay of excited ^{14}N from the second 1^+ state to the ground state. From this excited state, 4% of the excited $^{14}N^*$ nuclei decay directly to the ground state via an (E2 + M1) transition with an emission of 3.95

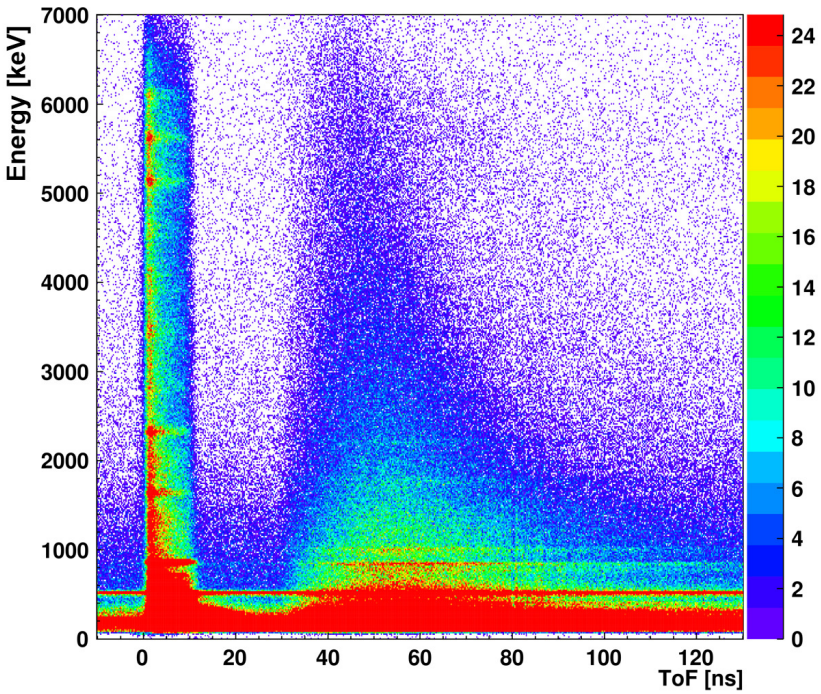

Figure 6.3.3: Correlation plot between the time-of-flight and energy signals registered in the $LaBr_3$:Ce scintillator from the interaction of a water target with a pulsed 20 MeV deuteron beam. Suppressing the slow component (neutrons) allows to visualize also low intensity prompt γ rays, especially above 1.5 MeV (see Fig. 6.3.4).

MeV γ rays, while the dominant decay branch proceeds via an M1 cascade of 1.64 MeV and 2.31 MeV to the ground state. Probably due to a tighter focusing of the deuteron beam with less interactions with beamline steel components, prompt γ rays from the 2_1^+ (^{12}C, 4.44 MeV) transition can be barely seen. The most prominent prompt γ transition above 3 MeV originates from the first excited 3^- state of ^{16}O at 6.13 MeV, visible in the time-filtered spectrum with its single- and double-escape peaks.

6.4 Compton camera commissioning with a therapeutic proton beam at the OncoRay facility (Dresden)

The first test of the LMU Compton camera prototype at a clinical proton beam was performed at the cyclotron of the OncoRay facility in Dresden (National Center for Radiation Research in Oncology and Universtäts Protonen Therapie Dresden [31]). Although this recently opened facility, which started treating patients in December 2014, is dedicated for cancer treatment, the proton beam can be sent to an experimental room, where the Compton camera was prepared to receive the beam in parallel to the patient treatment during the interrupts needed to position a patient (in practice, beam was periodically available typically for about 20 minutes during patient positioning after 2 minutes of treatment time).
The experimental setup used in this beam time is shown in Fig. 6.4.1. The Compton camera

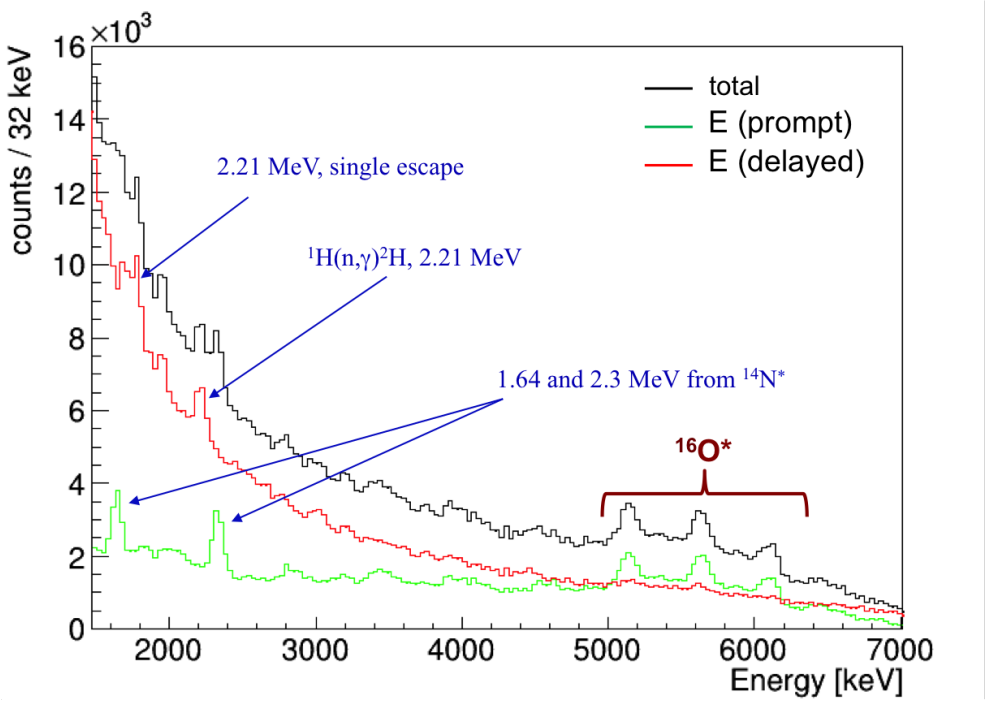

Figure 6.3.4: The complete γ-ray energy spectrum (black curve) of secondary radiation emitted during the interaction between a 20 MeV pulsed deuteron beam and a water target, measured by a $LaBr_3$:Ce scintillator. The use of the TOF technique enables to separate this spectrum into a delayed component (red curve) and prompt γ rays (green curve). The photopeak at 2.2 MeV and its corresponding single-escape peak in the delayed energy spectrum represent the deuteron binding energy, released during the neutron capture reaction $^1H(n,\gamma)^2H$. Eliminating the neutron background allows to recover the prompt γ peaks of 1.64 MeV and 2.31 MeV that are emitted during the cascaded decay of excited $^{14}N^*$ nuclei to the ground state. The high energy part of the spectrum is dominated by the prompt γ rays emitted from the deexcitation of the excited 3^- state in ^{16}O.

components were enclosed inside a copper-plated light-tight box, in order to prevent the silicon detector array (scatterers) from saturation resulting from light exposure. Moreover, this cage acted as a Faraday cage against external electric noise that might affect the readout electronics. The Compton camera box was positioned under 90^o relative to the beam axis and in 480 mm distance from the side surface of the cubic water phantom. This phantom, which is made of 5 mm thick Plexiglass plates, has an inner dimension of $400 \times 310 \times 200$ mm^3. It was placed in 510 mm distance from the beam exit. The center of the Compton camera entrance window was positioned perpendicularly to look at the calculated Bragg peak position of the proton beam, which varies depending on the proton energy and the type of the phantom material. In this experiment, 100 MeV, 160 MeV and 225 MeV proton beam energies with an average current of 200 pA, measured at the beam nozzle, were used to irradiate the water phantom for an effective measurement time of 3 h, 4.8 h and 6.5 h, respectively. Then, the water phantom was substituted with a PolyMethyl MethAcrylate (PMMA, $C_5H_8O_2$) phantom, formed by 10 slabs of various thicknesses (1×200 mm, 6×30 mm, 1×10 mm and 2×5 mm, in total 400 mm). They were arranged such that the thicker slabs were placed towards the beam exit. This phantom was irradiated by 100 MeV, 160 MeV and 225 MeV proton beams for about 1.5 h, 1.6 h and 1.3 h, respectively. In this described geometry of the Compton camera with respect to both water and PMMA phantoms, the triggering ($LaBr_3$:Ce) detector accepted an average rate of 1200 cps, which resulted in an average dead time of 75%.

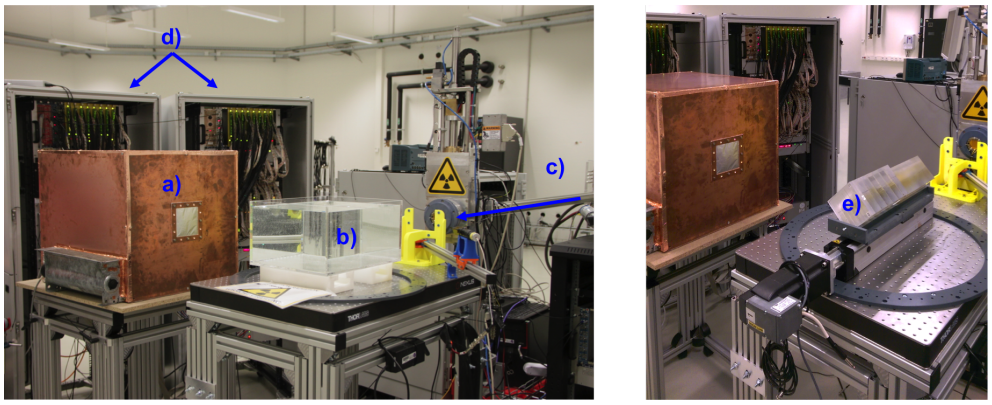

Figure 6.4.1: The experimental setup of the Compton camera's first test at the therapeutic proton beam of the OncoRay facility in Dresden. Left: the camera components, placed inside a light tight Faraday cage (a), are positioned in 480 mm distance from the irradiated water phantom (b) and under 90^o with respect to the proton beam (c) axis. The signal processing electronics (d), which is divided into two racks as discussed in Sect. 3.2.2.3, is located behind the camera cage. After finishing the water irradiation measurements, the phantom was replaced by a PMMA target (e) formed by 10 slabs of various thicknesses (in total 400 mm).

The block diagram of the DAQ system used in this experiment is shown in Fig. 3.2.17, where the signal processing electronics was distributed over two racks (see Sect. 3.2.2.3). The trigger signal was provided by the sum dynode of the H9500 PMT coupled to the $LaBr_3$:Ce scintillator. This signal was also used as a trigger for the scatter detectors, since their readout electronics, which was based on the GASSIPLEX ASIC, could not provide an external trigger. Based on that, the resulting data of the triggering $LaBr_3$:Ce scintillator will be presented first in the following section.

6.4.1 Absorbing component: $LaBr_3$:Ce scintillator

6.4.1.1 Time-of-flight (TOF) measurement

The IBA C230 isochronous cyclotron (Ion Beam Application SA, Louvain-la-Neuve, Belgium [115]), representing the backbone of the OncoRay proton therapy facility, operates at a radio frequency of 106 MHz, corresponding to a 9.4 ns time period between two consecutive beam bunches. This RF signal was used as stop signal for the time-of-flight (ToF) measurement, while the start signal was provided by the sum dynode of the H9500 PMT coupled to the $LaBr_3$:Ce scintillator.
Figure 6.4.2 shows the energy versus time-of-flight spectra for different energy ranges measured by the $LaBr_3$:Ce scintillator during the irradiation of a water phantom with 225 MeV protons. 13 beam pulses separated by 9.4 ns were accepted by the time digitizer (TDC) due to its time range of 130 ns. The full 2D energy-ToF spectrum (panel a) was split into low energy (0 - 3 MeV, panel b) and high energy (3 MeV - 7 MeV, panel c) regions, in order to illustrate the contribution of the delayed neutron-induced background, which is considerably reduced in the high-energy region, which is relevant for prompt-γ medical imaging. In the low-energy range, the two horizontal lines visible at 511 keV and 2.2 MeV represent the annihilation photons, produced during positron annihilation processes, and the deuteron binding energy, released as γ rays during the neutron capture on hydrogen (^{1}H(n,γ)^{2}H), respectively. In order to investigate the impact of these radiation components on the ToF pulse width, panels b) and c) of Fig. 6.4.2 were projected onto their timing axis as illustrated in panel a) and b) of Fig. 6.4.3, respectively.

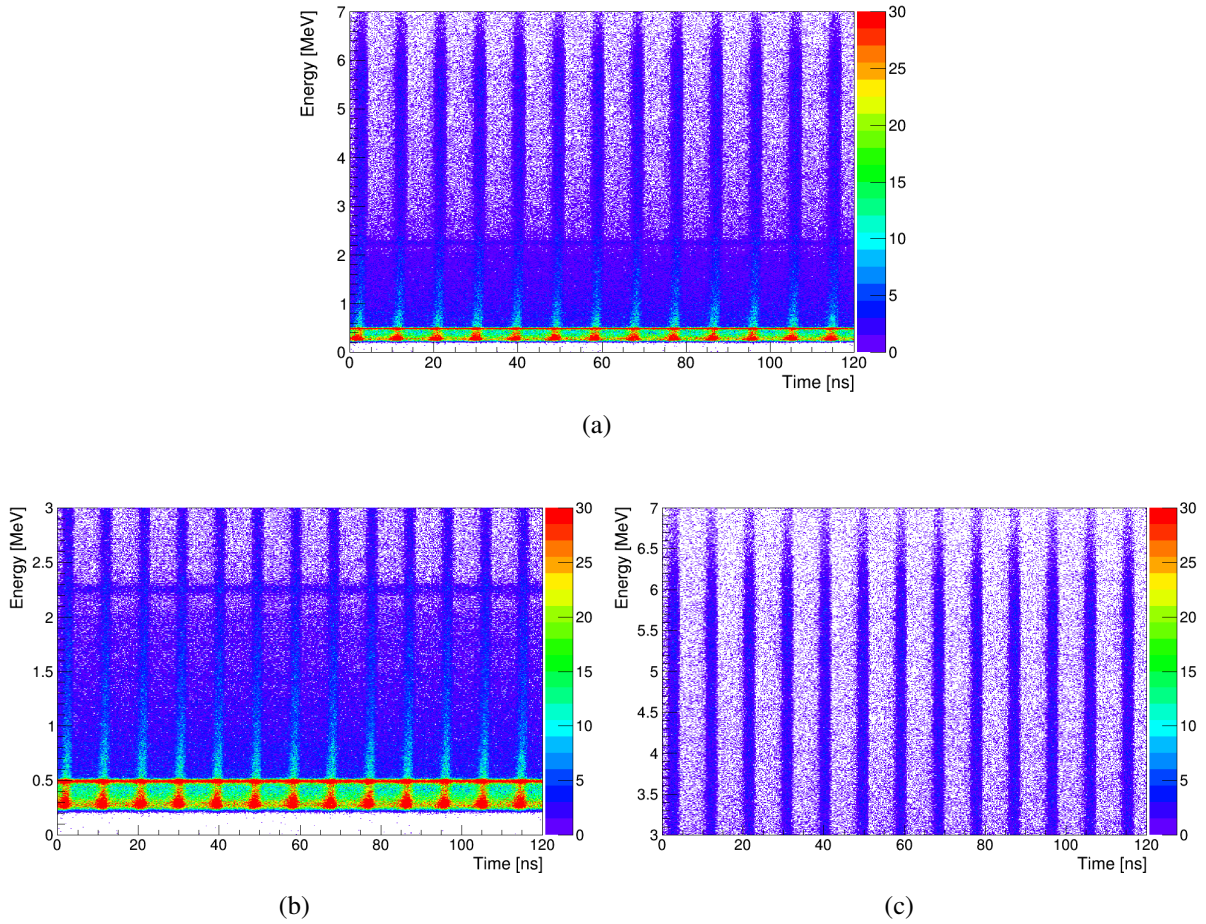

Figure 6.4.2: Total 2D energy-time-of-flight spectrum (panel a) of the $LaBr_3$:Ce scintillator, measured during the interaction between a 225 MeV proton beam with a water phantom. Panel b) and c) show the same data for low-energy region 0-3 MeV (b) and the high-energy region 3-7 MeV (c), the latter being relevant for the prompt-γ energy technique.

For the low energy case (panel a), the FWHM of a Gaussian fit to the prompt peaks of the ToF spectrum was found to be 2.20 $\pm$ 0.05 ns, whereas it turned out to slightly improve with 1.9 $\pm$ 0.03 ns for the prompt ToF pulse indicated in panel b). 2.2 ns represents as well the width of the ToF pulses in the absence of any energy condition, a trivial consequence of the fact that the overall width of the ToF peaks is dominated by the larger statistics in the energy range below 3 MeV, consisting to the strong delayed component and prompt transitions with low energies (0.5 MeV, 2.2 MeV). However, the width of the ToF peak does not reflect the time resolution of the $LaBr_3$:Ce scintillator (see Sect. 4.2), but it rather reflects the pulse structure of the accelerator. However, since the ToF peaks were formed by many γ rays emitted from different interaction positions along the proton beam path in the water phantom, the transit time of these γ rays contributes to the width of the measured prompt peaks. This was investigated by introducing a 7 cm collimation slit formed by 10 cm thick lead blocks positioned symmetrically around the line sight from the center of the Compton camera to the Bragg peak position at an angle of 90 ^{o} to the proton beam trajectory, as indicated in Fig. 6.4.4. The proton beam energy was kept the constant in order to avoid any time spread introduced to the proton bunches by the energy selection system of the accelerator. The resulting data, indicated in Tab. 6.1, reveal an improvement of about 25 % in the ToF peak width in the presence of the 7 cm slit collimation for the events with photon energies below 3 MeV. This improvement increases to about 40 %

Slit collimation [cm]	prompt ToF $<$ 3 MeV (FWHM)	prompt ToF $>$ 3 MeV (FWHM)
none	2.20 $\pm$ 0.05 ns	1.9 $\pm$ 0.03 ns
7	1.64 $\pm$ 0.06 ns	1.12 $\pm$ 0.02 ns

Table 6.1: Energy dependence of the ToF pulse width measured between the $LaBr_3$:Ce scintillator signal and the accelerator RF signal in the presence and absence of a 7 cm slit collimation around the perpendicular line-of-sight to the Bragg peak area in the water phantom, irradiated by 225 MeV protons.

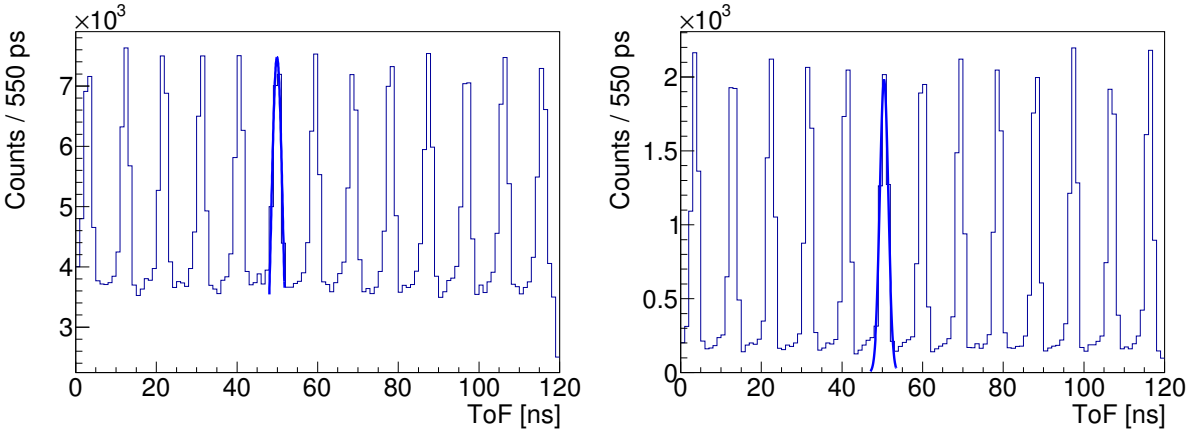

(a) (b)

Figure 6.4.3: Time-of-flight (ToF) spectra measured in a common start mode between the PMT sum dynode signal of the $LaBr_3$ scintillator (clock start) and the accelerator RF signal (clock stop) during the irradiation of the water phantom with a 225 MeV proton pulsed beam. The timing events whose energy below (panel a) and above (panel b) 3 MeV were plotted in order to investigate the impact of the later-arriving neutron-induced background on the time structure of the prompt γ emission.

in the prompt γ-ray energy region (3-7 MeV), where the FWHM is reduced from 1.9 $\pm$ 0.03 ns to 1.12 $\pm$ 0.02 ns. This value is only slightly different than 1.2 ns (FWHM) measured by [116], where a cylindrical $LaBr_3$:Ce scintillator (with a diameter and length of 76 mm) was exposed to the prompt γ rays through a $\sim$ 5 mm slit collimator opening placed under 90^o with respect to the 180 MeV proton beam path in the water phantom. This small difference may be due to the different proton beam energy, since the energy selection system of the accelerator affects the proton velocities which leads to a temporal broadening of the proton bunch with decreasing energy. As systematically reported in [116], the respective prompt time peak widths of the induced prompt γ-rays during the irradiation of a water phantom with proton beam energies of 120 MeV and 150 MeV are 2.9 ns (FWHM) and 1.9 ns (FWHM).

6.4.1.2 Prompt γ-ray energy measurements: water and PMMA phantoms

The energy spectra of the γ rays emitted during the irradiation of the water and PMMA phantoms with proton beams of 100 MeV, 160 MeV and 225 MeV were measured by the $LaBr_3$:Ce scintillator. During the effective data analysis, a time window of 2 ns was set around each of the 13 prompt peaks, shown in Fig. 6.4.2, in order to separate the delayed component from the prompt γ rays. This separation is clearly visible in Fig. 6.4.5 for the water (panel a) and PMMA (panel b) phantoms irradiated by 225 MeV protons. The delayed neutron-induced background

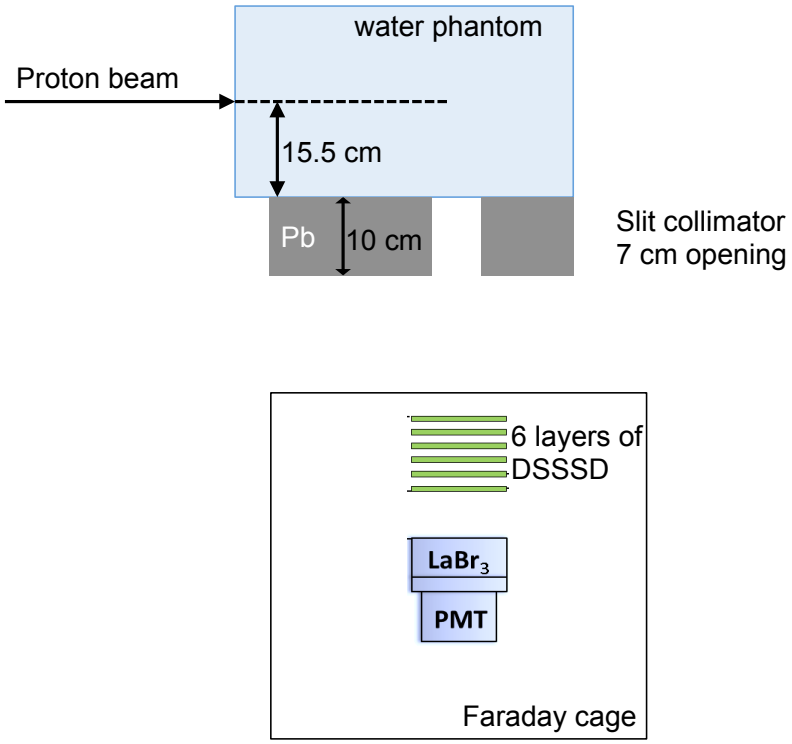

Figure 6.4.4: Experimental setup used to evaluate the impact of the γ-ray transit time from the varies emission points along the proton beam trajectory on the prompt γ-ray time structure. A slit collimator opening of 7 cm was introduced by a 10 cm thick Pb shielding in order to allow for the registration of only those prompt γ rays emitted along the 225 MeV proton beam path in the vicinity of the Bragg peak.

spectrum (red curve) shows a structureless distribution over a wide energy range besides the discrete γ line at 2.2 MeV, which is emitted as the deuteron binding energy during the process of neutron capture by a proton. This peak strongly appears together with its corresponding Compton edge and single-escape peak for the case of the water phantom. This is perhaps due to the less complex composition of water (H_2O) compared to the PMMA ($C_5H_8O_2$), which eases the break-up processes and in turn increases the amount of available protons in the case of the water phantom. As related to the phantom composition, the production intensity of prompt γ rays from particular excited nuclei obviously strongly depends on their intial concentration in the irradiated target material [117]. This can be observed when comparing the prompt γ spectra (green curve) of the irradiated water and PMMA phantoms presented in Fig. 6.4.5. For the water target case, the (high-energy) component of the prompt γ ray spectrum is dominated by the 6.129 MeV transition (plus its single- and double-escape peaks) emitted from the ground-state deexcitation of the 3^- state of $^{16}O^*$. In this target scenario, 4.4 MeV photons from excited ^{12}C nuclei can only be generated following a fragmentation reaction of ^{16}O. In contrast, since the PMMA phantom exhibits an inherently high carbon concentration, the main component of the prompt γ ray spectrum is 4.439 MeV emitted during the deexcitation of the $^{12}C^*$ from inelastic (p,p$'\gamma$) collisions. These features can consistently be observed when irradiating both phantoms with different proton energies, as indicated in Fig. 6.4.6. Besides the predominant prompt γ rays emitted from $^{16}O^*$ and $^{12}C^*$, some other prompt γ lines are clearly visible and identified for the case of the 160 MeV proton beam in the middle row of Fig. 6.4.6.

Comparing the 6.13 MeV prompt γ line emitted from ^{16}O(p, p$'$ $\gamma_{6.129MeV}$)^{16}O presented in the left column of Fig. 6.4.6 with the one measured at the MLL Tandem accelerator, where a small

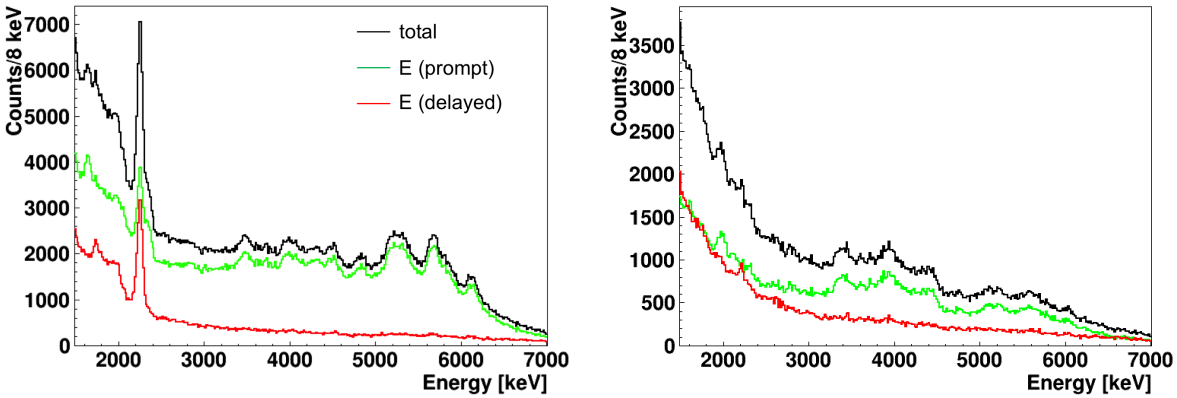

(a) water phantom (b) PMMA phantom

Figure 6.4.5: Energy spectra measured by the $LaBr_3$:Ce scintillator during the irradiation of water (a) and PMMA (b) phantoms by a 225 MeV proton beam. The total energy (black curve) can be disentangled divided into prompt (green curve) and delayed (red curve) components, using the time-of-flight conditions described in the text.

water phantom was irradiated by a 20 MeV proton beam (see Fig. 6.2.2), the photopeak intensity is considerably reduced for the case of the clinical proton beams. This is due to the fact that the cross section of the inelastic ^{16}O(p, p$'$ $\gamma_{6.129MeV}$)^{16}O reaction at 20 MeV proton beam energy is ten times higher than the one at 100 MeV [113] or 160 MeV proton beam energy [34]. Moreover, since the emitted prompt γ rays in the OncoRay setup pass through about 16 cm of water before reaching the $LaBr_3$:Ce scintillator, 32 % of them will already experience Compton scattering in the target under different scattering angles. This results both in a reduction of the registration efficiency due to the finite solid angle coverage of the Compton camera, together with a considerable reduction of the photopeak intensity due to the enhanced Compton scattering probability in the case of the large water phantom at OncoRay. This effect was much reduced for the case of the 20 MeV proton beam irradiation, since the small cylindrical water phantom had a diameter of only 30 mm, leading to a Compton scattering probability of emitted prompt 6.13 MeV photons of only 3.5 %.
The contribution of the delayed component to the prompt γ spectrum presented in Fig. 6.4.5 is rather moderate at clinical proton beam energies studied here. The ToF technique could improve the peak-to-background ratio only by 2 % for the dominant oxygen peak group measured with the water target. In the case of the PMMA phantom, the peak-to-background ratio of the dominant carbon group is improved by about 11 %. The different intensity of the neutron-induced background in both cases can be attributed to the different target material compositions and their resulting different reaction products.

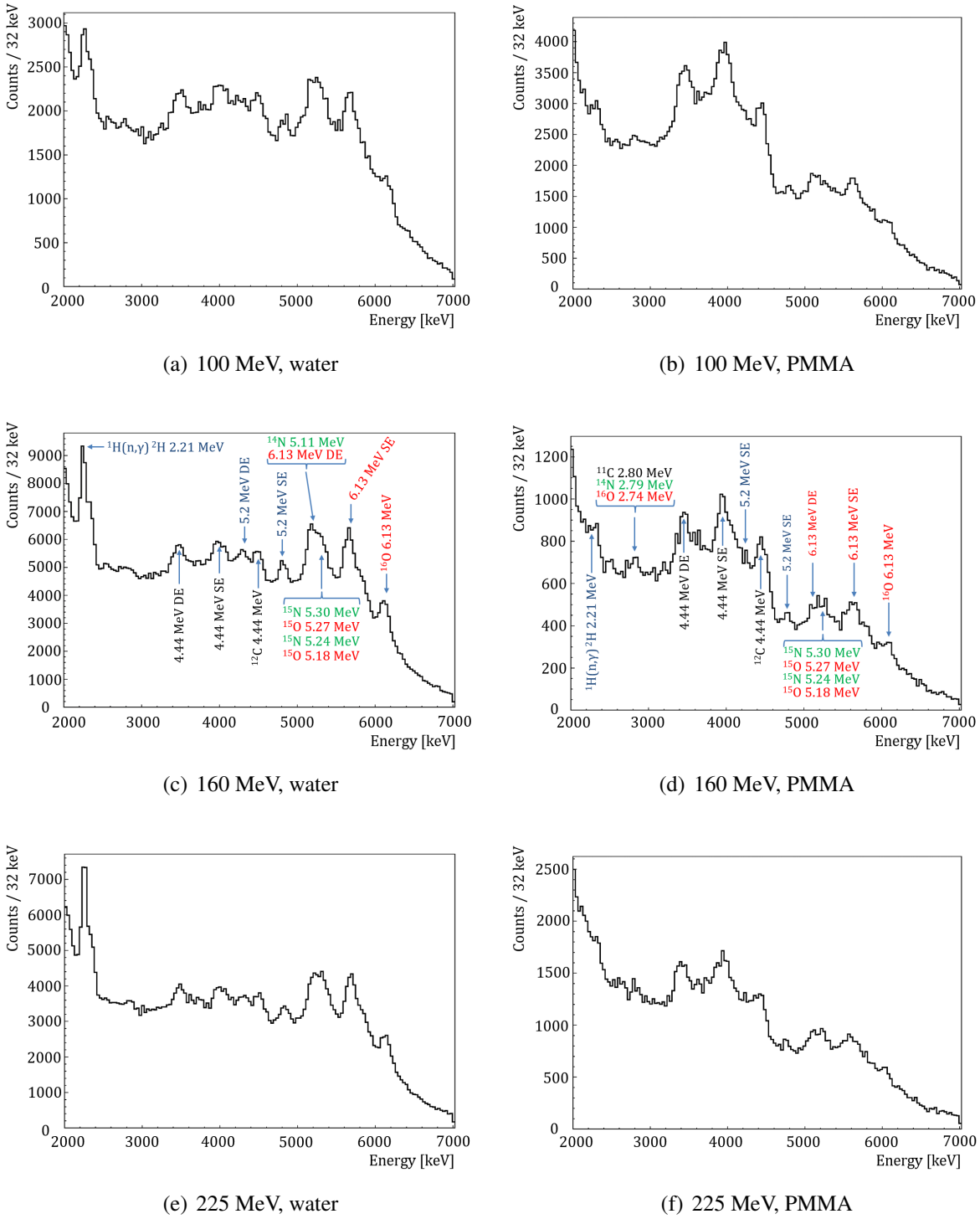

(a) 100 MeV, water

(b) 100 MeV, PMMA

(c) 160 MeV, water

(d) 160 MeV, PMMA

(e) 225 MeV, water

(f) 225 MeV, PMMA

Figure 6.4.6: Prompt γ-ray components of the total energy spectra measured by the $LaBr_3$:Ce scintillator during the irradiation of water (left column) and PMMA (right column) phantoms with 100 MeV (top row), 160 MeV (middle row) and 225 MeV (bottom row) proton beams. Assignments of the resolved γ-ray transitions are exemplarily given for the case of the 160 MeV irradiation.

6.4.2 Scatter detector: six layers of double-sided silicon strip detectors (DSSSD)

6.4.2.1 Compton electron energy measurement

The performance of the scatter detector components of the LMU Compton camera and their readout electronics was characterized in the targeted multi-MeV prompt γ-ray energy region during the irradiation of a water phantom with a clinical proton beam. The specific difference between the readout properties of the 6×128 n-side strip channels and their equal amount of p-side counterparts has already been addressed earlier in this chapter (see Sect. 6.1). Figure 6.4.7 (panel a) shows the total energy spectra (after energy pedestal subtraction) measured by the n-type strips of the six layers of the double-sided silicon strip detectors (DSSSD). From the signal intensity registered below the E-pedestal remnant, it appears at first glance that the modified front-end electronics for the n-side strips (see Sect. 3.2.2.2 for more details) could acquire events depositing energy above the energy pedestal peak, in the expected range of Compton-scattered electrons. In order to investigate the suspected correlation of these events with the targeted prompt γ rays, an energy window between 3 MeV and 6.5 MeV was applied as filter condition to the energy spectrum of the trigger detector ($LaBr_3$:Ce) the resulting data are shown in panel b). As could be expected, the observed statistics of the n-side strip events was considerably reduced due to this energy constraint. Moreover, besides the γ-ray energy condition, a further gating condition was applied to select only events in the prompt ToF peak of the time spectrum acquired with the $LaBr_3$:Ce detector. This results in the data presented in panel c). Only very few events remain as being registered by the n-type strips in prompt coincidence to the proton beam pulse. This in turn implies that the measured data, presented in panel a) and b), prominently belong to a delayed signal component. This was confirmed by applying, in addition to the energy gate from 3-6.5 MeV, the complementary ToF condition covering the area inbetween the prompt peaks, containing (besides uncorrelated background) delayed (neutron-induced) events. The resulting n-side DSSSD spectra, indicated in panel d), as expected reveal that almost all interactions registered in the n-side DSSSD strips for events depositing a rather high amount of energy in the scintillation detector of the Compton camera are not promptly correlated to the impinging proton bunch, but rather can be explained either by temporally uncorrelated background or, more likely, by neutron-induced delayed interaction. Once more this points to the inadequate performance of the modified n-side readout boards with respect to the very low-energy Compton electron signal, that will be buried in the broad energy pedestal background peak.

A completely different behaviour is observed for the p-side strips. A much larger statistics is registered above the threshold defined by the energy pedestal peak ranging up to about ADC channel 120. As already discussed earlier in the context of the Tandetron experiment with 4.4 MeV photons, also now the energy deposit of the Compton-scattered electrons can be observed with increasing intensity across the six detector layers. The resulting broad electron peak (integrating over the distribution of Compton-electron energies and scattering angles), despite the absence of detector cooling, is still well-separated from the E-pedestal peak and ranges from 125-145 ADC channels.

Beyond this peak, somewhat similar to the behaviour of the n-side strips, however with much higher statistics, higher-energy signals fill almost the full dynamic range of the 10-bit ADC, as can be seen in panel a) of Fig. 6.4.8. A similar analysis as applied above to the n-type strip data was applied also for the p-type strips, as can be seen in panel b), c) and d) of Fig. 6.4.8, showing the resulting data for the gating conditions of multi-MeV γ ray registration in the $LaBr_3$:Ce detector (panel b), additional prompt ToF gating (panel c) and alternatively delayed

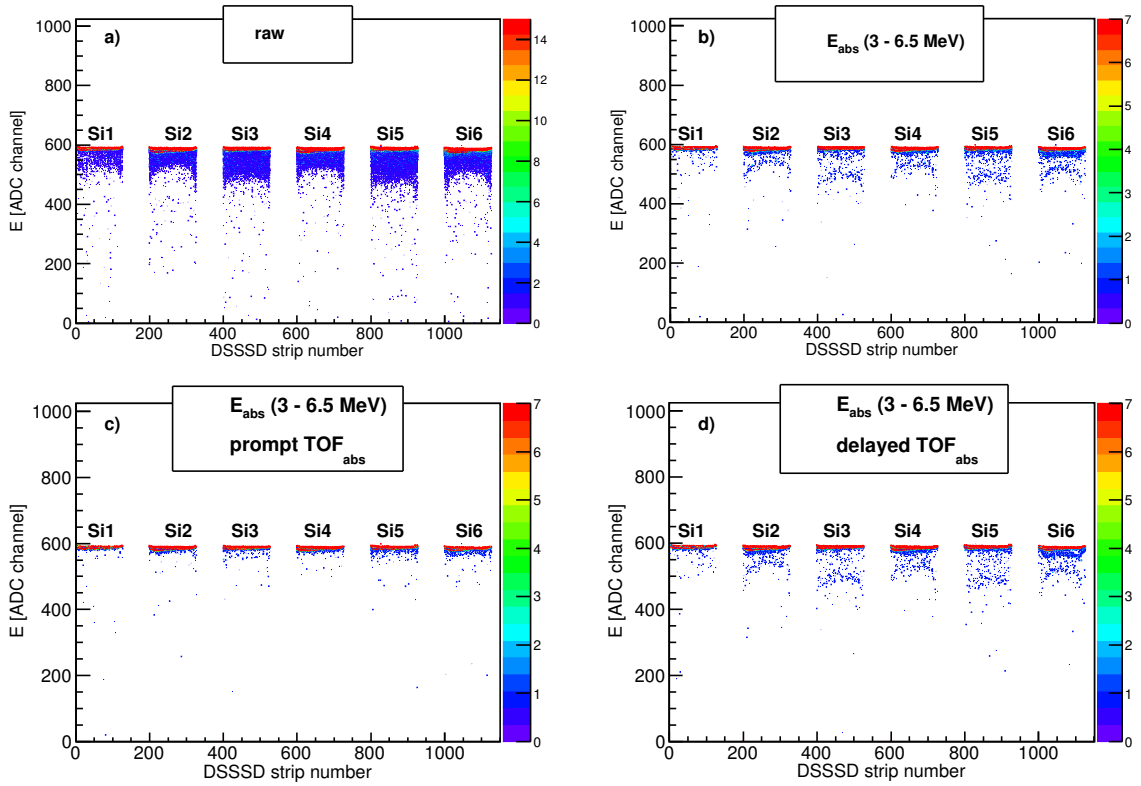

Figure 6.4.7: The total energy spectra (panel a) measured by the n-type strips of all six DSSSD layers can be decomposed based on multi-MeV γ ray energy (3-6.5 MeV) (panel b), additional prompt ToF (panel c) and delayed ToF (panel d) conditions applied to the triggering $LaBr_3$:Ce detector data. The high energy deposits almost disappear in the presence of the prompt ToF condition (panel c) and consequently re-appear in the complementary case of the delayed ToF condition. This implies that predominantly neutrons, produced from fragmentation reactions during the passage of the proton beam through the water phantom, induce (n,γ) or (n,n$'$ γ) reactions in the DSSSD volume.

ToF gating (panel d), respectively. In the presence of the prompt ToF condition (panel c), the measured signal statistics above 200 ADC channels is noticeably reduced compared to the cases shown in panels b) and d). In fact, this behaviour matches the observation made before in the n-type strip energy spectra illustrated in Fig. 6.4.7. However, the p-side data exhibit, besides a larger gain and lower energy pedestal, a much higher detection efficiency, all of them related to the performance of the p-sides signal processing chain, which was operated in this case as it was originally designed for positive input signals. Thus, signals in the multi-MeV energy range (panel b) are registered much more abundantly on the p-side compared to n-side of the DSSSD. Yet, the same behaviour can be observed when applying the prompt γ timing condition: again most of the signals beyond the Compton electron peak are temporally uncorrelated with the proton bunch and most likely represent neutron-induced delayed background. Further evidence for this interpretation comes from a comparison of the p-side data shown here with the ones obtained in the HZDR Tandetron experiment with 4.4 MeV photons (see Sect. 6.1), where no such energetic background beyond the Compton electron peak was observed. This ”clean” detection scenario did not allow for nuclear reactions producing neutron background in the way now registered with clinical proton beam energies.

In order to gain further insight into the spectral behaviour measured by the p-type and n-type

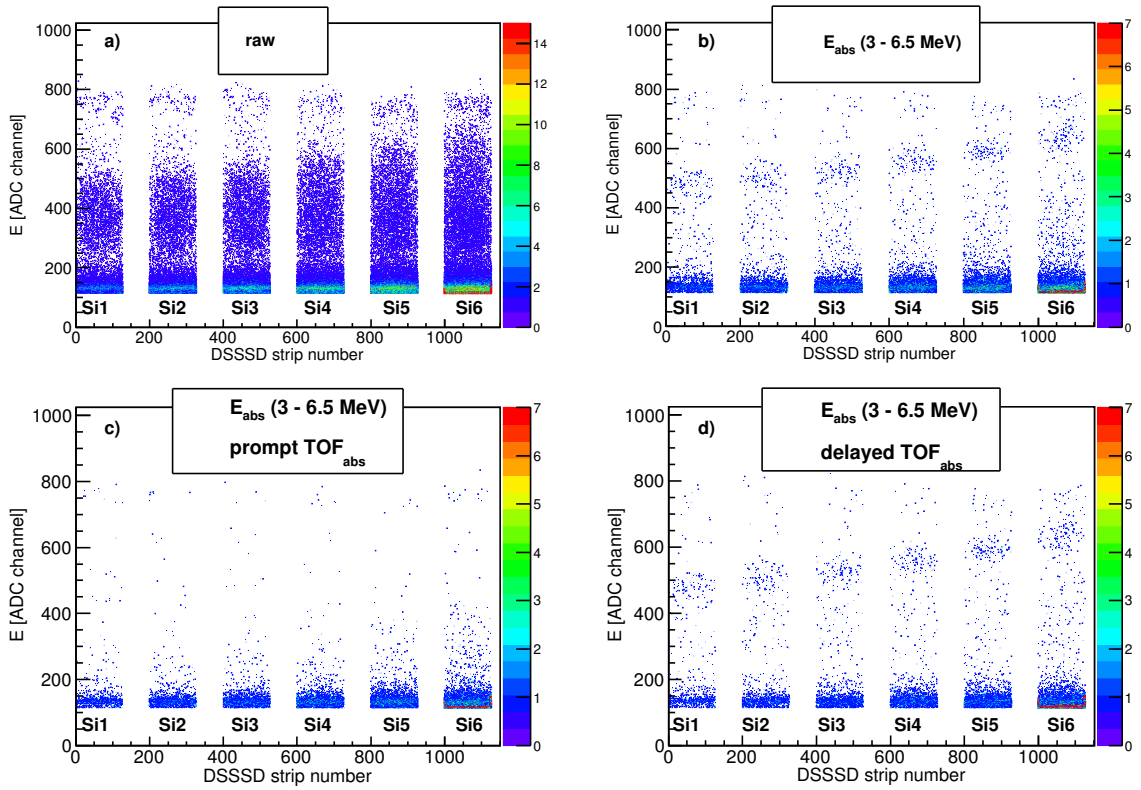

Figure 6.4.8: The total energy spectra (panel a) measured by the p-type strips of the six DSSSD layers can be decomposed based on multi-MeV γ-ray energy (3-6.5 MeV) (panel b), additional prompt ToF (panel c) and delayed ToF (panel d) conditions applied to the triggering $LaBr_3$:Ce detector data. The high energy deposits measured above $\sim$ 200 ADC channels are considerably reduced for the prompt signal component, whereas these events appear when gating on the complementary delayed ToF region of the $LaBr_3$:Ce scintillator (panel d). This indicates that these high energy deposits in the DSSSD originate from neutron-induced (n,γ) or (n,n$'\gamma$) background events.

strips of the six DSSSD layers correlated with the multi-MeV prompt γ-ray component, i.e. applying the filter conditions on prompt ToF and the energy range from 3 MeV to 6.5 MeV to the triggering $LaBr_3$:Ce detector, panels c) of both Fig. 6.4.8 and 6.4.7 are projected onto the energy axis as can be seen in Fig. 6.4.9 panel a) and b), respectively. The energy spectra of the p-type strips (panel a) clearly show a sequential increase of the Compton electron intensity resulting from the incident prompt γ rays, produced during the interaction between the 225 MeV proton beam and the water phantom, from layer one (light blue curve) to layer six (pink curve) similar to the findings in the HZDR Tandetron experiment with monoenergetic 4.439 MeV photons. The fact that already the first silicon detector layer exhibits a peak from Compton electron energy deposition, which indicates the occurrence of Compton interactions on the way from the photon origin to the first detector of the Compton camera. However, it should be taken into account that the promptly emitted γ rays have to travel through 160 mm of water to reach the detector, which is sufficient to induce Compton scattering for ca. 32% of the produced 6.13 MeV prompt γ rays before entering the first DSSSD layer. Thus, a peak of the Compton electron energy deposition appears already in the p-type strips of the first DSSSD layer. This was identically observed when the silicon detectors were exposed to 4.439 MeV monoenergetic γ rays induced from the ^{15}N(p, α $\gamma_{4.439MeV}$)^{12}C reaction, as illustrated in Fig. 6.1.8. On the

other hand, the n-type strips of the DSSSD barely register any low-energy signals beyond the high intensity of the remaining energy pedestal peak. It should be reminded that, due to the inverse characteristics of the n-side signal processing after raising the multiplexing amplifier's baseline of the FE module for negative input signals (see Sect. 3.2.2.2), the remaining pedestal peak of the n-type strips energy spectra represents the lowest accepted energy. Besides this adaptation of the n-type signal processing electronics, which contributes to increase the dark current level by almost a factor of 2 compared to the p-type readout, also the gain of the charge-sensitive amplifier included in the GASSIPLEX ASIC is about a factor of two lower for negative signals. These two reasons explain the absence of the Compton electron signals in the n-type energy spectra.

In order to further investigate the energy components displayed in Fig. 6.4.9, particularly in the n-type strips of the six DSSSD layers, the correlation between the n-type and p-type energy signals is plotted for each layer, as shown in Fig. 6.4.10. The Compton electron peak observed between ADC channel 125 and 145 of the p-type strips is predominantly correlated with the remaining fraction of the energy pedestal peak of the n-type strips electronics. In comparison, the prompt events observed above the n-side pedestal peak (see Fig 6.4.9 panel b) are mostly correlated with the high energy events observed above $\sim$ 200 ADC channels of the p-type strips. This small number of energy deposits in the scatter detectors may originate from inelastic nuclear reactions inducing the fast component of the neutron background. Thus, the resulting delayed (n,γ) or (n,n$'\gamma$) photons leak into the prompt gating condition and then appear in Fig. 6.4.10.

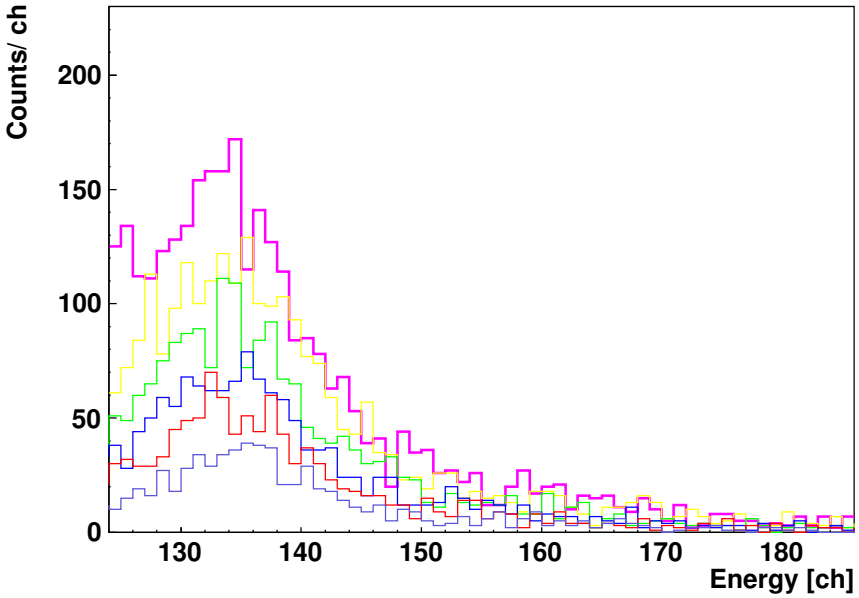

(a)

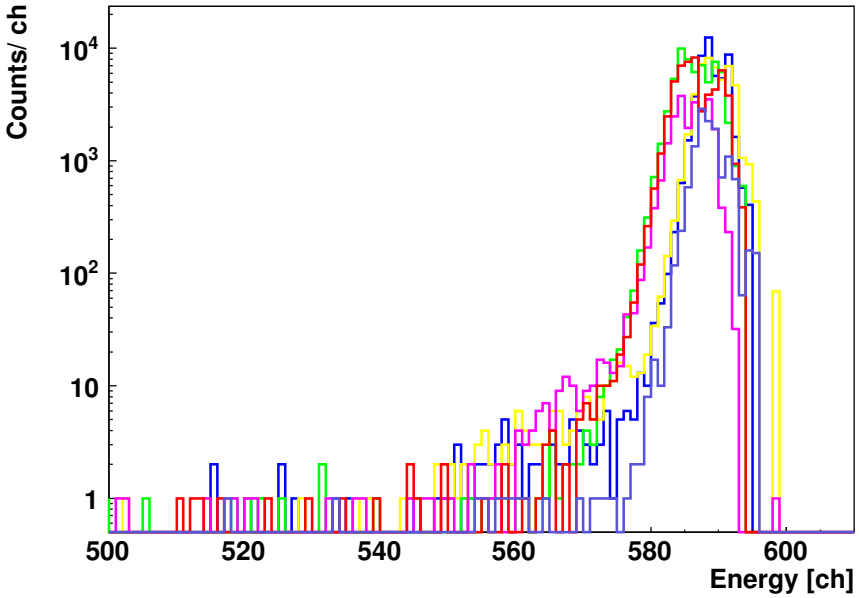

(b)

Figure 6.4.9: Energy spectra measured with the DSSSD detectors following the interaction of a water phantom with 225 MeV protons. The histograms were obtained by projecting panel c) of Fig. 6.4.8 and Fig. 6.4.7 onto the energy axis. Gating conditions requiring an energy window (3-6.5 MeV) and a prompt ToF registered in the trigger detector were applied for the p-type (panel a) and n-type (panel b) strips, respectively. The intensity of energy deposition peak of the Compton electrons measured by the p-type strips sequentially increases from layer one (light blue curve) to layer six (pink curve). In contrast, the remaining part of the energy pedestal peak hides the Compton electron energy deposits in the n-type strips, due to the factor of two lower amplifier gain and higher dark current of their readout electronics.

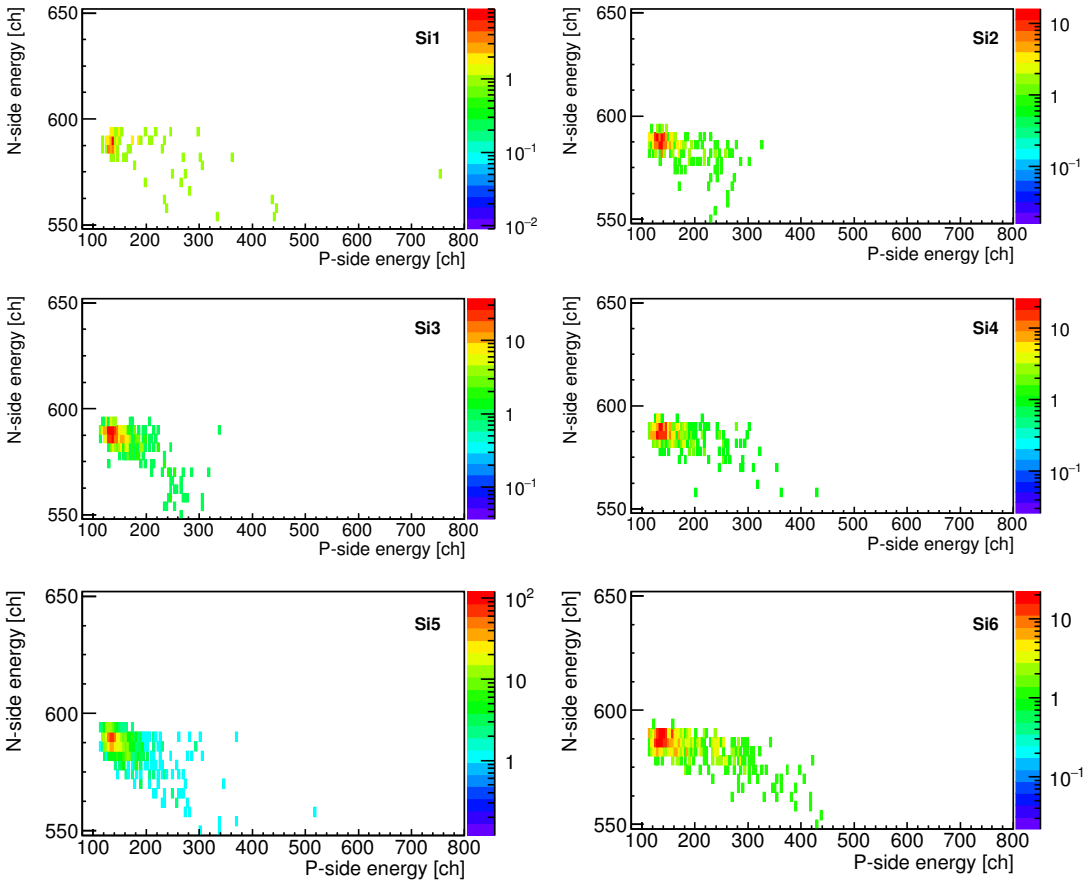

Figure 6.4.10: Energy correlation between the p-type and n-type strips of the six DSSSD layers after applying energy (3-6.5 MeV) and prompt ToF conditions to the data measured by the trigger ($LaBr_3$:Ce) detector. The energy distribution of the Compton electrons measured by the p-type strips mostly correlates with the remaining part of the energy pedestal peak of the n-type signal processing electronics. Above this pedestal peak, a small amount of events seen in Fig 6.4.9 b) correlates with energy deposits above the Compton electron peak (>200 ADC channels) in the p-type strips.

Since the trigger signal of the DSSSD readout electronics was provided by the $LaBr_3$:Ce scintillator, the energy correlation between the energy registered by the (sum dynode of the) scintillator and the sum energies of all n- and p-type strips, respectively, are plotted with and without applying the prompt time-of-flight (ToF) condition. Shown in Fig. 6.4.11 are the resulting data obtained during the irradiation of the water phantom with a 225 MeV proton beam. For the p-type strips (panel a and b), the remaining part of the energy pedestal peak has been entirely eliminated, as it is well distinguishable from the Compton electron energy peak. This electron peak is visible in the ADC channel range of 120-160 applying the prompt ToF condition and it correlates with energies registered in the $LaBr_3$:Ce detector up to 6.5 MeV. On the other hand, the strong baseline component visible for the n-type strips represents the remaining fraction of the energy pedestal peak. This fraction was intentionally not subtracted in order to avoid any potential loss of small energy signals that might be a signature for Compton electron energy deposits. It can be noticed that most of the n-type data as well as the p-type events recorded above ca. 200 ADC channels, are correlated with trigger events whose energies range between 6.5 MeV and 12.5 MeV.

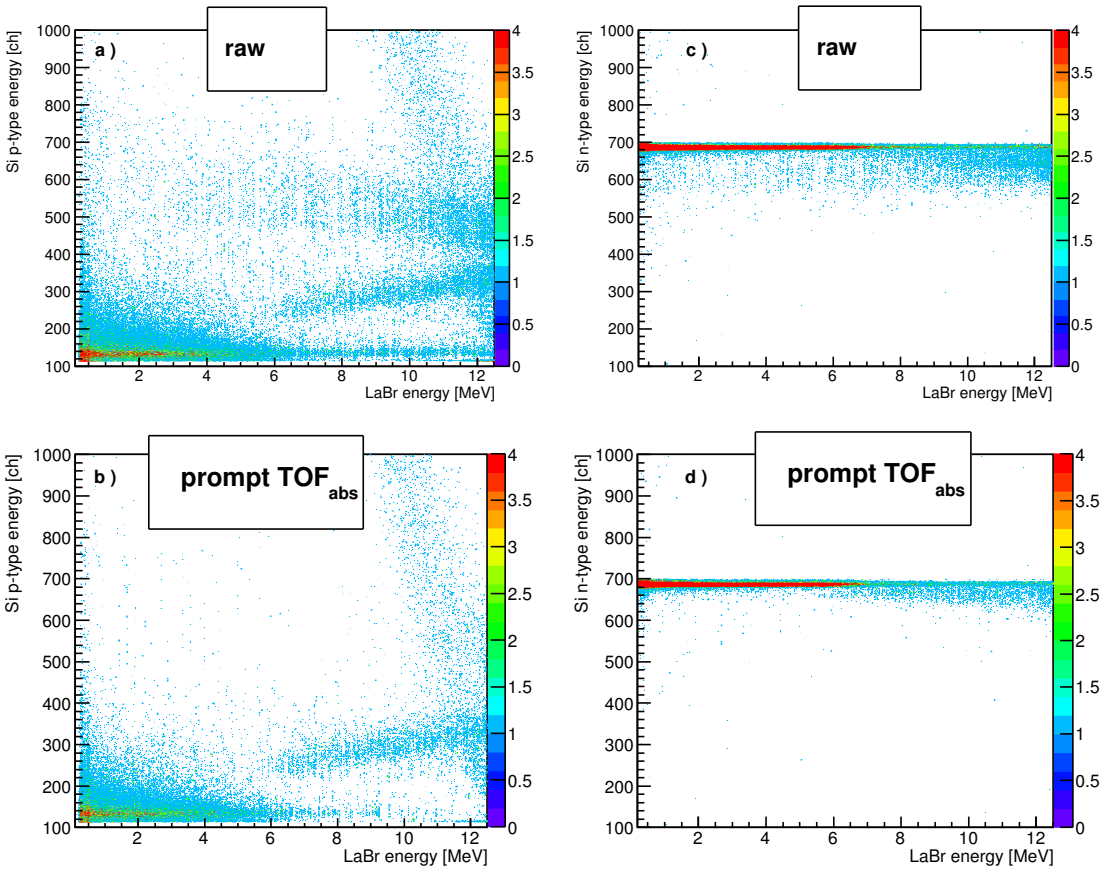

Figure 6.4.11: Correlation between the energy spectrum derived from the sum of all p- (left column) and n-type strips (right column) of the six DSSSD layers and the energy recorded in the triggering ($LaBr_3$:Ce) detector during the irradiation of a water phantom with a 225 MeV proton beam. The neutron-induced delayed background is included in the raw data shown in panels a) and c), while it is filtered out in panels b) and d), using a prompt ToF gating condition.

6.4.2.2 Multiplicity study

Even if it will be not possible to localize the Compton interaction in the DSSSD scatter detectors via a coincidence of p- and n-side electron deposit signals, due to the largely discussed deficit of the current n-side signal processing electronics, it is nevertheless instructive to characterize the DSSSD response not only on an inclusive level via their sum energies, but also to analyze the hit multiplicity response of the highly segmented modules. Therefore, the performance of the six DSSSD layers of the Compton camera scatter array was evaluated based on their strip multiplicities, as shown in Fig. 6.4.12 and 6.4.13 for the n- and p-type strips, respectively. Without applying any analysis conditions and reminding that the DSSSD data of n- and p-side strips contain sizeable amounts of remaining background from the abundant energy pedestal component, it is not surprising to see the raw multiplicity ranging out to large values, in most cases to strip multiplicities of more than $N_{strip} \sim 60$.

Adding the additional condition of a prompt photon registered in the (triggering) $LaBr_3$:Ce scintillator does not change the picture significantly (pink curve) with only a small reduction of the intensity of the strip hit multiplicity curve (while in general not affecting the multiplicity range significantly). Further intensity reduction is achieved when selecting only prompt, multi-MeV (E_γ = 3-6.5 MeV) photons in the trigger detector, resulting in the blue histograms.

The multiplicity distributions of the n-side strips exhibit a two-component characteristics, with an almost exponential slope from the dominant low multiplicity (84% N_{strip} = 1-3) to about N_{strip} = 30, where a saturation tends to start. Since these large multiplicities are predominantly associated with background events (mostly from incompletely suppressed dark current), the only relevant strip hit multiplicity distribution is reached when finally gating on the energy range of the energy deposit of Compton-scattered electrons in the layers of the tracking array. In order to test this condition even in view of the previously discussed issues of the n-side strips to resolve the Compton electron energy loss peak, a hybrid condition was applied instead: knowing that the Compton electron in case of a correct registration in the DSSSD would generate identical signals in the n-side and p-side readout chain, the well-defined gating condition of the Compton electron energy deposit in the p-side strips (typically covering the ADC range from channel 125-145) was applied also to the data registered on the n-side of the same detector. The resulting strip multiplicity distributions are displayed as red curves in Fig. 6.4.12 and 6.4.13.

Now all background events are removed and the physically relevant hit multiplicity emerges. Since no photon source image reconstruction will be attempted from the present data due to the widely discussed deficit of the current n-side readout electronics, preventing to select Compton-electron signal coincidences between n- and p-side strips, no further attempts were conducted to analyze the final hit multiplicity distributions in terms of a hit pattern analysis, e.g. unveiling the occurrence of charge sharing between neighbouring channels. Very general, though, it can be stated that the red curves presented in Fig. 6.4.13 show the dominance of hit multiplicity 1 and 2 of the targeted Compton electron signal for p-type strips of each DSSSD layer accounting together for 51% of all detector-related strip hits. Consequently, higher hit multiplicities per event represent a small fraction of about 49% of the total recorded data.

The p-type strip multiplicity, displayed in Fig. 6.4.13, shows a sudden cut-off at the multiplicity N_{strip} = 64 for all DSSSD layers. This cut-off has no physical meaning and can be related to the readout procedure of the n- and p-sides of the DSSSDs with 64 odd and even channels, respectively, being read out at opposite sides of the DSSSD module. In order to illustrate the occurrence of the N_{strip} = 64 cut-off, Fig. 6.4.14 for one detector layer exemplarily displays the multiplicity-integrated number of hits (for the raw data curve shown in Fig. 6.4.13) across the 128 strips of the p-side. Apparently staggering between odd and even strips occurs, with about two orders of magnitude more hits counted in the even strips compared to the odd ones. Ideally,

the entries of both even and odd strips should be comparable within statistical fluctuations. However, as they are processed by two independent FE electronics modules, the dark current that determines the width of energy pedestal peak can be different from one FE module to another. While the pedestal suppression is based on the individual recording of the pedestal peak, a subsequent Gaussian fit and the determination of the corresponding energy threshold as the peak centroid plus three times its width (expressed by σ), differences between the dark current and noise levels of individual FE boards are automatically accounted for. However, unexpected offsets added later to the modules (or their connecting bus card) would shift the pedestal peak to lower values and thus lead to a larger remaining fraction after applying the suppression procedure. Such a scenario readily explains the observed occurrence of the N_{strip} = 64 cut-off. When eliminating the contribution of the remaining part of the energy pedestals of the FE modules by setting an energy window around the Compton electrons peak, this artificial N_{strip} =64 cut-off disappears. The slightly different multiplicity behaviour of DSSSD module

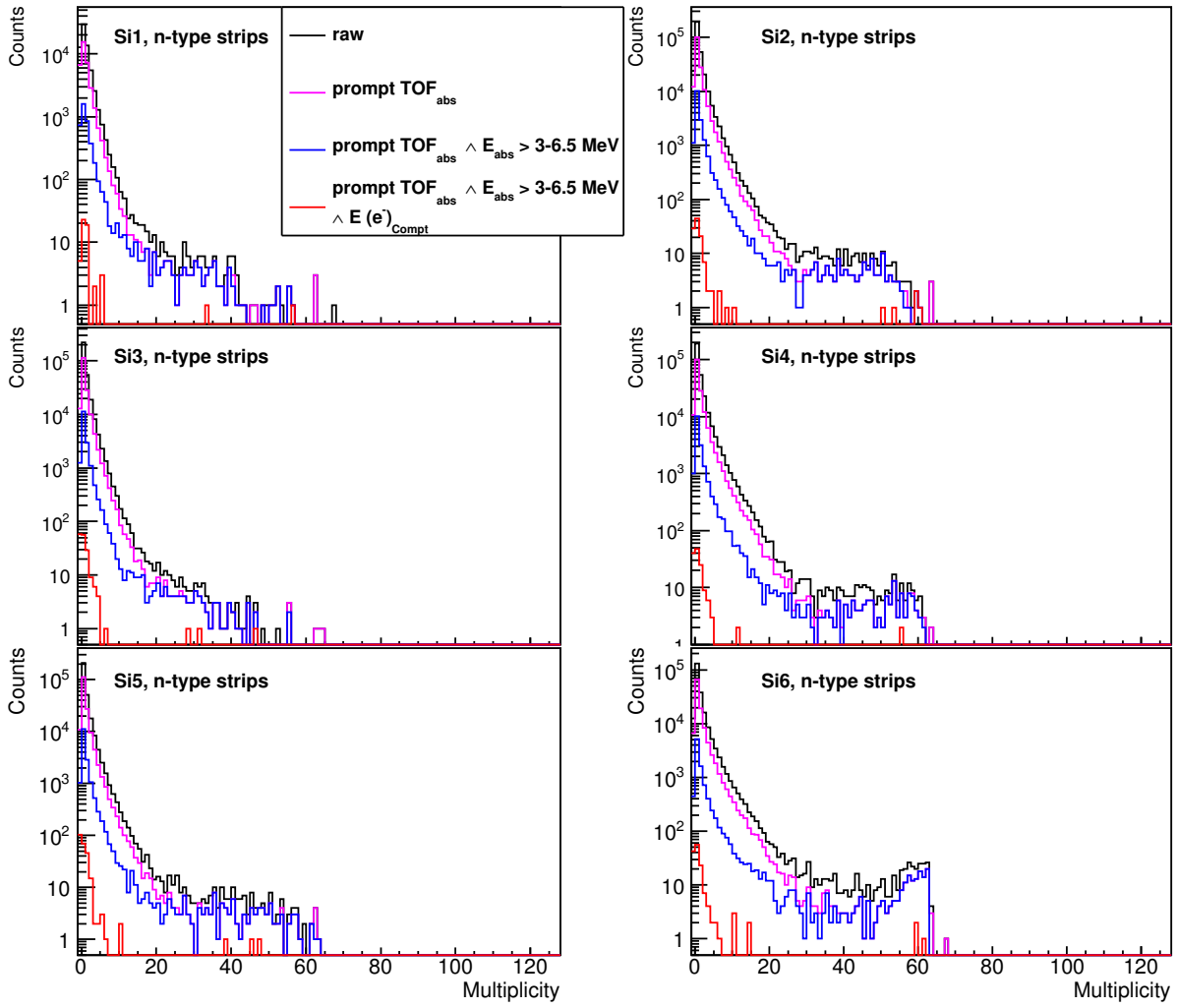

Figure 6.4.12: n-type strip multiplicity of the six DSSSD layers forming the Compton camera scatter component. The raw multiplicity (black curve) was filtered by a prompt ToF condition (pink curve) and a prompt ToF plus energy window (3-6.5 MeV) (blue curve) applied to the data of the trigger $LaBr_3$:Ce scintillator. In addition to the previous conditions, the multiplicity of the n-type strips was further conditioned by setting a gate around the Compton electron peak measured by the p-type strips, as shown in Fig. 6.4.9 panel a).

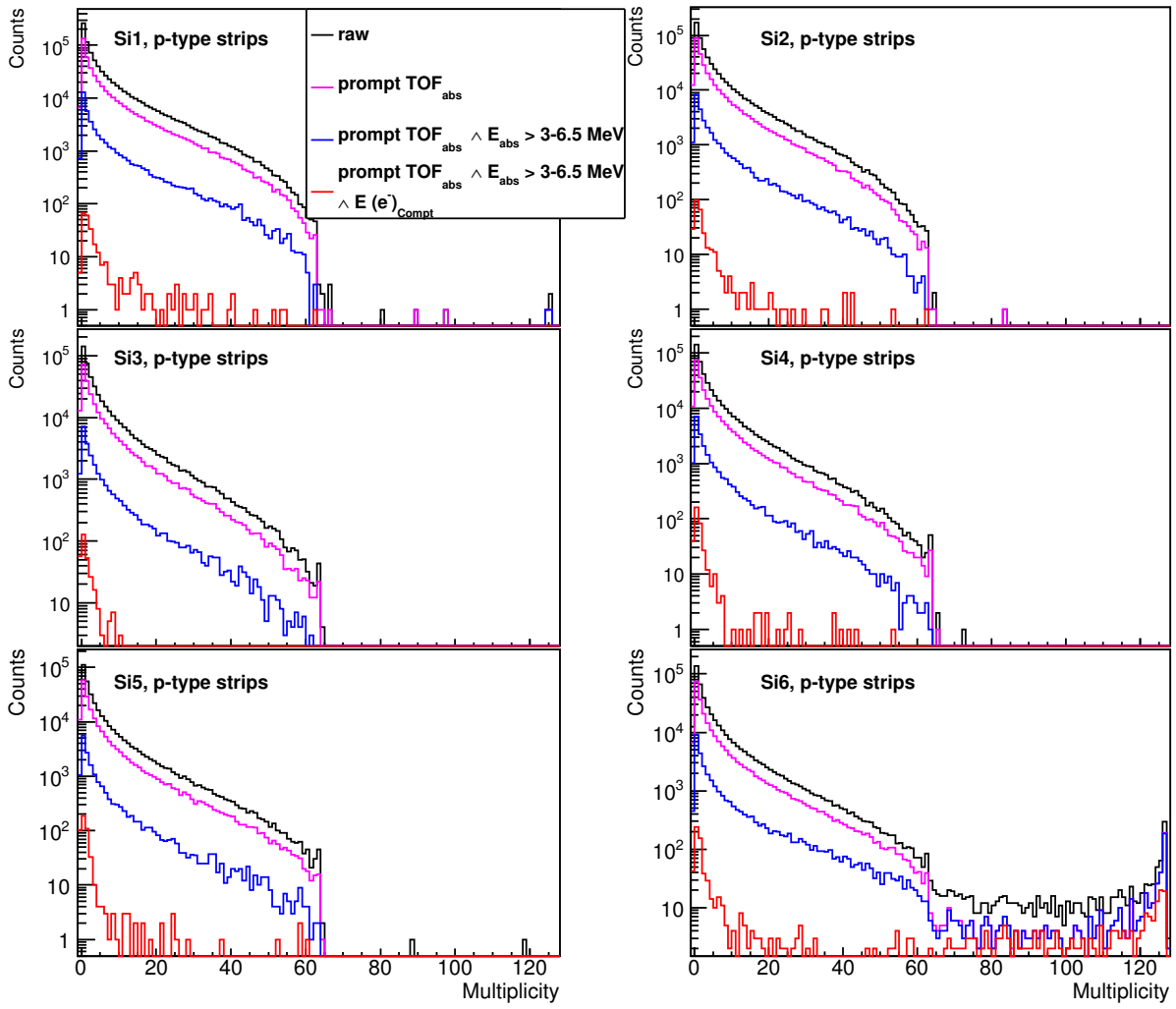

Figure 6.4.13: p-type strip multiplicity of the six DSSSD layers representing the Compton camera scatter component. The raw multiplicity (black curve) was divided based on the prompt ToF and prompt ToF plus energy (3-6.5 MeV) conditions applied to the triggering $LaBr_3$:Ce scintillator, as indicated by the pink and blue curves, respectively. Besides the previous conditions, an additional energy gate was set around the Compton electron energy peak measured by the p-type strips in order to eliminate the contribution of the remaining part of the pedestal energy peak as well as neutron-induced background and to reveal the final strip multiplicity (red curve) of each scatter layer.

six can be attributed to the in general twice as large leakage current of this detector module, potentially also fluctuating stronger than the other modules during operation and thus resulting in background-related high hit multiplicities.

A more general assignment of the response of the scatter/tracker array can be achieved by investigating not only the strip hit multiplicities of individual detector modules, but also the multiplicity of responding detector modules when being hit by radiation from the water phantom. So the performance of the Compton camera scatter detectors was studied based on the detector multiplicity, illustrated in Fig. 6.4.15. This multiplicity was derived from the data registered by the p-type strips of the DSSSDs, particularly those events where the energy deposit indicated the detection of the Compton-scattered electron. As shown in the figure, the dominant multiplicity $N_{det} = 0$ (99.6% of all events) refers to events recorded by the trigger ($LaBr_3$:Ce) detector

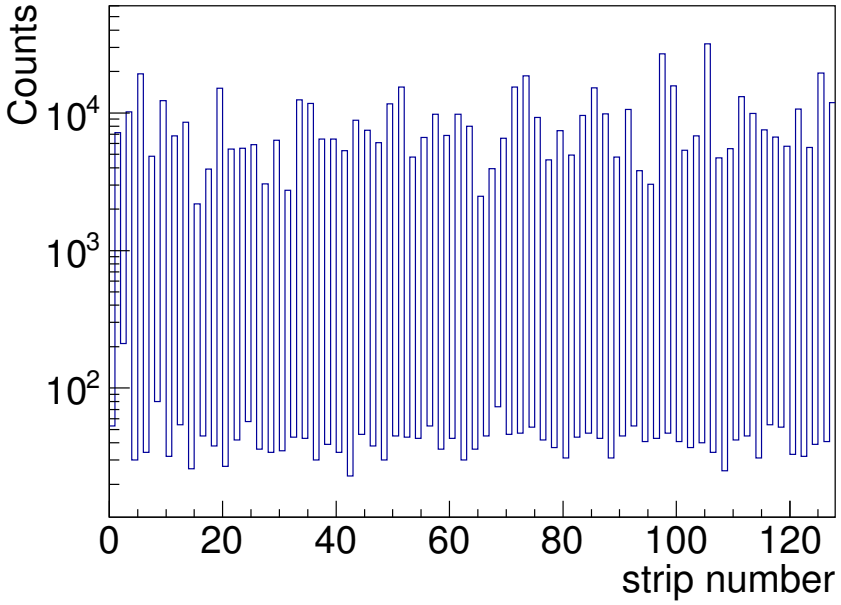

Figure 6.4.14: Exemplary illustration of the raw strip hit multiplicity data extracted from the p-type strips of one DSSSD layer. With this plot an explanation of the obvious cut-off at N_{strip} = 64, visible in the multiplicity distribution of Fig. 6.4.13, can be given (see text). The data show a high number of entries in every second (even) strip that most likely originates from a wider remaining part of the pedestal peak.

without any interaction registered in any of the six layers of the DSSSD array. Multiplicity N_{det} = 1 (0.24% of all trigger event) indicates that exactly one of the six scatter detectors registered the energy deposition of a Compton electron associated with a triggering prompt photon absorbed in the scintillation detector. Since the energies of Compton electrons from multi-MeV photons are expected to be much higher than the ones that could be absorbed already in one DSSSD module, this low multiplicity implies that the detected Compton electron is most likely scattered out of the acceptance of the array already after the first interaction.

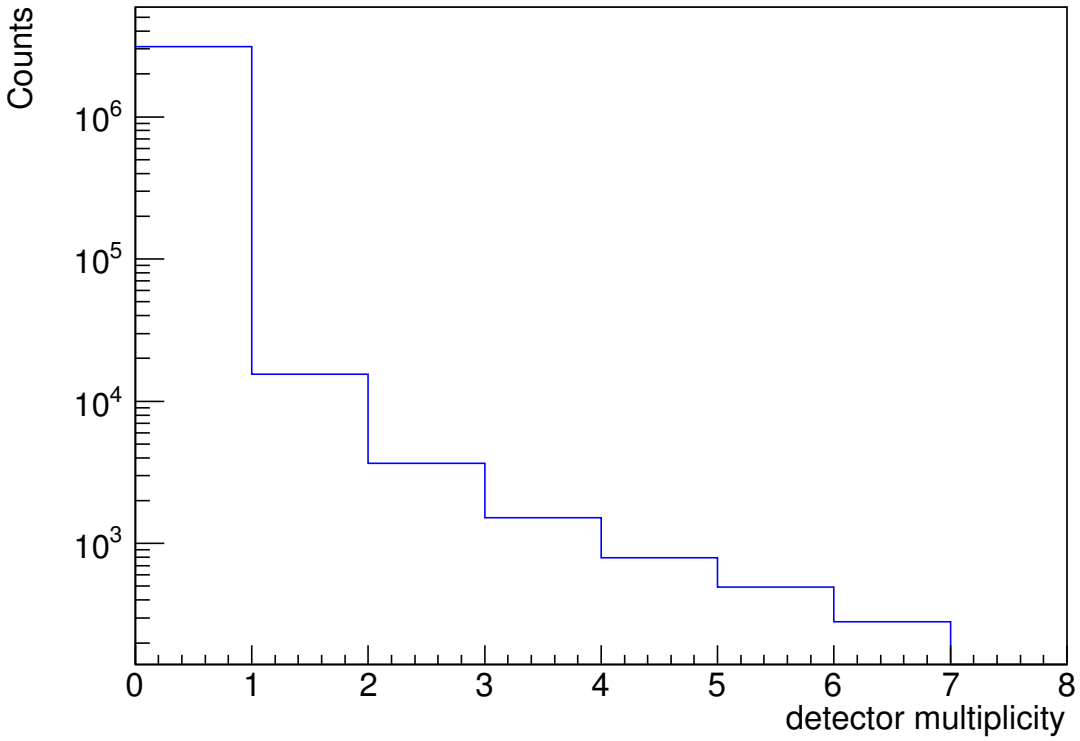

Figure 6.4.15: Detector multiplicity of the LMU Compton camera scatterer array. Multiplicity zero represents the absence of a hit in any of the six consecutive DSSSD layers.

6.4.2.3 Compton electron tracking

As the LMU Compton camera aims for tracking the recoil Compton electron in addition to the conventional photon tracking, in order to increase the reconstruction efficiency of the camera, the tracking capability of the camera's scatterer array (six layers of DSSSD) was investigated with the prompt γ rays induced from nuclear reactions between the clinical proton beam and a water phantom. In order to prove the existence of tracks across several detector modules formed by Compton-scattered electrons measured by the p-type strips of the six scatterers, as shown in Sect. 6.4.2.1, energy correlations between every two consecutive DSSSD layers were plotted from a selection of these events, where all scatter array members registered an energy deposit in the region of the Compton-electron peak. This filter condition ensured the maximum length of the tracking sequence across the detector stack. The resulting data is shown in Fig. 6.4.16 for events, where the summed energy of the p-side strips falls into the energy window of the Compton electrons (ADC channel range from 120-145). The presence of tracks of Compton electrons across six DSSSD layers is evidenced by the high intensity of the coincidently registered electron energies at around 135 ADC channels. While this inclusive analysis indicates the presence of electron tracks in the DSSSD array for the exemplary scenario of the largest possible tracks, the next step has to give insight into the geometrical disposition of the electron tracks by including the position interaction on the basis of the individual detector strips in each layer. Now, we also accept events with shorter track sequences, represented by consecutively registered Compton electron energies in 2-6 layers.
In order to visualize the path of the Compton electron tracks, the p-type strip number is plotted as a function of the electron energy for each scatterer, as illustrated in Fig. 6.4.17. This figure shows examples of Compton electrons that pass through two (left column), four (middle) or even six (right column) consecutive DSSSD layers. These plots nicely illustrate different tracks, either passing rather straight (panels d, h, i) or under some angle (panel g) through the detector array. It can be seen in the first row for three cases that here the Compton electrons start to transfer their energy already in the first scatterer. This indicates that the Compton interaction generating these electrons occurred already in front of the detector system. This can be understood for our experimental setup, since the primary prompt γ rays were induced at a lateral depth of x = 16 cm of water along the axis of the phantom. The resulting Compton scattering probability, for example calculated for the dominant 6.13 MeV photons from the excited ^{16}O, can be calculated using the linear attenuation coefficient (μ_l = 2.4 $\times$ 10^{-2} cm^{-1}) using the corresponding equation for the scattering probability

$$P_{scatt} = 1 - e^{-\mu_l \cdot x} \tag{6.4.1}$$

results in a value of 32 % of the 6.1 MeV photons emitted from the excited ^{16}O that experience Compton scattering already while passing through the water layer, thus generating Compton electrons of different energies depending on the scattering angle. As shown in Fig. 2.1.4, for the case of 5 MeV photons, the minimum electron energy that allows traversing all six tracking detector layers (ca. 800 keV) is reached for all Compton-scattering angles above 12^o. Therefore, we have to expect for the majority of Compton interactions from multi-MeV primary prompt photons energetic Compton-scattered electrons. These energetic electrons can pass through all six layers of the DSSSD stack, finally depositing their remaining energy together with the scattered photon in the absorber detector. The disappearance of the Compton electrons presented in panel a) and d) may be due to either a full absorption of the electron energy or scattering out of the acceptance of the next detector layer after passing the second (panel a) and fourth silicon layer (panel d), respectively. Nevertheless, these events are not useful for the imaging reconstruction, since the Compton interaction occurred outside the camera, thus making it

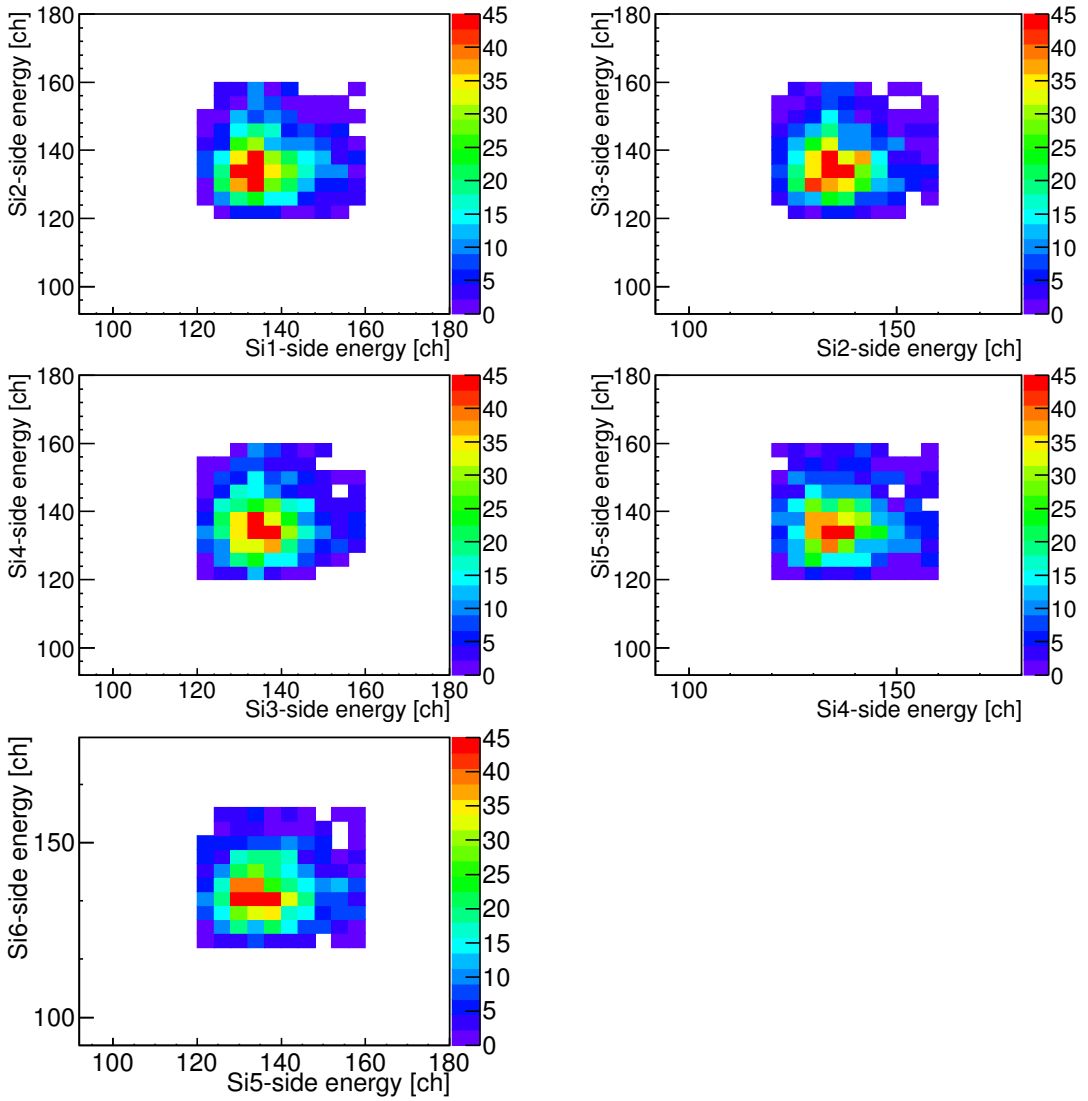

Figure 6.4.16: Energy correlation between the summed p-type strip energies of every two consecutive DSSSD layers for events that registered a scattered Compton detection signal (ADC channel range 120-145) in each of the scatter array members. The visibility of the Compton electron peak at around 135 ADC channels proves the ability of the scatterer array to observe electron tracks crossing sequentially all six detector layers.

possible to determine the correct energy information needed to be fed into the reconstruction procedure. A valid scattering event is represented by a track that starts at least after the first DSSSD layer in order to ensure that the Compton interaction occurred in the camera detection system. Such tracks can be seen in panel b) and e) of Fig. 6.4.17 for a track passing two and four silicon layers, respectively. For these two cases, assuring that the ending of the Compton electron track before the last detector layer can be attributed to a scattering interaction in the last observed layer that leads to prevent the occurrence of a hit in the following one, the Compton kinematics is affected, because part of the total energy of the incident photon is lost with the escaping electron. Consequently, such events introduce additional uncertainties to the reconstructed Compton scattering angle. In order to minimize the blurring effect of small-angle Molière scattering occurring along the electron trajectories (see Sect. 2.2.1) across the detector stack, according to [39] not more than three consecutive silicon layers should enter the electron trajectory reconstruction.

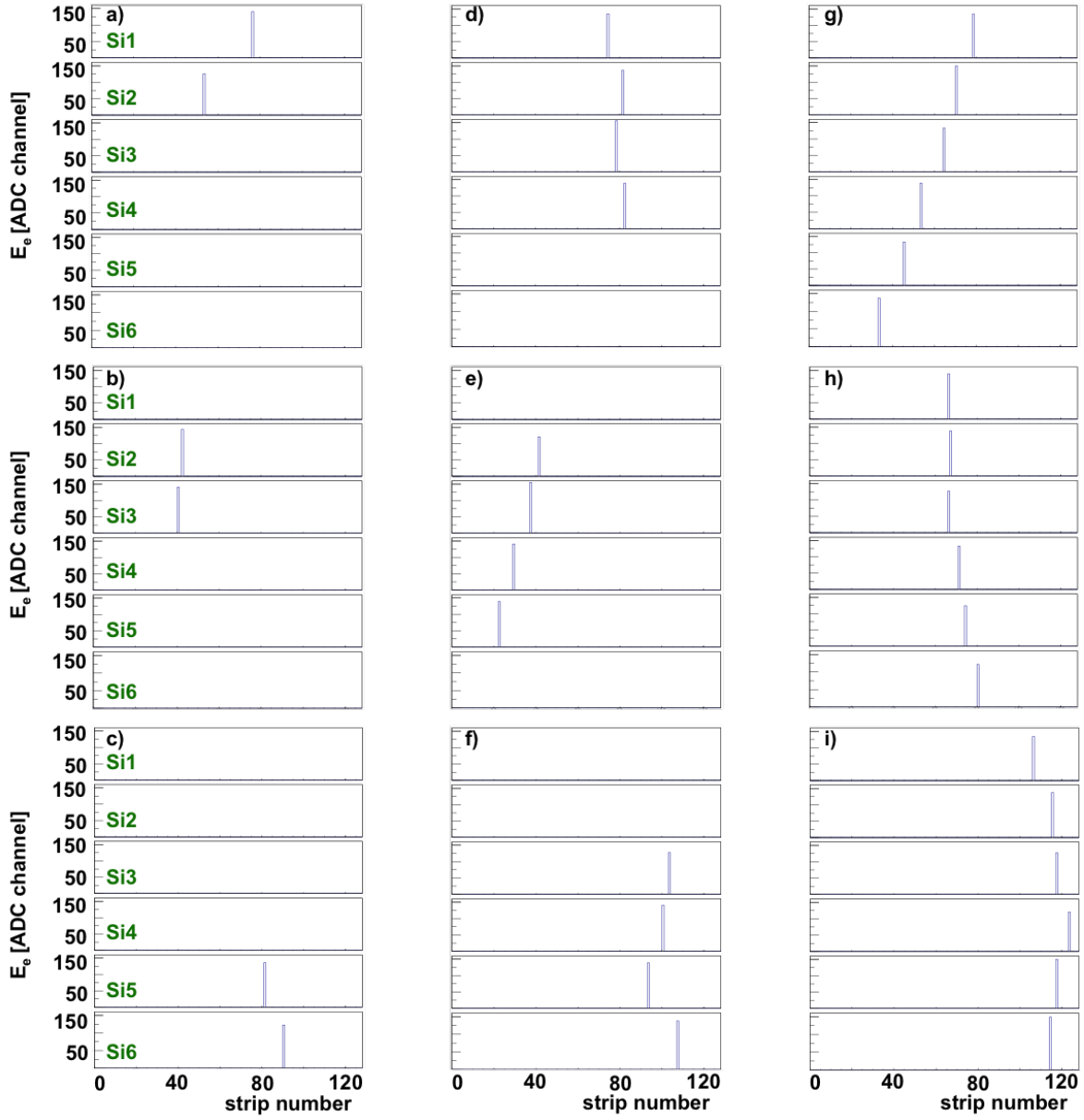

Figure 6.4.17: Visualization of Compton electron tracks observed by two (left column), four (middle column) and six (right column) consecutive DSSSD layers, represented by the p-side strip numbers that registered an energy deposit in the maximum of the Compton electron energy region.

Chapter 7

Summary and Future Perspectives

This chapter is intended to conclude this thesis with summarising the current status of the LMU Compton camera and highlighting the important findings determined during the commissioning phase. Moreover, future perspectives related to either of the Compton camera components and the system in general will be given.

7.1 Summary

Recently, hadron therapy has gained a huge interest in cancer treatments, particularly for tumors in the vicinity of critical organs-at-risk, due to the characteristic and well localized depth-dose deposition known as the Bragg peak. However, in order to exploit this feature by ensuring the maximum dose deposition is released in the targeted volume, a precise and preferably online ion beam range verification is a mandatory prerequisite to guarantee the success of the treatment. Therefore, the main objective of this thesis was to develop an online imaging system prototype based on a Compton camera to verify the particle beam (proton, ions) range by detecting prompt γ rays, induced as a result of nuclear reactions between the particle beam and biological tissue. The design and geometrical arrangement of the camera components allows to not only detect the incident photon, but it can also track the Compton electron (from multi-MeV prompt γ rays).
This motivates the 'non-conventional' layout of the LMU Compton camera, which consists of a stack of 6 layers of double-sided silicon strip detector (DSSSD) forming the scatterer component, while a monolithic $LaBr_3$:Ce scintillation detector ($50 \times 50 \times 30$ mm^3) represents the absorbing detector. The DSSSD detector, which has an active area of 50x50 mm^2, a thickness of 500 μm and a segmentation of 128 strips on each side, is processed by a compact ASIC based electronics (GASSIPLEX). This design represents a compromise in two regards: first of all the thickness of the DSSSD detectors is limited at present to 0.5 mm, due to the inavailability of thicker wafer material with high enough resistivity. This is a mandatory prerequisite to allow for an operation without active cryogenic cooling, which is prohibitive in an envisaged future clinical application. The low energy deposits of the Compton-scattered electrons require utmost efforts to reduce the electronic noise of the detector and the signal processing electronics. Moreover, the present readout via GASSIPLEX-based ASIC boards resulted from their easy and fast availability at the start of the project, while, as will be discussed later, now more and more the related limitations turn out to call for an upgrade. The $LaBr_3$:Ce detector is read out by a position-sensitive (16x16) multi-anode photomultiplier (PMT, Hamamatsu H9500), whose segments are then processed individually, using spectroscopy electronics. The energy and timing signals are digitized in a VME-based charge-to-digital converter and time-to-digital converter,

respectively. Also, here the design concept was based on the idea to start the performance characterization with a potentially optimum setup, yet quite complex, while the goal during the commissioning phase was to identify possibilities to relax some of the complexity without sacrificing performance. As will be discussed later, the PMT granularity turned out to be such a route towards reducing the complexity of the readout electronics at no performance losses. The Compton camera components are enclosed inside a copper plated box acting as a Faraday cage, providing an electric shielding against external electric fields. This box is equipped with a temperature monitoring system as well as a ventilation system based on a fan unit.

The $LaBr_3$:Ce scintillator was characterized with two crystal side-surface coating modalities (absorptive and reflective), aiming to identify the scenario providing the best performance for the Compton camera absorber detector. The spatially dependent energy resolution was investigated, revealing an excellent response for the case of the reflectively wrapped crystal, which was translated to an average energy resolution of ΔE / E = 3.8 % at 662 keV. With the same coating modality, the $LaBr_3$:Ce scintillator exhibited a superior time resolution of 273(6) ps (FWHM) that was measured using a coincident ^{60}Co source and a reference plastic detector. Moreover, the impact of the crystal coating options on the scintillation light behaviour inside the crystal was examined, using the light spread function (LSF) method. As could be expected, here the absorptively coated crystal showed a smaller value of the FWHM of the LSF, due to the ability of absorbing scattered light at either the corners or the side edges. Although the LSF was slightly degraded for the case of the reflectively wrapped $LaBr_3$:Ce scintillator, which, in fact, did not prevent the detector from resolving the movement of the tightly collimated source across the detector front face from the upper right to the bottom left corner (see Fig 4.4.4), the excellent properties obtained with the reflective coating modality motivated selecting this wrapping scenario to be used for the Compton camera absorbing detector.

In order to determine the photon interaction position inside the monolithic $LaBr_3$:Ce scintillator, which is a prerequisite to fulfill the Compton reconstruction requirements, specialized algorithms, namely the k-Nearest Neighbor (k-NN) algorithm and its improved version, the Categorical Average Pattern (CAP) method, developed at TU Delft, were implemented and adapted. These algorithms require a large reference library of 2D light amplitude distributions, determined by scanning the front face of the scintillator in a fine step size (0.5 mm) in x and y directions, using a tightly collimated (1 mm) radiation source. Two calibration sources, ^{137}Cs and ^{60}Co, were subsequently used to generate the required reference libraries in order to study the energy dependent spatial resolution of the $LaBr_3$:Ce scintillator. Besides the existing collimator (48 mm length, Densimet) adapted for 662 keV γ rays emitted from the ^{137}Cs source, a new collimation system, based on a cubic block of Densimet ($100 \times 100 \times 100$ mm^3) was constructed to host a ^{60}Co source with adequate shielding in all directions except the 1 mm collimation channel. The newly designed collimator was associated with modifications in the automatic scanning setup, where the $LaBr_3$:Ce scintillator was placed on a precision translation stage in front of the stationary collimated source. Also, the experimental protocol for acquiring the reference library needed to be optimized to enable the lengthy measurement campaigns realistically manageable.

The spatial resolution of the $LaBr_3$:Ce scintillator was determined by applying the so-called "leave-one-out" method, described in Sect. 5.1.1, to both the k-NN and CAP algorithms. In this study, the k-NN and CAP algorithms were investigated as a function of the number k of best matches among the 2D light amplitude distribution reference library and the number of photopeak events per irradiation position. Moreover, the impact of the scan pitch size (0.5 mm and 1 mm) of the reference library, as well as the energy of the impinging γ ray on the scintillator's spatial resolution were evaluated. It was also realized that the spatial resolution of the detector reached saturation for a reference library formed by more than 200 photopeak events

per irradiation position. Moreover, both the CAP and k-NN algorithms performed well with a reference library of 0.5 mm pitch size. Furthermore, the most important finding concerns the energy dependence of the spatial resolution. In a pessimistic approach one might have expected that a stronger illumination inside the monolithic crystal would render it more difficult to distinguish between closely neighboring photon interaction positions. In contrast, a considerable improvement of the detector's spatial resolution was observed with increasing energy of the incident photon. The best measured spatial resolution of the $LaBr_3$:Ce scintillator was found to be 3.7(1) mm (FWHM) at 1.3 MeV, applying the CAP algorithm. This even nourishes confidence in further improvement potential, as will be discussed in the following paragraph. Moreover, another important finding was related to the spatial resolution as a function of the PMT granularity. While our prototype detector was read out by a 256-fold (16×16) segmented photomultiplier tube, it turned out that a reduction to an 8×8 segmentation with only 64 segments provides an equal, if not even better spatial resolution. This will allow to reduce the readout electronics complexity in the future, in particular when aiming for an upgrade of the system towards a field of view applicable also for clinical application.

In addition, online commissioning of the Compton camera has been carried out at different particle beam facilities. Firstly, calibration and characterization studies of the individual camera components were performed at the Helmholtz-Zentrum Dresden-Rossendorf (HZDR) with monoenergetic 4.44 MeV γ rays, generated via the nuclear $^{15}N(p,\alpha\gamma)^{12}C^*$ reaction, which was associated with almost no background, thus providing a clean spectroscopic environment. In this γ-ray energy region, the $LaBr_3$:Ce scintillator revealed an excellent energy resolution, varying between 2.4 % and 2.2 %. For the DSSSD scatterer array, a gradual increase of the energy deposition of the Compton recoil electron was observed from the first layer to the last DSSSD layer in front of the absorber detector. Throughout the characterization study of both camera components with 4.44 MeV photons, their response was found in good agreement with Monte-Carlo (MC) simulations. The Compton camera was further characterized with prompt γ-rays induced from nuclear reactions between a 20 MeV proton beam and a water phantom, delivered by the Garching Tandem accelerator. The energy response of the $LaBr_3$:Ce scintillator to the impinging prompt γ rays was consistently matching the MC simulations. At the same accelerator facility, the time-of-flight (TOF) capability of the absorbing detector was investigated, using a 20 MeV pulsed (400 ns) deuteron beam hitting a water phantom, revealing prompt γ rays well separated from the slower neutrons. Finally, the performance of the LMU camera components was tested with different clinical proton beams (100 MeV, 160 MeV and 225 MeV), generated by the IBA C230 isochronous cyclotron operated at the Universtäts Protonen Therapie Dresden facility, stopping in either a water or a PMMA phantom. For all three proton beam energies, the registered prompt γ-ray energies in the $LaBr_3$:Ce scintillator were separated from the neutron induced background utilizing the TOF technique. The Compton recoil electrons were observed by the p-side strips of the DSSSD scatterer array, revealing again the expected sequential increase of the energy deposit intensity along the electron trajectory path. Due to a deficit in the signal processing readout electronics of the n-side strips, the Compton recoil electrons were mostly buried by the electronics' dark current noise. The performance of the scatterer array was further evaluated based on the p-side hit multiplicity, revealing that N_{strip} = 1 and 2 were dominant (ca 56% of all registered events) for the Compton electron energy region. From the energy correlation study between the 6 layers of DSSSD and the $LaBr_3$:Ce scintillator, the photon energy registered in the Compton camera absorber turned from a well-structured spectrum with closely resolved and prominent γ lines from photopeak, single- and double-escape both of the strong carbon (4.4 MeV) and oxygen (6.1 MeV) first excited states into an unstructured broad energy spectrum (see Fig. 7.1.1) when selecting only Compton-scattered events via a scatterer-absorber coincidence. Therefore, when aiming for a Compton event image reconstruction, one

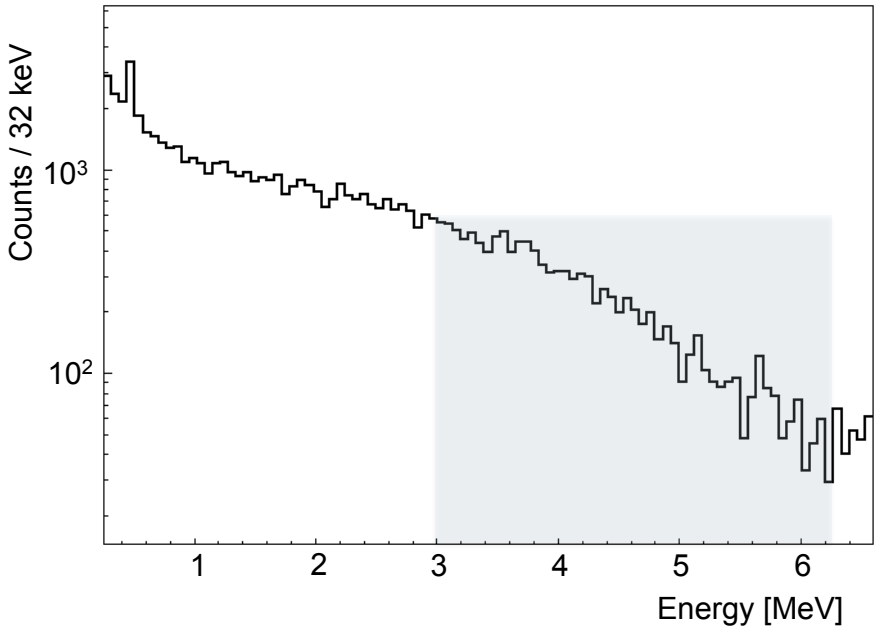

Figure 7.1.1: Prompt γ-ray energy spectrum measured by the $LaBr_3$:Ce scintillator for the case of at least one Compton scattering event observed in one of the six DSSSD layers during the irradiation of a water phantom by a 225 MeV proton beam. Obviously, the structured spectrum as shown in Fig. 6.4.6 was turned into a structureless energy distribution.

has to consider a broad prompt-γ energy window, (e.g. from 3-6.5 MeV as indicated by the shaded area in Fig. 7.1.1) rather than individual gates on the prompt-γ transition lines, as might be suggested by the peak structure of the initial energy spectrum.

7.2 Perspectives

7.2.1 Spatial resolution of the monolithic Compton camera absorbing detector

Since the energy dependent spatial resolution of the $LaBr_3$:Ce scintillator was determined in our laboratory studies with collimation sources for impinging γ rays ranging from 662 keV to 1.3 MeV with promising results and a trend of improving resolution with increasing energy, the interest should focus now to investigate the detector's spatial resolution with an even much higher photon energy in the range of the targeted prompt γ-ray energies ($\sim$ 5 MeV). This is not a trivial task, since a well-collimated multi-MeV photon beam is required with a special collimation system achieving as narrow as 1 mm collimator diameter. Moreover, a sufficiently intense photon beam is needed in order to acquire the reference library for the k-NN and the CAP algorithms in a reasonable time (i.e. in less than 1-2 weeks). These conditions can actually be achieved by exploiting the ultrahigh resolution γ-ray spectrometer GAMS6, which is installed in a beamline of the research reactor at the Institute Laue-Langevin (ILL) in Grenoble, France [118]. The multi-MeV γ rays are produced via an (n,γ) reaction, where production rate and energy depend on the chosen in-pile target. Then, the specific γ-ray energy can be selected through the GAMS6 setup, which is a high-precision γ-ray spectrometer based on a double crystal monochromator, equipped with a collimation system capable of providing a small beam spot of 1×1 mm^2.

In order to achieve the targeted γ-ray beam with a sufficient production rate, some considerations regarding the choice of the target material and the use of the GAMS6 spectrometer need to be taken into account. The target material should provide (after n capture) only a few γ lines in the energy range of interest, preferably separated with a sufficient energy distance larger than the resolution of the GAMS6 spectrometer. The appropriate choice for our application would be ^{12}C(n,γ)^{13}C , providing the highest and most intense transition line at 4945 keV. Here, the next γ-transition is located at 3684 keV, which is sufficiently far from the targeted line (4945 keV). The production rate of the desired transition can be enhanced with respect to the other γ-ray emissions by setting the appropriate angular resolution of the GAMS6 crystal spectrometer. The larger the angular acceptance of the spectrometer, the more photon throughput can be achieved. In our case, this condition would be much relaxed compared to the typical metrology-motivated high precision requirements of the instrument with only nano-rad acceptance and thus very restricted transmitted photon intensity. In our case, we could use a crystal with much relaxed precision requirements, in turn beneficial for the achievable photon-beam intensity. This photon intensity should be estimated in advance, since it will determine the time required to irradiate $\sim 10^4$ positions of the scintillator front face. Assuming a graphite target (12.6 g, surface of 36 cm^2) being exposed to of the neutron flux of the ILL reactor with a neutron capture rate of 2.5×10^{14}/s, the expected count rate behind a collimator of 1×1 mm^2 opening would be about 6×10^4/s. Moreover, the γ-ray beam angular divergence (0.3 mrad) behind the collimator and the Bragg angle (0.6 mrad), as well as the 10% assumed crystal reflectivity, would lead to a final count rate of about 2×10^3/s. From the 2D scan measurements performed earlier using ^{137}Cs and ^{60}Co, this estimated count rate would be sufficient to generate the required reference library of the 2D light amplitude distributions within a reasonable measurement time of a few days. In fact, this measurement will be performed in early 2017. We are confident to reach the targeted spatial resolution in the prompt-γ energy range of 3 mm (or even better) assisted by the increasing probability of pair creation with higher photon energies, thus providing a well-localized interaction scenario at higher photon energies.

7.2.2 Signal processing electronics of the Compton camera scatterer component

Throughout the characterization study of the stacked array of six double-sided silicon strip detectors (DSSSD), it has been realized that the registered signal of the Compton recoil electrons in the n-side strips was mostly buried by the noise of the signal processing electronics (based on the already aged GASSIPLEX-ASIC), despite the adaptation made for this electronics (see Sect. 3.2.2.2) to enable processing of negative input signals. A potential fast improvement could be reached by considering not only a ventilation of the detectors system as installed at present, but to consider cooling of both the detector and the electronics by installing an active cooling system based on a standard air conditioner. As discussed earlier, cryogenic cooling is not an option in view of the intended future application of the detector system in a clinical environment, where LN_2 based would not be tolerated. Already a reduction of the typical present operational temperature of about 26^o C by about 10-15 degrees could achieve a reduction of the electronic noise by more than a factor of two and maybe a better identification of the low-energy Compton electron signal. Such an installation would require a new design of the Compton camera Faraday cage, ensuring the electric shielding against an external strong electric field, also providing the light tightness conditions for the DSSSD detectors operated at air.
Alternatively, a complete replacement of the existing GASSIPLEX based electronics is under study at present. The new ASIC-based electronics candidate should be able to provide a trigger signal, have a high rate capability (in an ultimate and ideal detector configuration reading up

to a total rate throughput of about 1Mcps) and be able to process both negative and positive input signals. A first option under study is based on the AGET chip, which stands for ASIC for General Electronics for TPC (time projection chamber), developed at CEA (France) within the framework of a large international collaboration. At first glance, this ASIC provides all features that we are at present lacking with the GASSIPLEX-based signal processing. In its full version, this system is based on the μ-TCE bus standard, which originates from the telecommunication sector and should inherently be able to allow for a considerably higher data throughput than presently achievable with our VME-based DAQ system. Therefore, a 256-channel test system was acquired and used for first tests together with one module of the DSSSD detector array (conducted in the framework of another PhD thesis project). As it turns out, this readout system will not solve immediately all of our present limitations: probably most severe is the conceptual requirement to transfer the full signal trace of max. 512 data points to an external PC farm, where only then the energy determination by a suitable algorithm can be performed. Since our perspective goal is to provide an online information on the prompt-photon region position (and thus the position of the Bragg peak under therapeutic conditions), it may turn out to be inacceptable to invest this computational effort in view of the subsequent need of a not less computationally expensive determination of the spatial interaction of the impinging Compton-scattered photon in the absorbing scintillator. It would be highly desirable instead to leave the energy determination and digitization on the ASIC level. Thus present studies focus on the possibility to reduce the data output to a subset of the signal trace (with the prior knowledge of the expected energy range of the Compton-scattered electrons) and to a reduction of the event rate by a suitable threshold or trigger conditions. The latter also helps to reduce the dead time of the electronics, initially developed for TPC applications, where 50-100 μs dead time were acceptable.

Nevertheless, in view of the caveats still to be studied with the AGET-based electronics, also other options are considered. In doing this, also a conceptual perspective goal of merging the signal processing electronics of both scatter and absorber detectors into a common system should be considered. This would allow for a drastic reduction of the present complexity of the signal processing and data acquisition electronics, in particular desirable when aiming at an upgrade of the system towards a clinical applicable field of view (e.g. 20×20 cm^2 instead of the present 5×5 cm^2).

In addition to studying the performance of the AGET system, also other options are being considered. Concerning the data throughput necessities, the present restriction to maximum about 1 kcps is not given by the VME bus currently in use, but rather by the architecture of the associated DAQ software system and the controller module (VME CPU) that connects the VME environment to the outside world (DAQ PC). Here now commercial solutions are announced that promise to provide up to 128 MB/s data transfer rate, still based on VME electronics. This would be sufficient for our purpose, with the advantage that our present electronics environment could be used also in the future. In the same context a fully digitized electronics platform is envisaged to be introduced by a commercial supplier (mesytec) in the first half of 2017, that could allow the upgraded processing of scintillator and DSSSD data in the same framework. Otherwise, as in some concepts offered by other companies, a synchronization of the two event data streams from the absorber and scatterer would impose additional challenges. This central topic of an optimum future signal processing and data acquisition electronics for the Compton camera (usable under clinical rate conditions and scalable in the amount of signal channels to be handled) is part of an ongoing PhD thesis project [119].

7.2.3 Compton camera rate capability

A key issue of the envisaged Compton camera applications not only for pre-clinical small-animal irradiations, but also in a clinical treatment scenario, is the count rate capability of the detector system and its associated electronics. The latter is the bottleneck to be considered, since the scintillation material of the absorbing detector ($LaBr_3$:Ce) via its very short signal decay time of 16 ns is inherently capable of processing a high impinging photon flux, while the high granularity of the scatter detectors with individual signal processing also will allow for appropriate rate handling.
The actually occurring data rate for a clinical proton pencil-beam scanning scenario can be estimated as follows. The expected prompt γ-ray rate induced during a water phantom irradiation with a proton beam of 2 nA beam current ($\sim 1.2 \times 10^{10}$ protons/s measured at the beam nozzle [120]) can be calculated by knowing the prompt γ-ray production probability of about 0.16 γ rays /primary proton [120]. The resulting total prompt γ emission rate is 1.92×10^9 photons/s. About 30 % of these photons undergo Compton scattering while traveling through 16 cm of water, which represents the lateral length of the water for the case of the LMU water phantom. This percentage is estimated using the linear attenuation coefficient of 6.1 MeV photons interacting with water ($\mu_{L(water)}$ = 2.207×10^{-2}/cm). In a small-animal irradiation scenario, as anticipated for the future CALA laser driven proton irradiations, the solid angle covered by the Compton camera amounts to $\sim 8\%$ of 4π, which in a clinical situation would be reduced by another order of magnitude. Thus, the impinging photon rate would be ca. 1.5×10^8/s. Given the scattering probability of our DSSSD array (3 mm silicon in total) of about 1.5% (for the case of 6.1 MeV photons) and considering 40% total detection efficiency of the 3 cm thick $LaBr_3$:Ce scintillator, the coincidence trigger rate between scatterer and absorber will amount to $\sim 0.9 \times 10^6$/s. Therefore, it is safe to aim at a count rate and data transfer capability of ca. 1 Mcps. This rate should be handled with ideally less than 10% of deadtime.
From our present assessment of possible options, this goal appears to be achievable with already now or in the near future existing digital and compact electronics, as needed for an even upgraded and up-scaled Compton camera system.
So finally, the present thesis project resulted in a largely improved understanding of the Compton camera components's performance, together with the development of the technological and analysis tools to approach the initial design goals. In particular, the clinical topic of extracting the photon interaction position at rather large photon energies from a monolithic scintillator was brought to a very promising finding and a route has been identified for future improvement. From the various online characterization studies, the principle feasibility of the Compton electron tracking can be concluded, while critically needed upgrades of the signal readout electronics have been identified. This will also allow to develop the camera system another step closer to its transition into practical application, where a reduction of the electronic complexity and ideally a treatment of all detectors components in a joint signal and data processing chain will be desirable.
In that spirit, the current prototype detector system has already fulfilled a large portion of its envisaged duties, namely testing the limits of performance and identifying possibilities of relaxing its complexity without sacrificing quality. Thus one can be confident that prompt-γ medical imaging will continue to play a decisive role in the quest for the optimum diagnostic tool for in-vivo proton or ion beam range monitoring in hadron therapy.

Appendix A

List of publications and conference contributions

Publication

2014

P.G. Thirolf, C. Lang, S. Aldawood, H.G. v.d. Kolff, L. Maier, D.R. Schaart, K. Parodi, *Development of a Compton Camera for Online Range Monitoring of Laser-Accelerated Proton Beams via Prompt-Gamma Detection*, EPJ Web of Conferences 66, 11036 (2014).

2015

S. Aldawood, I. Castelhano, R. Gernhäuser, H. v.d. Kolff, C. Lang, R. Lutter, L. Maier, T. Marinšek, D.R. Schaart, K. Parodi, P.G. Thirolf, *Comparative characterization study of a $LaBr_3$(Ce) scintillation crystal in two surface wrapping scenarios: absorptive and reflective*, Frontiers in Oncology 5, 270 (2015).

2016

P.G. Thirolf, S. Aldawood, M. Böhmer, J. Bortfeldt, I. Castelhano, G. Dedes, F. Fiedler, R. Gernhäuser, C. Golnik, S. Helmbrecht, F. Hueso-Gonzalez, H. v.d. Kolff, T. Kormoll, C. Lang, S. Liprandi, R. Lutter, T. Marinšek, L. Maier, G. Pausch, J. Petzoldt, K. Römer, D. Schaart, K. Parodi, *Development of a Compton Camera Prototype for Medical Imaging*, EPJ Web of Conferences 117, 05005 (2016).

S. Aldawood, P.G. Thirolf, A. Miani, M. Böhmer, G. Dedes, R. Gernhäuser, C. Lang, S. Liprandi, T. Marinšek, L. Maier, D. Schaart, I. Valencia Lozano, K. Parodi, *Development of a Compton Camera for prompt-Gamma Medical Imaging*, submitted to Radiation Physics and Chemistry (2016).

Abstracts and conference proceedings

2016

A. Miani, S. Liprandi, S. Aldawood, T. Marinšek, L. Maier, C. Lang, H. van der Kolff, R. Lutter, R. Gernhäuser, D. R. Schaart, G. Dedes, K. Parodi, and P. G. Thirolf, *Study of the spatial resolution of methods for photon interaction position determination in a monolithic scintillator*, Verhandl. DPG (VI), 51, HK 45.33

S. Liprandi, S. Aldawood, A. Miani, T. Marinšek, I. Valencia, C. Lang, J. Bortfeldt, L. Maier, R. Lutter, R. Gernhäuser, D.R. Schaart, G. Pausch, F. Fiedler, W. Enghardt, G. Dedes, K. Parodi, and P.G. Thirolf, *Development of a Compton camera prototype for prompt gamma medical imaging*, Verhandl. DPG (VI), 51, HK 53.6

S. Aldawood, J. Bortfeldt, M. Böhmer, I. Castelhano, G. Dedes, W. Enghardt, F. Fiedler, R. Gernhäuser, C. Golnik, S. Helmbrecht, F. Hueso-Gonzalez, H. v. d. Kolff, T. Kormoll, C. Lang, S. Liprandi, R. Lutter, L. Maier, T. Marinšek, G. Pausch, J. Petzoldt, M. Pocevicius, K. Römer, I. Valencia Lozano, D.R. Schaart, K. Parodi and P.G. Thirolf, *Commissioning of a Compton camera for ion beam range verification via prompt-gamma detection using low-energy and clinical particle beams*, Radiation Therapy and Oncology 118, suppl. 1, s2 (2016), ISBN 0167-8140

2015

S. Aldawood, S. Liprandi, T. Marinšek, J. Bortfeldt, L. Maier, C. Lang, H. van der Kolff, I. Castelhano, R. Lutter, G. Dedes, R. Gernhäuser, D.R. Schaart, K. Parodi and P. G. Thirolf, *Development of a Compton Camera for online ion beam range verification via prompt γ detection*, Verhandl. DPG (VI) 50, HK 12.4 (2015).

S. Liprandi, S. Aldawood, T. Marinšek, J. Bortfeldt, L. Maier, C. Lang, H. van der Kolff, I. Castelhano, R. Lutter, G. Dedes, R. Gernhäuser, D.R. Schaart, K. Parodi and P. G. Thirolf, *Commissioning of the scatter component of a Compton camera consisting of a stack of Si strip detectors*, Verhandl. DPG (VI) 50, HK 48.48 (2015).

T. Marinšek, S. Aldawood, S. Liprandi, J. Bortfeldt, L. Maier, C. Lang, H. van der Kolff, I. Castelhano, R. Lutter, G. Dedes, R. Gernhäuser, D.R. Schaart, K. Parodi and P. G. Thirolf, *Characterization of a Compton camera $LaBr_3$ absorber detector*, Verhandl. DPG (VI) 50, HK 48.50 (2015).

P. Thirolf, T. Marinšek, S. Aldawood, M. Böhmer, J. Bortfeldt, I. Castelhano, R. Gernhäuser, H. van der Kolff, C. Lang, S. Liprandi, L. Maier, D.R. Schaart, K. Parodi, *Determination of the photon hit position in the monolithic absorber of a Compton camera*, DGMP, 2015.

2014

P.G. Thirolf, S. Aldawood, M. Böhmer, J. Bortfeldt, I. Castelhano, R. Gernhäuser, H. v.d. Kolff, C. Lang, L. Maier, D.R. Schaart, K. Parodi, *Status of the Compton Camera prototype for online*

range verification of proton beams, Joint Conference of the SSRMP, DGMP, OGMP, Zürich (Switzerland), September 7-10, 2014.

P.G. Thirolf, S. Aldawood, M. Böhmer, J. Bortfeldt, I. Castelhano, R. Gernhäuser, H. v.d. Kolff, C. Lang, L. Maier, D.R. Schaart and K. Parodi, *Development of a Compton Camera Prototype for Online Range Verification of Laser-Accelerated Proton Beams*, 56th Annual Meeting of AAPM, July 20-24, 2014, Austin (USA), Med. Phys. 41, 165 (2014).

S. Aldawood, C. Lang, H. v.d. Kolff, L. Maier, R. Lutter, J. Bortfeldt, K. Parodi, P.G. Thirolf, *Development of a Compton camera for online ion beam range verification via prompt γ detection*, Verhandl. DPG (VI) 49, HK 64.7 (2014).

B. Tegetmeyer, S. Aldawood, H. v.d. Kolff, C. Lang, K. Parodi, P. Thirolf, *Towards reaction cross section measurements of β^+ emitters produced in hadron therapy*, Verhandl. DPG (VI) 49, HK 46.38 (2014).

2013

P.G. Thirolf, S. Aldawood, C. Lang, K. Parodi, *Development of a Compton Camera for Online Range Monitoring of Laser-Accelerated Proton Beams*, Med. Phys. 40, 144 (2013).

P. Thirolf, C. Lang, S. Aldawood, H. v.d. Kolff, J. Bortfeldt, L. Maier, D.R. Schaart, K. Parodi, *Development of a Compton camera for online range monitoring of laser accelerated proton beams*, 44. Jahrestagung der Deutschen Gesellschaft für Medizinische Physik, Abstractband ISBN 978-3-9816002-1-6, p281-2 (2013).

P.G. Thirolf, C. Lang, S. Aldawood, D. Habs, L. Maier, K. Parodi, *Development of a Compton Camera for online monitoring and dosimetry of laser-accelerated proton beams*, Verhandl. DPG (VI) 48, HK 69.3 (2013).

S. Aldawood, C. Lang, D. Habs, L. Maier, K. Parodi, P.G. Thirolf, *Characterization of a $LaBr_3$ crystal with multi-anode PMT readout*, Verhandl. DPG (VI) 48, HK 52.7 (2013).

Bibliography

[1] J. C. Polf and K. Parodi. Imaging particle beams for cancer treatment. *Physics Today 68*, (10):28–33, 2015. doi: http://dx.doi.org/10.1063/PT.3.2945.

[2] W. C. Röntgen. On a new kind of rays. *Science 3*, (59):227–231, 1896. ISSN 0036-8075. doi: 10.1126/science.3.59.227.

[3] R. R. Wilson. Radiological use of fast protons. *Radiology 47*, (5):487–491, 1946. doi: 10.1148/47.5.487.

[4] A. N. Schreuder, S. G. Hedrick, J. R. Renegar, T. J. Netherton, M. D. Blakey H. C hen, M. E. Artz, B. H. Robison, A. G. Meek, and M Fagundes. A review of proton radiation therapy and the path to widespread clinical adoption. *Medical Physics International Journal 4*, (1):35–46, 2016. URL http://mpijournal.org/pdf/2016-01/MPI-2016-01-p035.pdf.

[5] M. Jermann. Particle therapy statistics in 2014. *International Journal of Particle Therapy 2*, (1):50–54, 2015. doi: 10.14338/IJPT-15-00013.

[6] E. Fokas, G. Kraft, H. An, and R. Engenhart-Cabillic. Ion beam radiobiology and cancer: Time to update ourselves. *Biochimica et Biophysica Acta (BBA) - Reviews on Cancer 1796*, 1796(2):216 – 229, 2009. ISSN 0304-419X. doi: http://dx.doi.org/10.1016/j.bbcan.2009.07.005.

[7] M. Engelsman, M. Schwarz, and L. Dong. Physics controversies in proton therapy. *Seminars in Radiation Oncology 23*, (2):88 – 96, 2013. ISSN 1053-4296. doi: http://dx.doi.org/10.1016/j.semradonc.2012.11.003.

[8] B. Schaffner and E. Pedroni. The precision of proton range calculations in proton radiotherapy treatment planning: experimental verification of the relation between CT-HU and proton stopping power. *Physics in Medicine and Biology 43*, (6):1579, 1998. URL http://stacks.iop.org/0031-9155/43/i=6/a=016.

[9] H. Paganetti. Range uncertainties in proton therapy and the role of Monte Carlo simulations. *Physics in Medicine and Biology 57*, (11):R99, 2012. URL http://stacks.iop.org/0031-9155/57/i=11/a=R99.

[10] F. H. González. *Nuclear methods for real-time range verification in proton therapy based on prompt gamma-ray imaging*. PhD thesis, Technical University Dresden, 2015.

[11] J. Tada, Y. Hayakawa, K. Hosono, and T. Inada. Time resolved properties of acoustic pulses generated in water and in soft tissue by pulsed proton beam irradiation—A possibility of doses distribution monitoring in proton radiation therapy. *Medical Physics 18*, pages 1100–1104, 1991. doi: 10.1118/1.596618.

[12] W. Assmann, S. Kellnberger, S. Reinhardt, S. Lehrack, A. Edlich, P. G. Thirolf, M. Moser, G. Dollinger, M. Omar, V. Ntziachristos, and K. Parodi. Ionoacoustic characterization of the proton bragg peak with submillimeter accuracy. *Medical Physics 42*, (2):567–574, 2015. doi: http://dx.doi.org/10.1118/1.4905047.

[13] S. Kellnberger, W. Assmann, S. Lehrack, S. Reinhardt, P. Thirolf, D. Queirós, G. Sergiadis, G. Dollinger, K. Parodi, and V. Ntziachristos. Ionoacoustic tomography of the proton Bragg peak in combination with ultrasound and optoacoustic imaging. *Scientific Reports 6*, page 29305, 2016. doi: http://dx.doi.org/10.1038/srep2930510.1038/srep29305.

[14] K. C. Jones, C. M. Seghal, and S. Avery. How proton pulse characteristics influence protoacoustic determination of proton-beam range: simulation studies. *Physics in Medicine and Biology 61*, (6):2213, 2016. URL http://stacks.iop.org/0031-9155/61/i=6/a=2213.

[15] F. Alsanea, V. Moskvin, and K. M. Stantz. Feasibility of RACT for 3D dose measurement and range verification in a water phantom. *Medical Physics 42*, (2):937–946, 2015. doi: 10.1118/1.4906241.

[16] H. D. Maccabee, U. Madhvanath, and M. R. Raju. Tissue activation studies with alpha-particle beams. *Physics in Medicine and Biology 14*, (2):213, 1969. URL http://stacks.iop.org/0031-9155/14/i=2/a=304.

[17] W. Enghardt, P. Crespo, F. Fiedler, R. Hinz, K. Parodi, J. Pawelke, and F Pönisch. Charged hadron tumour therapy monitoring by means of PET. *Nuclear Instruments and Methods in Physics Research Section 525*, (12):284 – 288, 2004. ISSN 0168-9002. doi: http://dx.doi.org/10.1016/j.nima.2004.03.128.

[18] K. Parodi, H. Paganetti, H. A. Shih, S. Michaud, J. S. Loeffler, T. F. DeLaney, N. J. Liebsch, J. E. Munzenrider, A. J. Fischman, A. Knopf, and T. Bortfeld. Patient study of in vivo verification of beam delivery and range, using positron emission tomography and computed tomography imaging after proton therapy. *International Journal of Radiation Oncology Biology Physics 68*, (3):920 – 934, 2007.

[19] X. Zhu and G. E. Fakhri. Proton therapy verification with pet imaging. *Theranostics 3*, (10):731–740, 2013. doi: 10.7150/thno.5162.

[20] W. Enghardt et al. Charged hadron tumour therapy monitoring by means of PET. *Nucl. Instrum. Methods A*, 525:284–288, 2004.

[21] K. Parodi et al. Comparison between in-beam and offline positron emission tomography imaging of proton and carbon ion therapeutic irradiation at synchrotron- and cyclotron-based facilities. *Int. J. Radiat Oncol. Biol. Phys. 71*, pages 945–56, 2008.

[22] J. Pawelke, W. Enghardt, T. Haberer, B. G. Hasch, R. Hinz, M. Kramer, E. Lauckner, and M. Sobiella. In-beam PET imaging for the control of heavy-ion tumour therapy. *IEEE Transactions on Nuclear Science 44*, (4):1492–1498, 1997. ISSN 0018-9499. doi: 10.1109/23.632694.

[23] Y. Iseki, H. Mizuno, Y. Futami, T. Tomitani, T. Kanai, M. Kanazawa, A. Kitagawa, T. Murakami, T. Nishio, M. Suda, E. Urakabe, A. Yunoki, and H. Sakai. Positron camera for range verification of heavy-ion radiotherapy. *Nuclear Instruments and Methods in*

Physics Research 515, (3):840 – 849, 2003. ISSN 0168-9002. doi: http://dx.doi.org/10.1016/j.nima.2003.07.005.

[24] T. Yamaya, T. Inaniwa, E. Yoshida, F. Nishikido, K. Shibuya, N. Inadama, and H. Murayama. Simulation studies of a new 'OpenPET' geometry based on a quad unit of detector rings. *Physics in Medicine and Biology 54*, (5):1223, 2009. URL http://stacks.iop.org/0031-9155/54/i=5/a=008.

[25] H. Tashima, T. Yamaya, E. Yoshida, S. Kinouchi, M. Watanabe, and E. Tanaka. A single-ring OpenPET enabling PET imaging during radiotherapy. *Physics in Medicine and Biology 57*, (14):4705, 2012. URL http://stacks.iop.org/0031-9155/57/i=14/a=4705.

[26] X. Zhu, S. España, H. Paganetti, T. Bortfeld, N. Liebsch, H. Shih, and G. El Fakhri. First in-room pet studies for range verification of proton therapy. *Journal of Nuclear Medicine 51*, (supplement 2):519, 2010. URL http://jnm.snmjournals.org/content/51/supplement_2/519.abstract.

[27] C. H. Min, C. H. Kim, M. Y. Youn, and J. W. Kim. Prompt gamma measurements for locating the dose falloff region in the proton therapy. *Applied Physics Letters 89*, (18):183517, 2006. doi: http://dx.doi.org/10.1063/1.2378561.

[28] J. Smeets, F. Roellinghoff, D. Prieels, F. Stichelbaut, A. Benilov, P. Busca, C. Fiorini, R. Peloso, M. Basilavecchia, T. Frizzi, J. C. Dehaes, and A. Dubus. Prompt gamma imaging with a slit camera for real-time range control in proton therapy. *Physics in Medicine and Biology 57*, (11):3371, 2012. URL http://stacks.iop.org/0031-9155/57/i=11/a=3371.

[29] I. Perali. *A prompt gamma camera for real-time range control in Proton Therapy*. PhD thesis, Politecnico Di Milano, 2015.

[30] J. Smeets. *Prompt gamma imaging with a slit camera for real time range control in particle therapy*. PhD thesis, Université Libre de Bruxelles, 2012.

[31] Center for Radiation Research in Oncology (OncoRay). Available at: http://oncoray.de/, Accessed: October 2016.

[32] C. Richter, G. Pausch, S. Barczyk, M. Priegnitz, I. Keitz, J. Thiele, J. Smeets, F. V. Stappen, L. Bombelli, C. Fiorini, L. Hotoiu, I. Perali, D. Prieels, W. Enghardt, and M. Baumann. First clinical application of a prompt gamma based in vivo proton range verification system. *Radiotherapy and Oncology 118*, (2):232 – 237, 2016. ISSN 0167-8140. doi: http://dx.doi.org/10.1016/j.radonc.2016.01.004.

[33] J. M. Verburg and J. Seco. Proton range verification through prompt gamma-ray spectroscopy. *Physics in Medicine and Biology 59*, (23):7089, 2014. URL http://stacks.iop.org/0031-9155/59/i=23/a=7089.

[34] J. Verburg. *Reducing Range Uncertainty in Proton Therapy*. PhD thesis, Eindhoven University of Technology, 2015.

[35] C. Golnik, F. Hueso-González, A. Müller, P. Dendooven, W. Enghardt, F. Fiedler, T. Kormoll, K. Roemer, J. Petzoldt, A. Wagner, and G. Pausch. Range assessment in particle therapy based on prompt γ-ray timing measurements. *Physics in Medicine and Biology 59*, (18):5399, 2014. URL http://stacks.iop.org/0031-9155/59/i=18/a=5399.

[36] F. Hueso-González, W. Enghardt, F. Fiedler, C. Golnik, G. Janssens, J. Petzoldt, D. Prieels, M. Priegnitz, K. Römer, J. Smeets, F. V. Stappen, A. Wagner, and G. Pausch. First test of the prompt gamma ray timing method with heterogeneous targets at a clinical proton therapy facility. *Physics in Medicine and Biology 60*, (16):6247, 2015. URL http://stacks.iop.org/0031-9155/60/i=16/a=6247.

[37] F. Hueso-González, F. Fiedler, C. Golnik, T. Kormoll, G. Pausch, J. Petzoldt, K. E. Römer, and W. Enghardt. Compton camera and prompt gamma ray timing: Two methods for in vivo range assessment in proton therapy. *Frontiers in Oncology 6*, page 80, 2016. ISSN 2234-943X. doi: 10.3389/fonc.2016.00080.

[38] C. Lang. *Design of a Compton camera for medical imaging and characterization of its components*. PhD thesis, LMU Munich, 2015.

[39] A.C. Zoglauer. *First light for the next generation of Compton and pair telescopes*. PhD thesis, Technical University Munich, 2005.

[40] G. Kanbach, R. Andritschke, A. Zoglauer, M. Ajello, M.L. McConnell, J.R. Macri, J.M. Ryan, P. Bloser, S. Hunter, G. DiCocco, J. Kurfess, and V. Reglero. Development and calibration of the tracking compton/pair telescope MEGA. *Nuclear Instruments and Methods in Physics Research 541*, (12):310 – 322, 2005. ISSN 0168-9002. doi: http://dx.doi.org/10.1016/j.nima.2005.01.071.

[41] J. Krimmer, J.-L. Ley, C. Abellan, J.-P. Cachemiche, L. Caponetto, X. Chen, M. Dahoumane, D. Dauvergne, N. Freud, B. Joly, D. Lambert, L. Lestand, J.M. Ltang, M. Magne, H. Mathez, V. Maxim, G. Montarou, C. Morel, M. Pinto, C. Ray, V. Reithinger, E. Testa, and Y. Zoccarato. Development of a Compton camera for medical applications based on silicon strip and scintillation detectors. *Nuclear Instruments and Methods in Physics Research 787*, pages 98 – 101, 2015. ISSN 0168-9002. doi: http://dx.doi.org/10.1016/j.nima.2014.11.042.

[42] M. H. Richard, M. Dahoumane, D. Dauvergne, G. Dedes, M. De Rydt, N. Freud, J. M. Ltang, X. Lojacono, J. Krimmer, V. Maxim, G. Montarou, C. Ray, F. Roellinghoff, E. Testa, and A. H. Walenta. Design study of the absorber detector of a Compton camera for on-line control in ion beam therapy. In *Nuclear Science Symposium and Medical Imaging Conference (NSS/MIC),IEEE*, 2011. doi: 10.1109/NSSMIC.2011.6152642.

[43] M.H. Richard. *Design study of a Compton Camera for prompt-gamma imaging during ion-beam therapy*. PhD thesis, University Lyon, 2012.

[44] T. Kormoll. *A Compton Camera For In-Vivo Dosimetry in Ion-Beam Radiotherapy*. PhD thesis, Technical University Dresden, 2012.

[45] C. Golnik, D. Bemmerer, W. Enghardt, F. Fiedler, F. Hueso-González, G. Pausch, K. Römer, H. Rohling, S. Schöne, L. Wagner, and T. Kormoll. Tests of a Compton imaging prototype in a monoenergetic 4.44 MeV photon field—a benchmark setup for prompt gamma-ray imaging devices. *Journal of Instrumentation 11*, (06):P06009, 2016. URL http://stacks.iop.org/1748-0221/11/i=06/a=P06009.

[46] G. Llosá, M. Trovato, J. Barrio, A. Etxebeste, E. Muñoz, C. Lacasta, J. F. Oliver, M. Rafecas, C. Solaz, and P. Solevi. First images of a three-layer Compton telescope prototype for treatment monitoring in hadron therapy. *Frontiers in Oncology 6*, page 14, 2016. ISSN 2234-943X. doi: 10.3389/fonc.2016.00014.

[47] P. Solevi, E. Muñoz, C. Solaz, M. Trovato, P. Dendooven, J. E. Gillam, C. Lacasta, J. F. Oliver, M. Rafecas, I. Torres-Espallardo, and G. Llosá. Performance of MACACO Compton telescope for ion-beam therapy monitoring: first test with proton beams. *Physics in Medicine and Biology 61*, (14):5149, 2016. URL http://stacks.iop.org/0031-9155/61/i=14/a=5149.

[48] J. C. Polf, S. Avery, D. S. Mackin, and S. Beddar. Imaging of prompt gamma rays emitted during delivery of clinical proton beams with a compton camera: feasibility studies for range verification. *Physics in Medicine and Biology 60*, (18):7085, 2015. URL http://stacks.iop.org/0031-9155/60/i=18/a=7085.

[49] M. McCleskey, W. Kaye, D.S. Mackin, S. Beddar, Z. He, and J.C. Polf. Evaluation of a multistage cdznte compton camera for prompt γ imaging for proton therapy. *Nuclear Instruments and Methods in Physics Research 785*, pages 163 – 169, 2015. ISSN 0168-9002. doi: http://dx.doi.org/10.1016/j.nima.2015.02.030.

[50] S. Kabuki, K. Hattori, R. Kohara, E. Kunieda, A. Kubo, H. Kubo, K. Miuchi, T. Nakahara, T. Nagayoshi, H. Nishimura, Y. Okada, R. Orito, H. Sekiya, T. Shirahata, A. Takada, T. Tanimori, and K. Ueno. Development of electron tracking Compton camera using micro pixel gas chamber for medical imaging. *Nuclear Instruments and Methods in Physics Research 580*, (2):1031 – 1035, 2007. ISSN 0168-9002. doi: http://dx.doi.org/10.1016/j.nima.2007.06.098.

[51] S. Kurosawa, H. Kubo, K. Ueno, S. Kabuki, S. Iwaki, M. Takahashi, K. Taniue, N. Higashi, K. Miuchi, T. Tanimori, D. Kim, and J. Kim. Prompt gamma detection for range verification in proton therapy. *Current Applied Physics 12*, (2):364 – 368, 2012. ISSN 1567-1739. doi: http://dx.doi.org/10.1016/j.cap.2011.07.027.

[52] P. G. Thirolf, C. Lang, S. Aldawood, H.G. v.d. Kolff, L. Maier, D.R. Schaart, and K. Parodi. Development of a Compton camera for online range monitoring of laser-accelerated proton beams via prompt-gamma detection. *EPJ Web of Conferences 66 (2014) 11036*. URL http://dx.doi.org/10.1051/epjconf/20146611036.

[53] C. Lang, D. Habs, K. Parodi, and P. G. Thirolf. Sub-millimeter nuclear medical imaging with high sensitivity in positron emission tomography using beta+gamma coincidences. *Journal of Instrumentation 9*, art. P01008, 2014. ISSN 1748-0221. doi: 10.1088/1748-0221/9/01/P01008.

[54] Center for Advanced Laser Applications (CALA). Available at: http://www.lex-photonics.de/cala/, Accessed: November 2016.

[55] G.F. Knoll. *Radiation detection and measurement*. John Wiley & Sons, 4 edition, 2010.

[56] National Institute of Standards and Technology, Standard Reference Data Program. http://www.physics.nist.gov/PhysRefData/Xcom/html/xcom1.html.

[57] G. Weber. Compton scattering calculator. Available at: http://web-docs.gsi.de/~stoe_exp/web_programs/compton/index.php , Accessed: October 2016.

[58] E. B. Podgoršak. *Radiation Physics for Medical Physicists*. Springer, 2 edition, 2010.

[59] Jesse W. M. Du Mond. Compton modified line structure and its relation to the electron theory of solid bodies. *Phys. Rev. 33*, pages 643–658, 1929. doi: 10.1103/PhysRev.33.643.

[60] R Ribberfors. Relationship of the relativistic compton cross section to the momentum distribution of bound electron states. *Phys. Rev. B, 12, pp. 2067-2074*, 1975. doi: 10.1103/PhysRevB.12.2067.

[61] A. Zoglauer and G. Kanbach. Doppler broadening as a lower limit to the angular resolution of next-generation compton telescopes. *Proc. SPIE 4851*, pages 1302–1309, 2003. doi: 10.1117/12.461177.

[62] M. J. Berger and S. M. Seltzer. Tables of energy losses and ranges of electrons and positrons. Technical Report NASA-SP-3012, NASA, 2004.

[63] National Institute of Standards and Technology, Standard Reference Data Program, PSTART. http://www.physics.nist.gov/PhysRefData/Star/Text/PSTAR.html.

[64] U. Fano. Ionization yield of radiations. ii. the fluctuations of the number of ions. *Phys. Rev. 72*, pages 26–29, 1947. doi: 10.1103/PhysRev.72.26.

[65] S. Takeda, Takahashi T., Watanabe S., Tajima H., Tanaka T., Nakazawa K., and Y Fukazawa. Double-sided silicon strip detector for x-ray imaging. *SPIE Newsroom*, Feb 2008. doi: 10.1117/2.1200802.0889.

[66] G. Bizarri, J.T.M. de Haas, P. Dorenbos, and C.W.E. van Eijk. Scintillation properties of ø1x;1 inch 3 $LaBr_3$:5% Ce $^{3+}$ crystal. *IEEE Transactions on Nuclear Science 53*, (2): 615–619, 2006. ISSN 0018-9499. doi: 10.1109/TNS.2006.870090.

[67] S. Tavernier et al. *Radiation detectors for medical imaging*. Springer, 2006.

[68] K.S. Shah. $CeBr_3$ scintillator, 2008. URL http://www.google.com/patents/US7405404. US Patent 7,405,404.

[69] G. Kanbach and MEGA Collaboration. MEGA-A next generation mission in medium energy gamma-ray astronomy. *AIP Conference Proceedings 587*, (1):887–891, 2001. doi: http://dx.doi.org/10.1063/1.1419516.

[70] R. Brun and F. Rademakers. ROOT - and object oriented data analysis framework. *Nucl. Instr. Meth.*, 389:81–86, 1997.

[71] CiS. Forschungsinstitut für Mikrosensorik und Photovoltaik GmbH, 2016. Available at: http://www.cismst.org.

[72] MHV-4 data sheet, 2016. http://www.mesytec.com/products/datasheets/MHV-4.pdf.

[73] Inc. Saint-Gobain Ceramics and Plastics. BrilLanCe^{TM} 380 scintillation material, 2004.

[74] Hamamatsu H9500 PMT data sheet. Available at: http://www.hamamatsu.com/resources/pdf/etd/H9500_H9500-03_TPMH1309E.pdf, Accessed: October 2016.

[75] E.V.D van Loef, P. Dorenbos, C.W.E van Eijk, K.W Krämer, and H.U Güdel. Scintillation properties of $LaBr_3$:Ce^{3+} crystals: fast, efficient and high-energy-resolution scintillators. *Nucl. Instr. Meth. A 486*, pages 254 – 258, 2002. ISSN 0168-9002. doi: http://dx.doi.org/10.1016/S0168-9002(02)00712-X.

[76] K.S. Shah, J. Glodo, M. Klugerman, W.W. Moses, S.E. Derenzo, and M.J. Weber. $LaBr_3$:Ce scintillators for gamma-ray spectroscopy. *IEEE Transactions on Nuclear Science 50*, (6):2410–2413, 2003. ISSN 0018-9499. doi: 10.1109/TNS.2003.820614.

[77] W.M. Higgins, A. Churilov, E. van Loef, J. Glodo, M. Squillante, and K. Shah. Crystal growth of large diameter $LaBr_3$:Ce and $CeBr_3$. *Journal of Crystal Growth 310*, (7–9): 2085–2089, 2008. ISSN 0022-0248. doi: 10.1016/j.jcrysgro.2007.12.041.

[78] I. Mazumdar, D.A. Gothe, G. Anil Kumar, N. Yadav, P.B. Chavan, and S.M. Patel. Studying the properties and response of a large volume (946 cm^3) $LaBr_3$:Ce detector with up to 22.5 MeV. *Nucl. Instr. Meth. A 705*, pages 85 – 92, 2013. ISSN 0168-9002. doi: http://dx.doi.org/10.1016/j.nima.2012.12.093.

[79] A.A. Sonzogni. Nuclear Data Sheets for A = 138. *Nuclear Data Sheets*, 98(3):515–664, 2003. ISSN 0090-3752. doi: 10.1006/ndsh.2003.0004. URL http://www.sciencedirect.com/science/article/pii/S0090375203900044.

[80] F.G.A. Quarati, I.V. Khodyuk, C.W.E. van Eijk, P. Quarati, and P. Dorenbos. Study of ^{138}La radioactive decays using $LaBr_3$ scintillators. *Nucl. Instr. Meth.*, 683:46–52, 2012.

[81] 2000 GASSIPLEX, a 16 integrated channels front-end analog amplifiers with multiplexed serial readout. Ref. PC 2000/107 , http://www-subatech.in2p3.fr.

[82] K. Zeitelhack, A. Elhardt, J. Friese, R. Gernhäuser, J. Homolka, A. Kastenmüller, P. Kienle, H.-J. Körner, P. Maier-Komor, M. Münch, W. Przygoda, W. Schön, A. Ulrich, and J. Wieser. The HADES RICH detector. *Nuclear Instruments and Methods in Physics Research Section A: Accelerators, Spectrometers, Detectors and Associated Equipment*, 433(12):201 – 206, 1999. ISSN 0168-9002. doi: http://dx.doi.org/10.1016/S0168-9002(99)00371-X. URL http://www.sciencedirect.com/science/article/pii/S016890029900371X.

[83] CES Creative Electronics Systems. RIO3 8064 datasheet, 2000.

[84] A. Kastenmüller, M. Böhmer, J. Friese, R. Gernhäuser, J. Homolka, P. Kienle, H.-J. Körner, D. Maier, M. Münch, C. Theurer, and K. Zeitelhack. Fast detector readout for the hades-rich. *Nuclear Instruments and Methods in Physics Research Section A: Accelerators, Spectrometers, Detectors and Associated Equipment*, 433(12):438 – 443, 1999. ISSN 0168-9002. doi: http://dx.doi.org/10.1016/S0168-9002(99)00321-6. URL http://www.sciencedirect.com/science/article/pii/S0168900299003216.

[85] E. L. Holzman. Wideband measurement of the dielectric constant of an fr4 substrate using a parallel-coupled microstrip resonator. *IEEE Transactions on Microwave Theory and Techniques*, 54(7):3127–3130, July 2006. ISSN 0018-9480. doi: 10.1109/TMTT.2006.877061.

[86] Megtron 6 data sheet, 2016. http://www.matrixelectronics.comwp-contentuploads201506/15060431_MEG6_R-5775_R-5670.pdf.

[87] Megtron 7 data sheet, 2016. http://industrial.panasonic.com/ww/products/electronic-materials/circuit-board-materials/megtron/megtron7.

[88] A. Kastenmüller. 64-channel preprocessing frontend module. Technical University Munich, 2001, http://www.e12.ph.tum.de/ gernhaus/projects/pfm/pfm.pdf, 2001.

[89] Burr-Brown Corporation. 10-bit, 20 MHz Sampling Analog-to-Digital Converter, last access Mar. 2016. http://www.ti.com.

[90] Elantec. EL4441C data sheet, last access Mar. 2016. http://www.e12.ph.tum.de/ mboehmer.

[91] M. Hoek, L. Rubáček, M. Düren, M. Hartig, T. Keri, S. Lu, B. Seitz, W. Sommer, and H. Stenzel. Performance and response of scintillating fiber modules to protons and pions. *Nuclear Instruments and Methods in Physics Research Section 572*, (2):808 – 816, 2007. ISSN 0168-9002. doi: http://dx.doi.org/10.1016/j.nima.2006.12.023.

[92] J. Bortfeldt. Development of micro -pattern gaseous detectors - micromegas. Diploma thesis, LMU Munich, 2010.

[93] M. Böhmer. Das Auslesesystem für den ringabbildenden Cerenkovdetektor im HADES Spektrometer. Diploma thesis, Technical University Munich, 1999.

[94] MCFD-16 data sheet, 2016. http://www.mesytec.com/datasheets/MCFD-16.pdf, Accessed: October 2016.

[95] MTDC-32 data sheet, 2016. http://www.mesytec.com/datasheets/MQDC-32.pdf, Accessed: October 2016.

[96] MTDC-32 data sheet, 2016. http://www.mesytec.com/datasheets/MTDC-32.pdf, Accessed: October 2016.

[97] J. Hoffmann, N. Kurz, and M. Richter. Triva 5 VME trigger module, 2009.

[98] H. G. Essel and N. Kurz. The general purpose data acquisition system mbs. *IEEE Transactions on Nuclear Science*, 47(2):337–339, Apr 2000. ISSN 0018-9499. doi: 10.1109/23.846176.

[99] R. Lutter, O. Schaile, K. Schoffel, K. Steinberger, P. Thirolf, and C. Broude. Maraboou - a mbs and root based online/offline utility. *IEEE Transactions on Nuclear Science*, 47 (2):280–283, Apr 2000. ISSN 0018-9499. doi: 10.1109/23.846164.

[100] item Industrietechnik GmbH. Profiles, 2016. Available at: http://product.item24.de/en/products/product-catalogue/products/profiles.html.

[101] Pico Technology. PT-104 Data Logger Data Sheet, 2016. Available at: https://www.picotech.com/download/datasheets/usbpt104pg.en-2.pdf.

[102] P. L. Reeder and D. C. Stromswold. Performance of large nai(tl) gamma-raydetectors over temperature-50°c to +60°c ". Pacific Northwest National Laboratory report PPNL14735, Available at: http://www.pnl.gov/main/publications/external/technical_reports/pnnl14735.pdf, 2004.

[103] M. Moszynski, J. Zalipska, M. Balcerzyk, M. Kapusta, W. Mengesha, and J.D. Valentine. Intrinsic energy resolution of nai(tl)1. *Nucl. Instr. Meth. A*, 484(13):259 – 269, 2002. ISSN 0168-9002. doi: http://dx.doi.org/10.1016/S0168-9002(01)01964-7. URL http://www.sciencedirect.com/science/article/pii/S0168900201019647.

[104] R. Pani, M.N. Cinti, R. Scafé, R. Pellegrini, F. Vittorini, P. Bennati, S. Ridolfi, S. Lo Meo, M. Mattioli, G. Baldazzi, F. Pisacane, F. Navarria, G. Moschini, P. Boccaccio, V. Orsolini Cencelli, and D. Sacco. Energy resolution measurements of $LaBr_3$:Ce scintillating crystals with an ultra-high quantum efficiency photomultiplier tube. *Nucl. Instr. Meth. A 610*, (1):41 – 44, 2009. ISSN 0168-9002. doi: http://dx.doi.org/10.1016/j.nima.2009.05.058.

[105] A. Kuhn, S. Surti, J.S. Karp, P.S. Raby, K.S. Shah, A.E. Perkins, and G. Muehllehner. Design of a lanthanum bromide detector for time-of-flight PET. *IEEE Transactions on Nuclear Science 51*, (5):2550–2557, 2004. ISSN 0018-9499. doi: 10.1109/TNS.2004.835777.

[106] Woon-Seng Choong. Timing resolution of scintillation-detector systems: a Monte Carlo analysis. *Physics in medicine and biology 54 (21) 2009*, (21):6495. ISSN 0031-9155. doi: 10.1088/0031-9155/54/21/004.

[107] P. Lecoq, E. Auffray, S. Brunner, H. Hillemanns, P. Jarron, A. Knapitsch, T. Meyer, and F. Powolny. Factors influencing time resolution of scintillators and ways to improve them. *IEEE Transactions on Nuclear Science 57*, (5):2411–2416, 2010. ISSN 0018-9499. doi: 10.1109/TNS.2010.2049860.

[108] B.D. Milbrath, B.J. Choate, J.E. Fast, W.K. Hensley, R.T. Kouzes, and J.E. Schweppe. Comparison of $LaBr_3$:Ce and NaI(Tl) scintillators for radio-isotope identification devices. *Nucl. Instr. Meth. A 572*, (2):774–784, 2007. ISSN 0168-9002. doi: 10.1016/j.nima.2006.12.003.

[109] H.T. van Dam et al. Improved nearest neighbor methods for gamma photon interaction position determination in monolithic scintillator PET detectors. *IEEE Transactions on Nuclear Science*, 58(5):2139–2147, October 2011.

[110] DENSIMET-INERMET Manual. Available at: https://www.plansee.com/pdfs/Densimet_Inermet_forShieldingandAerospace.pdf, Accessed: September 2016.

[111] Tungsten Carbide Gardes, Hartmetall®-Gesellschaft. Available at: https:http://www.hmtg.com/catalog/round.hartmetall, Accessed: September 2016.

[112] Michele Marta, Erik Trompler, Daniel Bemmerer, Roland Beyer, Carlo Broggini, Antonio Caciolli, Martin Erhard, Zsolt Fülöp, Eckart Grosse, György Gyürky, Roland Hannaske, Arnd R. Junghans, Roberto Menegazzo, Chithra Nair, Ronald Schwengner, Tamás Szücs, Simone Vezzú, Andreas Wagner, and Dmitry Yakorev. Resonance strengths in the $^{14}\mathrm{N}(p,\gamma)^{15}\mathrm{O}$ and $^{15}\mathrm{N}(p,\alpha\gamma)^{12}\mathrm{C}$ reactions. *Phys. Rev. C 81*, page 055807, 2010. doi: 10.1103/PhysRevC.81.055807.

[113] B. Kozlovsky et al. Nuclear deexcitation gamma-ray lines from accelerated particle interactions. *Astrophysics J. 141*, pages 523–541, 2002.

[114] D. Pelte and D. Schwalm. *In-beam γ- ray spectroscopy with heavy ions, Vol. 3, Heavy Ion Collisions, ed. R. Bock*. North Holland Publishing, 1982.

[115] Ion Beam Application SA (IBA). Available at: https://iba-worldwide.com/, Accessed: October 2016.

[116] J. M. Verburg, K. Riley, T. Bortfeld, and J. Seco. Energy- and time-resolved detection of prompt gamma-rays for proton range verification. *Physics in Medicine and Biology 58*, (20):L37, 2013. URL http://stacks.iop.org/0031-9155/58/i=20/a=L37.

[117] J. C. Polf, R. Panthi, D. S. Mackin, M. McCleskey, A. Saastamoinen, B. T. Roeder, and S. Beddar. Measurement of characteristic prompt gamma rays emitted from oxygen and carbon in tissue-equivalent samples during proton beam irradiation. *Physics in Medicine and Biology 58*, (17):5821, 2013. URL http://stacks.iop.org/0031-9155/58/i=17/a=5821.

[118] Institute Laue-Langevin (ILL). Available at: https://www.ill.eu/ Accessed: October 2016.

[119] S. Liprandi. *In preparation*. PhD thesis, LMU Munich, 2017.

[120] F. Hueso-Gonzalez, G. Pausch, J. Petzoldt, K. E. Roemer, and W. Enghardt. Prompt gamma rays detected with a BGO block Compton camera reveal range deviations of therapeutic proton beams. *IEEE Transactions on Nuclear Science PP*, (99):1–1, 2016. ISSN 0018-9499. doi: 10.1109/TNS.2016.2622162.

Acknowledgements

Without giving thanks, the blessings would not appear. This study appears in its current form due to the guidance of my advisor, assistance from my family and support from other people. Many thanks are giving to those people who have been with me during my study.
I would like to express my deepest appreciation and thanks to my supervisor PD Dr. Peter G. Thirolf for his endless support during my PhD study. His encouragement, motivation, patience, guidance and the infinite experimental advice helped me in writing this thesis. Being a member of Peter's group has enriched my physics experience.
I would like to take this opportunity to thank Prof. Dr. Katia Parodi for her encouragement, guidance, valuable feedback, insightful comments and suggestions during either the group seminar or our special Compton camera meeting.
I am grateful to Dr. Ludwig Maier, Dr. Michael Böhmer and Dr. Jonathan Bortfeldt for not only proving us with the readout electronics of the Compton camera scatterer array, but also for the continuous support during the operation phase. This task would have not been completed without the big support from Mr. Rudi Lutter, who did a great job in implementing the borrowed readout electronics in the software of our DAQ system in a very short time. I am thankful to him for giving me the spirit to learn and improve my programming skills. Also, I would like to thank Dr. Otto Schaile for his much valuable advice during the analysis of my experimental data.
The work of my thesis would have not been completed without the support provided by the LMU electronics and hardware workshop. So, I am deeply grateful to Mr. Johann Krapfl , Mr Rolf Oehm and their teams for their help and advice regarding the design and manufacturing the required components for the Compton camera. Moreover, special thanks go to the staff member of the MLL Tandem accelerator lab for their assistance and support during my experimental beam times.
In addition, I would like to thank the team members of our Compton camera project for sharing not only their scientific knowledge, but also their social life. Many thanks go to Dr. Christian Lang for introducing me to the Compton camera lab and DAQ system. My thanks also go to Silvia Liprandi, who joined the team two years ago as a PhD student, for her kindness, support and valuable discussion. I appreciate her kind and warm invitation to her home town Milan and I will keep it in my consideration in the near future. Special thanks are giving to present and past MSc students, namely Hugh von der Kolff, Ines Castelhano, Tim Marinšek, Agnese Miani, Michael Mayerhofer and Tim Binder. It has been a great experience to work with them.
I greatly appreciate Dr. George Dedes for introducing me to the GEANT4 simulation toolkit and for the fruitful discussion during our regular Compton camera meeting.
I owe many thanks to king Saud University (KSU) for funding my PhD study. I hope I can benefit and serve this university in future.
Also, my sincere thanks go to Andrea Leinthaler who eased all administrative works during the period of my PhD. I really appreciate this effort.
Many thanks are giving to my friends. Special thanks to Abdulaziz Alhazmi and Ayman Alismail for making me feel home by speaking to me in Arabic and for keeping the traditional weekly lunch.
I thank my fellow labmates Lars von der Wense, Dr. Christine Weber, Benedict Seiferle, Franz Englbrecht, Sebastian Lehrack and Matthias Würl for the wonderful time that we had either in

the lab or outside the lab's wall. We spent great time together.
Last but not the least, I am indebted to my beloved parents, brothers and sisters for the infinite support and encouragements received during the journey towards my PhD degree. I know that being abroad for a long period of time has not been easy for you, therefore I deeply appreciate your emotional patience.